UNIVERSITÀ
DI PAVIA

SCUOLA DI ALTA FORMAZIONE DOTTORALE
MACRO-AREA SCIENZE E TECNOLOGIE

Dottorato di Ricerca in Scienze della Terra e dell'ambiente

Hugo W. van Schrojenstein Lantman

Garnets and their inclusions as key to unravel *P-T* paths, deformation history, and fluid-rock interaction in the ultrahigh-pressure metamorphic Lago di Cignana unit, Western Alps, Italy

Anno Accademico 2019-2020
Ciclo XXXIII

Coordinatore
Prof. Roberto Sacchi

Tutor
Prof. Matteo Alvaro

Co-tutors
Prof. Marco Scambelluri
Dr. David Wallis

Contents

CHAPTER 1
Introduction

This thesis deals with several issues that form the current limit of our knowledge on deep processes in the earth. Before introducing the individual topics that are treated in following chapters, various challenges and current questions in research on deeply subducted terranes are presented in section 1.1. Principles like metamorphic conditions, stress states in tectonics, and fluids in the deep earth are also introduced. This is followed by an overview the more conventional tools that can help us tackle these issues in section 1.2, emphasising the multitude of ways in which minerals can be recorders of these geological parameters. It is explained how garnet can be interrogated for this information, and in what ways these methods and techniques are currently falling short to obtain the full picture of metamorphism during subduction. Section 1.3 explains elastic geothermobarometry, a relatively new method that can overcome several challenges that limit other techniques, and thus will aid in taking the next step in our understanding of the deep Earth. Finally, section 1.4 presents scope of this thesis, and an overview of all chapters of this thesis.

1.1 Tectonics, pressure, temperature, and fluids

Since the formation of the Earth's crust, the dynamic upper zone of the Earth has been governed by plate tectonics, responsible for volcanism, earthquakes and other natural hazards, large-scale elemental cycles, and the formation of economically viable mineral deposits (Garson & Mitchell, 1977; Satake & Atwater, 2007; Spandler & Pirard, 2013; Jagoutz & Kelemen, 2015; Hawkesworth et al., 2017). As rocks are pushed, dragged, or buried deeper in the Earth, an increase in temperature and pressure causes the minerals in these rocks to respond accordingly, by mineral reactions. This process is called metamorphism. The reactions that take place in these rocks are directly controlled by metamorphic pressure *P* and temperature *T* (Spear, 1993).

1.1.1 The use of metamorphic conditions

Despite the unequivocal importance of subduction zones in modern plate tectonics, our understanding of processes at depth is limited due to the challenge of in-situ studies. This problem is overcome by techniques like seismic tomography, using variations in the propagation of seismic waves to study structures and composition of the deeper earth (Zhao, 2001; Deschamps & Trampert, 2003), or through the study of high-pressure metamorphic rocks exhumed at suture zones (Penniston-Dorland et al., 2015). The latter allows us to study the microscale fingerprints of mechanisms that cause, or are caused by, tectonics at depth. To place these processes into the context of active tectonics, their place within the subduction setting must be established, commonly done through metamorphic conditions. Metamorphic pressure is often considered to be a direct indicator of depth, based on the assumption that differential stress has an insignificant effect on pressure P, and therefore the density ϱ of overlying rocks and the gravitational acceleration g can be used to estimate depth h:

$$P = \rho \times g \times h$$

An example of the use of determining pressure-temperature conditions for metamorphic systems is to find the link between deep earthquakes and their origin, suggested to be related to mineral reactions and/or fluid activity (Abers et al., 2013; Okazaki & Hirth, 2016), which are sensitive to metamorphic conditions. Furthermore, the relation between pressure and temperature yields geothermal gradients. Temperature takes longer to re-equilibrate after perturbances of tectonic and/or magmatic origin, thus studying geothermal gradients aid in understanding geodynamic settings. Several issues regarding metamorphic conditions in subduction zones are still debated, for example the strong deviation between observed metamorphic conditions from exhumed rocks and conditions modelled for present day subducting slabs (Van Keken et al., 2018), possibly a bias on the exhumation of particularly hot subduction zone rocks. Another main issue concerns if pressure is a trustworthy measure for depth (Schmalholz & Podladchikov, 2014; Gerya, 2015; Tajčmanová et al., 2015; Yamato & Brun, 2017).

1.1.2 Differential stress and non-lithostatic pressure

The use of metamorphic pressure as indicator of depth relies on the assumption of lithostatic stress, where the three principal stress components are equal to the pressure exerted by overlying rocks. Principal stresses are defined as the isotropic components of the stress tensor, perpendicular to one another, where $\sigma 1$ is the highest stress and σ_3 is the lowest. A deviation from a lithostatic (or hydrostatic) state of stress can also have an impact on the pressure which is calculated as the mean of the principal stresses:

$$P = \frac{\sigma_1 + \sigma_2 + \sigma_3}{3}$$

Following this formula, an increase in σ_1 will result in an increase of P at a third of that value. Differential stress, defined as the difference between σ_1 and σ_3, is required for the deformation of rocks and thus tectonics as a whole. Therefore, true lithostatic pressure is an exception rather than the standard. The questions that follow, are how far the deviation from lithostatic pressure can be, how these deviations originate and on what scales they can occur.

A recent development in metamorphic geology is the recognition of strong pressure deviations in natural systems, experiments, numerical simulations, and analogue models (e.g., Gerya, 2015; Tajčmanová et al., 2015; Chu et al., 2017; Cionoiu et al., 2019; Luisier et al., 2019; Moulas et al., 2019). Additionally, well-studied high-pressure systems were re-interpreted as the result of local pressure perturbations (Vrijmoed et al., 2009; Jamtveit et al., 2018; Cutts et al., 2020). Several models have been developed for the distribution of stress and/or pressure in the earth that deviate from the lithostatic standard, also referred to as over- and underpressure. These models can be divided into grain- to outcrop-scale, and large scale.

Yamato and Brun (2017) provide a simple view on large-scale overpressure resulting from high differential stress in subduction zones, based on a trend between peak metamorphic pressure and post-peak isothermal pressure drop observed in (ultra)high-pressure ((U)H*P*) metamorphic rocks. This model involves a horizontal stress component which is significantly higher than the vertical lithostatic stress component during compression, and significantly lower during extension (see Figure 1.1a for the effect on P of an increased σ_1; this effect is reversed during extension). Based on this suggestion, the pressure recorded in subduction-zone rocks overestimates depth by a factor 2. Numerical simulations of subduction systems back up the occurrence of strong large-scale over- and underpressures (Gerya, 2015), up to GPa scale and/or over 50% higher than the lithostatic pressure. Depending on the style of subduction, the upper part of the downgoing slab experiences overpressure while the lower part is at underpressure, or vice versa (Li et al., 2010). The presence of such large-scale overpressures is challenging to reveal based on natural systems, as exhumed (U)H*P* metamorphic rocks are generally dismembered and only rarely yield insights into continuous km-scale pressure variations. So far, Pleuger and Podladchikov (2014) and Zuza et al. (2020) have proposed large-scale geological models that do not fit without overpressure.

An issue for the high differential stress proposed by Yamato and Brun (2017) is that it is generally deemed unfeasible on a large scale due to the comparatively low strength of rocks in the ductile regime (Stöckhert, 2002; Bürgmann & Dresen, 2008). The strength of dry rocks can be in the order of 100 MPa, however this is limited to the brittle regime. The occurrence of differential stress in the order of >300 MPa is uncommon and often described as short-lived exceptions (Küster & Stöckhert, 1999; Trepmann & Stöckhert, 2001; Andersen & Austrheim, 2006).

However, there is abundant evidence for small-scale overpressure. Host-inclusion systems with an inclusion that should undergo further volume increase than the host allows, are a prime example of pressure perturbations in earth systems. Straightforward examples are mineral inclusions, e.g. quartz in garnet (Alvaro et al., 2020) or coesite in diamond (Howell et al., 2010), which become stressed during exhumation as a result of contrasting elastic properties. Although these examples mostly regard systems that are inert from a metamorphic point of view as pressures are generated during exhumation, there are other similar systems that are relevant at depth. Generation of melt in an impermeable system can lead to overpressurization of the melt body and subsequent recording of higher pressures than lithostatic (Vrijmoed et al., 2009; Chu et al., 2017; Cutts et al., 2020). Additionally, it has been demonstrated though experiments, numerical simulations, and in natural systems, that rigid objects in a weaker deforming matrix will result in an increase of pressure in the matrix around the object (Moulas et al., 2014; Vrijmoed & Podladchikov, 2015; Cionoiu et al.,

2019; Luisier et al., 2019). The reverse is also valid for weak objects in a rigid matrix (Figure 1.1b; Tajčmanová et al., 2015; Jamtveit et al., 2018). In essence, metamorphic rocks form aggregates of materials with contrasting properties and when stressed, these rocks will be under a heterogeneous pressure (Tajčmanová et al., 2015). Fluids other than pressurised melt pockets also contribute to the heterogeneity of pressure in metamorphic systems, by fluid pressure which can be anywhere from lower than lithostatic (Küster et al., 1999; Connolly & Podladchikov, 2013) to higher than lithostatic, bound by the tensional strength of the rock (Connolly, 2010; Tarling et al., 2019).

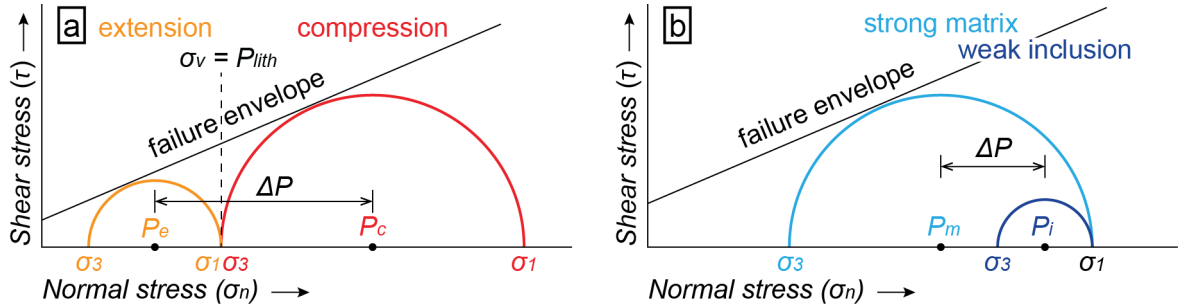

Figure 1.1: Two Mohr circle models for overpressure expressed by principal stresses. See main text for explanation on symbols and further background. For simplicity, σ_2 is not taken into account, although in reality it does matter for the magnitude of $\perp P$, which will be equal to or up to 1/3rd lower than in this diagram. (a) The model of tectonic over- and underpressure as proposed by Yamato and Brun (2017). Under a lithostatic vertical stress, a strong drop of horizontal stress from $\sigma_n >>> \sigma_v$ to $\sigma_n <<< \sigma_v$ at the transition from compression to extension, leads to a drop in P in the order of up to several GPa. Note how both systems deviate significantly from the lithostatic pressure value. (b) The overpressure model for weak inclusions in a strong matrix, modified after Jamtveit et al. (2018). This model relies on the elevation of σ_3 localized in a weak inclusion within a strong matrix under high differential stress.

Currently it is possible to estimate the magnitude of differential stress during deformation by the study of mineral deformation and how it relates differential stress and strain rate to other variables like (sub-) grain size or dislocation density (e.g., De Bresser, 1996; Stipp & Tullis, 2003; Goddard et al., 2020). However, there is no method available for determining the differential stress recorded in minerals during metamorphism rather than during deformation. Such a method would yield valuable insights into the evolution of differential stress during tectonics, how they relate to metamorphic pressure, and eventually, a way to accurately determine depth for metamorphic systems.

1.1.3 Fluids in the deep Earth

The importance of fluids in subduction systems is well established, as they control rheology, metamorphism, metasomatism, and volcanism (Peacock, 1990; Scambelluri & Philippot, 2001; Bürgmann & Dresen, 2008; Putnis & Austrheim, 2010; Gerya & Meilick, 2011; Spandler & Pirard, 2013). At a small scale, fluids are a key element in metamorphism as they drastically increase diffusion rates in grain boundaries, and thus enhance transport of elements to reaction sites (Rubie, 1986). In dry systems, this transport forms a limiting factor on reaction kinetics.

At the scale of subduction zones, the volumes of fluids released from the slab (Van Keken et al., 2011) and the difference in fluid composition from dehydration at the source rock to solute-rich fluid in the mantle wedge, require that fluid-rock interaction takes place along the intervening pathways (Hermann et al., 2006; Bebout, 2007; Herms et al., 2012; Dragovic et al., 2015; Taetz et al., 2018; Brovarone et al., 2020). A viable process of fluid interaction with high-pressure rocks is dissolution-precipitation (e.g., Ague & Nicolescu, 2014; Angiboust et al., 2017; Ferrando et al., 2017; Giuntoli et al., 2018). As this mechanism can take place at low differential stresses, it is widespread in subduction zones (Wassmann et al., 2011; Wassman & Stöckhert, 2013b). However,

as precipitation does not necessarily occur at or near the site of dissolution, this fluid-driven process can facilitate mass loss at the reaction sites and mass transfer in subducting slabs while leaving barely perceptible traces. Several factors such as complex solubilities and speciation, retrograde overprinting, limited exhumation and exposure, dismemberment of large-scale fluid systems, and other gaps in the rock record challenge our progress in this field. Exhumed high-pressure rocks that exhibit evidence of fluid-rock interaction should therefore be inspected carefully and be treated as open systems.

1.2 Garnet as recorder of geological events

Garnet is a common metamorphic mineral, forming a key part of mineral assemblages throughout a wide range of metamorphic facies and lithologies. Besides this widespread occurrence, garnet is also resistant to retrograde breakdown during exhumation, and can record the evolution, age, and conditions of its host rock in a variety of ways (Ague & Carlson, 2013; Baxter & Scherer, 2013; Baxter et al., 2013; Caddick & Kohn, 2013) (Figure 1.2). This capacity makes garnet one of the most useful metamorphic minerals to interrogate for information on geological events. Before going into detail about how garnet can store geological information, we must consider metamorphic mineral reactions in general and what they tell us.

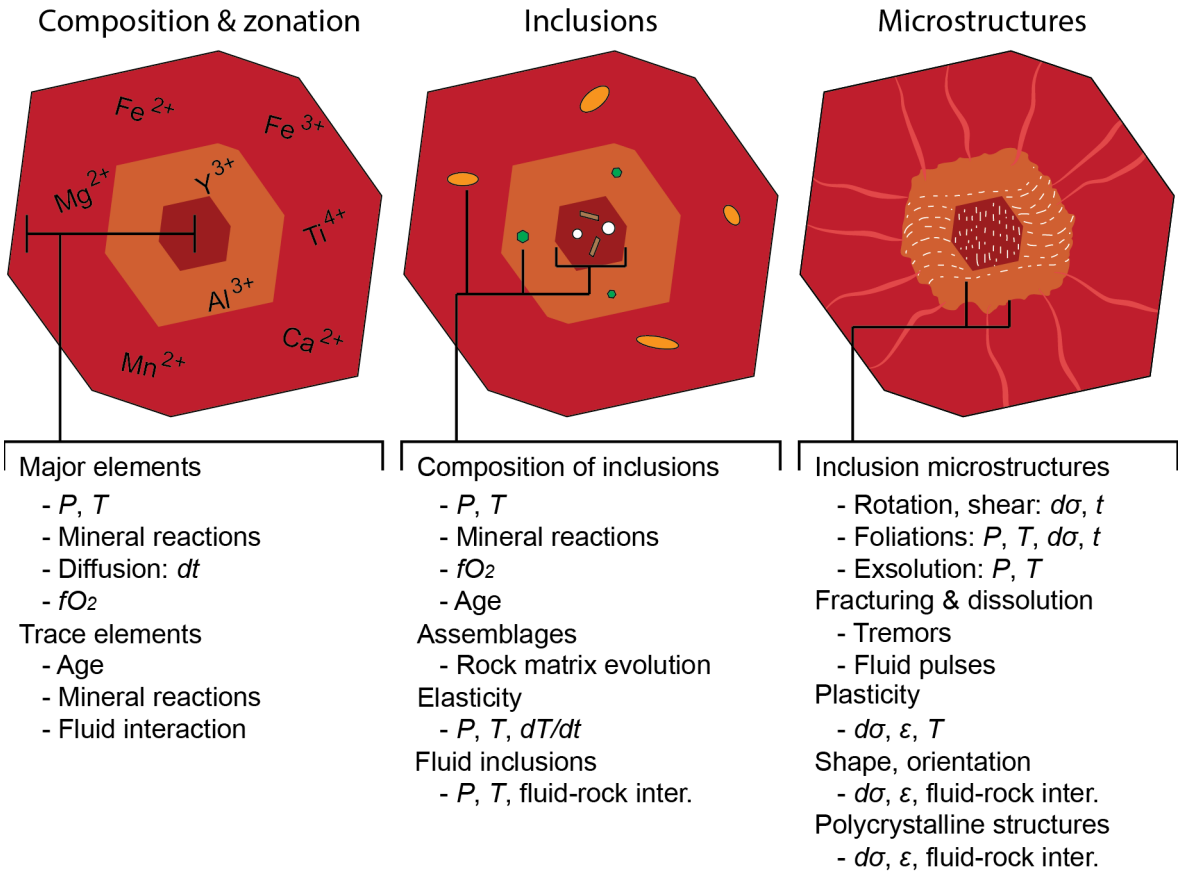

Figure 1.2: Subdivision in three types of ways in which garnet can be a recorder of events of metamorphism, deformation, fluid-rock interaction, and how it can record duration and age of events. This can be recorded in terms of chemical composition of major and trace elements and isotopes, through the preservation of inclusions of other minerals which are by themselves evidence for earlier metamorphic stages, and through microstructural evidence of growth and deformation.

1.2.1 Insight from mineral reactions

Thermodynamics dictate how temperature and pressure affect the stability, and by extent the composition, of minerals. As temperature and pressure conditions change, the free energy of a mineral can change at a different rate than that of a hypothetical isochemical counterpart, leading to a reaction at conditions where the counterpart becomes more stable and when kinetics allow for the reaction to occur. Commonly observed reactions are incorporated in definitions of metamorphic facies due to their use for distinguishing broad pressure-temperature ranges and by extension, tectonic settings. Key mineral reactions for high- and ultrahigh-pressure metamorphism are:

(1) $NaAlSi_3O_8$ (albite) = $NaAlSi_2O_6$ (jadeite) + SiO_2 (quartz)

(2) SiO_2 (quartz) = SiO_2 (coesite)

(3) C (graphite) = C (diamond)

Reaction 1 defines the eclogite metamorphic facies, where the presence of albite indicates lower pressure metamorphism, and the formation of coesite after quartz (reaction 2) is used as the definition for ultra-high pressure metamorphism (Chopin, 1984). The stability of diamond over graphite (reaction 3) is also commonly considered evidence for ultrahigh-pressure metamorphism (Sobolev & Shatsky, 1990). The mechanism of diamond formation and thus the involved reaction is still debated, but it is likely not formed from graphite (Martin & Hammouda, 2011; Sverjensky et al., 2014; Smith et al., 2016; Maeda et al., 2017; Frezzotti, 2019). As result, the observation of relict coesite and jadeite component in clinopyroxene (omphacite), are commonly used indicators for deep subduction metamorphism. Other tools often utilized for the determination of these metamorphic conditions, are experiments and thermodynamic modelling for the determination of mineral reactions and assemblages (e.g., Hermann, 2003; Massonne & Fockenberg, 2012).

1.2.2 Mineral composition

Not all (ultra)high-pressure rocks have the right bulk chemical composition for the previously mentioned reactions to have occurred, but there are other ways in which mineral reactions can indicate extreme metamorphic pressures. The composition of minerals is also affected by changes in pressure and temperature, as various endmembers of a solid solution series have different thermodynamic properties. In order for the composition of a mineral to be dependent on *P-T*, an exchange with one or more other minerals must be able to take place. Basic examples involve the exchange of Mg and Fe between two minerals, but these exchange reactions can involve many more minerals. Many cation exchange geothermobarometers have been calibrated to utilize these reactions (e.g., Krogh & Råheim, 1978; Krogh Ravna & Terry, 2004), and thermodynamic modelling allows for the study of mineral compositions as function of *P-T* (Powell & Holland, 2010).

Minerals that grow gradually over longer time spans may form compositional zoning if *P-T* conditions, and as result also the fractionation of free elements between minerals, evolve in response to active tectonics (e.g., Dutrow & Henry, 2011; Caddick & Kohn, 2013). As newer grown zones surround and protect the inner part of the crystal from re-equilibration, a wide range of compositions can be preserved (Figure 1.3a), and in some cases even recording multiple orogenic cycles (Rubatto et al., 2011). Garnet in particular is commonly studied for its capacity to preserve multi-component internal zoning, yielding high quality insight into the evolution of metamorphic conditions (e.g., Le Bayon et al., 2006; Herwartz et al., 2011). Combining this zonation in garnet with thermodynamic modelling based on corresponding changes to the effective bulk chemical composition of the rock, or rather the volume of equilibrium relevant for the garnet, it is possible to reconstruct the entire P-T path of garnet growth (Tinkham & Ghent, 2005; Moynihan & Pattison, 2013; Vrijmoed & Hacker, 2014; Lanari et al., 2017). This approach is particularly powerful

when combined with inclusions preserved in garnet (see section 1.2.3).

Oscillatory zonation is a succession of reversed compositional changes akin to tree rings, a peculiar type of zonation that can form by various mechanisms and is often linked to disequilibrium (e.g. Stowell et al., 2011), thus rendering garnet composition unsuitable for thermodynamic modelling. Open-system behaviour caused by the circulation of external fluids can alter the growth environment of garnet in cycles, recording valuable data on the origin and composition of the fluids (Clechenko & Valley, 2003; Park et al., 2019). In exceptional cases, an oscillation or irregularity in the *P-T* path can result in oscillatory zoning (García-Casco et al., 2002; Kohn, 2004).

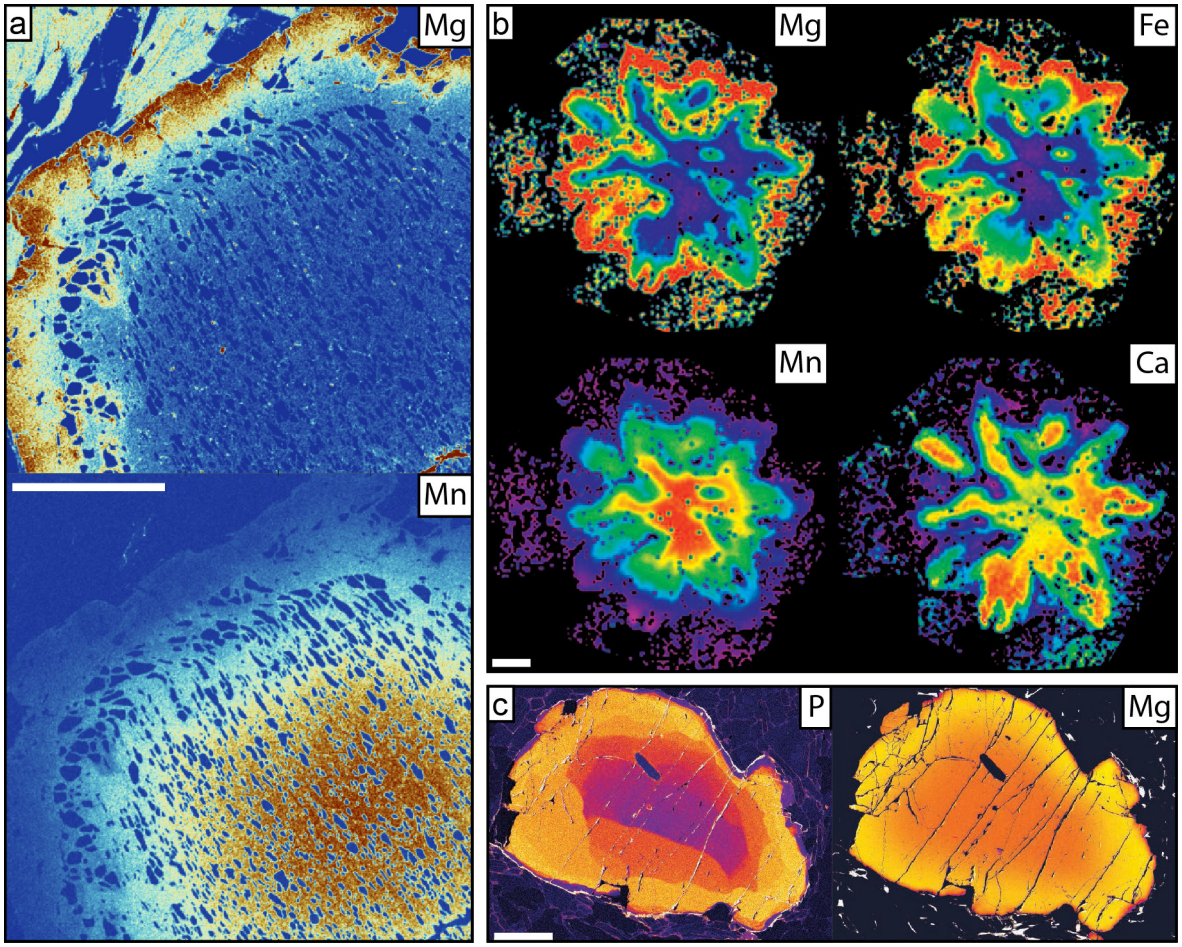

Figure 1.3: Examples of different types of zonation in garnet, illustrated by element distribution maps. (a) Regular, concentric metamorphic zonation of Mg and Mn of a metapelite from the Sierra de los Filabres, SE Spain. Temperatures experienced by this garnet were not sufficient to result in significant diffusion (Van Schrojenstein Lantman et al., unpublished data). (b) Chaotic element distribution as result of textural sector zoning of Mg, Fe, Mn and Ca in garnet that grew in a chemical disequilibrium, from Connecticut, USA (modified after Wilbur & Ague, 2006). (c) P and Mg element distribution in eclogite-facies granulite garnet from the Saxon Granulite Massif, Germany. The distribution of P still exhibits the zonation caused by a process of dissolution-reprecipitation, whereas Mg has been redistributed by diffusion (modified after Ague & Axler, 2016). White scale bars represent 500 μm.

Parts of the geological record preserved in compositional zoning can be obscured by mineral dissolution phases interrupting growth, mineral replacement, irregular and/or disequilibrium growth, and diffusion (Figure 1.3; Wilbur & Ague, 2006; Caddick et al., 2010; Angiboust et al., 2011; Ague & Axler, 2016; Rubatto et al., 2020). However, these each do provide other insights into the conditions during crystal growth, modification, and/or dissolution-precipitation. Additionally, diffusion of garnet zonation can be used as a tool for unravelling the timescale of

heating stages (Caddick et al., 2010).

The previously discussed geothermobarometry methods all rely on the assumption of equilibrium between the targeted minerals. In reality, many situations of disequilibrium have been observed, often the result of overstepping due to sluggish kinetics and nucleation or reaction affinities (Rubie, 1998; Waters & Lovegrove, 2002; Pattison et al., 2011). Overstepping can also result in compositional zoning in garnet that appear to record different P-T conditions than in reality (Spear & Wolfe, 2019). As not all elements behave similarly, it is likely depending on metamorphic grade that equilibrium on a thin-section scale was only achieved by certain elements (Carlson, 2002).

In order to apply trace element thermometers such as Zr-in-rutile, Ti-in-zircon and Ti-in-quartz (Zack et al., 2004; Watson & Harrison, 2005; Wark & Watson, 2006), all three minerals need to be in equilibrium together. If this is not the case, the system is either not saturated in the required element, or may even lead to higher concentration of this element than is expected from equilibrium (Ferry & Watson, 2007). Other issues arise from bulk composition adjustments caused by open-system behaviour, and element fractionation and capture in growing crystals (Vance & Mahar, 1998; Evans & Bickle, 2005; Tinkham & Ghent, 2005; Goncalves et al., 2013). Finally, certain methods may not be calibrated for unconventional mineral compositions, for example by the presence of an element that only fractionates into one mineral or an uncommon bulk composition, which can also greatly alter the stability of certain minerals (Ashworth, 1975).

1.2.3 Preservation of inclusions

Similar to how mineral compositions formed during an earlier metamorphic stage can be preserved in the core of crystals, so can other minerals be entrapped during the growth of a host crystal, and preserved as inclusions. Inclusions form an effective way of assessing metamorphic evolution in a rock matrix that is completely overprinted by later stages, particularly when the inclusion minerals become highly unstable between formation and exhumation. Coesite is an example of such an unstable mineral that is only rarely observed as intergranular phase (Liou & Zhang, 1996), and is more commonly observed as inclusions in minerals that are more resistant to breakdown such as garnet, omphacite, tourmaline, diamond, apatite, and dolomite (e.g., Chopin, 1984; Schertl & Okay, 1994; Reinecke, 1998). The composition of inclusions is also preserved when post-entrapment conditions did not reach high enough temperatures at sufficient timescales to result in effective volume diffusion. Not only single crystals are trapped as inclusions in garnet. Inclusions of fluids and melts can also be preserved, representing the composition of the fluid in which the host mineral grew (Frezzotti et al., 2011; Korsakov et al., 2011; Cesare et al., 2015).

Certain processes can affect the preservation of inclusions, like host fracturing (Whitney, 1996), melting of inclusions within the host (Perchuk et al., 2008), and chemical interaction between inclusion and host (Frezzotti et al., 2011; Zhou et al., 2020). However, when studied thoroughly, inclusions form an effective way of reconstructing the evolution of the mineral assemblage of the rock matrix, and how the compositions of those minerals evolved during the growth of their host mineral.

1.2.4 Microstructures

Microstructural aspects of garnet can record deformation and metamorphism features from before, during and after its growth (Figure 1.2). A well-studied example of a microstructure that strongly relies on the matrix before and during garnet growth, is that of inclusion trails and snowball-garnet. A metamorphic fabric that exhibits heterogeneous distribution of minerals is likely to lead to different quantities of inclusions as soon as garnet grows over it. Often this is the case for

quartz inclusions, as many garnet-forming reactions do not consume quartz (Hawkins et al., 2007; Robyr et al., 2007). As a result, the foliation before garnet growth is preserved as inclusions. When the rock fabric actively undergoes deformation, this can result in a complex sequence of different orientations of inclusion trails. The origin of rotated inclusion trails is still debated, resulting from syn-growth rotation of the garnet, and/or rotation of the dominant foliation (Bell & Johnson, 1989; Passchier et al., 1992; Robyr et al., 2009). In the latter case, the orientation of inclusion trails can be used to reconstruct large-scale tectonics (e.g., Aerden, 2004; Aerden & Ruiz-Fuentes, 2020).

Other single-crystal microstructures in garnet are generally the result of deformation (Figure 1.2). The majority of deformation in garnet will result in grain flattening, be it through ductile deformation (Kleinschrodt & Duyster, 2002) or pressure solution (Smit et al., 2011). Fracturing and cataclasis are also common microstructural features in garnet deformed in the brittle regime or as result of extreme strain rates in the ductile regime (e.g., Prior, 1994; Trepmann & Stöckhert, 2002; Yamato et al., 2019).

The arrangement of several garnets into polycrystal structures is also a potential indicator of growth and deformation features. Coronitic garnet is a disequilibrium texture of garnet crystals along grain contacts of partially reacted magmatic precursor minerals, formed in diffusion-limited metamorphism and signifying an incomplete reaction (Mørk, 1986). Garnet aggregates can also grow from separate nucleation and eventual coalescence between individual garnets, aligning their crystallographic orientation and resulting in one large polycrystalline mass (Spiess et al., 2001). In contrast to these growth-related microstructures, garnets stacked into chains resulted the motion of rigid garnets in an actively deforming matrix, eventually aligning the garnets (Massey et al., 2011).

1.2.5 Interaction of stress, deformation and composition

Geothermobarometry normally assumes that the pressure in a system is hydrostatic. Under natural conditions, hydrostatic pressure is exception rather than rule, yet the effect of differential stress on mineral reactions is poorly understood (Wheeler, 2014). One example where a reaction is affected by differential stress, is the quartz to coesite transition, which depends on the maximum principal stress rather than the mean stress or confining pressure (Richter et al., 2016). This study also suggests that deformation enhances reaction kinetics. Another example is that the dehydration of gypsum is not controlled by confining pressure, but rather by fluid pressure (Llana-Fúnez et al., 2012).

A part of the effect of differential stress on metamorphism and mineral reactions falls back on differential stress controlling pressure and being problematic as proxy for depth. A study by Moore et al. (2019) outlines how reaction products in grain boundaries between plagioclase are dependent on the orientation of the grain boundary with respect to the orientation of σ_1 and σ_3. The result is that two distinct mineral assemblages are observed representing 0.9 and 1.1 GPa respectively, formed simultaneously within the same domain of the rock. This case is similar to the locally-induced reaction of calcite to aragonite in the experiment of Cionoiu et al. (2019). Without context, these minerals or mineral assemblages could be interpreted as separate events at different depths. Even if the difference in pressure caused by local perturbations and differential stress is not sufficient to cross a discrete mineral reaction boundary, it can still result in a significant change in mineral composition within the system (Tajčmanová et al., 2015).

1.3 Elastic geothermobarometry

The recent development of elastic geothermobarometry provides a solution for metamorphic, hydrothermal and possibly even magmatic systems where any of the previously discussed problems prevent conventional geothermobarometry. This method relies on the contrast in elastic properties between a stiff host and a soft inclusion. Figure 1.4 provides a schematic overview of the principle behind the development of elastic strains in host-inclusion systems. As a mineral is entrapped by a host, thus becoming an inclusion, the trapped mineral occupies the same volume as the cavity within the host where this inclusion is located. When *P-T* conditions change following entrapment, the inclusion and host will respond differently to the changing conditions. In case the inclusion is driven to expand further than the host mineral allows it to, the inclusion and the adjacent part of the host will become strained to partially accommodate this expansion. The elastic strain of inclusions can be determined by analysis with X-ray diffraction or Raman spectroscopy, and subsequently an isomeke (line in *P-T* space for a constant inclusion pressure) can be calculated for the entrapment conditions of the inclusion. This method has been carefully calibrated and applied to quartz in garnet, zircon in garnet, and several minerals in diamond (Anzolini et al., 2019; Bonazzi et al., 2019; Zhong et al., 2019; Alvaro et al., 2020; Campomenosi et al., 2020; Nestola, 2020 and references therein).

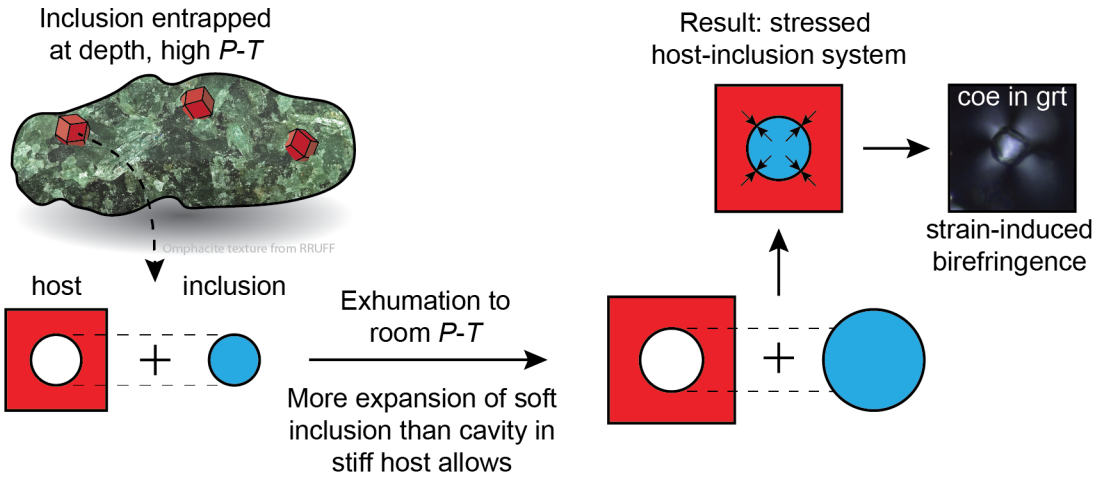

Figure 1.4: Schematic diagram of the basic concept behind elastic strains in inclusions. See main text for further explanation of how this method works. Figure on the right titled "coe in grt" is an optical micrograph of a coesite inclusion in garnet under cross-polarized light.

The compressibility and thermal expansion of minerals, which determine how volume changes under influence of pressure and temperature respectively, do not scale equally between minerals. The ratios of compressibility and thermal expansion between host and inclusion will determine the slope of the isomekes. Host-inclusion systems where the contrast in elastic properties is largest for compressibility will function as a geobarometer, for example quartz inclusions in garnet. Alternatively, zircon is less compressible than garnet under relevant metamorphic conditions, yet due to the difference in thermal expansion, zircon inclusions in garnet function as geothermometer (Zaffiro, 2020). In order to use a single type of inclusion to determine *P-T* conditions of garnet growth, an independent geothermobarometer may be required. It is also possible to combine several host-inclusion systems to obtain well-constrained *P-T* results (Zhong et al., 2019).

When reversing this method, strain states can be calculated for inclusions entrapped at defined metamorphic conditions. The resulting strain states will be valid for host-inclusion systems

that formed under hydrostatic stress, as differential stress during entrapment can currently not be taken into account. However, this also means that any significant deviation from these strain states obtained from inclusions can indicate differential stresses during entrapment (Bonazzi et al., 2019). Thus, studying the elastic strains of inclusions provides a direct, yet currently unquantifiable, approach of probing not only the *P-T* conditions of entrapment but also potentially the stress state.

Host-inclusion systems can be (partially) reset (Zhong et al., 2018; Cesare et al., 2021), which relies on modification of the host, allowing for a reset of the hypothetical difference in volume of the relaxed inclusion and host. Plastic deformation of the host is the expected mechanism for resetting, essentially imposing a closure temperature on the system due to the strong temperature effect on plastic deformation (Zhong et al., 2020). However, a significant strain may be necessary to overcome the strength of the host. As internal strain is also adjusted during resetting and depends on the initial entrapment, the potential for resetting must be considered separately per case.

1.4 Scope of this thesis

The aim of this thesis is to utilize and further develop the use of garnets and inclusions therein as tool of unravelling metamorphic conditions, fluid-rock interaction, deformation, stress, and strain, in systems where these are otherwise unobtainable. The ultrahigh-pressure metamorphic Lago di Cignana unit (LCU) in the Western Alps of Italy is the focal point of this thesis. This locality provides an example of fluid-rich metamorphic rocks within the subduction zone, allowing us to test several of the topics summarized in Chapter 1, with the aim of a combined understanding of the extent and interaction of stress state, deformation, and fluid-rock interaction.

Chapter 2 provides a background on the geology of the LCU, starting out from the larger geological setting of the Western Alps and zooming in step-wise to the outcrop scale. Field observations and samples are also be described here.

Chapter 3 contains detailed descriptions of all the methods, analytical techniques, and calculations used in this thesis.

Chapter 4 is the paper titled *Extensive fluid-rock interaction and pressure solution in a UHP fluid pathway recorded by garnetite, Lago di Cignana, Western Alps* and is accepted for publication in Journal of Metamorphic Geology under the same title by Van Schrojenstein Lantman, Scambelluri, Gilio, Wallis and Alvaro. This paper combines the study of garnet microstructures, chemical composition, and quartz inclusions in garnet, of a garnetite-bearing quartzite from the LCU, with the aim of reconstructing the evolution of metamorphism and fluid-rock interaction. These lithologies contain a record of pulsed fluid flow throughout prograde and peak subduction metamorphism, resulting in dissolution of quartz, carbonates and garnet. The latter are concentrated as result of their relative insolubility, comprising a newly described mechanism for the formation of garnetite. The formation of what are essentially garnet stylolites, results in pressure solution and grain boundary migration as the garnet crystals get into contact. Quartz inclusions trapped in euhedral garnet overgrowths on deformed garnetite are analysed by Raman spectroscopy for their elastic strain, resulting in the insight that the host garnet grew at (near-) hydrostatic conditions in a fluid-rich environment. Overall, the paper provides an extreme example of fluid-rock interaction along a long-lived major fluid pathway accommodating the migration of fluids produced in the subducting slab.

Chapter 5, titled *Garnet deformation and recrystallization at (U)HP-LT conditions: pressure solution and grain-boundary migration*, is a study on the microstructural aspects of garnet crystals within several garnetite bodies of the Lago di Cignana unit. Within this chapter, the history of deformation that these rocks underwent is explored, to understand how garnet deforms in a fluid rich environment at temperatures where plastic deformation is not feasible. Furthermore, this microstructural analysis provides extra constraints on the formation and evolution of the garnetite bodies as was initially established in Chapter 4, and the role that these lithologies play in the rheology of the metasedimentary unit that they are a part of. This chapter provides the first detailed look at grain-boundary migration within garnet, and is also the first to analyse pressure solution at ultra-high pressures in-depth. Particularly because of the latter, this research is the next step taken in understanding the behaviour of cold slabs at great depths, as pressure solution creep was predicted at these conditions but never confirmed before this study.

Chapter 6, titled *Elastic geothermobarometry on zircon in garnet: resetting of a host-inclusion system by fracturing and sealing, and the preservation of metastable inclusions*, studies the effect of fracturing and sealing of garnet, on zircon and coesite inclusions preserved therein. Chemical composition relationships link this episode of fracturing and sealing to the outermost rim of these garnets, which contains quartz inclusions. Therefore, the preservation of coesite within the fractured garnet mantle is peculiar. To test the degree to which these inclusions were affected by the fracturing, zircons in the same zone as the coesite inclusions were analysed with Raman spectroscopy to obtain their elastic state of strain, and calculate conditions of entrapment. These zircon inclusions yield entrapment conditions that are at temperatures significantly higher than the retrograde, clockwise *P-T* path determined for the Lago di Cignana unit. It is currently unclear what the cause of this overestimation is, however if it is indeed related to resetting of the host, then the fracturing and sealing must be a rapid process in the order of days for the coesite to be preserved.

Chapter 7, titled *Trace element analysis of garnet and its inclusions: separating contamination from mineral composition*, is focused on the trace element aspects of the garnetite-bearing quartzite that is studied in detail in Chapter 4. The first purpose of trace analysis of garnet within this system is to study the different garnet populations in order to gain further insight into the metamorphic evolution and fluid-rock interaction recorded by garnet. One of the garnet populations is consistently contaminated by sub-micron inclusions of rutile and minor zircon, however. Using the varying degree of contamination, data is filtered into garnet composition and contamination composition. Zr-in-rutile geothermometry is then applied to the contaminant rutile.

Chapter 8 is part of the manuscript titled *Trace-element migration during crystal-plastic deformation in UHP rutile: dislocations in low-angle boundaries as high-diffusivity pathways* and is currently in advanced preparation to be submitted to a journal, by R. Verberne, H.W. van Schrojenstein Lantman et al. In this chapter, the formation and deformation of rutile in an omphacite vein in eclogite from the LCU are explored. Firstly, the conditions of rutile growth and vein formation are studied by identification of quartz and coesite inclusions, and Zr-in-rutile thermometry. Subsequently, we analysed the deformation of large rutile grains that resulted in the formation of low-angle boundaries using a range of techniques down to the atom scale, including transmission electron microscopy and atom probe tomography. This analysis demonstrates how low-angle boundaries acted as fast diffusion pathways during metamorphism.

Chapter 9 summarises the conclusions of this PhD thesis, outlines how the results advance our knowledge in this field of study, and explores future steps to take.

Appendix A is a repository for data used in Chapter 4, namely full Electron Probe Micro-Analysis (EPMA) analyses, Raman peak positions, shifts, and elastic strains in quartz. This Appendix also contains a figure displaying the locations of EPMA analyses.

Appendix B contains section overviews with Electron Backscatter Diffraction (EBSD) map locations, an Euler colormap for crystal orientation figures used in Chapter 5, and all EBSD maps used for aspect ratio and SPO analysis in Chapter 5.

Appendix C contains the peak positions and fitting errors for Raman spectra of zircon inclusions and the zircon reference crystal used in Chapter 6.

Appendix D is a compilation of all the LA-ICP-MS data including uncertainties and detection limits, mostly used in Chapter 7 but also in Chapter 8.

Appendix E contains the acquisition conditions for rutile needles analysed in Chapter 8.

References

Abers, G.A., Nakajima, J., Van Keken, P.E., Kita, S., Hacker, B.R., 2013. Thermal-petrological controls on the location of earthquakes within subducting plates. Earth and Planetary Science Letters, 369–370, 178–187

Aerden, D.G.A.M., 2004. Correlating deformation in Variscan NW-Iberia using porphyroblasts; implications for the Ibero-Armorican Arc. Journal of Structural Geology, 26(1), 177–196

Aerden, D.G.A.M., Ruiz-Fuentes, A., 2020. X-ray computed micro-tomography of spiral garnets: A new test of how they form. Journal of Structural Geology, 136, 104054

Ague, J.J., Carlson, W.D., 2013. Metamorphism as Garnet Sees It: The Kinetics of Nucleation and Growth, Equilibration, and Diffusional Relaxation. Elements, 9, 439–445

Ague, J.J., Nicolescu, S., 2014. Carbon dioxide released from subduction zones by fluid-mediated reactions. Nature Geoscience, 7, 355-360. DOI: 10.1038/NGEO2143

Ague, J.J., Axler, J.A., 2016. Interface coupled dissolution-reprecipitation in garnet from subducted granulites and ultrahigh-pressure rocks revealed by phosphorous, sodium, and titanium zonation. American Mineralogist, 101, 1696–1699

Alvaro, M., Mazzucchelli, M.L., Angel, R.J., Campomenosi, N., Scambelluri, M., Nestola, F., Korsakov, A., Tomilenko, A.A., Marone, F., Morana, M., 2020. Geology, 48(1), 24–28

Andersen, T.N., Austrheim, H., 2006. Fossil earthquakes recorded by pseudotachylites in mantle peridotite from the Alpine subduction complex of Corsica. Earth and Planetary Science Letters, 242(1-2), 58–72

Angiboust, S., Agard, P., Raimbourg, H., Yamato, P., Huet, B., 2011. Subduction interface processes recorded by eclogite-facies shear zones (Monviso, W. Alps). Lithos, 127, 222–238

Angiboust, S., Yamato, P., Hertgen, S., Hyppolito, T., Bebout, G.E., Morales, L., 2017. Fluid pathways and high-*P* metasomatism in a subducted continental slice (Mt. Emilius Klippe, W. Alps). Journal of metamorphic geology, 35, 471–492

Anzolini, C., Nestola, F., Mazzucchelli, M.L., Alvaro, M., Nimis, P., Gianese, A., Morganti, S., Marone, F., Campione, M., Hutchinson, M.T., Harris, J.W., 2019. Depth of diamond formation obtained from single periclase inclusions. Geology, 47(3), 219–222

Ashworth, J.R., 1975. Staurolite at Anomalously High Grade. Contrib. Mineral Petrol., 53, 281–291

Bebout, G.E., 2007. Metamorphic chemical geodynamics of subduction zones. Earth and Planetary Science Letters, 260, 373–393

Baxter, E.F., Caddick, M.J., Ague, J.J., 2013. Garnet: Common Mineral, Uncommonly Useful. Elements, 9, 415–419

Baxter, E.F., Scherer, E.E., 2013. Garnet Geocrhonology: Timekeeper of Tectonometamorphic Processes. Elements, 9, 433–438

Bell, T.H., Johnson, S.E., 1989. Porphyroblast inclusion trails: the key to orogenesis. Journal of Metamorphic Geology,

7, 279–310

Bonazzi, M., Tumiati, S., Thomas, J.B., Angel, R.J., Alvaro, M., 2019. Assessment of the reliability of elastic geobarometry with quartz inclusions. Lithos, 350–351, 105201

Brovarone, A.V., Tumiati, S., Piccoli, F., Ague, J.J., Connolly, J.A.D., Beyssac, O., 2020. Fluid-mediated selective dissolution of subducting carbonaceous material: Implications for carbon recycling and fluid fluxes at forearc depths. Chemical Geology, 549, 119682

Bürgmann, R., Dresen, G., 2008. Rheology of the Lower Crust and Upper Mantle: Evidence from Rock Mechanics, Geodesy, and Field Observations. Annual Review of Earth and Planetary Sciences, 36, 531–567

Caddick, M.J., Konopásek, J., Thompson, A.B., 2010. Preservation of Garnet Growth Zoning and the Duration of Prograde Metamorphism. Journal of Petrology, 51(11), 2327-2347

Caddick, M.J., Kohn, M.J., 2013. Garnet: Witness to the Evolution of Destructive Plate Boundaries. Elements, 9, 427–432

Campomenosi, N., Rubatto, D., Hermann, J., Mihailova, B., Scambelluri, M., Alvaro, M., 2020. Establishing a protocol for the selection of zircon inclusions in garnet for Raman thermobarometry. American Mineralogist 105 992–1001

Carlson, W.D., 2002. Scales of disequilibrium and rates of equilibrium during metamorphism. American Mineralogist, 87, 185–204

Cesare, B., Acosta-Vigil, A., Bartli, O., Ferrero, S., 2015. What can we learn from melt inclusions in mignatites and granulites? Lithos, 239, 186–216

Cesare, B., Parisatto, M., Mancini, L., Peruzzo, L., Franceschi, M., Tacchetto, T., Reddy, S.M., Spiess, R., Nestola, F., Marone, F., 2021. Mineral inclusions are not immutable: Evidence of post-entrapment thermally-induced shape change of quartz in garnet. Earth and Planetary Science Letters, 555, 116708

Chopin, C., 1984. Coesite and pure pyrope in high-grade blueschists of the Western Alps: a first record and some consequences. Contributions to Mineralogy and Petrology, 86, 107–118

Chu, X., Ague, J.J., Podladchikov, Y., Tian, M., 2017. Ultrafast eclogite formation via melting-induced overpressure. Earth and Planetary Science Letters, 479, 1–17

Cionoiu, S., Moulas, E., Tajčmanová, L., 2019. Impact of interseismic deformation on phase transformations and rock properties in subduction zones. Scientific Reports, 9, 19561

Clechenko, C.C., Valley, J.W., 2003. Oscillatory zoning in garnet from the Wilsboro Wollastonite Skarn, Adirondack Mts, New York: a record of shallow hydrothermal processes preserve in a granulite facies terrane. Journal of Metamorphic Geology, 21, 771–784

Connolly, J.A.D., 2010. The Mechanics of Metamorphic Fluid Expulsion. Elements, 6, 165–172

Connolly, J.A.D., Podladchikov, Y.Y., 2013. A Hydromechanical Model for Lower Crustal Fluid Flow. In: Metasomatism and the Chemical Transformation of Rock. Lecture Notes in Earth System Sciences. Springer, Berlin, Heidelberg

Cutts, J.A., Smit, M.A., Vrijmoed, J.C., 2020. Evidence for non-lithostatic pressure in subducted continental crust. Contributions to Mineralogy and Petrology, 175, 3

De Bresser, J.H.P., 1996. Steady state dislocation densities in experimentally deformed calcite materials: Single crystals versus polycrystals. Journal of Geophysical Research, 101(B10),22189-22201

Deschamps, F., Trampert, J., 2003. Mantle tomography and its relation to temperature and composition. Physics of the Earth and Planetary Interiors, 140, 277–291

Dragovic, B., Baxter, E.F., Caddick, M.J., 2015. Pulsed dehydration and garnet growth during subduction revealed by zoned garnet geochronology and thermodynamic modeling, Sifnos, Greece. Earth and Planetary Science Letters, 413, 111–122

Evans, K.A., Bickle, M.J., 2005. An investigation of the relationship between bulk composition, inferred reaction progress and fluid-flow parameters for layered micaceous carbonates from Maine, USA. Journal of Metamorphic Geology, 23, 181–197

Ferrando, S., Groppo, C., Frezzotti, M.L., Castelli, D., Proyer, A., 2017. Dissolving dolomite in a stable UHP mineral assemblage: Evidence from Cal-Dol marbles of the Dora Maira Massif (Italian Western Alps). American Mineralogist, 102, 42–60

Ferry, J.M., Watson, E.B., 2007. New thermodynamic models and revised calibrations for the Ti-in-zircon and Zr-in-rutile thermometers. Contributions to Mineralogy and Petrology, 154, 429–437 DOI: 10.1007/s00410-007-0201-0

Frezzotti, M.L., Selverstone, J., Sharp, Z.D., Compagnoni, R., 2011. Carbonate dissolution during subduction revealed by diamond-bearing rocks from the Alps. Nature Geoscience, 4, 703–706 DOI: 10.1038/NGEO1246

Frezzotti, M.L., 2019. Diamond growth from organic compounds in hydrous fluids deep within the Earth. Nature Communications, 10, 49

García-Casco, A., Torres-Roldán, R.L., Millán, G., Monié, P., Schneider, J., 2002. Oscillatory zoning in eclogitic garnet and amphibole, Northern Serpentinite Melange, Cuba: a record of tectonic instability during subduction? Journal of Metamorphic Geology, 20, 581–598

Garson, M.S., Mitchell, A.H.G., 1977. Mineralization at destructive plate boundaries: a brief review. Geological Society, London, Special Publications, 7, 81–97

Gerya, T.V., Meilick, F.I., 2011. Geodynamic regimes of subduction under an active margin: effects of rheological weakening by fluids and melts. Journal of Metamorphic Geology, 29, 7–31

Gerya, T., 2015. Tectonic overpressure and underpressure in lithospheric tectonics and metamorphism. Journal of Metamorphic Geology, 33, 785–800

Giuntoli, F., Lanari, P., Engi, M., 2018. Deeply subducted continental fragments - Part 1: Fracturing, dissolution-precipitation, and diffusion processes recorded by garnet textures of the central Sesia Zone (western Italian Alps). Solid Earth, 9, 167–189

Goddard, R.M., Hansen, L.N., D. Wallis, M. Stipp, Holyoke, C.W. III, Kumamoto, K.M., Kohlstedt, D.L., 2020. A Subgrain-Size Piezometer Calibrated for EBSD. Geophysical Research Letters

Goncalves, P., Marquer, D., Oliot, E., Durand, C., 2013. Thermodynamic Modeling and Thermobarometry of Metasomatized Rocks. In: D.E. Harlov and H. Austrheim, Metasomatism and the Chemical Transformation of Rock, Lecture Notes in Earth System Sciences, Springer-Verlag Berlin Heidelberg

Hawkesworth, C.J., Cawood, P.A., Dhuime, B., Kemp, T.I.S., 2017. Earth's Continental Lithosphere Through Time. Annual Review of Earth and Planetary Sciences, 45, 169–98

Hawkins, A.T., Selverstone, J., Brearly, A.J., Beane, R.J., Ketcham, R.A., Carlson, W.D., 2007. Origin and mechanical significance of honeycomb garnet in high-pressure metasedimentary rocks from the Tauern Window, Eastern Alps. Journal of Metamorphic Geology, 25, 565–583

Hermann, J., 2003. Experimental evidence for diamond-facies metamorphism in the Dora-Maira massif. Lithos, 70, 163–182

Hermann, J., Spandler, C., Hack, A., Korsakov, A.V., 2006. Aqueous fluids and hydrous melts in high-pressure and ultra-high pressure rocks: Implications for element transfer in subduction zones. Lithos, 92, 399–417

Herms, P., John, T., Bakker, R.J., Schenk, V., 2012. Evidence for channelized external fluid flow and element transfer in subducting slabs (Raspas Complex, Ecuador). Chemical Geology, 310–311, 79–96

Herwartz, D., Nagel, T.J., Münker, C., Scherer, E.E., Froitzheim, N., 2011. Tracing two orogenic cycles in one eclogite sample by Lu-Hf garnet chronometry. Nature Geoscience, 4, 178–183

Howell, D., Wood, I.G., Dobson, D.P., Jones, A.P., Nasdala, L., Harris, J.W., 2010. Quantifying strain birefringence halos around inclusions in diamond. Contributions to Mineralogy and Petrology, 160, 705–717

Jagoutz, O., Kelemen, P.B., 2015. Role of Arc Processes in the Formation of Continental Crust. Annual Review of Earth and Planetary Sciences, 43, 363–404

Jamtveit, B., Moulas, E., Andersen, T.B., Austrheim, H., Corfu, F., Petley-Ragan, A., Schmalholz, S.M., 2018. High Pressure Metamorphism Caused by Fluid Induced Weakening of Deep Continental Crust. Scientific Reports, 8, 17011

Kleinschrodt, R., Duyster, J.P., 2002. HT-deformation of garnet: an EBSD study on granulites from Sri Lanka, India and the Ivrea Zone. Journal of Structural Geology, 24, 1829–1844

Kohn, M.J., 2004. Oscillatory- and sector-zoned garnets record cyclic (?) rapid thrusting in central Nepal. Geochemistry Geophysics Geosystems, 5, 12

Korsakov, A.V., Dieing, T., Golovin, A., Toporski, J., 2011. Raman imaging of fluid inclusions in garnet from UHPM rocks (Kokchetav massif, Northern Kazakhstan). Spectrochimica Acta Part A: Molecular and Biomolecular Spectroscopy, 80, 88–95

Krogh, E.J., Råheim, A., 1978. Temperature and Pressure Dependence of Fe – Mg Partitioning Between Garnet and Phengite, With Particular Reference to Eclogites. Contributions to Mineralogy and Petrology, 66, 75–80

Krogh Ravna, E.J., Terry, M.P., 2004. Geothermobarmetry of UH*P* and H*P* eclogites and schists – an evaluation

of equilibria among garnet–clinopyroxene–kyanite–phengite–coesite/quartz. Journal of Metamorphic Geology, 22, 579–592

Küster, M., Stöckhert, B., 1999. High differential stress and sublithostatic pore fluid pressure in the ductile regime – microstructural evidence for short-term post-seismic creep in the Sesia Zone, Western Alps. Tectonophysics, 303, 263–277

Lanari, P., Giuntoli, F., Loury, C., Burn, M., Engi, M., 2017. An inverse modeling approach to obtain *P-T* conditions of metamorphic stages involving garnet growth and resorption. European Journal of Mineralogy, 29, 181–199

Le Bayon, B., Pitra, P., Ballevre, M., Bohn, M., 2006. Reconstructing *P-T* paths during continental collision using multi-stage garnet (Gran Paradiso nappe, Western Alps). Journal of Metamorphic Geology, 24, 478–496

Li, Z.H., Gerya, T.V., Burg, J.-P., 2010. Influence of tectonic overpressure on *P–T* paths of HP–UHP rocks in continental collision zones: thermomechanical modelling. Journal of Metamorphic Geology, 28, 227–247

Liou, J.G., Zhang, R.Y., 1996. Occurrences of intergranular coesite in ultrahigh-*P* rocks from the Sulu region, eastern China: Implications for lack of fluid during exhumation. American Mineralogist, 81, 1217–1221

Llana-Fúnez, S., Wheeler, J., Faulkner, D.R., 2012. Metamorphic reaction rate controlled by fluid pressure not confining pressure: implications of dehydration experiments with gypsum. Contributions to Mineralogy and Petrology, 164, 69-79

Luisier, C., Baumgartner, L., Schmalholz, S.M., Siron, G., Vennemann, T., 2019. Metamorphic pressure variation in a coherent Alpine nappe challenges lithostatic pressure paradigm. Nature communications, 10, 4734

Maeda, F., Ohtani, E., Kamada, S., Sakamaki, T., Hirao, N., Ohishi, Y., 2017. Diamond formation in the deep lower mantle: a high-pressure reaction of MgCO3 and SiO2. Scientific Reports, 7, 40602

Martin, A.M., Hammouda, T., 2011. Role of iron and reducing conditions on the stability of dolomite + coesite between 4.25 and 6 GPa – a potential mechanism for diamond formation during subduction. European Journal of Mineralogy, 23, 5–16

Massey, M.A., Prior, D.J., Moecher, D.P., 2011. Microstructure and crystallographic preferred orientation of polycrystalline microgarnet aggregates developed during progressive creep, recovery, and grain boundary sliding. Journal of Structural Geology, 33, 713–730

Massonne, H.-J., Fockenberg, T., 2012. Melting of metasedimentary rocks at ultrahigh pressure – Insights from experiments and thermodynamic calculations. Lithosphere, 4(4), 269–285

Moore, J., Beinlich, A., Austrheim, H., Putnis, A., 2019. Stress orientation-dependent reactions during metamorphism. Geology, 47(2), 151–154

Mørk, M.B.E., 1986. Coronite and eclogite formation in olivine gabbro (Western Norway): reaction paths and garnet zoning. Mineralogical Magazine, 50, 417–426

Moulas, E., Burg, J.-P., Podladchikov, Y., 2014. Stress field associated with elliptical inclusions in a deforming matrix: Mathematical model and implications for tectonic overpressure in the lithosphere. Tectonophysics, 631, 37–49

Moulas, E., Sokoutis, D., Willingshofer, E., 2019. Pressure build-up and stress variations within the Earth's crust in the light of analogue models. Scientific Reports, 9, 2310

Moynihan, D.P., Pattison, D.R.M., 2013. An automated method for the calculation of *P-T* paths from garnet zoning, with application to metapelitic schist from the Kootenay Arc, British Columbia, Canada. Journal of Metamorphic Geology, 31(5), 525–548

Nestola, F., 2020. The role of elastic anisotropy in determining the depth of formation for diamonds and their inclusions. Rendiconti Lincei. Scienze Fisiche e Naturali, 31, 285–293

Okazaki, K., Hirth, G., 2016. Dehydration of lawsonite could directly trigger earthquakes in subducting oceanic crust. Nature, 530, 81–84

Park, C., Park, C., Song, Y., Choi S.-G., 2019. Sequential trace element analysis of zoned skarn garnet: Implications for multi-stage fluxing and flow of magmatic fluid into a skarn system. Lithos, 350-351, 105213

Passchier, C.W., Trouw, R.A.J., Zwart, H.J., Vissers, R.L.M., 1992. Porphyroblast rotation: eppur si muove*? Journal of Metamorphic Geology, 10, 283-294

Pattison, D.R.M., De Capitani, C., Gaidies, F., 2011. Petrological consequences of variations in metamorphic reaction affinity. Journal of Metamorphic Geology, 29, 953–977

Peacock, S.M., 1990. Fluid Processes in Subduction Zones. Science, 248, 329–337

Penniston-Dorland, S.C., Kohn, M.J., Manning, C.E., 2015. The global range of subduction zone thermal structures from exhumed blueschist and eclogites: Rocks are hotter than models. Earth and Planetary Science Letters, 428, 243–254

Perchuk, A.L., Burchard, M., Maresch, W.V., Schertl, H.-P., 2008. Melting of hydrous and carbonate mineral inclusions in garnet host during ultrahigh pressure experiments. Lithos 103 (1-2) 25–45

Pleuger, J., Podladchikov, Y.Y., 2014. A purely structural restoration of the NFP20-East cross section and potential tectonic overpressure in the Adula nappe (central Alps). Tectonics, 33, 656–685

Plümper, O., John, T., Podladchikov, Y.Y., Vrijmoed, J.C., Scambelluri, M., 2017. Fluid escape from subduction zones controlled by channel-forming reactive porosity. Nature geoscience, 10, 150–158 DOI: 10.1038/NGEO2865

Powell, R., Holland, T., 2010. Using Equilibrium Thermodynamics to Understand Metamorphism and Metamorphic Rocks. Elements, 6, 309–314

Prior, D.J., 1994. Sub-critical fracture and associated retrogression of garnet during mylonitic deformation. Contributions to Mineralogy and Petrology, 113(4), 545–556

Putnis, A., Austrheim, H., 2010. Fluid-induced processes: metasomatism and metamorphism. Geofluids, 10, 254–269

Reinecke, T., 1998. Prograde high- to ultahigh-pressure metamorphism and exhumation of oceanic sediments at Lago di Cignana, Zermatt-Saas Zone, western Alps. Lithos. 42, 147–189

Richter, B., Stünitz, H., Heilbronner, R., 2016. Stresses and pressures at the quartz-to-coesite phase transformation in shear deformation experiments. Journal of Geophysical Research: Solid Earth, 121, 8015-8033, doi:10.1002/2016JB013084

Robyr, M., Vonlanthen, P., Baumgartner, L.P., Grobety, B., 2007. Growth mechanism of snowball garnets from the Lukmanier Pass area (Central Alps, Switzerland): a combined μCT/EPMA/EBSD study. Terra Nova, 19, 240–244

Robyr, M., Carlson, W.D., Passchier, C., Vonlanthen, P., 2009. Microstructural, chemical and textural records during growth of snowball garnet. Journal of Metamorphic Geology, 27, 423–437

Rubatto, D., Regis, D., Hermann, J., Boston, K., Engi, M., Beltrando, M., McAlpine, S.R.B., 2011. Yo-yo subduction recorded by accessory minerals in the Italian Western Alps. Nature Geoscience, 4, 338–342

Rubatto, D., Burger, M., Lanari, P., Hattendorf, B., Schwarz, G., Neff, C., Schmidt, P.K., Hermann, J., Vho, A., Günther, D., 2020. Identification of growth mechanisms in metamorphic garnet by high-resolution trace element mapping with LA-ICP-TOFMS. Contributions to Mineralogy and Petrology, 175:61

Rubie, D.C., 1986. The catalysis of mineral reactions by water and restrictions on the presence of aqueous fluid during metamorphism. Mineralogical Magazine, 50, 399-415

Rubie, D.C., 1998. Disequilibrium during metamorphism: the role of nucleation kinetics. Geological Society, London, Special Publications, 138, 199–214, https://doi.org/10.1144/GSL.SP.1996.138.01.12

Satake, K., Atwater, B.F., 2007. Long-Term Perspectives on Giant Earthquakes and Tsunamis at Subduction Zones. Annual Review of Earth and Planetary Sciences, 35, 349–74

Scambelluri, M., Philippot, P., 2001. Deep fluids in subduction zones. Lithos. 55, 213–227

Schertl, H.-P., Okay, A. I., 1994. A coesite inclusion in dolomite in Dabie Shan, China: Petrological and rheological significance. European Journal of Mineralogy, 6, 995–1000

Schmalholz, S.M., Podladchikov, Y., 2014. Metamorphism under stress: The problem of relating minerals to depth. Geology, 42(8), 733–734

Schumacher, R., Rötzler, K., Maresch, W.V., 1999. Subtle oscillatory zoning in garnet from regional metamorphic phyllites and mica schists, Western Erzgebirge, Germany. The Canadian Mineralogist, 37, 381–402

Smit, M.A., Scherer, E.E., John, T., Janssen, A., 2011. Creep of garnet in eclogite: Mechanisms and implications. Earth and Planetary Science Letters, 311, 411–419

Smith, E.M., Shirey, S.B., Nestola, F., Bullock, E.S., Wang, J., Richardson, S.H., Wang, W., 2016. Large gem diamonds from metallic liquid in Earth's deep mantle. Science, 354(6318), 1403–1405

Sobolev, N.V., Shatsky, V.S., 1990. Diamond inclusions in garnets from metamorphic rocks: a new environment of diamond formation. Nature, 343, 742–746

Spandler, C., Pirard, C., 2013. Element recycling from subducting slabs to arc crust: A review. Lithos,

170-171, 208–223

Spear, F.S., 1993. Metamorphic Phase Equilibria and Pressure-Temperature-Time Paths Mineralogical Society of America. ISBN 0-939950-34-0. Mineralogical Magazine, 60(403), 992–993

Spear, F.S., Wolfe, O.M., 2019. Implications of overstepping of garnet nucleation for geothermometry, geobarometry and P-T path calculations. Chemical Geology, 530, 119323

Spiess, R., Peruzzo, L., Prior, D.J., Wheeler, J., 2001. Development of garnet porphyroblasts by multiple nucleation, coalescence and boundary misorientation-driven rotations. J. metamorphic Geol., 19, 259–290

Stipp, M., Tullis, J., 2003. The recrystallized grain size piezometer for quartz. Geophysical Research Letters, 30(21), 2088

Stöckhert, B., 2002. Stress and deformation in subduction zones: insight from the record of exhumed metamorphic rocks. Geological Society, London, Special Publications, 200, 255–274

Stowell, H., Zuluaga, C., Boyle, A., Bulman, G., 2011. Garnet sector and oscillatory zoning linked with changes in crystal morphology during rapid growth, North Cascades, Washington. American Mineralogist, 96, 1354–1362

Sverjensky, D.A., Stagno, V., Huang, F., 2014. Important role for organic carbon in subduction-zone fluids in the deep carbon cycle. Nature Geoscience, 7, 909–913

Taetz, S., John, T., Bröcker, M., Spandler, C., Stracke, A., 2018. Fast intraslab fluid-flow events linked to pulses of high pore fluid pressure at the subducted plate interface. Earth and Planetary Science Letters, 482, 33–43

Tajčmanová, L., Vrijmoed, J., Moulas, E., 2015. Grain-scale pressure variations in metamorphic rocks: implications for the interpretation of petrographic observations. Lithos 216-217, 338–351

Tarling, M.S., Smith, S.A.F., Scott, J.M., 2019. Fluid overpressure from chemical reactions in serpentinite within the source region of deep episodic tremor. Nature Geoscience, 12, 1034–1042

Tinkham, D.K., Ghent, E.D., 2005. Estimating *P-T* conditions of garnet growth with isochemical phase-diagram sections and the problem of effective bulk-composition. The Canadian Mineralogist, 43, 35–50

Trepmann, C., Stöckhert, B., 2001. Mechanical twinning of jadeite – an indication of synseismic loading beneath the brittle-plastic transition. International Journal of Earth Sciences, 90, 4–13

Trepmann, C.A., Stöckhert, B., 2002. Cataclastic deformation of garnet: a record of synseismic loading and postseismic creep. Journal of Structural Geology, 24, 1845–1856

Vance, D., Mahar, E., 1998. Pressure-temperature paths from *P-T* pseudosections and zoned garnets: potential, limitations and examples from the Zanskar Himalaya, NW India. Contrib Mineral Petrol., 132, 225–245

Van Keken, P.E., Hacker, B.R., Syracuse, E.M., Abers, G.A., 2011. Subduction factory: 4. Depthdependent flux of H2O from subducting slabs worldwide. Journal of Geophysical Research, 116. DOI: 10.1029/2010JB007922

Van Keken, P.E., Wada, I., Abers, G.A., Hacker, B.R., Wang, K., 2018. Mafic High-Pressure Rocks Are Preferentially Exhumed From Warm Subduction Settings. Geochemistry, Geophysics, Geosystems, 19, 2934–2961, https://doi.org/10.1029/2018GC007624

Vrijmoed, J.C., Podladchikov, Y., Andersen, T.B., Hartz, E.H., 2009. An alternative model for ultra-high pressure in the Svartberget Fe-Ti garnet-peridotite, Western Gneiss Region, Norway. European Journal of Mineralogy, 21, 1119–1133

Vrijmoed, J.C., Hacker, B.R., 2014. Determining *P-T* paths from garnet zoning using a brute-force computational method. Contributions to Mineralogy and Petrology, 167, 997

Vrijmoed, J.C., Podladchikov, Y.Y., 2015. Thermodynamic equilibrium at heterogeneous pressure. Contributions to Mineralogy and Petrology, 170, 10

Wark, D.A., Watson, E.B., 2006. TitaniQ: a titanium-in-quartz geothermometer. Contributions to Mineralogy and Petrology, 152, 743–754

Wassmann, S., Stöckhert, B., 2013a. Low stress deformation of garnet by incongruent dissolution precipitation creep. Journal of Structural Geology. 46, 200–219

Wassmann, S., Stöckhert, B., 2013b. Rheology of the plate interface - Dissolution precipitation creep in high pressure metamorphic rocks. Tectonophysics. 608, 1–29

Waters, D.J., Lovegrove, D.P., 2002. Assessing the extent of disequilibrium and overstepping of prograde metamorphic reactions in metapelites from the Bushveld Complex aureole, South Africa. Journal of Metamorphic Geology, 20, 135–149

Watson, E.B., Harrison, T.M., 2005. Zircon Thermometer Reveals Minimumm Melting Conditions on Earliest Earth. Science, 308, 841–844

Wilbur, D.E., Ague, J.J., 2006. Chemical disequilibrium during garnet growth: Monte Carlo simulations of natural crystal morphologies. Geology, 34(8), 689–692

Wheeler, J., 2014. Dramatic effects of stress on metamorphic reactions. Geology, 42(8), 647–650

Whitney, D.L., 1996. Garnets as open systems during regional metamorphism. Geology, 24(2), 147– 150

Yamato, P., Brun, J.P., 2017. Metamorphic record of catastrophic pressure drops in subduction zones. Nature Geoscience, 10, 46–50, DOI: 10.1038/NGEO2852

Yamato, P., Duretz, T., Angiboust, S., 2019. Brittle/Ductile Deformation of Eclogites: Insights From Numerical Models. Geochemistry, Geophysics, Geosystems, 20, 3116–3133

Zack, T., Moraes, R., Kronz, A., 2004. Temperature dependence of Zr in rutile: empirical calibration of a rutile thermometer. Contributions to Mineralogy and Petrology, 148, 471–488

Zaffiro, G., 2020. Constraints on the Equations of State of rutile and zircon: implications for elastic geothermobarometry. PhD Thesis, Cycle XXXII, University of Pavia

Zhao, D., 2001. New advances of seismic tomography and its applications to subduction zones and earthquake fault zones: A review. The Island Arc, 10, 68–84

Zhong, X., Moulas, E., Tajčmanová, L., 2018. Tiny timekeepers witnessing high-rate exhumation processes. Scientific reports, 8:2234

Zhong, X., Andersen, N.H., Dabrowski, M., Jamtveit, B., 2019. Zircon and quartz inclusions in garnet used for complementary Raman thermobarometry: application to the Holsnøy eclogite, Bergen Arcs, Western Norway. Cotributions to Mineralogy and Petrology, 174, 50

Zhong, X., Moulas, E., Tajčmanová, L., 2020. Post-entrapment modification of residual inclusion pressure and its implications for Raman elastic thermobarometry. Solid Earth, 11, 223–240

Zhou, T., Li, Q., Klemd, R., Shi, Y., Tang, X., Li, C., Lui, Y., 2020. Multi-system geochronology of North Dabie eclogite: Ineffective garnet 'shielding' on rutile inclusions under multi-thermal conditions. Lithos 368–369

Zuza, A.V., Levy, D.A., Mulligan, S.R., 2020. Geologic field evidence for non-lithostatic overpressure recorded in the North American Cordillera hinterland, northeast Nevada. Geoscience Frontiers, DOI: https://doi.org/10.1016/j.gsf.2020.10.006

CHAPTER 2
Geological Setting

The Alpine chain in the Mediterranean area is an orogen resulting from a long and complex collision between the Eurasian and African plates. This complexity is exemplified by the Alps, formed by the protracted convergence and eventual collision of Europe and Greater Adria (Zanchetta et al., 2012; Van Hinsbergen et al., 2020), but also involving the microcontinents Margna-Sesia (or Cervinia) and Briançonnais (Stampfli et al., 1998; Rosenbaum & Lister, 2005; Pleuger et al., 2007). The former is often considered as a part of the Austro-Alpine domain, the latter as part of the Iberian plate. Furthermore, the collisions between (micro-) continents resulted in several short-lived subduction zones within the Alpine Tethys (Rosenbaum & Lister, 2005; Weber et al., 2015).

The Alps can be subdivided into the Adria-derived Austro-Alpine nappes, the Europe-derived Helvetic nappes, and the Penninic Domain in between which represent remnants of the Alpine Tethys, essentially forming the suture between Europe and Adria. Peak metamorphic ages of (ultra)high-pressure metamorphic rocks from Alpine subduction range from ~90 Ma in the Austro-Alpine Domain in the Eastern Alps up until 33 – 31 Ma in the Penninic Domain in the Western Alps and the Tauern Window in the Eastern Alps (Duchêne et al., 1997; Glodny et al., 2005; Thöni, 2006).

2.1 Penninic Domain of the Western Alps

The Penninic Domain comprises the metamorphic core of the Western Alps, forming an arcuate range from Genoa around the Po Plain up to the Swiss Rhône. Further towards the northwest, the Penninic Domain borders the Austro-Alpine Southern Alps and Helvetic Lepontine Alps, and the external units flank it to the south and east (Figure 2.1a). A general trend of increasing metamorphic grade towards the core of the arcuate orogen characterizes the Penninic Domain, from the greenschist- to blueschist-facies Briançonnais Domain in the outer part to the eclogite-facies Internal Crystalline Massifs and the blueschist- to eclogite-facies Piemonte zone (green in Figure 2.1a). Peak metamorphic ages in the Penninic Domain trend inversely to metamorphic peak conditions, thus younger ages towards the east (Beltrando et al., 2010). This distribution of metamorphic ages is an indicator of the sequence of subduction and collision of the several oceanic and (micro-) continental Alpine Domains (Rosenbaum & Lister, 2005).

2.2 Zermatt-Saas zone

The Alpine high-pressure ophiolites of the Piemonte zone (Figure 2.1) are the dismembered remnants of the Mesozoic Tethyan Ocean that was subducted during Alpine plate convergence and orogeny (Dal Piaz et al., 1999 and references therein). The Piemonte zone consists of several domains that can be characterized by different metamorphic conditions (Figure 2.2). The Lago di Cignana Unit is a coesite- and diamond-bearing ultrahigh-pressure metamorphic (UHPM) ophiolitic sliver cropping out between two major metaophiolitic units: the underlying Zermatt-Saas Zone (ZSZ) recording eclogite-facies metamorphic conditions of 520 ± 20 °C, 2.3 GPa (Angiboust et al., 2009), and the overlying Combin Zone (CZ) recording blueschist-facies conditions of 300–345 °C, ~0.9 GPa (Reddy et al., 1999).

The relation between the LCU and the ZSZ is still debated. One possibility is that the LCU is one of several minor bodies of diverse origin that crop out along the contact between the ZSZ and CZ (Dal Piaz et al., 2001; Gilio et al., 2019), which differ in their peak-metamorphic age, *P-T* evolution, and provenance (Theodul Glacier Unit, Etirol-Levaz Slice, Allalin Gabbro; Weber et al., 2015; Bucher & Grapes, 2009; Beltrando et al., 2010). The alternative is that the LCU is located within the upper levels of the ZSZ, and only deviates in terms of peak metamorphic pressure, while metamorphic ages and temperatures match (Groppo et al., 2009; Skora et al., 2015).

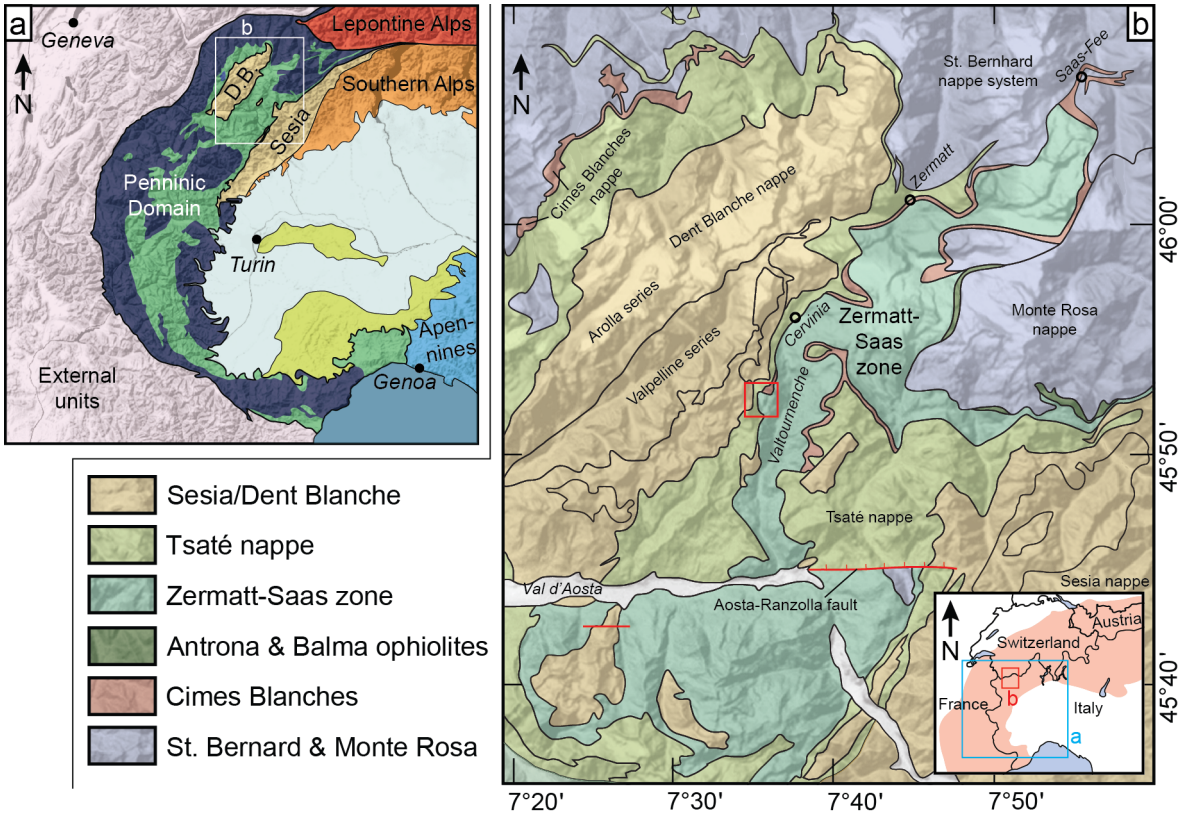

Figure 2.1: (a) Geological overview of the Western Alps, modified after Beltrando et al., 2010. The light green zone in the Penninic Domain marks the Piemonte zone. D.B.: Dent Blanche nappe. White square labelled b indicates the location of the map in (b). (b) Geological map of the large-scale context of the Zermatt-Saas zone in the vicinity of the Lago di Cignana unit, modified after Kirst & Leiss (2017) and references therein. The red square in the main map indicates the location of Lago di Cignana and Figure 2.2a. The inset provides the location of (a) and (b).

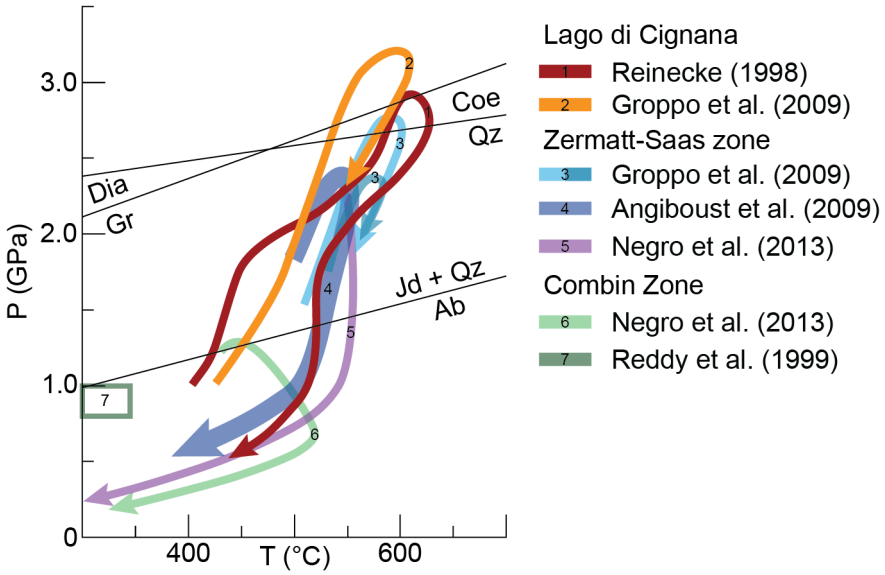

Figure 2.2: Overview of *P-T* paths for the LCU, ZSZ and CZ. The LCU *P-T* path by Reinecke (1998) is determined based on metasediments, the one by Groppo et al. (2009) on eclogite. The two paths for the ZSZ by Groppo et al. (2009) concern eclogites directly above (higher *P*) and below (lower *P*) the LCU.

2.3 Lago di Cignana unit

The LCU (Figure 2.3) consists of coesite-bearing eclogite, serpentinite (Gilio et al., 2019) and metasediments varying from calcschist and marble to several types of manganiferous quartzites (Reinecke, 1998; Forster et al., 2004). The quartzite varies from schistose garnet-amphibole-phengite quartzites, to purple, hydrothermally Mn-enriched quartzite similar to other Mn-rich metasediments from the ZSZ (Tumiati et al., 2010).

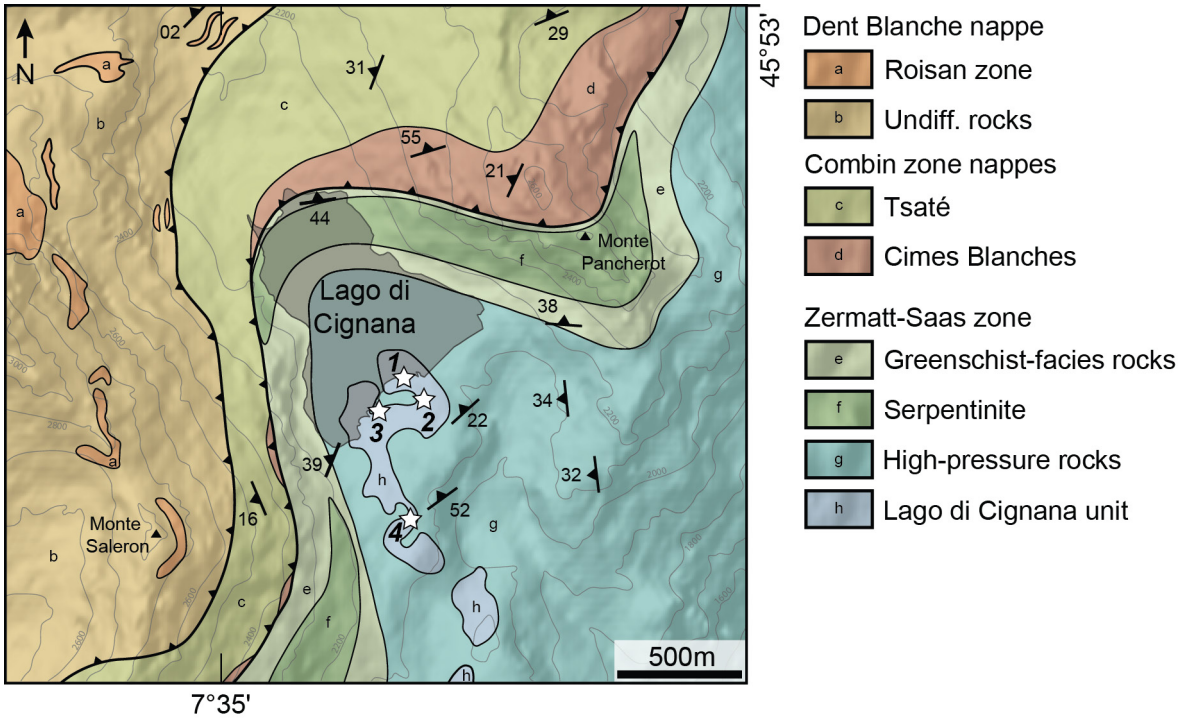

Figure 2.3: (a) Geological map of the Lago di Cignana area, modified after Kirst & Leiss (2017) and references therein. Stars indicate sample locations for 1: eclogites LCG1401, C18-09. 2: schistose quartzite and garnetite EC5.1, EC5.3, metasedimentary garnetite C18-3. 3: metasedimentary garnetite C18-6. 4: garnetite in quartz vein C18-10.

Garnetite is present in several metasediments and eclogites as lenses and boudins. Certain LCU garnetites contain fluid inclusions with solutes that originated from the dissolution of carbonate and quartz (Frezzotti et al., 2011). Furthermore, Hawkins et al. (2009) observed an assemblage of daughter minerals in fluid inclusions in garnetite, consisting of jadeite, paragonite, phengite, chlorite, amphibole, titanite and K-feldspar alongside Ca-sulfates, phosphates and oxides. This evidence suggests the dissolution of a polymineralic component of the system during garnet growth, beyond quartz and carbonates (Frezzotti et al., 2011; Hawkins et al., 2009). Boron concentrations and isotopic ratios in white mica within several lithologies in the LCU area indicate that a fluid derived from partially dehydrated serpentinites was the driver behind fluid-rock interaction in quartzite, but not in eclogite (Halama et al., 2020).

Garnet- and glaucophane-rich zones in the eclogite are suggested to reflect compositional differences related to pillow basalts (Van der Klauw et al., 1997). The peak metamorphic assemblage consists of garnet, omphacite, glaucophane, lawsonite, phengite, rutile and minor coesite and zircon. The latter two are also present as inclusions in omphacite and garnet (Groppo et al., 2009; King et al., 2004). Lawsonite has broken down to pseudomorphs of epidote and paragonite. Titanite, ilmenite, Ca-amphibole, and biotite preserved as inclusions in garnet cores represent an early prograde metamorphic mineral assemblage. The eclogite is rich in TiO_2 (>2 wt. %), result-

ing in an abundance of rutile (Groppo et al., 2009). A multitude of veins has been identified in the LCU eclogites, consisting of, for example, omphacite, glaucophane, quartz (potentially after coesite), epidote/clinozoisite and retrogressed lawsonite (Borghini et al., 2015). The relative timings of vein formation range from UHP metamorphism to retrograde metamorphic stages during exhumation.

The LCU eclogites were pervasively deformed by dislocation creep of pyroxene with dynamic recrystallisation resulting from grain boundary migration. At the onset of extension, the deformation became localized leading to the formation of shear bands (Van der Klauw et al., 1997). Little to no deformation took place in the eclogites during the first 40 km of exhumation, down to P-T conditions of <1.5 GPa, 500–550 °C (Van der Klauw et al., 1997). Following this part of exhumation, further deformation within eclogites is associated with a retrograde mineral assemblage of hornblende, albite, and epidote (Kirst and Leiss, 2017).

2.4 Outcrops and samples

2.4.1 Studied lithologies

The garnetite-bearing schistose quartzite displayed in Figure 2.4a is the subject of study for a significant part of this thesis. Garnetite is a common occurrence in metasesdiments in the LCU, but this particular one contains a high amount of garnetite and best preserved the relationship between host rock and garnetite. The Mn-rich schistose quartzite forms a 5 m-thick layer, at the centre of which is a 30 cm-thick zone where the majority of the garnetite is located. This outcrop, labelled EC5, is mainly studied through quartzite sample EC5.3 and garnetite + quartzite sample EC5.1.

The variety in metasediments in the LCU also results in a variety in garnetites that they host, exhibiting different colours, sizes, and structures (Figure 2.4b,c). As material for comparison to the garnetite in the previously described outcrop, several other garnetites from various metasediments were also sampled. Most notable are garnetites C18-6 (Figure 2.4b), C18-10 and C18-3. C18-10 consists of several broken up pieces of garnetite hosted in a quartz vein. C18-3 is located within the same lithology as EC5.3, and appears to be a quartz-rich variety of garnetite EC5.1.

Eclogite is also sampled for study, in particular for its garnetite and omphacite veins. Garnetite is not as common an occurrence in eclogite as it is in metasediments, and is mostly present in glacier-polished surfaces, making it challenging to sample. As result, only one sample was obtained of garnetite in eclogite (C19-08), which does not represent the full system as is displayed in Figure 2.4d. Therefore, only the garnetite itself could be studied properly and not its relation to the local host eclogite. An omphacite-glaucophane vein of approximately 1 cm thick was also sampled (LCG1401; Figure 2.4e). Like the other veins observed in the eclogite, this sampled vein appears undeformed in the outcrop. The omphacite crystals in these veins exhibit a strong shape preferred orientation and are up to 1 mm in length. Garnet is only present in the wall rock.

Locations of all studied samples are given in Figure 2.3. Although not sampled, and not part of the LCU, an important lithology in the vicinity is the partially dehydrated serpentinite. The ZSZ serpentinite displayed in Figure 2.4f is a scree block from Mt. Pancherot (Figure 2.3), and contains many olivine veins formed in fractures with a preferential orientation.

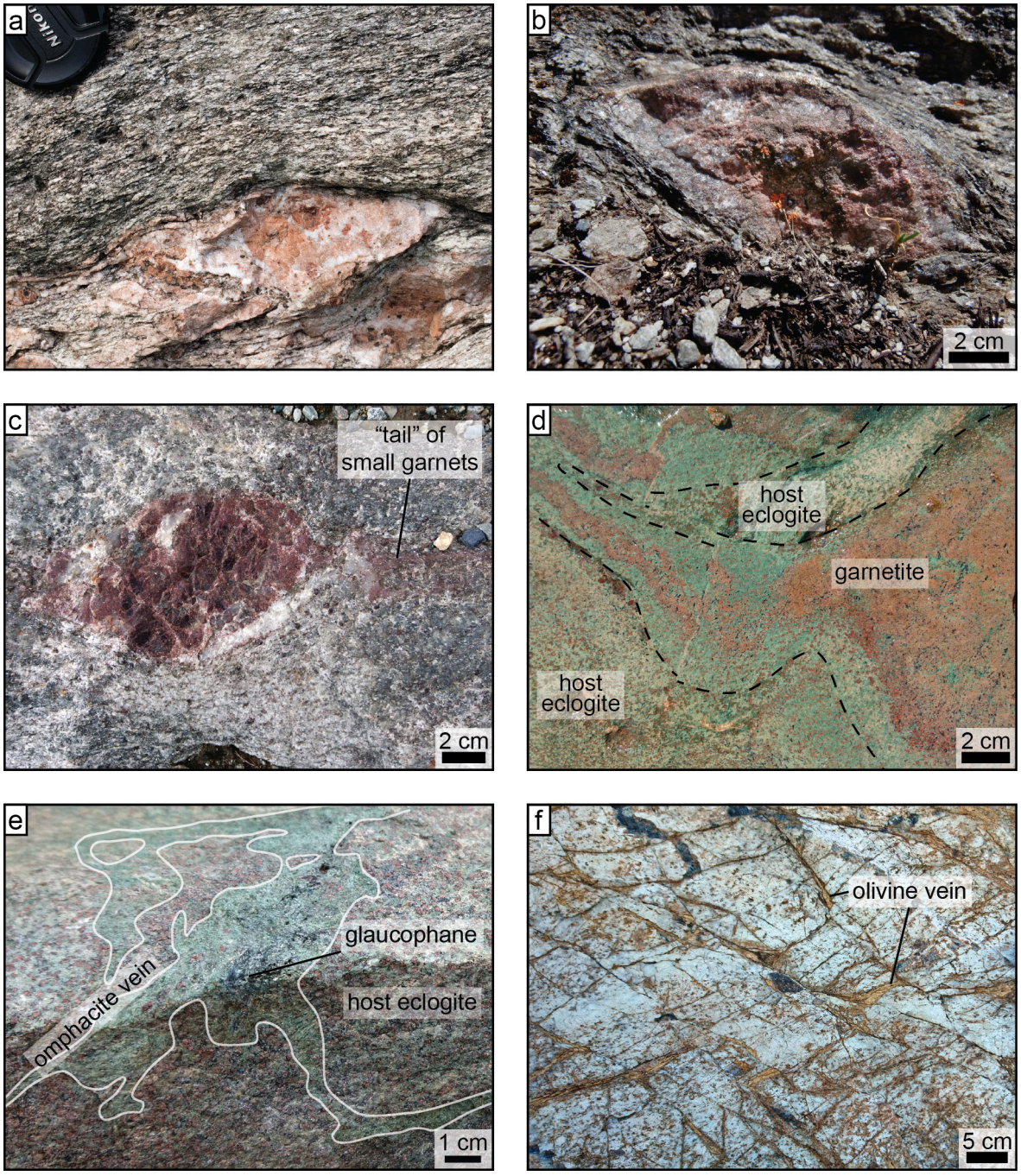

Figure 2.4: Overview of revelant lithologies. (a) Garnetite-bearing schistose quartzite outcrop EC5. (b) Metasediment-hosted garnetite C18-6. (c) Not sampled garnetite, possible type of diamond-bearing garnetite. (d) Garnetite lens and layers in eclogite. (e) Omphacite-glaucophane vein in eclogite. (f) Serpentinite with olivine veins, from ZSZ scree closeby LCU.

2.4.2 Outcrop structures

Garnetite in metasediments generally occurs as lenses, discontinuous layers, dismembered fold hinges and limbs transposed along a phengite foliation (Figure 2.5a). Isoclinal folding in garnetite progressed to a high degree (Figure 2.5a), further supported by a thin layer of phengite foliation included within garnetite (Figure 2.5b). The competent nature of garnetite with respect to the quartzite is also highlighted by its boudinaged nature, and by how the foliation in the quartzite is strongly dependent on the configuration of the garnetite (Figure 2.5c). Locally, garnetite occurs as

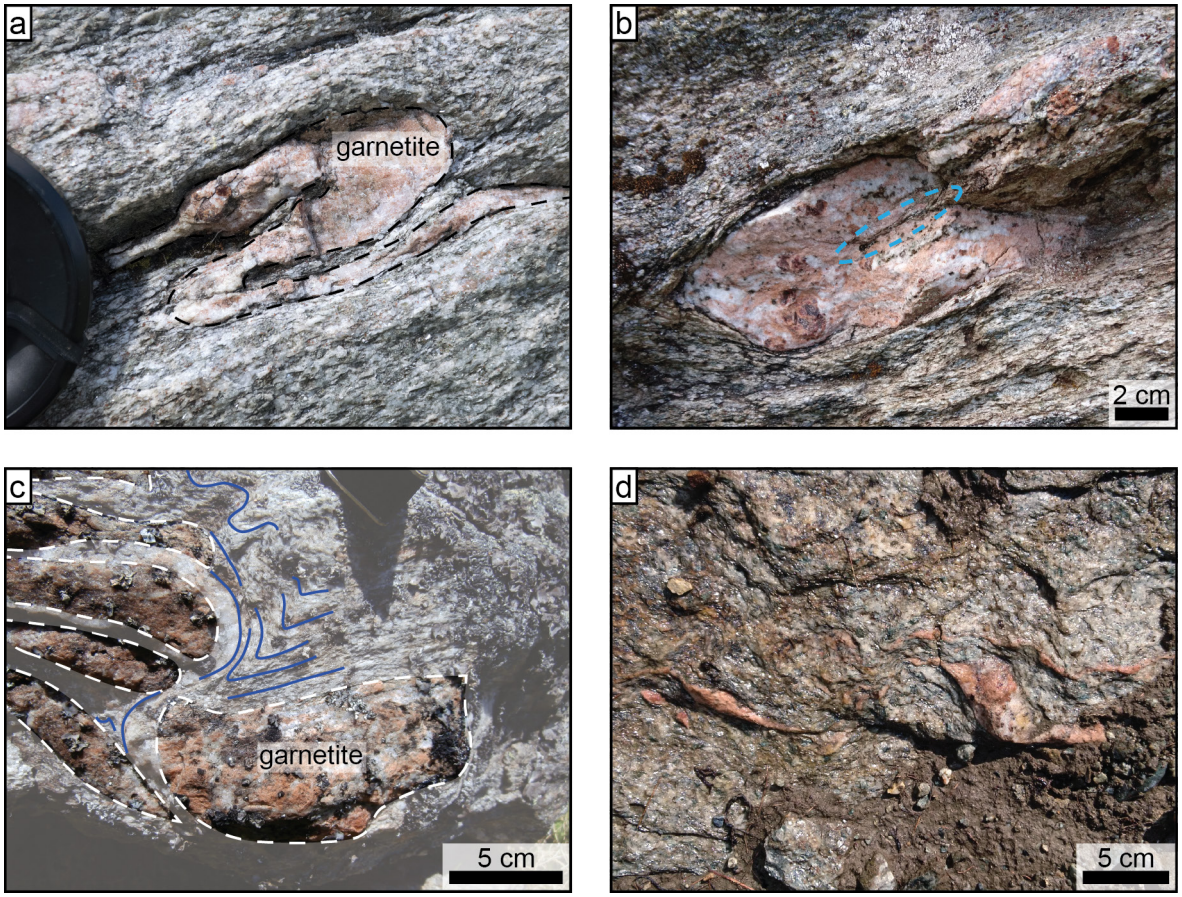

Figure 2.5: Outcrop-scale garnetite microstructures. (a) A thin garnetite layer thickened in a fold hinge. (b) Garnetite folded around a thin layer of host rock, highlighted by the light blue dashed ellipse. (c) Stack of several garnetite bodies, indicated by white dashed lines. Solid blue lines indicate the highly folded foliation in the host rock. (d) An array of sigmoidal clasts of garnetite in schistose quartzite.

sigmoidal clasts (Figure 2.5d). Internally, garnetite can exhibit a strongly heterogeneous nature in terms of garnet content (highlighted by colour; see Figures 2.4a, 2.5b,c) and commonly includes patches and veins of quartz (Figure 2.4a,c, 2.5b).

The garnetite-bearing metasediments rarely exhibit signs of folding at a distance from the garnetite. However, isoclinal folding highlighted by differential weathering in garnetite-less calcschists (Figure 2.6a,b), underlines the strongly deformed nature of the LCU. Isoclinal folding is also observed within eclogite (Figure 2.6c). Mafic boudins locally occur within metasedimentary layers (Figure 2.6d).

Overall, the LCU exhibits widespread evidence for strong deformation of most lithologies, albeit expressed by different microstructures. The eclogite hosting omphacite veins forms an exception to the pervasive deformation of peak-metamorphic assemblages. Fold axes and foliation are generally subhorizontal to slightly NE-dipping, consistent with the larger-scale structure of the LCU and ZSZ (Forster et al., 2004). The metasedimentary units appear less competent than the garnetite found therein, and also weaker than the mafic bodies.

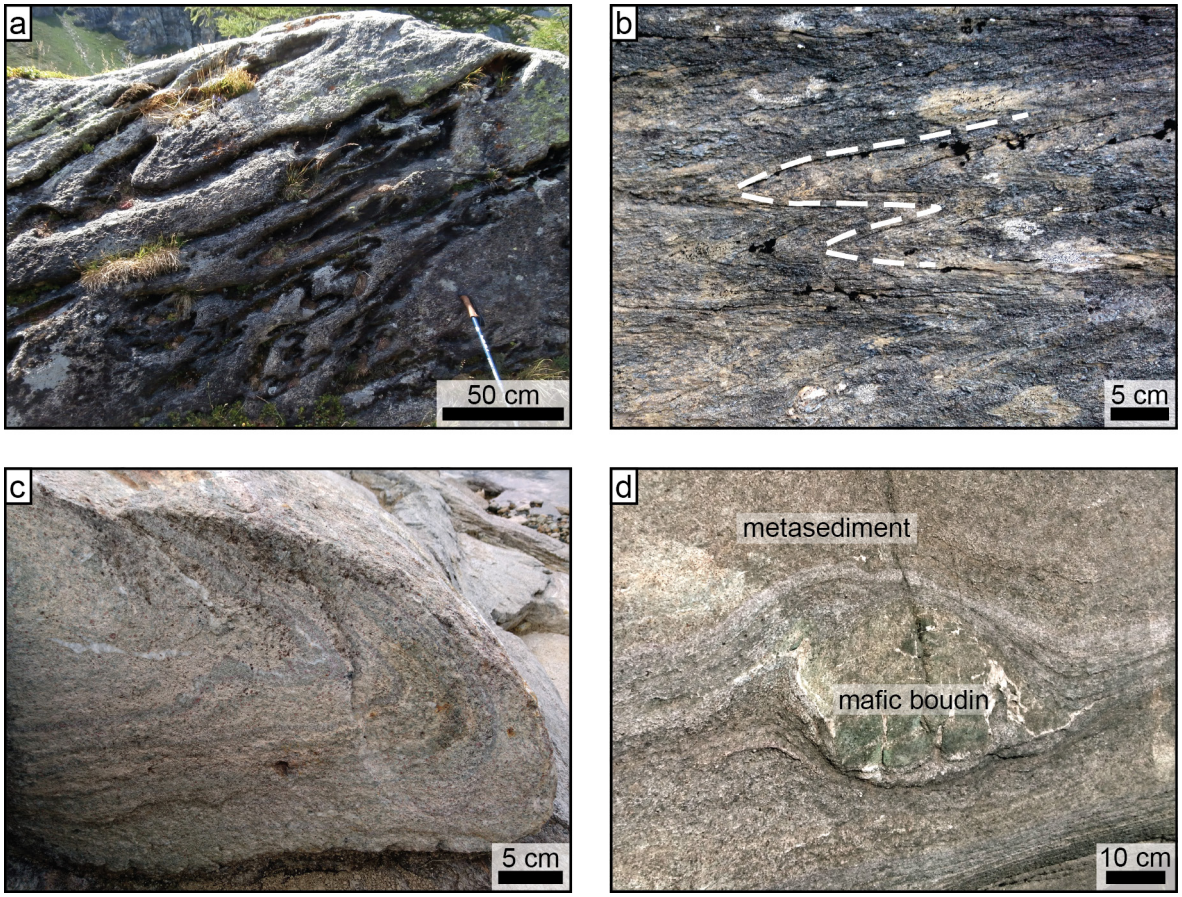

Figure 2.6: Outcrop-scale microstructures. (a) Differential weathering exposing isoclinal folds of several scales in calcschist. White dashed lines indicates foliation. (b) Isoclinal folding in calcschist. (c) Isoclinal folding in eclogite. (d) Mafic boudin hosted in metasediments.

References

Angiboust, S., Agard, P., Jolivet, L., Beyssac, O., 2009. The Zermatt-Saas ophiolite: the largest (60-km wide) and deepest (c. 70–80 km) continuous slice of oceanic lithosphere detached from a subduction zone? Terra Nova, 21(3), 171–180

Beltrando, M., Compagnoni, R., Lombardo, B., 2010. (Ultra-) High-pressure metamorphism and orogenesis: An Alpine perspective. Gondwana Research, 18, 147–166

Borghini, A., Ferrando, S., Groppo, C.T., 2015. Geologic and petrographic study of the veins in the metabasites of the ultra-high pressure Lago di Cignana Unit (upper Valtournenche, western Alps). Congresso SGI-SIMP Florence, abstract. http://hdl.handle.net/2318/1524973

Bucher, K., Grapes, R., 2009. The Eclogite-facies Allalin Gabbro of the Zermatt-Saas Ophiolite, Western Alps: a Record of Subduction Zone Hydration. Journal of Petrology, 50-8, 1405–1442

Dal Piaz, G., 1999. The Austroalpine–Piedmont nappe stack and the puzzle of Alpine Tethys. Memorie di Scienze Geologiche, 51, 155–176

Dal Piaz, G.V., Cortiana, G., Del Moro, A., Martin, S., Pennacchioni, G., Tartarotti, P., 2001. Tertiary age and paleostructural inferences of the eclogitic imprint in the Austroalpine outliers and Zermatt-Saas ophiolite, western Alps. International Journal of Earth Sciences, 90, 668–684 DOI: 10.1007/s005310000177

Duchêne, S., Blichert-Toft, J., Luais, B., Télouk, P., Lardeaux, J.-M., Albarède, F., 1997. The Lu –Hf dating of garnets and the ages of the Alpine high-pressure metamorphism. Nature, 387, 586 –589

Forster, M., Lister, G., Compagnoni, R., Giles, D., Hills, Q., Betts, P., Beltrando, M. & Tamagno, E., 2004. Mapping of oceanic crust with" H*P*" to" UH*P*" metamorphism: The Lago di Cignana Unit (Western Alps). Mapping geology in Italy: Geological Society of London

Frezzotti, M.L., Selverstone, J., Sharp, Z.D., Compagnoni, R., 2011. Carbonate dissolution during subduction revealed by diamond-bearing rocks from the Alps. Nature Geoscience, 4, 703–706 DOI: 10.1038/NGEO1246

Gilio, M., Scambelluri, M., Agostini, S., Godard, M., Peters, D., Pettke, T., 2019. Petrology and Geochemistry of Serpentinites Associated with the Ultra-High Pressure Lago di Cignana Unit (Italian Western Alps). Journal of Petrology, 60, 6 DOI: 10.1093/petrology/egz030

Groppo, C., Beltrando, M., Compagnoni, R., 2009. The *P-T* path of the ultra-high pressure Lago di Cignana and adjoining high-pressure meta-ophiolitic units: insights into the evolution of the subducting Tethyan slab. Journal of Metamorphic Geology, 27, 207–231

Halama, R., Konrad-Schmolke, M., De Hoog, J.C.M., 2020. Boron isotope record of peak metamorphic ultrahigh-pressure and retrograde fluid-rock interaction in white mica (Lago di Cignana, Western Alps). Contributions to Mineralogy and Petrology, 175, 20 DOI: 10.1007/s00410-020-1661-8

Hawkins, A.T., Selverstone, J., King, P.L., Frezzotti, M.L., 2009. H*P*/UH*P* fluids preserved in Mn-rich garnets from Lago di Cignana, Italy. Geological Society of America Abstracts with Programs. 41(7), 238

King, R. L., Bebout, G. E., Kobayashi, K., Nakamura, E., Van Der Klauw, S. N., 2004. Ultrahigh-pressure metabasaltic garnets as probes into deep subduction zone chemical cycling: Geochemistry, Geophysics, Geosystems, 5, 12

Kirst, F., Leiss, B., 2017. Kinematics of syn- and post-exhumational shear zones at Lago di Cignana (Western Alps, Italy): constraints on the exhumation of Zermatt-Saas (ultra)high-pressure rocks and deformation along the Combin Fault and Dent Blanche Basal Thrust. International Journal of Earth Sciences, 106, 215–236 DOI: 10.1007/s00531-016-1316-1

Pleuger, J., Roller, S., Walter, J.M., Jansen, E., Froitzheim, N., 2007. Structural evolution of the contact between two Penninic nappes (Zermatt-Saas zone and Combin zone, Western Alps) and implications for the exhumation mechanism and palaeogeography. International Journal of Earth Sciences, 96, 229–252

Reddy, S.M., Wheeler, J., Cliff, R.A., 1999. The geometry and timing of orogenic extension: an example from the Western Italian Alps. Journal of Metamorphic Geology, 17, 573–589

Reinecke, T., 1998. Prograde high- to ultahigh-pressure metamorphism and exhumation of oceanic sediments at Lago di Cignana, Zermatt-Saas Zone, western Alps. Lithos, 42, 147–189

Rosenbaum, G., Lister, G.S., 2005. The Western Alps from the Jurassic to Oligocene: spatio-temporal constraints and evolutionary reconstructions. Earth-Science Reviews, 69, 281–306

Skora, S., Mahlen, N., Johnson, C. M., Baumgartner, L. P., Lapen, T., Beard, B. L., Szilvagyi, E., 2015. Evidence for protracted prograde metamorphism followed by rapid exhumation of the Zermatt-Saas Fee ophiolite. Journal of Metamorphic Geology, 33, 7, 711–734

Stampfli, G.M., Mosar, J., Marquer, D., Marchant, R., Baudin, T., Borel, G., 1998. Tectonophysics, 296, 159–204

Thöni, M., 2006. Dating eclogite-facies metamorphism in the Eastern Alps – approaches, results, interpretations: a review. Mineralogy and Petrology, 88, 123–148

Tumiati, S., Martin, S., Godard, G., 2010. Hydrothermal origin of manganese in the high-pressure ophiolite metasediments of Praborna ore deposit (Aosta Valley, Western Alps). European Journal of Mineralogy, 22, 577–594

Van der Klauw, S., Reinecke, T., Stöckhert, B., 1997. Exhumation of ultrahigh-pressure metamorphic oceanic crust from Lago di Cignana, Piemontese zone, western Alps: the structural record in metabasites. Lithos, 41(1-3), 79–102

Van Hinsbergen, D.J.J., Torsvik, T.H., Schmid, S.M., Matenco, L.C., Maffione, M., Vissers, R.L.M., Gürer, D., Spakman, W., 2020. Orogenic architecture of the Mediterranean region and kinematic reconstruction o its tectonic evolution since the Triassic. Gondwana Research, 81, 79–229

Weber, S., Sandmann, S., Miladinova, I., Fonseca, R.O.C., Froitzheim, N., Münker, C., Bucher, K., 2015. Dating the initiation of Piemonte-Liguria Ocean subduction: Lu-Hf garnet chronometry of eclogites from the Theodul Glacier Unit (Zermatt-Saas zone, Switzerland). Swiss Journal of Geosciences, 108, 183–199

Zanchetta, S., Garzanti, E., Doglioni, C., Zanchi, A., 2012. The Alps in the Cretaceous: a doubly vergent pre-collisional orogen. Terra Nova, 24, 351–356

CHAPTER 3
Methods

3.1 Sample preparation

Samples were processed into sections 100 μm thick for petrographic analysis and electron microscopy. For the purpose of strain analysis on inclusions in garnet, sections 250 μm thick were prepared to maximize the number of inclusions without strain dissipation due to proximity to the surface of the section. Sections were polished with a 0.05-μm colloidal-silica suspension in preparation for high-quality electron microscopy.

3.2 Electron Probe Micro-Analysis

Electron probe micro-analysis (EPMA) measurements of major elements were performed using a JEOL JXA 8200 Superprobe at the Department of Earth Sciences, University of Milan. An accelerating potential of 15 kV and a beam current of 15 nA were used for spot analyses with a 30 second counting time. Measurements for element-distribution maps were performed with a combination of wavelength-dispersive spectroscopy (WDS) and EDS, at 15 nA and 100 nA for high-detail maps. Standards used for WDS calibration are grossular for Si, Al, Ca; ilmenite for Ti; metal for Cr; fayalite for Fe; forsterite for Mg; rhodonite for Mn; omphacite for Na; K-feldspar for K. Element distribution maps were plotted using the "Oslo" or the inverted "roma" colour-blind-friendly and constant-contrast scientific colour maps (Crameri, 2018).

3.3 Electron Backscatter Diffraction

Electron backscatter diffraction (EBSD) data (for Chapter 4, 5; see 3.7 for Chapter 8) were acquired on a Phillips XL-30 field-emission gun scanning electron microscope equipped with an Oxford Instruments' Nordlys-Nano EBSD detector and AZtec 3.3 acquisition software. EBSD maps were acquired at an accelerating voltage of 30 kV. Map dimensions and step sizes are given in the appendix of the corresponding chapter. Data were processed using the MTEX v5.1.1 toolbox (Bachmann et al., 2010) for MATLAB®. Crystal structure data of spessartine (Geiger & Armbruster, 1997) was used for processing of EBSD data.

Grain reconstruction was performed with a minimum misorientation value for grain boundaries of 2° in Chapter 4, and 1° for grain boundaries and 0.2° for subgrain boundaries in Chapter 5. Although these values are low, no subgrain boundaries were misidentified as grain boundaries by comparing reconstructed grains to compositional zoning. All grains below 5 pixels in size were considered to result from misindexing and were removed. Unindexed areas 1 pixel in size were filled in by interpolation. Grains in contact with the outer boundary of the map were removed from grain-size analysis.

Grain shape analysis for the purpose of determining the aspect ratio and orientation of the long axis, was performed using the improved fitEllipse function (https://github.com/mtex-toolbox/mtex/issues/332) for MTEX, fitting ellipses of equal area as the grains. This method is not perfect with respect to more complex grain morphologies. To reduce noise, and because undeformed garnet crystals will not result in an aspect ratio of 1.0, only grains with an aspect ratio of at least 1.4 were taken into account for shape preferred orientation polar plots. Fitting of strain ellipses to calculated grain ellipse apexes of long and short axes was performed using the function EllipseDirectFit by Chernov (2020) after Fitzgibbon et al. (1999). The EBSD maps were colour coded using the "Imola" and inverted "roma" colour-blind-friendly and constant-contrast scientific colour maps (Crameri, 2018), unless specified otherwise.

3.4 Raman spectroscopy

Raman spectra of a variety of mineral inclusions in garnet, rutile, and omphacite were collected with a Horiba LabRam HR Evolution spectrometer (holographic gratings of 1800 grooves/mm) equipped with an Olympus BX41 confocal microscope at the controlled temperature of 20(1) °C. Raman spectra were excited using the 514.532 nm line of a solid state (YAG) laser. The laser power on the sample surface was approximately 1–2 mW. The spectrometer was calibrated to the silicon Raman peak at 520.5 cm^{-1}. The spectra were baseline corrected for the continuum luminescence background when necessary, temperature reduced to account for the Bose-Einstein occupation factor (Kuzmany, 2009) and normalized to the acquisition time. Peak positions, full-widths at half maximum (FWHMs), and integrated intensities were determined from fits with pseudo-Voigt functions (*pseudoVoigt = (1-q)*Lorentz+q*Gauss*, where *q* is the mixing coefficient). Spacing between datapoints of a spectrum is 0.522 cm^{-1}, so the analytical error derived from the maximum distance of any point along a spectrum to a datapoint is 0.261 cm^{-1}.

3.5 Elastic-strain analysis

Elastic strains were determined for quartz and zircon inclusions in garnet by using the relationship between strain and shifts in the position of selected Raman peaks (Angel et al., 2019; Murri et al., 2019). The shift, $\Delta\omega$, of each Raman peak is the difference between the peak positions in the inclusion, ωi, and an unstrained reference crystal, $\omega 0$. To reduce shifts in peak position due to instrumental drift and/or minor changes to room temperature, the unstrained standard was measured multiple times per session. The $\omega 0$ values were averaged and then subtracted from the ωi of the strained inclusions analysed in between two consecutive standards. Sets of $\Delta\omega$ (modes 128, 206, 464 and, when available, 265) for each inclusion were converted to strain using the software stRAinMAN (Angel et al., 2019), applying the Grüneisen tensors for the inclusion mineral (quartz: Murri et al., 2018; zircon: Stangarone et al., 2019) and relaxation of the strains (Angel et al., 2014a). Strain interference can occur due to complex inclusion geometries or inclusion proximity to the sample surface, outer edge of the garnet, or other inclusions. Therefore, we only analysed non-faceted, rounded and sub-rounded inclusions, isolated by at least three times their radius (Campomenosi et al., 2018; Mazzucchelli et al., 2018; Zhang, 1998).

From the strain states of inclusions, isomekes were calculated using the Cij method in the online application EntraPT (Mazzucchelli et al., 2021). In this application, a garnet endmember must be selected for the elastic properties of the host. The host garnets mainly consist of an almandine + spessartine mixture, however a complete set of elastic and thermodynamic properties for these two garnet endmembers is unavailable in literature. Thus, we calculated expected strains for given entrapment *P-T* conditions using data for grossular and/or pyrope. Grossular is closest to the elastic behaviour of spessartine, and results for a spessartine host should fall between those of grossular and pyrope. Differences between elastic properties of garnet endmembers are small, and as a result, only minor variations (<5% at near-identical ratio of $\varepsilon_1+\varepsilon_2$ vs. ε_3) in expected strains should occur when using properties of a different endmember (Zaffiro, 2020).

3.5.1 Quartz inclusions

A gem-quality quartz crystal was selected as unstrained reference crystal. As quartz does not incorporate amounts of trace elements that significantly alter its elastic properties or Raman spectrum, no chemical analysis was required.

Out of twelve Raman-active modes of quartz, four were selected to be used for the determination of elastic strains (Figure 3.1). Selection criteria are that peaks must not overlap with the spectrum of the host garnet, and that the peaks must be sufficiently sensitive to strain to result in significant peak shifts compared to the analytical error. The selected peaks are similarly sensitive to $\varepsilon_1+\varepsilon_2$ vs. ε_3, which will result in a large uncertainty along the lines of constant peak position (Figure 3.1).

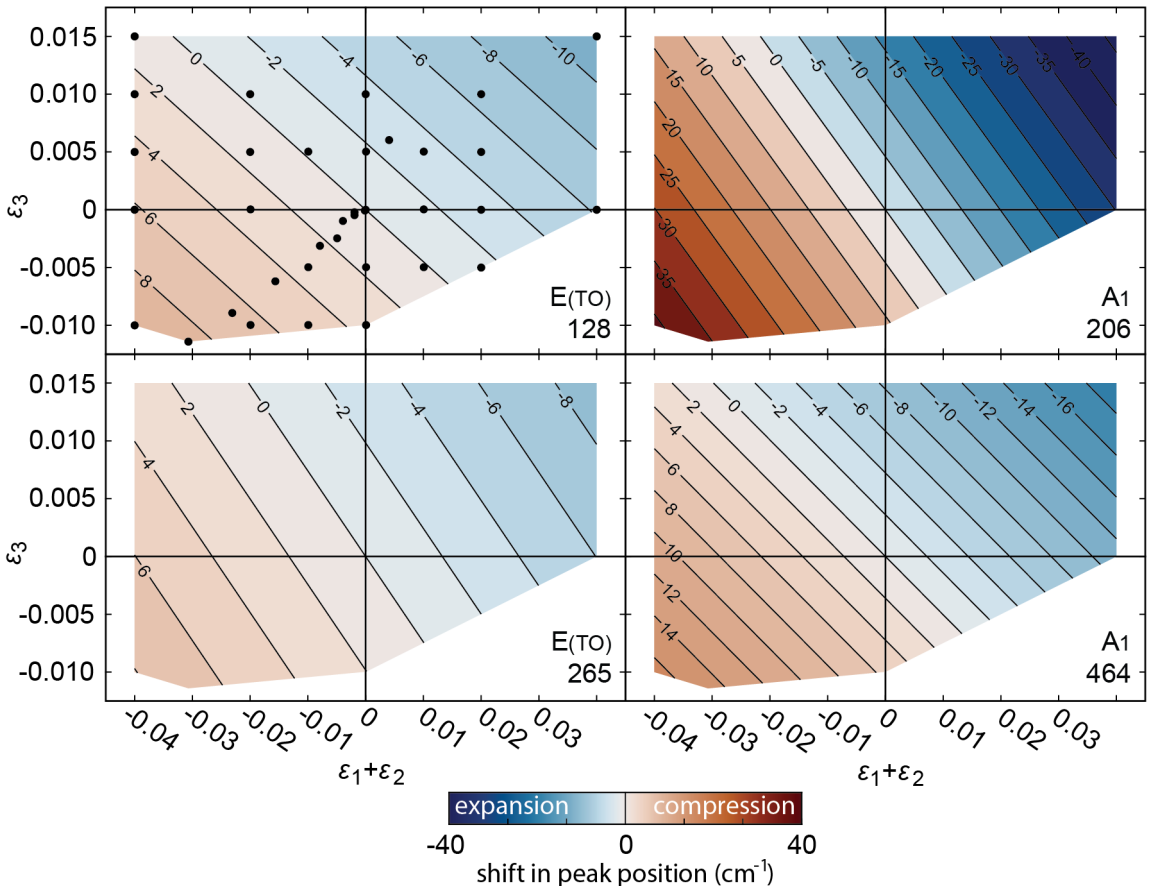

Figure 3.1: Overview of the effect of strain components $\varepsilon_1+\varepsilon_2$ vs. ε_3 on the shift in the peak position ω (cm^{-1}) for four selected Raman modes of quartz. Data is from Murri et al. (2018), colormap is "Vik" (Crameri, 2018). The strain values of used density functional theory simulations are given as black circles in the top left graph. See text for explanation on selection of modes.

3.5.2 Zircon inclusions

A gem quality zircon crystal from the Mud Tank carbonatite complex in Australia was used as reference (Gain et al., 2019). This crystal is the same material as is used in the study by Zaffiro (2020) for the determination of the equation of state of zircon.

The Raman spectrum of Zircon has thirteen Raman-active modes, which vary in sensitivity to strain and in the degree of sensitivity to $\varepsilon_1+\varepsilon_2$ vs. ε_3. The sensitivity of seven selected modes (Campomenosi et al., 2020) to $\varepsilon_1+\varepsilon_2$ vs. ε_3 results in the spacing between, and slope of, lines of equal shift of the Raman peak (Figure 3.2). Obtaining strain values with a low uncertainty relies on the use of multiple Raman modes, preferably with a high as possible sensitivity, and a high variety in isoline slope. A high analytical error or fitting error compared to the shift in peak position should be avoided, and therefore less sensitive peaks are usually unreliable.

The chemical composition and metamictization of zircon can have a strong impact on its Raman spectrum and elastic properties (Campomenosi et al., 2020 and references therein). A

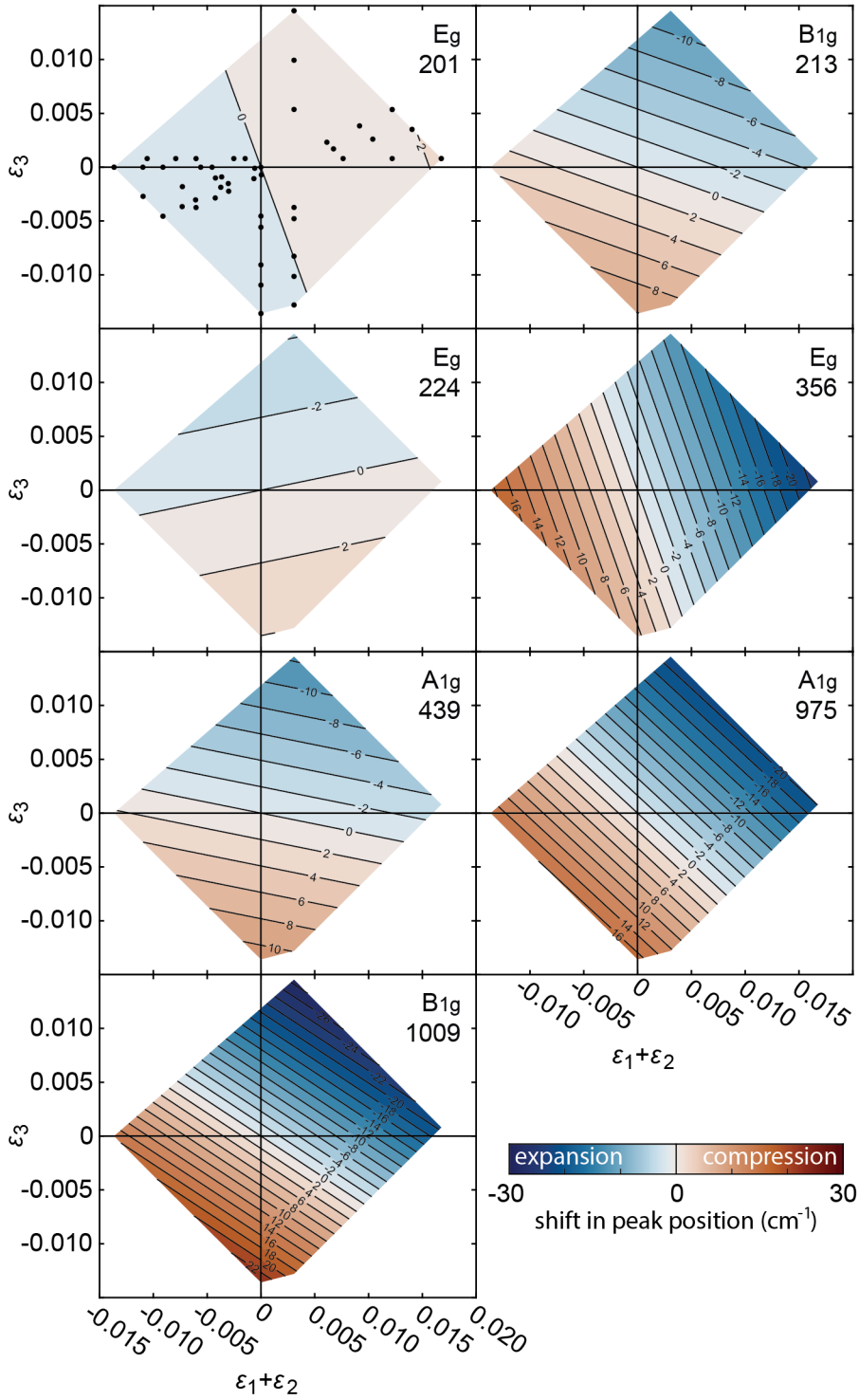

Figure 3.2: Overview of the effect of strain components $\varepsilon_1+\varepsilon_2$ vs. ε_3 on the shift in the peak position ω (cm^{-1}) for seven selected Raman modes of zircon. Data is from Stangarone et al. (2019), colormap is "Vik" (Crameri, 2018). The strain values of used DFT simulations are given as black dots in the top left graph. See text for explanation on selection of modes.

protocol to test for metamictization in zircon inclusions was established by Campomenosi et al. (2020), using the full width at half maximum (FWHM) of the B_{1g} Raman mode at approximately 1009 cm^{-1}. The suggested FWHM for zircon crystals is smaller than 5 cm^{-1}, illustrated by a relation between FWHM and a negative shift in the peak position of the 1009 mode ("trend 1" in Figure 2 of Campomenosi et al., 2020). The value of 5 cm^{-1} as limit for the FWHM is based on a Raman

spectroscope with a spectral resolution of 2 cm^{-1}, whereas the spectrometer used in this study has a spectral resolution of 0.52 cm^{-1}. Therefore, a stricter limit could be applied.

3.6 LA-ICP-MS

Trace element mineral composition of rutile was determined by laser ablation inductively coupled plasma mass spectrometry (LA-ICP-MS) at the IGG-CNR (Istituto di Geoscienze e Georisorse of the National Research Council) of Pavia. The instrument couples an Excimer Laser 193 nm ArF (GeoLas200 Microlas) with a Triple Quadrupole (8900 QQQ from Agilent). Elements that were measured are: 7 Li, 9 Be, 11 B, 23 Na, 25 Mg, 27 Al, 29 Si, 39 K, 43 Ca, 44 Ca, 45 Sc, 47 Ti, 51 V, 53 Cr, 55 Mn, 57 Fe, 59 Co, 60 Ni, 63 Cu, 66 Zn, 75 As, 85 Rb, 88 Sr, 89 Y, 90 Zr, 93 Nb, 95 Mo, 118 Sn, 121 Sb, 133 Cs, 138 Ba, 139 La, 140 Ce, 141 Pr, 146 Nd, 149 Sm, 151 Eu, 157 Gd, 159 Tb, 163 Dy, 165 Ho, 167 Er, 169 Tm, 173 Yb, 175 Lu, 177 Hf, 181 Ta, 182 W, 208 Pb, 232 Th and 238 U.

NIST-SRM610 was used as an external standard, whereas Ti was adopted as internal standard for rutile, and Si for garnet. In each analytical run the USGS reference samples BCR2 and NIST612 (Norman et al., 1996; Pearce et al., 1997; Rocholl et al., 1997) were analysed together with the unknowns for quality control. Precision and accuracy are better than 5% and 10%, respectively. Data reduction was performed using the Glitter software package (Van Achterbergh, 2001). A 50 μm wide laser beam was deployed to analyse 16 spots over six rutile grains, measuring core and rim separately when grain size allowed it, and using an average TiO_2 content of 99 wt% as internal standard. The wt% SiO_2 as internal standard for garnet was determined per garnet population (see Appendix D for values). Rare earth element composition diagrams display concentrations that were normalized against the chondrite composition from McDonough & Sun (1995).

3.7 Scanning Electron Microscopy

Rutile was characterised by using the TESCAN MIRA3 field-emission scanning electron microscope (SEM) at the John de Laeter Centre (JdLC), Curtin University, Perth, Australia. BSE images were collected at a working distance of 15 mm and an accelerating voltage of 20 kV. For combined electron backscatter diffraction (EBSD) and energy dispersive x-ray spectroscopy (EDS) imaging the SEM was operated at a working distance of 15 mm with the stage tilted to 70°. An accelerating voltage of 20 kV was applied with a beam intensity of 17, yielding a beam current of 3 nA. EBSD data were acquired at a step size of 1 μm and the match units for rutile (Swope et al., 1995) and omphacite (Oberti and Caporuscio, 1991) were obtained from the American Mineralogist crystallography database (801 448-45x).

Transmission Kikuchi Diffraction (TKD) was performed on the Atom Probe tomography (APT) specimens to assist with targeting the low-angle boundaries during sample preparation for ATP and to provide correlation with APT data. TKD was performed with a step size of 15 nm and at a working distance of 9 mm, 90° tilt, an accelerating voltage of 30 kV, and a beam intensity of 15, yielding a beam current of 2 nA.

Post-processing of EBSD (for Chapter 8 only) and TKD data was performed in Matlab®, version R2019a, using the free toolbox MTEX Version 5.3 (Bachmann et al., 2010). Images were plotted using the colourblind friend colourkey of Crameri (2018). Post-processing involved a noise reduction procedure by applying a wildspike correction and removal of 'grains' < 5 pixels. The procedure was followed by applying a 5x5 pixel Median Filter, part of the MTEX toolbox. The function works similar to a nearest-neighbour extrapolation in for example Channel5. The filter smooths the EBSD data and is designed to preserve subgrain boundaries in the process.

3.8 Focused-Ion-Beam SEM

Specimen preparation for transmission electron microscopy (TEM) and APT was conducted on the Tescan Lyra Ga+ Focused Ion Beam Scanning Electron Microscope (FIB-SEM), which is part of the Advanced Resource Characterization Facility (ARCF) within the JdLC. The FIB-SEM was operated at an accelerating voltage of 30 kV. TEM and APT specimens were extracted from one low-angle boundary in a single grain. The TEM foil was mounted on a copper half-grid and thinned to < 100 nm followed by a 2 kV cleaning routine to remove damage induced by 30 kV specimen preparation. APT specimens were precisely targeted using electron-beam deposited markers and followed by the standard lift-out and sharpening procedures and 2 kV clean up routine (Rickard et al., 2020). TKD imaging ensured the low-angle boundary (LAB; see Chapter 8) was present close to the apex of the tip after final sample preparation and consequently within the field-of-view for APT analysis. Final secondary electron (SE) imaging was performed in SEM-mode only at a working distance of 6 mm and an accelerating voltage of 10 kV.

3.9 Transmission Electron Microscopy

TEM analysis was performed on the FEI Talos FS200X Field Emission Gun TEM equipped with a Super-X EDS detector housed in the John de Laeter Centre, Curtin University, Australia. The TEM was operated at 200 kV. TEM imaging was conducted in both bright- and dark-field (BF and DF) modes. The TEM diffraction investigation was conducted with the assistance of Kikuchi patterns that were generated by convergent beam electron diffraction (CBED). A small spot was used to minimize the beam-related damage to the sample, and the sample was tilted to align a zone axis or meet a two-beam condition to acquire selected area diffraction (SAD) patterns. Both BF and DF TEM imaging were undertaken with the objective apertures after tilting the sample to a diffraction condition within 20°.

Chemical analysis was conducted using the attached two pairs of Super-X detectors. The TEM is fitted with four scanning transmission electron microscopy (S/TEM) detection systems: High Angle Annular Dark Field (HAADF), upper Dark Field (DF4), lower Dark Field (DF2), and Bright Field (BF). The contrast in HAADF images results predominantly from chemical/phase differences and the contrast in BF images results predominantly from orientation differences. The DF4 and DF2 detectors reveal both chemical and orientation contrasts at different angles. TEM, S/TEM, and EDS data acquisition were conducted with the Velox software.

3.10 Atom Probe Tomography

Five needle-shaped specimens were run in the atom probe yielding 38×106–95×106 ion counts. All specimens remained intact after the run. APT analyses were performed on a Cameca Local Electrode Atom Probe (LEAP) 4000X HR that is part of the ARCF in the JdlC. The LEAP was operated in laser-assisted mode at a pulse rate of 200 kHz, a laser pulse energy of 50 pJ, a base temperature of 50 K and a detection rate of 0.8% (1600 ions s^{-1}) based on recommendations by Verberne et al. (2019). Post-processing was performed using Cameca's Integrated Visualization and Analysis Software (IVAS) 3.8.0. Peaks in the mass spectra were labelled per individual element for specific ionization states and ranged with a constant width of 0.2 Da unless resulting in the measurement of background signals. Detailed information about acquisition and post-processing is provided in Appendix E based on Blum et al. (2018). For visualization and compositional analyses, isoconcentration surfaces were computed in 3D using IVAS (Hellman et al., 2000).

References

Angel, R.J., Mazzucchelli, M.L., Alvaro, M., Nimis, P., Nestola, F., 2014a. Geothermobarometry from host-inclusion systems: The role of elastic relaxation. American Mineralogist, 99, 2146–2149

Angel, R.J., Gonzalez-Platas, J., Alvaro, M., 2014b. EosFit-7c and a Fortran module (library) for equation of state calculations. Zeitschrift für Kristallographie, 2009, 405–419

Angel, R.J., Murri, M., Mihailova, B., Alvaro, M., 2019. Stress, strain and Raman shifts. Zeitschrift für Kristallographie - Crystalline materials, 234(2), 129–140. DOI: https://doi.org/10.1515/zkri-2018-2112

Bachmann, F., Hielscher, R., Schaeben, H., 2010. Texture Analysis with MTEX - Free and Open Source Software Toolbox. Solid State Phenomena, 160, 63–68

Blum, T.B., Darling, J.R., Kelly, T.F., Larson, D.J., Moser, D.E., Perez-Huerta, A., Prosa, T.J., Reddy, S.M., Reinhard, D.A., Saxey, D.W., Ulfig, R.M., Valley, J.W., 2018. Best Practices for Reporting Atom Probe Analysis of Geological Materials: In D.E. Moser, F. Corfu, J.R. Darling, S.M. Reddy, and K. Tait, Eds., Microstructural Geochronology. Planetary records down to atom scale, 369–373, Wiley

Campomenosi, N., Mazzucchelli, M.L., Mihailova, B., Scambelluri, M., Angel, R.J., Nestola, F., Reali, A., Alvaro, M., 2018. How geometry and anisotropy affect residual strain in host-inclusion systems: Coupling experimental and numerical approaches. American Mineralogist, 103(12), 2032–2035. DOI: 10.2138/am-2018-6700CCBY

Campomenosi, N., Rubatto, D., Hermann, J., Mihailova, B., Scambelluri, M., Alvaro, M., 2020. Establishing a protocol for the selection of zircon inclusions in garnet for Raman thermobarometry. American Mineralogist 105 992–1001

Chernov, N., 2020. Ellipse Fit (Direct Method). MATLAB Central File Exchange, https://www.mathworks.com/matlabcentral/fileexchange/22684-ellipse-fit-direct-method

Crameri, F., 2018. Scientific colour-maps. Zenodo. http://doi.org/10.5281/zenodo.1243862

Fitzgibbon, A., Pilu, M., Fisher, R.B., 1999. Direct least square fitting of ellipses. IEEE Transactions on Pattern Analysis and Machine Intelligence, 21(5), 476–480

Gain, S.E.M., Gréau, Y., Henry, H., Belousova, E., Dainis, I., Griffin, W.L., O'Reilly, S.Y., 2019. Geostandards and Geoanalytical Research, 43(3), 339–354

Geiger, C.A., Armbruster, T., 1997. $Mn_3Al_2Si_3O_{12}$ spessartine and $Ca_3Al_2Si_3O_{12}$ grossular garnet: Structural dynamic and thermodynamic properties. American Mineralogist, 82, 740–747

Groppo, C., Beltrando, M., Compagnoni, R., 2009. The *P-T* path of the ultra-high pressure Lago di Cignana and adjoining high-pressure meta-ophiolitic units: insights into the evolution of the subducting Tethyan slab. Journal of Metamorphic Geology, 27, 207–231

Hellman, O. C., Vandenbroucke, J. A., Rusing, J., Isheim, D., Seidman, D. N., 2000. Analysis of Three-dimensional Atom probe Data by the Proximity Histogram. Microscopy and Microanalysis, 6(5), 437–444

Kuzmany, H., 2009. Light Scattering Spectroscopy. In: Solid-State Spectroscopy. Springer, Berlin, Heidelberg

Mazzucchelli, M.L., Burnley, P., Angel, R.J., Morganti, S., Domeneghetti, M.C., Nestola, F., Alvaro, M., 2018. Elastic geothermobarometry: Corrections for the geometry of the host-inclusion system. Geology, 46(3), 231–234

Mazzucchelli, M.L., Angel, R.J., Alvaro, M., 2021. EntraPT: an online platform for elastic geothermobarometry. American Mineralogist, in press. DOI: https://doi.org/10.2138/am-2021-7693CCBYNCND

McDonough, W.F., Sun, S.-s., 1995. The composition of the Earth. Chemical Geology, 120(3-4), 223–253

Murri, M., Mazzucchelli, M.L., Campomenosi, N., Korsakov, A.V., Prencipe, M., Mihailova, B.D., Scambelluri, M., Angel, R.J., Alvaro, M., 2018. Raman elastic geobarometry for anisotropic mineral inclusions. American Mineralogist, 103(11), 1869–1872

Murri, M., Alvaro, M., Angel, R.J., Prencipe, M., Mihailova, B.D., 2019. The effects of non-hydrostatic stress on the structure and properties of alpha-quartz. Physics and Chemistry of Minerals, 46, 487–499. DOI: 10.1007/s00269-018-01018-6

Norman, M., Pearson, N., Sharma, A., Griffin, W., 1996. Quantitative analysis of trace elements in geological materials by laser ablation ICPMS: instrumental operating conditions and calibration values of NIST glasses. Geostandards Newsletter, 20(2), 247–261

Oberti, R., Caporuscio, F. A., 1991. Crystal chemistry of clinopyroxenes from mantle eclogites: a study of the key role of the M2 site population by means of crystal-structure refinement: American Mineralogist, 76, 7-8, 1141–1152

Pearce, N. J., Perkins, W. T., Westgate, J. A., Gorton, M. P., Jackson, S. E., Neal, C. R., Chenery, S. P., 1997. A compilation of new and published major and trace element data for NIST SRM 610 and NIST SRM 612 glass reference materials. Geostandards newsletter, 21(1), 115–144

Reinecke, T., 1998. Prograde high- to ultahigh-pressure metamorphism and exhumation of oceanic sediments at Lago di Cignana, Zermatt-Saas Zone, western Alps. Lithos. 42, 147–189

Rickard, W. D., Reddy, S. M., Saxey, D. W., Fougerouse, D., Timms, N. E., Daly, L., Peterman, E., Cavosie, A. J., Jourdan, F., 2020. Novel Applications of FIB-SEM-Based ToF-SIMS in Atom Probe Tomography Workflows. Microscopy and Microanalysis, 1–8

Rocholl, A. B., Simon, K., Jochum, K. P., Bruhn, F., Gehann, R., Kramar, U., Luecke, W., Molzahn, M., Pernicka, E., Seufert, M., 1997. Chemical Characterisation of NIST Silicate Glass Certified Reference Material SRM 610 by ICP-MS, TIMS, LIMS, SSMS, INAA, AAS and PIXE. Geostandards Newsletter, 21(1), 101–114

Stangarone, C., Angel, R. J., Prencipe, M., Campomenosi, N., Mihailova, B., Alvaro, M., 2019. Measurements of strains in zircon inclusions by Raman spectroscopy. European Journal of Mineralogy, 31(4), 685–694

Swope, R. J., Smyth, J. R., Larson, A. C., 1995. H in rutile-type compounds: I. Single-crystal neutron and X-ray diffraction study of H in rutile. American Mineralogist, 80, 5-6, 448–453

Van Achterbergh, E., 2001. Data reduction software for LA-ICP-MS. Laser Ablation-ICP-mass spectrometry in the earth sciences: principles and applications, 239–243

Verberne, R., Saxey, D. W., Reddy, S. M., Rickard, W. D., Fougerouse, D., Clark, C., 2019. Analysis of Natural Rutile (TiO2) by Laser-assisted Atom Probe Tomography. Microscopy and Microanalysis, 1–8

Zaffiro, G., 2020. Constraints on the Equations of State of rutile and zircon: implications for elastic geothermobarometry. PhD Thesis, Cycle XXXII, University of Pavia

Zhang, Y., 1998. Mechanical and phase equilibria in inclusion-host systems. Earth and Planetary Science Letters, 157, 209–222

CHAPTER 4

Extensive fluid-rock interaction and pressure solution in a UH*P* fluid pathway recorded by garnetite

Abstract

This study combines the microstructural and petrological analysis of garnet and its inclusions in quartzite-hosted garnetite from the ultrahigh-pressure Lago di Cignana metaophiolite (Western Alps). We present a comprehensive record of metamorphism, compaction, and the state of stress during interaction between oceanic metasediments and infiltrating fluids along a major open-system fluid pathway.

The arrangement of garnet into garnetite layers is attributed to concomitant compaction and dissolution that resulted in the formation of a garnet stylolite. The fluid pulses that were accommodated by this pathway subsequently resulted in several stages of garnet deformation, dissolution, local reprecipitation, and recrystallization. Abundant evidence for pressure solution in garnet, alongside near-hydrostatic to hydrostatic conditions indicated by elastic strains of quartz inclusions in garnet obtained through Raman spectroscopy, support low differential stresses during fluid-rock interaction.

The high degree of dissolution recorded by the garnetite showcases the strong potential for compaction by fluid-assisted volume loss and mass transfer. Dehydration of subducting rocks with subsequent migration of resulting fluids through the slab provides a mechanism of mass transfer and has the potential to drive compaction and exert control on differential stress along fluid pathways.

Published as: Van Schrojenstein Lantman, H.W., Scambelluri, M., Gilio, M., Wallis, D., Alvaro, M., 2021. Extensive fluid-rock interaction and pressure solution in a UHP fluid pathway recorded by garnetite, Lago di Cignana, Western Alps. Journal of Metamorphic Geology, doi.org/10.1111/jmg.12585

4.1 Introduction

The importance of fluids in subduction systems is well established, as they control rheology, metamorphism, metasomatism, and volcanism (Peacock, 1990; Scambelluri & Philippot, 2001; Bürgmann & Dresen, 2008; Gerya & Meilick, 2011; Spandler & Pirard, 2013). In subduction zones, the volumes of fluids released from the slab (Van Keken et al., 2011) and the difference in fluid composition from dehydration at the source rock to solute-rich fluid in the mantle wedge, require that fluid-rock interaction takes place along the intervening pathways (Hermann et al., 2006; Bebout, 2007; Herms et al., 2012; Dragovic et al., 2015; Taetz et al., 2018; Brovarone et al., 2020). Despite the relevance of fluid-rock interaction for interpreting geological processes, several factors, such as complex solubilities and speciation, retrograde overprinting, limited exhumation and exposure, and other gaps in the rock record challenge our progress in this field.

A viable process of fluid interaction with high-pressure rocks is dissolution-precipitation (e.g., Ague & Nicolescu, 2014; Angiboust et al., 2017; Ferrando et al., 2017; Giuntoli et al., 2018). As this mechanism can take place at low differential stresses, it is widespread in subduction zones (Wassmann et al., 2011; Wassman & Stöckhert, 2013b). However, as precipitation does not necessarily occur at or near the site of dissolution, this fluid-driven process can facilitate mass loss at the reaction sites and mass transfer in subducting slabs while leaving barely perceptible traces. Tracing dissolution can be further complicated by retrograde overprinting, which is common in high-pressure terranes. Considering the long distances of up to several kilometres over which mass transport is hypothesized in subduction settings, finding an intact fluid pathway on this scale within dismembered high-pressure terranes is unlikely. Therefore, field-based studies will only probe small portions of fluid pathways, which should be treated as open systems (Plümper et al., 2017). Consequently, to understand the process of mass transfer through the slab, the single components of such large-scale systems must be studied individually.

The ultrahigh-pressure metamorphic (UHPM) Lago di Cignana unit (LCU) is a famous coesite- and diamond-bearing Alpine meta-ophiolite (Reinecke, 1991; Frezzotti et al., 2011) and a rare example of oceanic crust that reached 90-110 km depths (Reinecke, 1998; Groppo et al., 2009). Garnetite is common to various LCU lithologies, and although garnetites are typically sedimentary, metasomatic, melt- or fluid-related in origin (e.g., Spry et al., 2000; Vrijmoed et al., 2006; Angiboust et al., 2017; Hadjzobir et al., 2017), no origin mechanism has been established for the LCU garnetites. Infiltration of external fluids and extensive fluid-rock interaction within this unit have been revealed by detailed fluid-inclusion and geochemical studies, suggesting influx of locally solute-rich serpentinite-derived fluids (Hawkins et al., 2009; Frezzotti et al., 2011; Halama et al., 2020). Therefore, the LCU potentially includes remnants of a large-scale fluid pathway, which has not yet been identified and described in detail.

In this study, we examine the relation between the LCU Mn-rich quartzites and the garnetite lenses that they host using a combination of petrological, mineralogical and microstructural data. The observations elucidate how fluid pathways shaped the metasediments, how garnetite formed by a newly-described mechanism involving pressure solution, how fluid-rock interaction evolved over time during metamorphism, and the stress regime during this process.

4.2 Geological background

The Alpine high-pressure ophiolites of the Piemonte zone (Figure 4.1) are the dismembered remnants of the Mesozoic Tethyan Ocean that was subducted during Alpine plate convergence and orogeny (Dal Piaz et al., 1999 and references therein). The Lago di Cignana Unit is a coesite- and diamond-bearing UHPM ophiolitic sliver cropping out between two major metaophiolitic units:

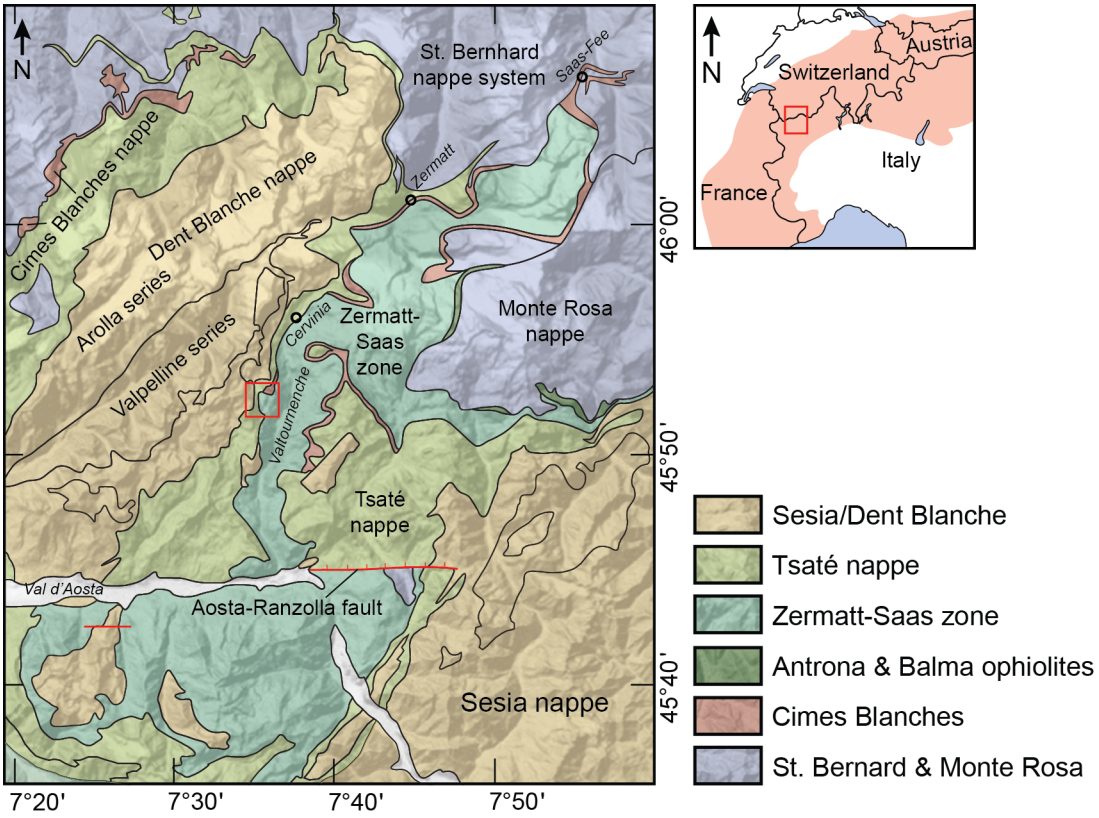

Figure 4.1: Geological map of the large-scale context of the Zermatt-Saas zone in the vicinity of the Lago di Cignana unit, modified after Kirst and Leiss (2017) and references therein. The red square in the main map indicates the location of Lago di Cignana and Figure 4.2a.

the underlying Zermatt-Saas Zone (ZSZ) recording eclogite-facies metamorphic conditions of 520 ± 20 °C, 2.3 GPa (Angiboust et al., 2009), and the overlying Combin Zone (CZ) recording blueschist-facies conditions of 300–345 °C, ~0.9 GPa (Reddy et al., 1999).

The relation between the LCU and the ZSZ is still debated. One possibility is that the LCU is one of several minor bodies of diverse origin that crop out along the contact between the ZSZ and CZ (Dal Piaz et al., 2001; Gilio et al., 2019), which differ in their peak-metamorphic age, *P-T* evolution, and provenance (Theodul Glacier Unit, Etirol-Levaz Slice, Allalin Gabbro; Weber et al., 2015; Bucher & Grapes, 2009; Beltrando et al., 2010). The alternative is that the LCU is located within the upper levels of the ZSZ, and only deviates in terms of peak metamorphic pressure, while metamorphic ages and temperatures match (Groppo et al., 2009; Skora et al., 2015).

The LCU consists of coesite-bearing eclogite, serpentinite (Gilio et al., 2019) and metasediments varying from calcschist and marble to several types of manganiferous quartzites (Reinecke, 1998; Forster et al., 2004). The quartzite varies from schistose garnet-amphibole-phengite quartzites, to purple, hydrothermally Mn-enriched quartzite similar to other Mn-rich metasediments from the ZSZ (Tumiati et al., 2010). Garnetite is present in several metasediments and eclogites as lenses and boudins. Certain LCU garnetites contain fluid inclusions with solutes that originated from the dissolution of carbonate and quartz (Frezzotti et al., 2011). Furthermore, Hawkins et al. (2009) observed an assemblage of daughter minerals in fluid inclusions in garnetite, consisting of jadeite, paragonite, phengite, chlorite, amphibole, titanite and K-feldspar alongside Ca-sulfates, phosphates and oxides. This evidence suggests the dissolution of a polymineralic component of the system during garnet growth, beyond quartz and carbonates (Frezzotti et al., 2011; Hawkins et al., 2009). Boron concentrations and isotopic ratios in white mica within several lithologies in the LCU area indicate that a fluid derived from partially dehydrated serpentinites was the driver behind fluid-rock interaction in quartzite, but not in eclogite (Halama et al., 2020).

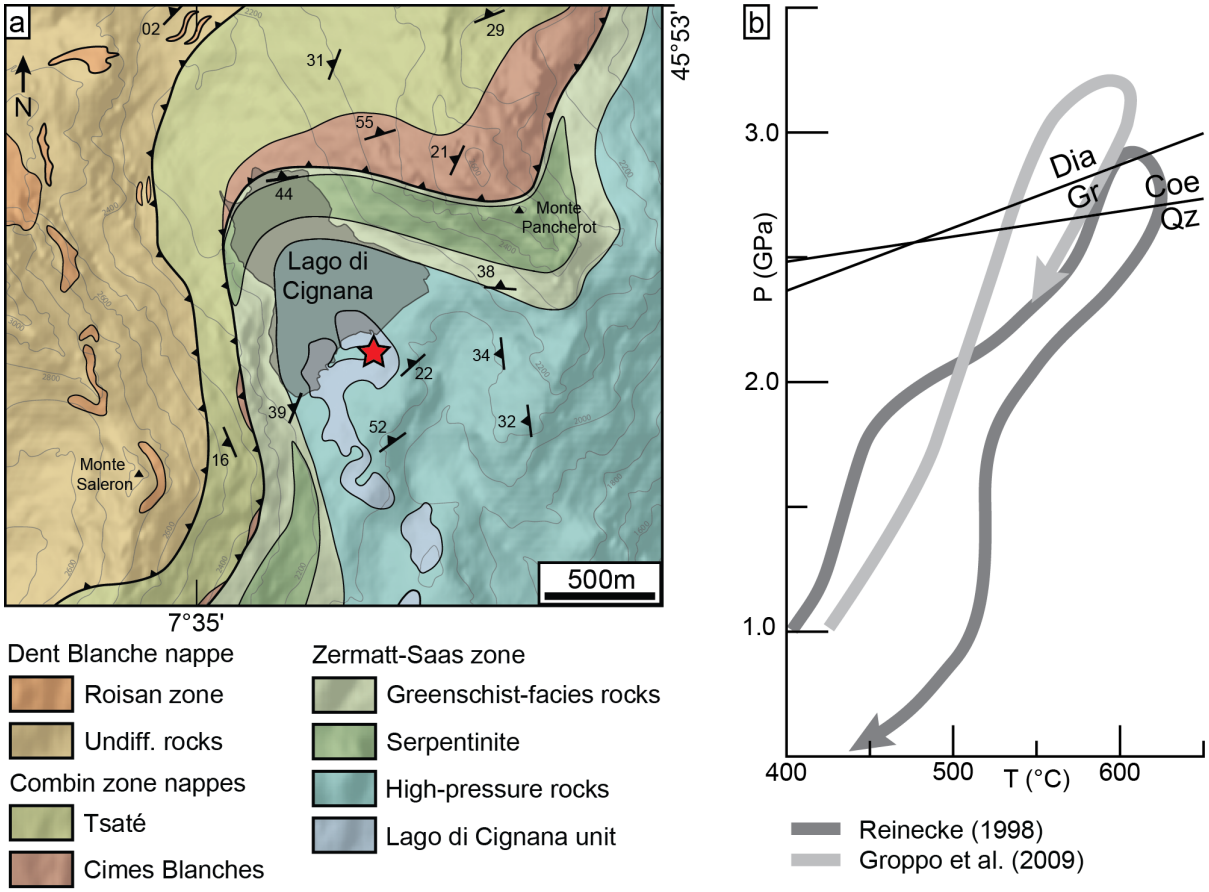

Figure 4.2: (a) Geological map of the Lago di Cignana area with sample location, modified after Kirst and Leiss (2017) and references therein. (b) *P-T* paths determined for Lago di Cignana based on metasediments (Reinecke, 1998) and eclogite (Groppo et al., 2009). Mineral abbreviations are from Whitney and Evans (2010).

4.3 Methods

4.3.1 Sample preparation

Samples were processed into sections 100 µm thick for petrographic analysis and electron microscopy. For the purpose of strain analysis on inclusions in garnet, sections 250 µm thick were prepared to maximize the number of inclusions without strain dissipation due to proximity to the surface of the section. Sections were polished with a 0.05-µm colloidal-silica suspension in preparation for high-quality electron microscopy.

4.3.2 Electron microscopy

Electron probe micro-analysis (EPMA) measurements of major elements were performed using a JEOL JXA 8200 Superprobe at the Department of Earth Sciences, University of Milan. An accelerating potential of 15 kV and a beam current of 15 nA were used for spot analyses with a 30 second counting time. Measurements for element-distribution maps were performed with a combination of WDS and EDS, at 15 nA and 100 nA for high-detail maps. Element distribution maps were plotted using an inversion of the "roma" scientific colour map (Crameri, 2018).

4.3.3 Electron Backscatter Diffraction

Electron backscatter diffraction (EBSD) data were acquired on a Phillips XL-30 field-emission gun scanning electron microscope equipped with an Oxford Instruments' Nordlys-Nano EBSD detector and AZtec 3.3 acquisition software. An EBSD map of 1638 x 1228 pixels was acquired at a step size of 0.9 μm and an accelerating voltage of 30 kV. Data were processed using the MTEX v5.1.1 toolbox (Bachmann et al., 2010) for MATLAB®. Grain reconstruction was performed with a minimum misorientation value for grain boundaries of 2°. Although this value is low, no subgrain boundaries were misidentified as grain boundaries as subgrains are absent in the analysed garnet crystals. All grains below 5 pixels in size were considered to result from misindexing and were removed. Unindexed areas 1 pixel in size were filled in by interpolation. Grains in contact with the outer boundary of the map were removed from grain-size analysis. The EBSD map was colour coded by grain size using an inversion of the "roma" scientific colour map (Crameri, 2018).

4.3.4 Raman spectroscopy

Raman spectra of quartz inclusions in garnet were collected with a Horiba LabRam HR Evolution spectrometer (holographic gratings of 1800 grooves/mm) equipped with an Olympus BX41 confocal microscope at the controlled temperature of 20(1) °C. Raman spectra were excited using the 514.532 nm line of a solid state (YAG) laser. The laser power on the sample surface was approximately 1–2 mW. The spectrometer was calibrated to the silicon Raman peak at 520.5 cm^{-1}. The spectra were baseline corrected for the continuum luminescence background when necessary, temperature reduced to account for the Bose-Einstein occupation factor (Kuzmany, 2009) and normalized to the acquisition time. Peak positions, full-widths at half maximum (FWHM), and integrated intensities were determined from fits with pseudo-Voigt functions (*pseudoVoigt = (1-q)*Lorentz+q*Gauss*, where *q* is the mixing coefficient).

4.3.5 Elastic-strain analysis

Elastic strains in quartz were determined for 17 quartz inclusions in garnet by using the relationship between strain and shifts in the position of selected Raman peaks (Angel et al., 2019; Murri et al., 2019). The shift, $\Delta\omega$, of each Raman peak is the difference between the peak positions in the inclusion, ωi, and an unstrained reference crystal, $\omega 0$. To reduce shifts in peak position due to instrumental drift and/or minor changes to room temperature, the unstrained standard was measured multiple times per session. The $\omega 0$ values were averaged and then subtracted from the ωi of the strained inclusions analysed in between two consecutive standards. Sets of $\Delta\omega$ (modes 128, 206, 464 and, when available, 265) for each inclusion were converted to strain using the software stRAinMAN (Angel et al., 2019), applying the Grüneisen tensors for quartz (Murri et al., 2018) and relaxation of the strains (Angel et al., 2014a). Strain interference can occur due to complex inclusion geometries or inclusion proximity to the sample surface, outer edge of the garnet, or other inclusions. Therefore, we only analysed non-faceted, rounded and sub-rounded inclusions, isolated by at least three times their radius (Campomenosi et al., 2018; Mazzucchelli et al., 2018; Zhang, 1998).

For comparison with the strain state in inclusions measured with Raman, numerically predicted strains were calculated based on expected entrapment conditions using the software EosFit7c (Angel et al., 2014b). The prograde *P-T* path for the LCU (Reinecke, 1998; Groppo et al., 2009) was divided into four segments of 0.5 GPa by 100 °C (varying with pressure along the *P-T* path), from 1.0 GPa to 3.0 GPa. Pressure was extended into the coesite field to accommodate

any potential overstepping of the quartz-coesite transformation. Precise *P-T* values and resulting calculated strain states are available in the supplementary material. The host garnet mainly consists of an almandine + spessartine mixture, however a complete set of elastic and thermodynamic properties for these two garnet endmembers is unavailable in literature. Thus, we calculated expected strains for given entrapment *P-T* conditions using data for grossular. Differences between elastic properties of garnet endmembers are small, and as a result, only minor variations (< 5% at near-identical ratio of $\varepsilon_1+\varepsilon_2$ vs. ε_3) in expected strains should occur when using properties of a different endmember (Zaffiro, 2020).

4.4 Sample description

Garnetite layers and lenses are present in several of the LCU lithologies, including the Mn-rich schistose quartzite investigated here (Figure 4.3a–c) and eclogite (Figure 4.3d). However, this quartzite best preserves the relationship between the host rock and the garnetite. In contrast, the eclogite contains only sparse garnetite, and the structural relationship between eclogite and garnetite is unclear.

The Mn-rich schistose quartzite forms a 5 m-thick layer, at the centre of which is a 30 cm-thick zone where the majority of the garnetite is located. Here, the garnetite occurs as lenses, discon-

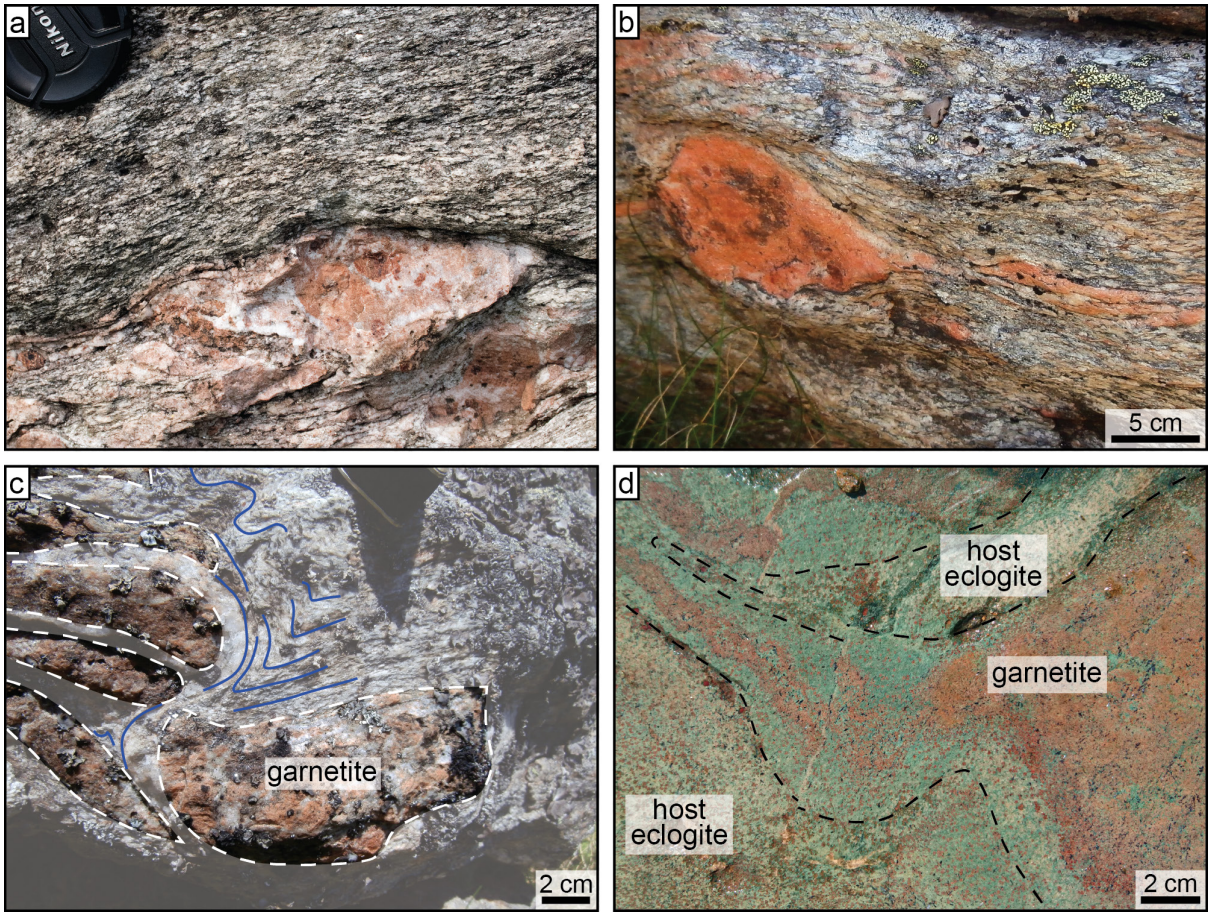

Figure 4.3: Outcrop photographs of the garnetite pods in quartzite. (a) Fresh cross section through quartzite with garnetite lens, displaying the complex interior of the garnetite. (b) Deformed garnetite lens exhibiting the sheared nature of these rocks. Garnetite continues as a layer of thin boudins through the exposure. (c) Stack of several garnetite bodies, indicated by white dashed lines. Solid blue lines indicate the highly folded foliation in the host rock. (d) Garnetite as occurring in eclogite from the LCU. A garnet-poor, omphacite-rich rim surrounds the garnetite layers and lenses. Dashed black line indicates the inferred boundary between host rock and garnetite with rim.

tinuous layers, dismembered fold hinges and limbs transposed along a phengite foliation (Figure 4.3a–c). This garnet quartzite can thus be subdivided into (i) garnet- and phengite-bearing schistose host rock and (ii) garnetite (Figure 4.3a). Boudinage of the garnetite indicates a competence contrast between the garnetite and the quartzite host rock (Figure 4.3b,c). The garnetite lenses, particularly the thicker parts, are structurally complex and appear heterogeneous in terms of garnet content based on colour variations. Some quartz-rich veins and patches cross cut the lens and its outer margins.

4.4.1 Host rock

The matrix of the host-rock quartzite exhibits a foliation defined by phengite, and contains garnets as euhedral grains < 1 mm in size (Figure 4.4b). Smaller anhedral garnet crystals are concentrated into lenses and layers < 1 cm across. The host rock also contains strongly zoned epidotes and aggregates of amphibole of a composition between magnesio-hornblende, actinolite, and winchite, alongside phengite, biotite, and quartz.
Two distinct mineral assemblages are present as inclusions in garnet (Table 4.1). In the cores of this garnet, inclusions of quartz, apatite, magnesite, dolomite, rutile, and zircon are present. Rutile is often < 1 μm in size, giving the garnet core an orange hue. In the garnet mantle, an assemblage of coesite, kyanite, clinozoisite, phengite, rutile, and zircon is present. The euhedral garnet rims contain occasional quartz inclusions.

Table 4.1: Overview of inclusion assemblages in garnet. An "x" indicates that the corresponding garnet zone is not present or indistinguishable from the core.

Rock type	Garnet type	core	mantle	rim
Host rock	Rock forming	Qz, Rt*, Dol, Mgs, Ap, Zrn	Coe, Ky, Czo, Ph, Zrn	Qz
Outer garnetite	Rock forming	Qz, Rt*, Dol, Mgs, Ap, Zrn	none	none
Inner garnetite	Rock forming	Qz, Rt*, Dol, Mgs, Ap, Zrn	x	x
Inner garnetite	Rock forming	Qz, Ap	x	x

4.4.2 Garnetite

The garnetite is microstructurally diverse (Figure 4.4a), and can be subdivided into an inner and outer garnetite. This subdivision is based on garnet size and on quartz content, with the outer garnetite having more interstitial quartz and larger garnets (Figure 4.4c). Besides being smaller and having less to no interstitial quartz, garnets in the inner garnetite have a "welded" appearance (Figure 4.4d). Large euhedral garnets are locally present on the outer margin of the inner garnetite (Figure 4.4e). The outer garnetite contains up to ~50% interstitial quartz by volume and occasional quartz veins cross cut the entire garnetite (Figure 4.4a). Rare accessory minerals, including phengite, apatite, biotite, and sulphides, are present in the garnetite. A variety of structures are present within the garnetite. The garnets in the outer garnetite are mostly euhedral and are often distributed in chains separated by quartz (Figure 4.4c). Garnets within this zone also exhibit a weak shape preferred orientation, as their long axis is subparallel to the host-rock foliation and perpendicular to the garnet chains.

In both garnetite zones the main inclusion assemblage is similar to that of host rock garnet

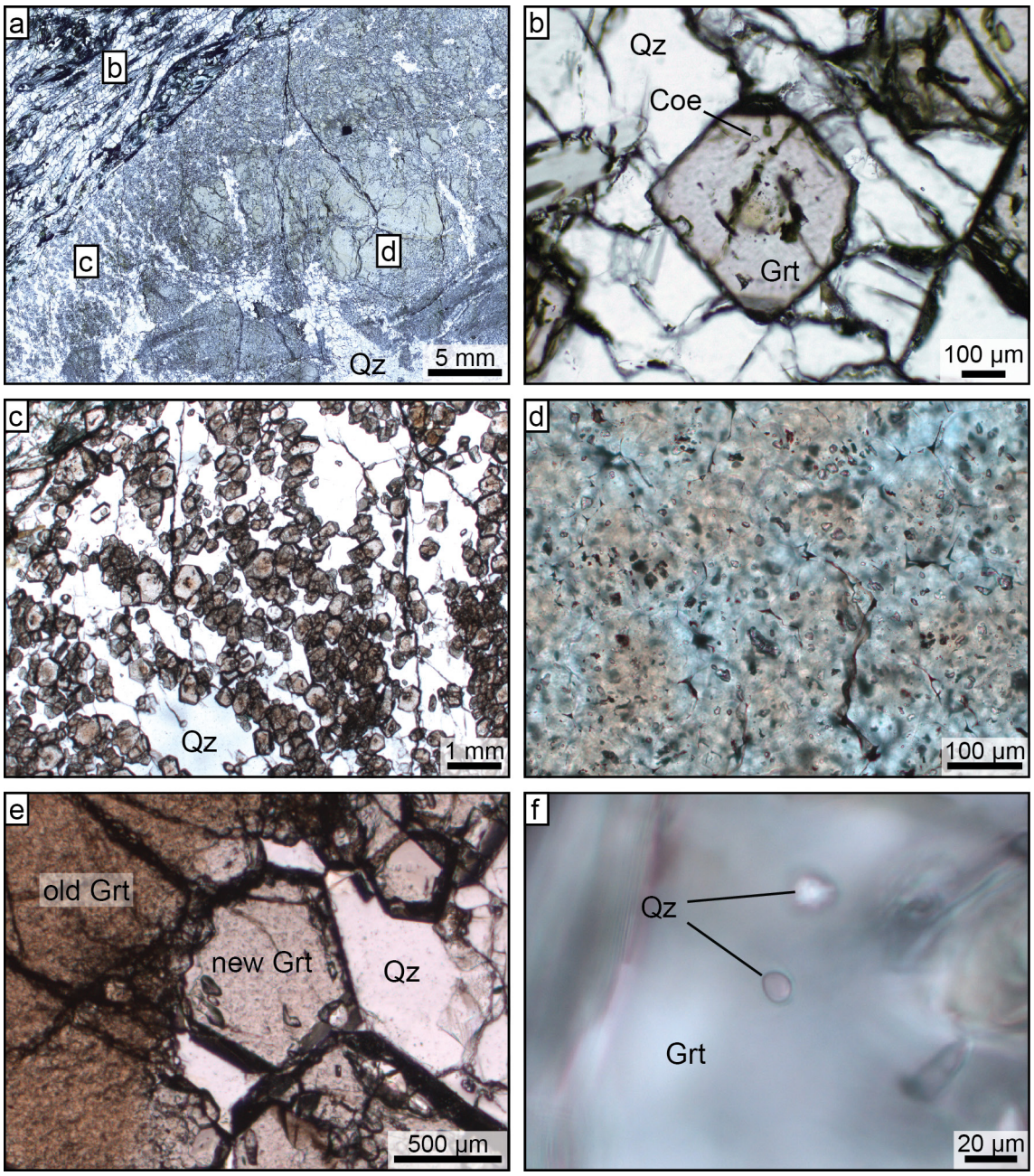

Figure 4.4: Micrographs of 100 µm-thick sections of host rock and garnetite, taken with plane-polarized transmitted light. (a) Overview of the section, including host rock in the top left corner. Locations for (b–d) are marked. (b) A garnet typical of those in the host rock. (c) Outer garnetite, occasionally consisting of chains of garnet separated by quartz, (d) Inner garnetite, consisting of "welded" garnet with numerous inclusions. (e) Euhedral garnet crystals grown over inner garnetite. (f) Quartz inclusions located inside euhedral garnet overgrowth in (e).

cores and consists of quartz, apatite, magnesite, dolomite, rutile, and zircon (Table 4.1). As in the host-rock garnets, rutile is usually sub-micron sized and occurs in clusters, which give the garnet an orange hue (Figure 4.4d). In the outer garnetite an inclusion-free rim is present around the inclusion-rich garnet core. The euhedral garnet overgrowth on the outer margin of the inner garnetite contains quartz inclusions (Figure 4.4f). No coesite has been observed in the garnetite.

4.5 Garnet structures and compsosition

4.5.1 Host rock

The backscattered electron (BSE) image of a representative host-rock garnet displays strong compositional zonation that is locally complicated by irregularities (Figure 4.5a). Radial veinlets that appear with the same brightness in BSE as the euhedral rims cross cut the darker garnet. The garnet cores do not exhibit any irregularity in zonation besides radial veinlets. In contrast, the growth zones surrounding the core (garnet mantle) are separated by irregular boundaries between compositional zones.

EPMA analyses and element distrution mapping of representative host rock garnets reveal a strong compositional zonation (Figure 4.7a,d,g, Figure 4.8a). Garnet compositions corresponding to coesite inclusions in host-rock garnet are marked as representing UHPM garnet growth (Figure 4.7a,d; Figure 4.8). From these analyses, two trends can be distinguished. The first compositional trend (labelled 1 in Figure 4.8a) forms the common prograde metamorphic zoning trend. Mn-rich garnet cores progress to compositions richer in Fe, whereas Mg initially increases in the intermediate mantle before decreasing so that Mg concentrations are similar between earliest and latest compositions. This metamorphic zonation is interrupted by irregular compositional boundaries located within the Mg-richer UHPM zone.

A second trend in garnet compositions also depletes in Mn and enriches in Fe, yet without the Mg–richer excursion, essentially forming a series of intermediate compositions between the earliest prograde growth stage and the latest growth stage (Figure 4.8). Compositions related to this trend occur along the radial veinlets, in the cores of garnets, and as the outer rim (very similar BSE intensity in Figure 4.5a; Figure 4.7a,d). The veinlets appear to radiate from the core of the garnet, where a ~50–100 μm zone of elevated Ti signal can be found, linked to the presence of sub-micron rutile inclusions (Figure 4.7g).

4.5.2 Garnetite

Garnets in the outer garnetite exhibit several similarities with garnets in the host rock (Figure 4.5b–e). One irregular boundary between compositional zones is typically present (Figure 4.5c) and, in addition, these garnet crystals display truncation of the metamorphic zones at garnet-garnet contacts (Figure 4.5b,c). The truncation involves portions of the garnet core and mantle, and is locally overgrown by another zone of garnet (Figure 4.5c). Radial veinlets are common to garnets in the outer garnetite (Figure 4.5b–e). Occasionally, garnets exhibit interlocking lobate structures between two cores (Figure 4.5d,e). The outer zone of the garnets is euhedral and free of veinlets. Particularly in the garnet-richer zones of the outer garnetite, garnet-garnet contacts are often sealed with a late growth of garnet (Figure 4.5b,e).

Garnets in the inner garnetite do not resemble the other garnet types, as they do not exhibit a distinct metamorphic zonation and lack radial veinlets (Figure 4.5f). In addition, these garnets exhibit irregular grain shapes, illustrated by interlocking lobes of dark grey garnet (Figure 4.5f). Interlocking features are more common in garnetite with lower quartz content. Most garnet-garnet grain boundaries are sealed with a late growth of garnet (e.g., Figure 4.5e), which also gives the inner garnetite a single-crystal appearance in thin section and hand specimen. The euhedral garnets at the outer margin of the inner garnetite locally contain inclusions of garnet from the inner garnetite (see Appendix A Figure A1f).

Grain boundaries in the inner garnetite can be difficult to distinguish based on compositional zones alone. However, individual grains can be clearly separated based on crystal orien-

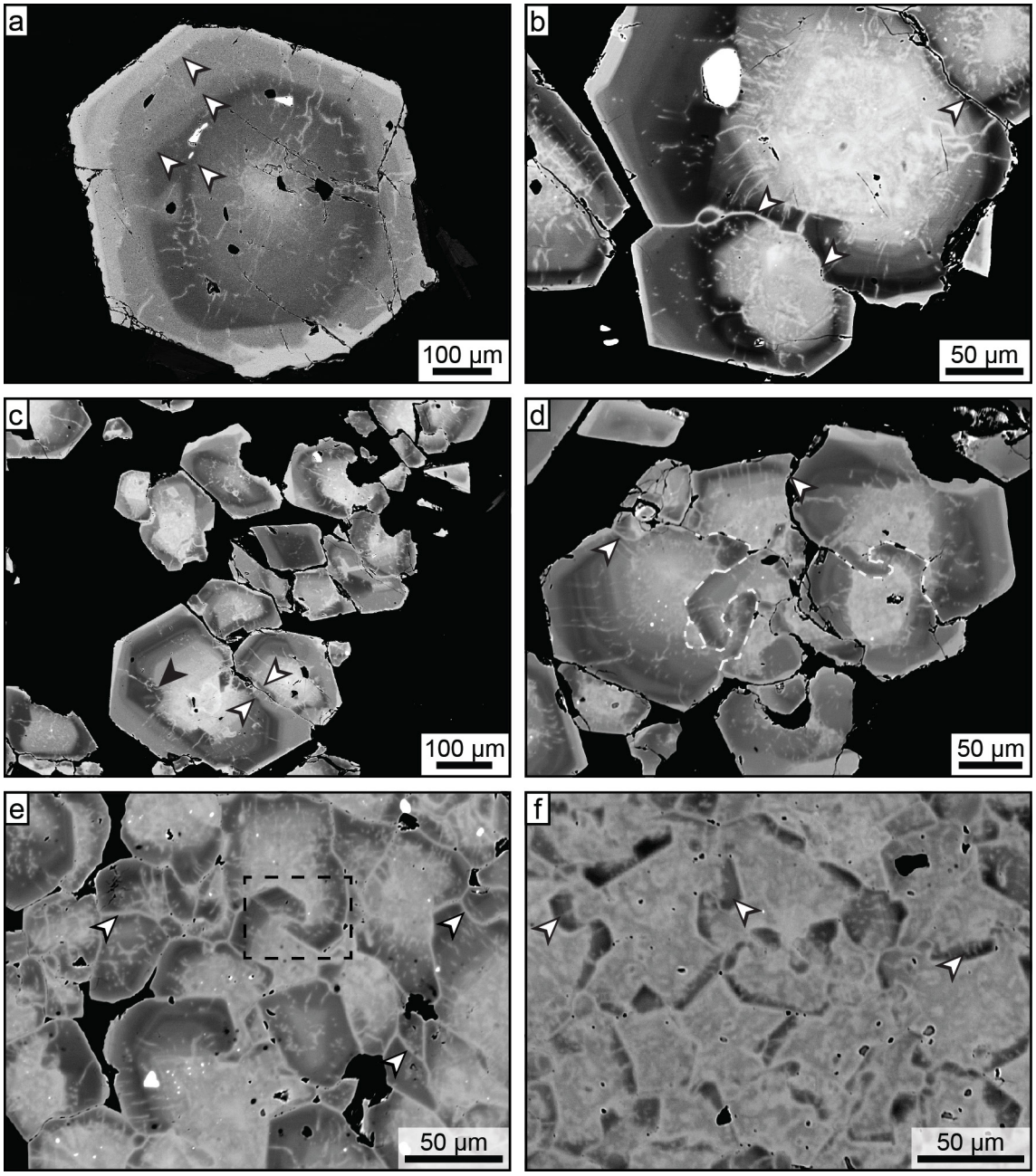

Figure 4.5: Backscattered electron (BSE) images with contrast adjusted so all minerals besides garnet are black or white and zones within garnet are highlighted. (a) Host-rock garnet exhibiting irregular boundaries between compositional zones, four of which are marked with white arrows. Brighter thin features often perpendicular to the zoning are radial veinlets. (b) Garnets in the outer garnetite exhibit truncated of zones at the grain contacts, as indicated by white arrows. Garnet-garnet contacts are sealed with late-stage garnet. Note the similar BSE contrast for the outermost garnet rim, the garnet inside garnet-garnet contacts and within the radial veinlets. The large, white inclusion is rutile. (c) Garnets in the outer garnetite in part of a garnet chain, with white markers indicating truncated zones with late stage zones grown over the truncation. Black marker indicates an irregular boundary between garnet zones of different compositions. (d) Small aggregate of garnets in the outer garnetite exhibiting truncated zones, indicated by markers, alongside interlocking garnet structures. Selected grain boundaries have been marked by dashed white lines to emphasise the interlocking structure. (e) Outer garnetite with a low amount of interstitial quartz. Markers indicate a late growth of garnet along grain boundaries with a bright shade in BSE, similar in composition to radial veinlets throughout the garnets and related alteration focused in the cores. Black dashed box highlights an interlocking structure between two neighbouring garnets. (f) Mass of garnets in the inner garnetite. Several recrystallized zones by grain-boundary migration have been marked.

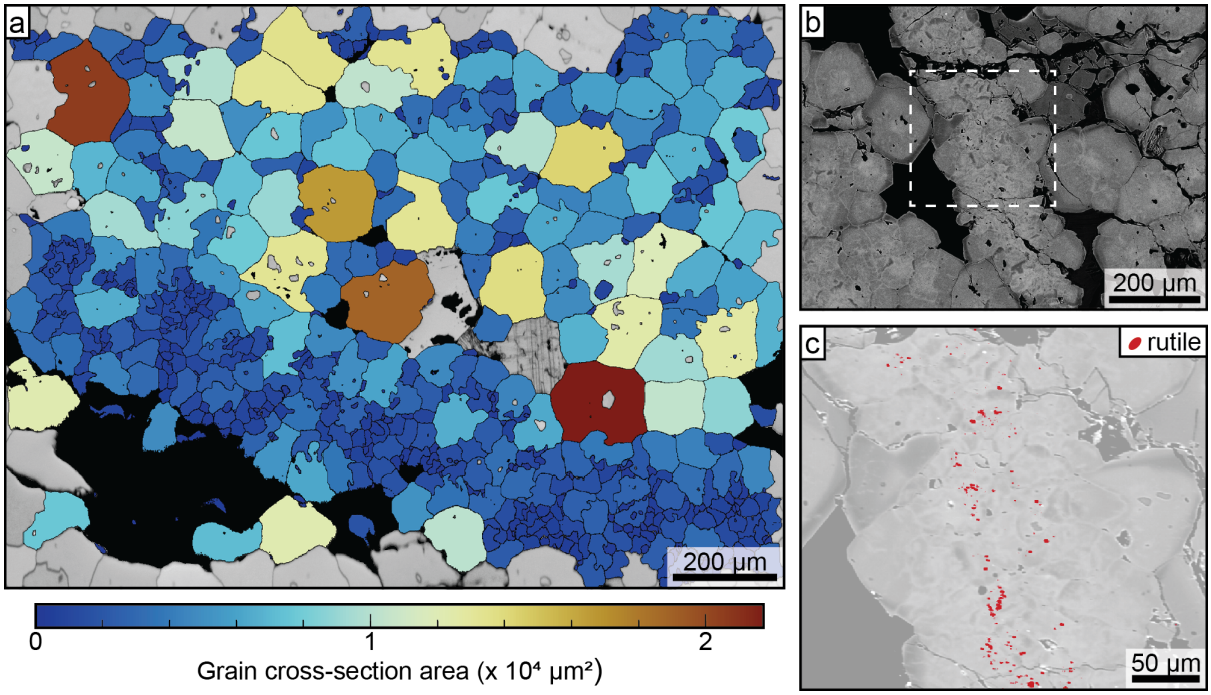

Figure 4.6: Zones of reduced grain size within the garnetite. (a) EBSD grain-boundary map with grains coloured based on surface area, overlain on the band-contrast image. Grains on the edge of the map were removed. (b) BSE image of a similar zone of reduced grain size. (c) Zoom-in of area marked in (b), in which areas of high Ti content as measured with EPMA element mapping are highlighted in red.

tations measured by EBSD. Figure 4.6a presents an EBSD map of a portion of inner garnetite. Whereas the majority of the garnetite has a relatively consistent distribution of grain size, some bands of a consistently finer grain size, a few hundred micrometres thick (blue domain in Figure 4.6a), are present within the inner garnetite. In BSE images, these zones exhibit an increase in complexity of grain shape and zonation relative to the adjacent garnetite (Figure 4.6a,b), and abundant rutile and zircon grains, with strong BSE signal and often < 1 µm in size. Figure 6c presents an extreme case of rutile and zircon enrichment along these fine-grained zones.

Despite differences in microstructures, the same two trends (1: metamorphic zoning, and 2: recrystallization) as are present in the compositions of host-rock garnet, are recognizable in the garnetite garnets (Figure 4.8). The compositions along this trend are somewhat enriched in Mn in the outer and inner garnetite relative to those corresponding to UHPM and late growth in the host rock. In the outer garnetite, the garnet zone with compositions matching the UHPM garnet is significantly thinner than in host-rock garnets, despite a similar size of garnet cores (Figure 4.7a–b, d–e, g–h). Garnet growth over the truncated zones (Figure 4.7b,e; see line labelled "Truncation boundary" in Figure 4.8b) corresponds to compositions of coesite domains in host-rock garnets. Garnet cores in the garnetite, often displaying erratic zonation (Figure 4.7b,c,e,f), adhere to the recrystallization trend also found in the host rock (Figure 4.8). In the inner garnetite, garnet of the same composition as the coesite zone in host-rock garnet is barely present, only occurring as minor component in interlocking lobes and in the euhedral overgrowth at the outer margin. This overgrowth does not correspond to the euhedral late-stage growth that is observed in the outer garnetite and host rock, based on their different compositions.

Compositions matching the second trend in the outer garnetite occur mainly in recrystallized garnet cores, alongside Ti enrichment attributed to rutile inclusions (Figure 4.7g–i). The interlocking lobes lack these rutile inclusions, similar to garnet of corresponding compositions in the outer garnetite and host rock. Garnet-garnet grain boundaries are also sealed with garnet of a

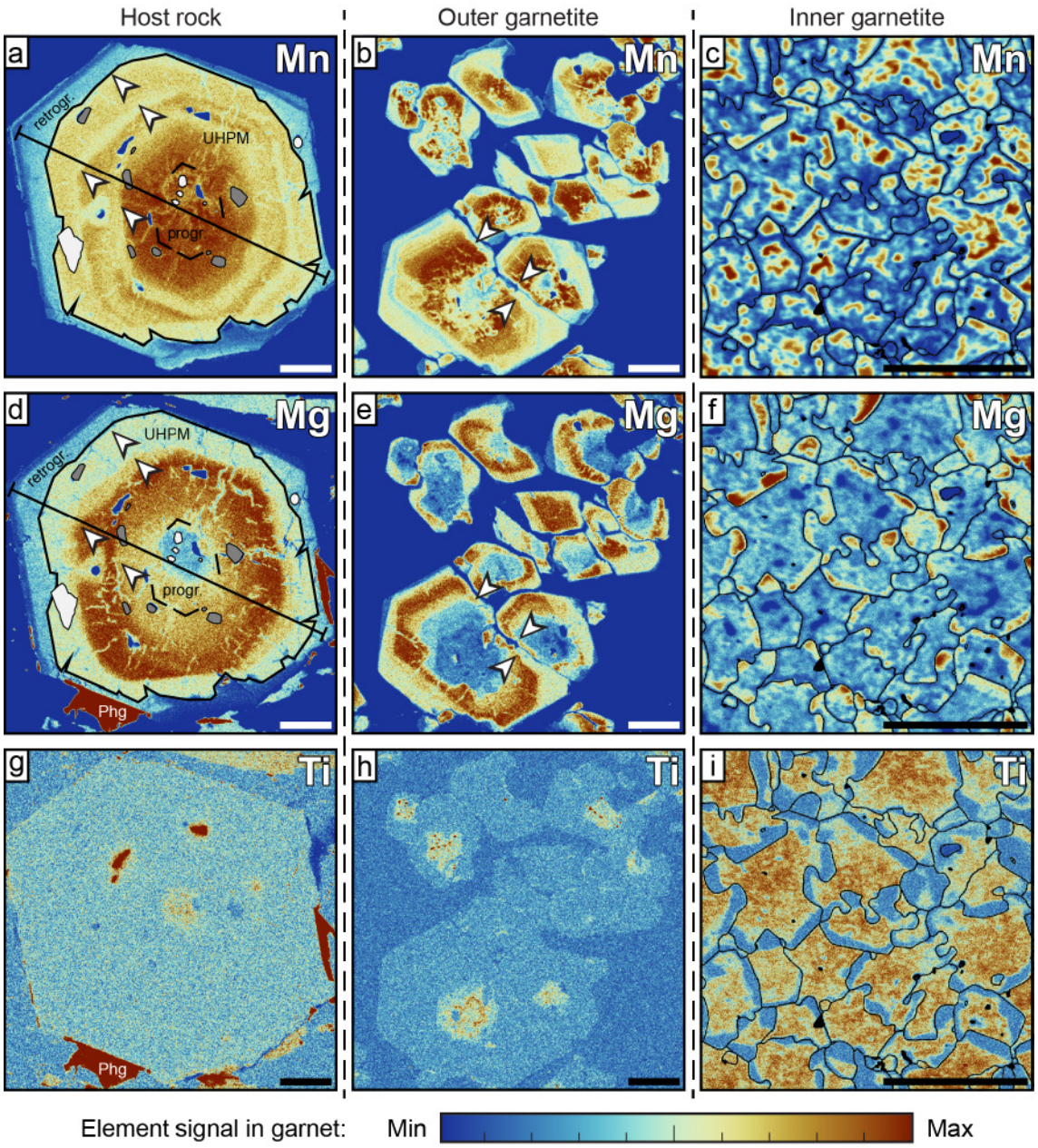

Figure 4.7: EPMA element distribution maps for Mn (a–c), Mg (d–f) and Ti (g–i) of garnet from three different zones. The host-rock garnet maps (a, d, g) correspond to Figure 4.5a. Quartz and coesite inclusions as identified by Raman spectroscopy, and the transect along which garnet composition was measured (Figure 4.8a), are marked in (a) and (d). Based on the inclusions, the garnet has been subdivided into prograde, UHPM (peak) and retrograde zones. Irregular boundaries marking a contrast in composition are indicated with arrows. The outer garnetite zone displayed here (b, e, h) corresponds to Figure 4.5c. In (b) and (e), markers indicate truncated zones with late stage zones grown over the truncation. The area of inner garnetite (c, f, i) corresponds to Figure 4.5f. Grain boundaries as obtained by EBSD, alongside areas that were not indexed, are indicated in black. Ti map (i) appears more enriched than (g) and (h), as a result of a beam current of 100 nA instead of the 15 nA used for the other maps. Scale bars represent 100 µm.

Fe-rich composition along either trend. This trend of garnet compositions is also observed along radial veinlets and as an outer garnet rim. That the recrystallization of garnet cores resulted in a similar composition as garnet within veinlets is most visible in Figure 4.7b, where veinlets and the recrystallized core appear strongly related. Recrystallization processes partially overprinted and obscured original zonation of garnet cores in the garnetite.

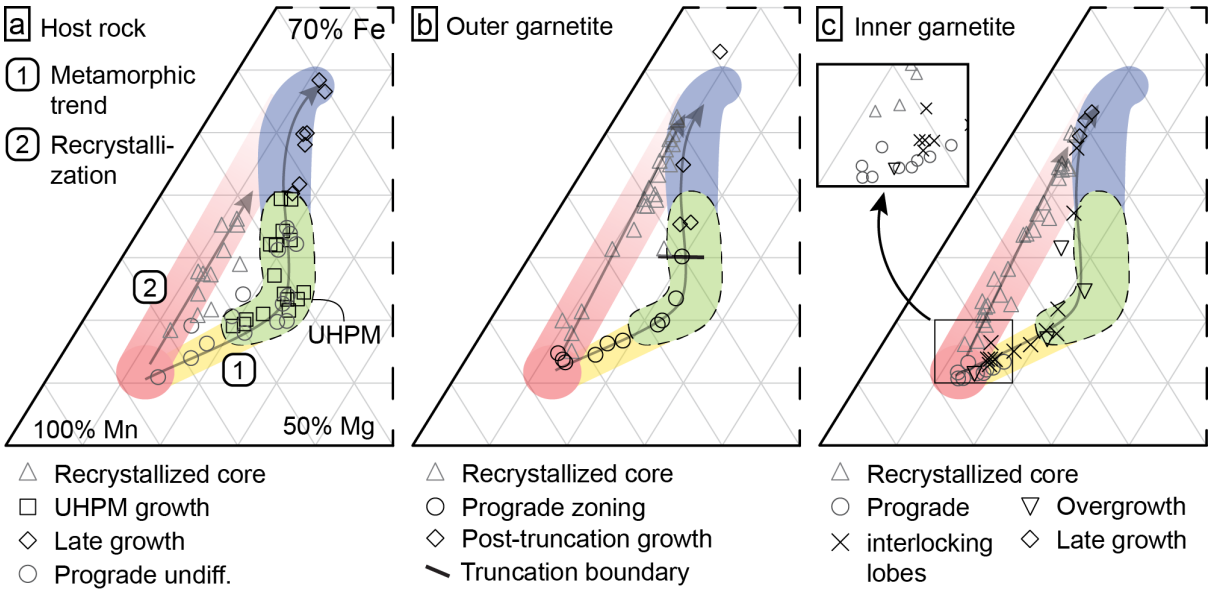

Figure 4.8: Overview of garnet compositions from the host rock, outer garnetite, and inner garnetite. All EPMA measurements are given with locations in Appendix A Tables A1–A7 and Figure A1. (a–c) Ternary diagrams of major-element compositional zonation by garnet type. Density of measurements is no indicator for relative volume of the corresponding composition. Zoning trends are indicated with grey arrows and are labelled in (a). The approximate composition of new growth over the truncated zones at garnet-garnet contacts in the outer garnetite is marked in (b). The area of compositions that contain coesite inclusions in the host-rock garnet has been indicated in diagrams (b–c) for comparison. As calcium concentrations vary only slightly, Ca was not included in these diagrams.

4.6 Strain state of quartz inclusions in garnet

Elastic strain analysis via Raman spectroscopy allowed for the determination of the strain state and associated 2σ variance-covariance ellipsoid for quartz inclusions located in the euhedral garnet overgrowth at the outside margin of the inner garnetite (Figure 4.9a, corresponding to Figure 4.4e,f; upside-down triangles in Figure 4.8c). These inclusions were measured to study the relationship between stress and fluid-driven mechanisms. Only the quartz inclusions in this specific garnet population was used, to avoid potential interference from radial veinlets or recrystallization as is observed in other garnet populations.

The method of elastic geothermobarometry was developed for the primary aim of obtaining entrapment *P-T* conditions. However, we can also numerically predict what values of $\varepsilon_1+\varepsilon_2$ and ε_3 are expected for hydrostatic entrapment conditions and envisage deviations from these calculated strains as factors external to the host-inclusion, either during formation or afterwards (Figure 9b; Alvaro et al., 2020; Bonazzi et al., 2019; see Appendix A Tables A8–A11 for full data). The expected strain states based on LCU *P-T* data from literature (Figure 2b; Reinecke 1998; Groppo et al., 2009) have been provided for comparison.

Typical strain values obtained from the quartz inclusions are between -0.024 and -0.012 for $\varepsilon_1+\varepsilon_2$, and between -0.0054 and 0.0014 for ε_3. Within error, most inclusions cluster along or near both the hydrostatic stress line and the expected strains for the LCU. Two inclusions (i14 and i20) have no apparent strain, probably having been affected by fractures in the host garnet. The strain states of the majority of measured quartz inclusions cluster around the line corresponding to 0.75 GPa inclusion pressure (Figure 4.9a,b), in accordance with entrapment conditions between 1.5 and 2.0 GPa for the prograde temperatures of the LCU.

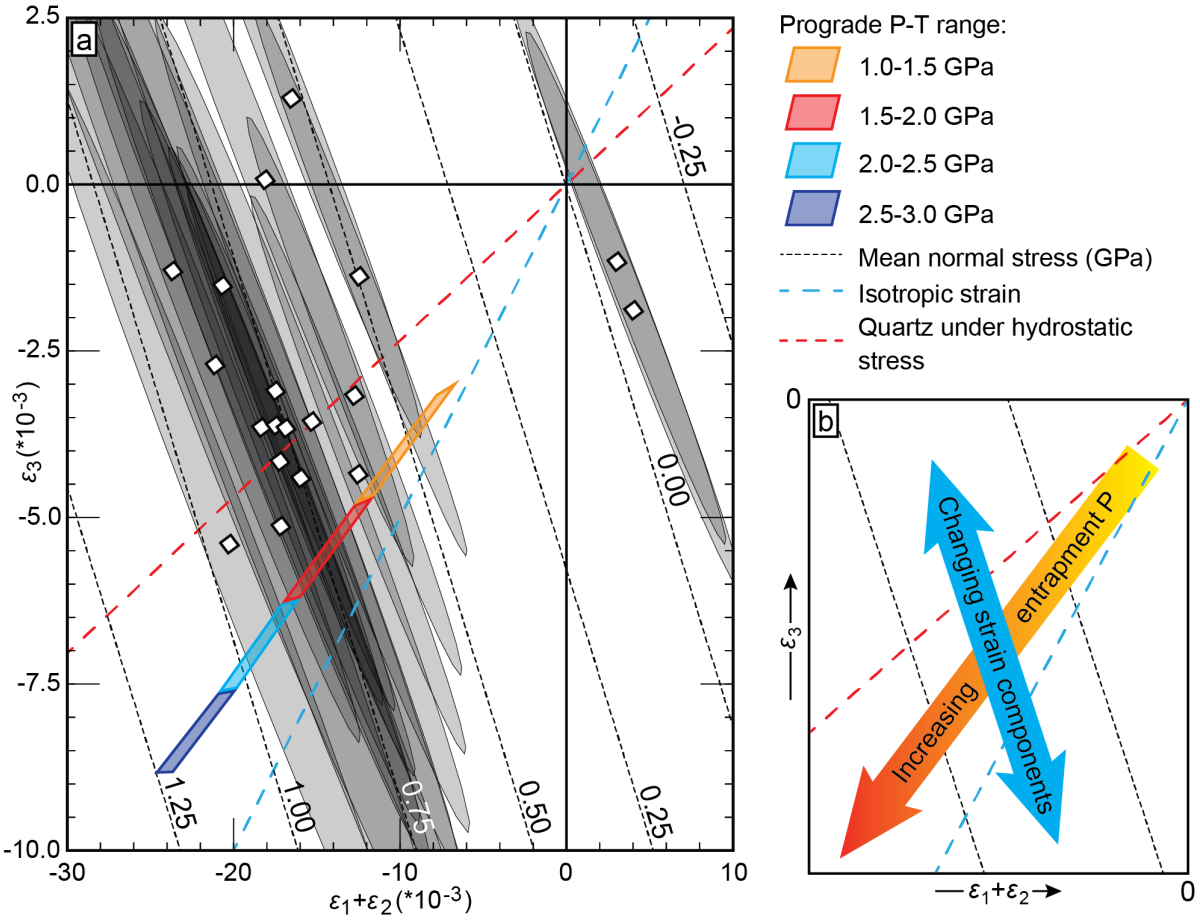

Figure 4.9: (a) Strain diagram of quartz inclusions in garnet, comparing $\varepsilon_1+\varepsilon_2$ with ε_3. Strain states are plotted per inclusion including the 2σ variance-covariance ellipsoid. Strain states predicted based on four segments of the LCU prograde *P-T* path have been plotted for comparison. The dashed red line indicates the strain ratio for quartz under hydrostatic stress and the green line represents isotropic strain. Black dashed lines indicate states of strain corresponding to the same inclusion pressure. Calculated and predicted strain values are available in the Appendix A Tables A10–A11. (b) Simplified $\varepsilon_1+\varepsilon_2$ vs. ε_3 diagram indicating how the strain measured in exhumed quartz inclusions in garnet is affected by entrapment conditions.

4.7 Discussion

The garnet microstructures and compositions and the mineral inclusions in garnet described here provide key information on the subduction-zone evolution of the Lago di Cignana UHP garnet-quartzite and garnetite. Importantly, our data demonstrate that garnetite formed through a process of mineral compaction and pressure solution. Moreover, the inclusion populations in garnet provide information on the possible evolution of matrix minerals through time and during garnet growth, and Raman spectroscopy of quartz inclusions in garnetite helps understanding the stress regime operating during garnet fluid-mediated deformation and dissolution in garnetite.

4.7.1 Evidence for fluid-rock interaction

4.7.1.1 Host rock

In the UHPM garnet quartzite presented here, host-rock garnets display zonation patterns that are interrupted by irregular boundaries of contrasting composition (Figures 4.5a,c; 4.7a,d). These

boundaries are spatially related to resorption of Mn (Figure 4.7a), suggesting that periods of garnet growth were halted by stages of garnet dissolution driven by disequilibrium between garnet and an infiltrating fluid (Figures 4.5a–c; 4.7a,d). The cyclicality of dissolution and growth suggests that fluids pulsed over an extended period during metamorphism.

In host-rock garnets, ubiquitous radial veinlets of a late-stage garnet composition cross cut the majority of the zonation. These veinlets, indicate a mechanism of selective garnet replacement along fractures formed during retrograde metamorphism (Whitney, 1996; Angiboust et al., 2012; Giuntoli et al., 2018; Broadwell et al., 2019; Rubatto et al., 2020). Currently known mechanisms for garnet fracturing during metamorphism, either seismic fracturing (Angiboust et al., 2012; Giuntoli et al., 2018), or hydrofracturing due to increased pore fluid pressure (Rimša et al., 2007), normally do not generate radial fractures. The radial nature of the observed fractures could derive from stressed mineral inclusions in the garnet cores (Van der Molen & Van Roermund, 1986).

In the host-rock garnet, the mineral inclusion assemblages are: (i) quartz, rutile, dolomite, magnesite, apatite, zircon in the core, (ii) coesite, kyanite, clinozoisite, phengite, zircon in the mantle, (iii) quartz in the rim (Table 4.1). The distribution of quartz and coesite in this garnet (Figure 4.7a,d) indicates a primary origin of such inclusions, despite the fractures in the host garnets which could have re-equilibrated the inclusions (Whitney, 1996; Griffiths et al., 2014). The inclusions thus correspond to preserved remnants of the evolving rock matrix at different stages of garnet growth. Absence in the matrix of key inclusion minerals present in the host-rock garnet (e.g. carbonates) suggests that such minerals might have been involved in the same mineral dissolution process recorded by the garnet. Overall, the quartzite hosting the garnetite layers retains evidence of dissolution that affected the garnet and some matrix minerals.

4.7.1.2 Garnetite

The majority of garnet-garnet contacts in the outer garnetite exhibit discontinuous zonation (Figure 5b–e) interrupted by an irregular pattern of garnet grain boundaries where garnets indent and flatten each other. These microstructures are the result of pressure solution, a fluid-mediated deformation mechanism that operates through the increased solubility at stressed grain contacts, resulting in localized dissolution and potential reprecipitation at lower-stress areas. This mechanism has previously been recognized for garnet (Smit et al., 2011; Wassmann & Stöckhert, 2013a), and can be distinguished from undeformed polycrystalline garnet aggregates as only deformation by pressure solution will lead to discontinuous zonation across grain boundaries (Smit et al., 2011). Figures 5c and 7b,e display garnet that has overgrown truncated garnet-garnet contacts, indicating that pressure solution was not a retrograde feature as described by Wassmann and Stöckhert (2013a) but instead took place during prograde to peak metamorphism.

Delicate garnet-chain microstructures are preserved in quartz-rich domains of the outer garnetite (Figure 4.4c) and coincide with garnet flattening and truncation of compositional zones by pressure solution. The garnet-chain microstructure resembles stacked garnet as described and interpreted by Massey et al. (2011) as the result of flattening in a direction parallel to the chains coupled with lateral stretching, accommodated by pressure solution and reprecipitation of interstitial quartz. In the case of the LCU outer garnetite, the host-rock foliation is near perpendicular to the garnet chains, supporting the notion that the shortening direction is parallel to the chains. Moreover, the origin and preservation of this microstructure relies on little to no simple shear. Truncated zonation from pressure solution is also observed in parts of garnetite that are not rich in quartz (Figure 5e), suggesting that flattening strain in garnetite did not rely on the local remobilization of quartz alone, as was suggested for this microstructure by Massey et al. (2011). The garnet stacking provides no constraints on strain perpendicular to the stacking and instead can also

indicate uniaxial strain with no related stretching, which relies on the reduction of volume by local dissolution coupled with removal of mass from the system.

Most garnet-garnet contacts in the inner garnetite and a few in the outer garnetite have developed highly interlocking lobate structures by recrystallization through grain boundary migration (GBM) (Figure 4.5d–f). This recrystallization mechanism is a process where grain boundaries sweep over part of an old grain, recrystallizing it as part of the neighbouring grain. As a result, the grain morphology is altered, yielding a higher degree of interlocking than is known from pressure solution (see microstructures of chemically-induced GBM in calcite; Hay & Evans, 1987; Smit et al., 2011). The GBM-recrystallized garnet differs from the precursor garnet as the result of a change in garnet composition during recrystallization (Figure 4.5f, 4.7c,f,i). For the composition to change, an input and output of solutes is required, particularly as this mechanism should destroy and regrow equal amounts of garnet. GBM took place along all grain boundaries where garnet cores were in contact, and therefore a saturated wetting fluid was present throughout the garnetite. GBM in the outer garnetite relied on pressure solution to expose two garnet core and bring them into contact; core-mantle contact yielded no GBM (Figure 4.5b).

The bands with finer grain size that cross cut the inner garnetite (Figure 4.6) differ from surrounding garnetite in grain size and in enrichment of rutile and zircon. Both differences can be explained by a higher degree of garnet dissolution within the fine-grained bands, leading to a grain-size reduction and the liberation of less soluble inclusions (zircon, rutile). Alternatively, release of Zr from the garnet could drive zircon precipitation. An alternative mechanism for the accumulation of rutile is an influx of a Ti-bearing fluid (Scambelluri & Philippot, 2001) leading to rutile precipitation. Either way, rearrangement of pre-existing rutile grains into an evolving garnet microstructure, or rutile precipitation in trails within this garnet, are both fluid-mediated processes.

In quartz-poor areas of the garnetite, garnet-garnet contacts are sealed by a final stage of garnet growth. This garnet is of similar composition to garnet in the radial veinlets and outermost garnet rim in the outer garnetite and host rock (Figure 4.5b), corresponding to the Fe-rich part of the composition range (Figure 8; note lower Mg and Mn of this garnet in Figure 4.7). Since no interstitial minerals were present to drive a garnet-forming reaction, either within fractures or along grain boundaries, the garnet must have precipitated from a fluid. An alternative mechanism relies on the selective replacement of garnet similar to the formation of radial veinlets by a fluid along fractures. The textures presented here thus indicate that the garnetite garnet was wetted by fluids during GBM and during late-stage garnet growth and/or replacement in fractures, grain boundaries, and as tiny rims.

In the inner and outer garnetite, carbonates only occur as inclusions in the garnet core and are absent as intergranular phases, pointing to dissolution of intergranular carbonate. A lack of interstitial quartz in the inner garnetite, where quartz inclusions are common, suggests that intergranular quartz was also removed. This mineral dissolution supports the finding of (i) bicarbonate and carbonate ions and silica monomers in fluid inclusions and of (ii) associated microdiamonds in other, nearby, garnetite lenses in the LCU (Frezzotti et al., 2011).

4.7.1.3 Reconstruction

Garnet microstructures can be linked to the well-established *P-T* path of the LCU (Figure 2b) by comparing garnet composition linked to those microstructures to the presence of primary quartz and coesite inclusions in host-rock garnet of the same composition. Although garnet morphology varies between garnetite and host rock, the studied garnets exhibit a near-identical compositional evolution (Figure 8), the only difference being a slight Mn enrichment in the garnetite. This simi-

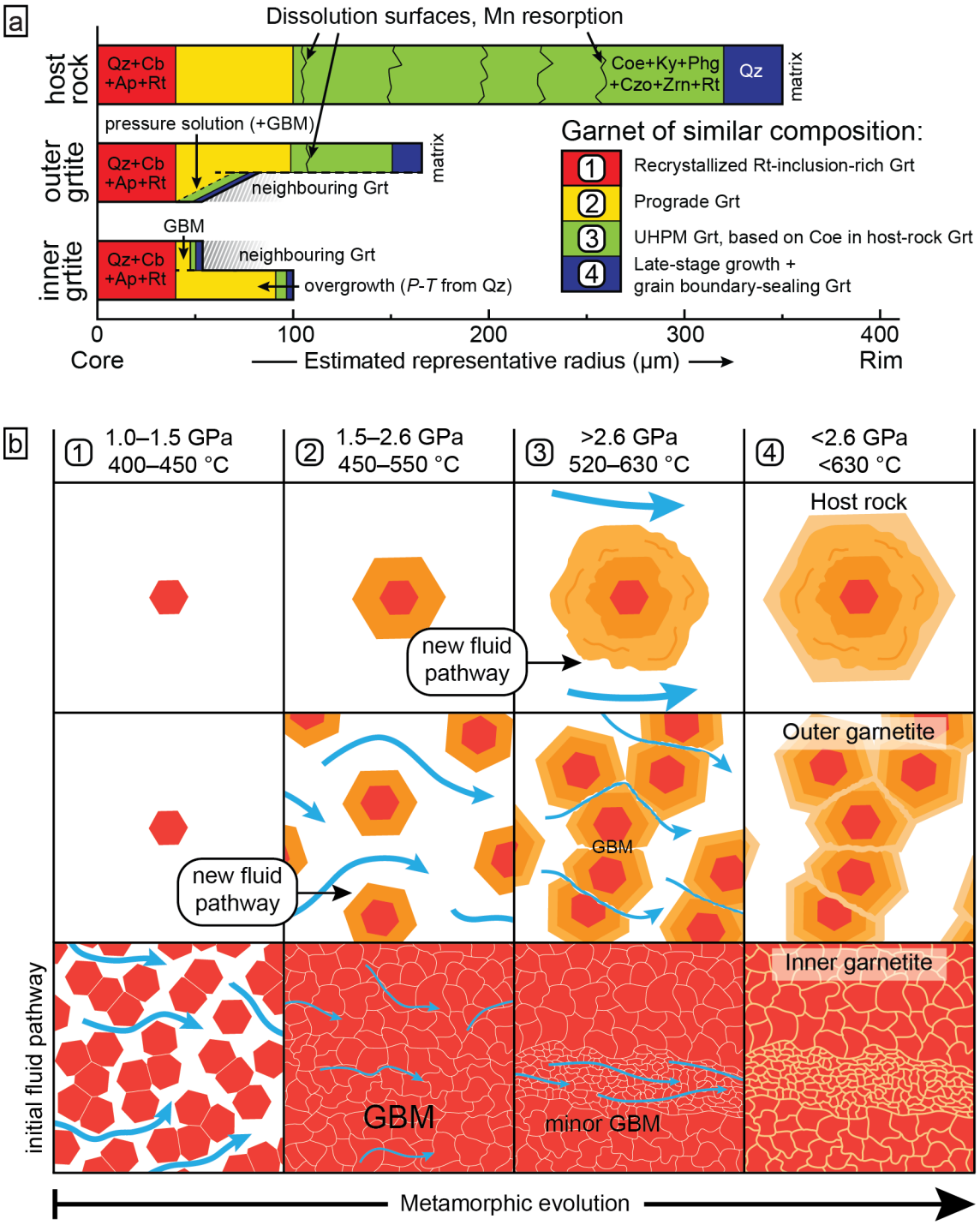

Figure 4.10: (a) Schematic diagram providing a representative overview of garnet zones for the host rock, outer garnetite and inner garnetite. Garnet has been colour-coded to match the colours used in Figure 8a–c, numbers correspond to (b). The recrystallization trend has been grouped with the rt-inclusion-rich core as they generally coincide. Two situations are displayed for garnets in the outer garnetite. The top case is representative for free growth whereas the lower indicates garnet zonation at garnet-garnet contacts. Garnets in the inner garnetite are also represented by two scenarios. The top case is for garnets that are in contact and were recrystallized by GBM at grain contacts, the bottom is for garnet at the outer margin of the inner garnetite with an overgrowth of prograde garnet composition. (b) Schematic diagram of garnet growth and microstructural evolution and their relation to fluid flow. Garnet growth, microstructures, and fluid flow are indicated per developing zone of the host rock–garnetite system. Blue arrows indicate fluid flow. White can be assumed to be primarily quartz, but could have included other matrix minerals that have since dissolved. An estimated range of *P-T* conditions is given per phase.

larity, together with the similar size (Figure 4.7g–i) and reactivity of inner garnet cores in all garnet types, suggests a common initial garnet-forming reaction at a similar rate of nucleation versus growth. Based on this linked garnet growth, the composition and inclusions of quartz versus coesite in the host rock garnets are used as a tool for relative timing and an estimate for UHPM conditions of garnet growth throughout the system.

The temporal link between the rock domains established through garnet composition is used to reconstruct their evolution in terms of garnet growth, dissolution, deformation, and recrystallization, and related fluid flow patterns (Figure 4.10). After the initial growth of garnet cores at approximately 1.0 GPa and 400 °C (Reinecke, 1998), the first stage of compaction by fluid-rock interaction took place by dissolving and transporting interstitial material (stage 1, Figure 4.10b). The above processes concentrated garnet in what is now the inner garnetite, essentially forming a garnet stylolite. The euhedral garnet growing at the outer margins of the inner garnetite formed after this compaction, and the lower range of *P-T* conditions obtained from quartz inclusions in this garnet (~1.5–2.0 GPa) indicate that compaction took place at conditions of 1.0–1.5 GPa and 400–450 °C. No fluid-rock interaction during this phase is recorded in the host rock.

The second stage (stage 2, Figure 4.10b) was marked by the dissolution of matrix minerals adjacent to the inner garnetite and related arrangement of garnets in the garnet chain microstructure, while host-rock garnets continued regular metamorphic growth. While the outer garnetite was compacting and partially dissolving into an infiltrated fluid, the inner garnetite underwent GBM and growth of euhedral crystals at the outer margin. This phase took place at conditions between stage 1 and UHPM conditions, thus 1.5–2.6 GPa and 450–550 °C.

During UHP metamorphism (stage 3, Figure 4.10b), the host rock and to a lesser degree the outer garnetite were affected by fluid pulses that induced cycles of dissolution and growth in garnet. Only local fluid pathways still allowed fluid flow in the inner garnetite. By examining the youngest preserved garnet before pressure solution and the garnet that grew over truncated zonation (Figures 5c and 7b,e), a window for pressure solution in the outer garnetite is constrained as prograde to the first part of UHPM (Figure 4.8b,d), coincident with formation of the mantle of host-rock garnet.

In the final stage (stage 4, Figure 4.10b) during exhumation, garnets in the outer garnetite and host rock were fractured radially. These fractures provided a fast pathway for fluids, leading to selective replacement of garnet in cores, along fractures, and along grain boundaries. This event was coeval with a final phase of garnet growth, sealing all garnet-garnet grain boundaries and forming a euhedral outer rim on garnets throughout the system.

The above evidence suggests that fluid flow and mineral dissolution during prograde metamorphism was focused in and directly adjacent to the inner garnetite, whereas most of the fluid pulses during UHPM were focused in the host rock, with lesser impact on the outer garnetite. This progression suggests a shift over time of the fluid pathway, not only migrating from the inner garnetite towards the host rock but also widening in the process.

4.7.2 Evaluation of stress conditions from quartz inclusions

The studied quartz inclusions are inside euhedral garnet crystals located at the outer margin of the inner garnetite. This euhedral garnet grew from circulating fluids, after formation of the inner garnetite and coeval with GBM, and are considered representative of the stress conditions during garnet growth at approximate *P-T* conditions of 1.5–2.0 GPa and 450–490 °C.

Factors external to the host-inclusion system, such as differential stress during entrapment, can change the strain components from the expected strain state. As a result, inclusions that are entrapped under hydrostatic conditions should correspond to calculated strains for the *P-T* condi-

tions of entrapment, while a significant differential stress during entrapment will lead to a deviation from the predicted strains, along a line of constant inclusion pressure (Figure 4.9b; Bonazzi et al., 2019). This method is not calibrated as quantitative, so currently no magnitude of differential stress during entrapment can be obtained.

With the exception of two outliers, the calculated strain states of all measured quartz inclusions fall within uncertainty of the line that indicates the strain ratio expected for quartz under hydrostatic stress, and the expected strain states for hydrostatic entrapment along the prograde *P-T* path for the LCU. Depending on the peak metamorphic temperature of the LCU (590–605 °C, Groppo et al., 2009; 630 °C, Reikecke, 1998), little to no plastic deformation occurred in garnet, and therefore the state of strain and inclusion pressure of the quartz is reliable (Voegelé et al., 1998; Zhong et al., 2020).

The inferred hydrostatic entrapment conditions for quartz in garnet fit the fluid-driven deformation process envisaged, with a fluid wetting the garnet crystals. Load-bearing and consequently stressed grain contacts resulted in local pressure solution, while other parts of the garnet were coated by a fluid, where quartz subsequently recorded (near-) hydrostatic stress during entrapment.

4.7.3 Implications

Reconstructing the evolution of the garnetite-host-rock system in the LCU quartzite has yielded several gaps in the rock record, most notably when comparing the inclusion mineral assemblages to the current matrix mineral assemblages. The extensive evidence for garnet dissolution presented here is not coupled with concomitant reprecipitation, which implies that the whole process took place under open system conditions, with overall loss of material. The fluids responsible for mineral dissolution were externally derived and likely made available by dehydration of nearby serpentinite (Halama et al., 2020). Because garnets are concentrated into garnetite by dissolution of more soluble interstitial minerals along a fluid pathway, the garnetite can be considered a stylolite. The genesis of garnetite is generally linked to precipitation from a fluid or melt, or sedimentary processes (e.g., Spry et al., 2000; Vrijmoed et al., 2006; Angiboust et al., 2017; Hadjzobir et al., 2017); therefore, the process described here provides a new mechanism for garnetite formation.

The fluid pathway described in this study involves mass removal via dissolution and transport of quartz, garnet, and carbonates, due to circulation of large amounts of fluids (Vernon et al., 1987). When considered as a whole, the host rock-garnetite system acted as a fluid pathway throughout metamorphism. The observed fluid-mediated deformation in combination with near-hydrostatic to hydrostatic stresses inferred for garnet growth based on the elastic strain of quartz inclusions in garnet, showcases the capacity of fluids to result in significant compaction at low differential stress.

The mechanisms that operated in the LCU quartzite and garnetite provide new insights into the possible evolution of aqueous-carbonic fluids released by dehydration of oceanic slabs. By dissolving minerals located in specific rock domains through the pressure-solution process documented here, fluids may become enriched in rock-forming components, driving enrichment of silicates in water- and carbon-rich solutions when moving across different lithologies within the subducting plates.

4.8 Conclusions

The combination of microstructures, mineral inclusions, and garnet compositions provide a record of metamorphism and fluid-rock interaction for the UHPM garnetite-bearing quartzite of Lago di Cignana. This fluid-rock interaction record showcases the longevity of this system as a major fluid pathway throughout subduction. The externally derived fluids locally led to a significant compaction and mass removal by pressure solution of minerals such as quartz, carbonates, and garnet. Due to its relatively low solubility, garnet was concentrated into garnetite stylolites, constituting a new potential mechanism for the formation of garnetite. Quartz inclusions entrapped in euhedral garnet overgrowths on garnetite yield strains that indicate near-hydrostatic stress conditions during garnet growth. Considering pressure solution as the main mechanism of mass removal, this fluid-rock interaction also operated as a means of exerting control on deformation during metamorphism.

Upcoming chapters in this thesis will deal with several aspects introduced in this chapter but not yet studied in detail. Microstructural analysis of garnet is aimed at better understanding the role of pressure solution in garnetite from the LCU, and GBM is also studied further. The presence of coesite and zircon in host-rock garnets is studied by Raman spectroscopy and elastic geothermobarometry on the zircon inclusions to gain a better understanding of the effect of fracturing and sealing of a host on the inclusions. The relation between garnet from the garnetite and host rock is also investigated by the use of trace elements. This same study includes the contamination of sub-micron rutile and zircon inclusions as is found in garnet cores (Figure 4.7). Finally, rutile is used as main investigated mineral in omphacite veins in eclogite from the LCU to gain insight in the formation of the veins in a different nearby system, and to study how deformation can affect the composition of the rutile.

Acknowledgements

This project has received funding from the European Research Council under the European Union's Horizon 2020 research and innovation program grant agreement 714936 to M. Alvaro. M. Scambelluri acknowledges funding by the Italian MIUR to the PRIN program n. 2017ZE49E7. The authors have no conflict of interest to declare. Andrea Risplendente is thanked for performing the EPMA analyses. B. Dragovic and two anonymous reviewers are gratefully acknowledged for their helpful comments. Many thanks to B. Cesare for editorial handling.

References

Ague, J.J., Nicolescu, S., 2014. Carbon dioxide released from subduction zones by fluid-mediated reactions. Nature Geoscience, 7, 355-360 DOI: 10.1038/NGEO2143

Alvaro, M., Mazzucchelli, M.L., Angel, R.J., Murri, M., Campomenosi, N., Scambelluri, M., Nestola, F., Korsakov, A., Tomilenko, A.A., Marone, F., Morana, A., 2020. Fossil subduction recorded by quartz from the coesite stability field. Geology, 48(1), 24–28

Angel, R.J., Mazzucchelli, M.L., Alvaro, M., Nimis, P., Nestola, F., 2014a. Geothermobarometry from host-inclusion systems: The role of elastic relaxation. American Mineralogist, 99, 2146–2149

Angel, R.J., Gonzalez-Platas, J., Alvaro, M., 2014b. EosFit-7c and a Fortran module (library) for equation of state calculations. Zeitschrift für Kristallographie, 2009, 405–419

Angel, R.J., Murri, M., Mihailova, B., Alvaro, M., 2019. Stress, strain and Raman shifts. Zeitschrift für Kristallographie - Crystalline materials, 234(2), 129–140. DOI: https://doi.org/10.1515/zkri-2018-2112

Angiboust, S., Agard, P., Jolivet, L., Beyssac, O., 2009. The Zermatt-Saas ophiolite: the largest (60-km wide) and deepest (c. 70-80 km) continuous slice of oceanic lithosphere detached from a subduction zone? Terra Nova, 21, 171-180 DOI: 10.1111/j.1365-3121.2009.00870.x

Angiboust, S., Agard, P., Yamato, P., Raimbourg, H., 2012. Eclogite breccias in a subducted ophiolite: A record of intermediate depth earthquakes? Geology, 40, 707–710

Angiboust, S., Yamato, P., Hertgen, S., Hyppolito, T., Bebout, G.E., Morales, L., 2017. Fluid pathways and high-P metasomatism in a subducted continental slice (Mt. Emilius Klippe, W. Alps). Journal of metamorphic geology, 35, 471–492

Bachmann, F., Hielscher, R., Schaeben, H., 2010. Texture Analysis with MTEX - Free and Open Source Software Toolbox. Solid State Phenomena, 160, 63–68

Bebout, G.E., 2007. Metamorphic chemical geodynamics of subduction zones. Earth and Planetary Science Letters, 260, 373–393

Beltrando, M., Rubatto, D., Manatschal, G., 2010. From passive margins to orogens: The link between ocean-continent transition zones and (ultra)high-pressure metamorphism. Geology, 38, 559–562

Bonazzi, M., Tumiati, S., Thomas, J.B., Angel, R.J., Alvaro, M., 2019. Assessment of the reliability of elastic geobarometry with quartz inclusions. Lithos, 350–351, 105201 DOI: 10.1016/j.lithos.2019.105201

Broadwell, K.S., Locatelli, M., Verlaguet, A., Agard, P., Caddick, M.J., 2019. Transient and periodic brittle deformation of eclogites during intermediate-depth subduction. Earth and Planetary Science Letters, 521, 91-102

Brovarone, A.V., Tumiati, S., Piccoli, F., Ague, J.J., Connolly, J.A.D., Beyssac, O., 2020. Fluid-mediated selective dissolution of subducting carbonaceous material: Implications for carbon recycling and fluid fluxes at forearc depths. Chemical Geology, 549, 119682

Bucher, K., Grapes, R., 2009. The Eclogite-facies Allalin Gabbro of the Zermatt-Saas Ophiolite, Western Alps: a Record of Subduction Zone Hydration. Journal of Petrology, 50-8, 1405–1442

Bürgmann, R., Dresen, G., 2008. Rheology of the Lower Crust and Upper Mantle: Evidence from Rock Mechanics, Geodesy, and Field Observations. Annual Review of Earth and Planetary Sciences, 36, 531–567

Campomenosi, N., Mazzucchelli, M.L., Mihailova, B., Scambelluri, M., Angel, R.J., Nestola, F., Reali, A., Alvaro, M., 2018. How geometry and anisotropy affect residual strain in host-inclusion systems: Coupling experimental and numerical approaches. American Mineralogist, 103(12), 2032–2035 DOI: 10.2138/am-2018-6700CCBY

Crameri, F., 2018. Scientific colour-maps. Zenodo. DOI: http://doi.org/10.5281/zenodo.1243862

Dal Piaz, G., 1999. The Austroalpine–Piedmont nappe stack and the puzzle of Alpine Tethys. Memorie di Scienze Geologiche, 51, 155–176

Dal Piaz, G.V., Cortiana, G., Del Moro, A., Martin, S., Pennacchioni, G., Tartarotti, P., 2001. Tertiary age and paleostructural inferences of the eclogitic imprint in the Austroalpine outliers and Zermatt-Saas ophiolite, western Alps. International Journal of Earth Sciences, 90, 668–684 DOI: 10.1007/s005310000177

Dragovic, B., Baxter, E.F., Caddick, M.J., 2015. Pulsed dehydration and garnet growth during subduction revealed by zoned garnet geochronology and thermodynamic modeling, Sifnos, Greece. Earth and Planetary Science Letters, 413, 111–122

Ferrando, S., Groppo, C., Frezzotti, M.L., Castelli, D., Proyer, A., 2017. Dissolving dolomite in a stable UH*P* mineral assemblage: Evidence from Cal-Dol marbles of the Dora Maira Massif (Italian Western Alps). American Mineralogist, 102, 42–60

Forster, M., Lister, G., Compagnoni, R., Giles, D., Hills, Q., Betts, P., Beltrando, M. & Tamagno, E., 2004. Mapping of oceanic crust with" H*P*" to" UH*P*" metamorphism: The Lago di Cignana Unit (Western Alps). Mapping geology in Italy: Geological Society of London

Frezzotti, M.L., Selverstone, J., Sharp, Z.D., Compagnoni, R., 2011. Carbonate dissolution during subduction revealed by diamond-bearing rocks from the Alps. Nature Geoscience, 4, 703-706. DOI: 10.1038/NGEO1246

Gerya, T.V., Meilick, F.I., 2011. Geodynamic regimes of subduction under an active margin: effects of rheological weakening by fluids and melts. Journal of Metamorphic Geology, 29, 7–31

Gilio, M., Scambelluri, M., Agostini, S., Godard, M., Peters, D., Pettke, T., 2019. Petrology and Geochemistry of Serpentinites Associated with the Ultra-High Pressure Lago di Cignana Unit (Italian Western Alps). Journal of Petrology, 60, 6 DOI: 10.1093/petrology/egz030

Giuntoli, F., Lanari, P., Engi, M., 2018. Deeply subducted continental fragments - Part 1: Fracturing, dissolution-precipitation, and diffusion processes recorded by garnet textures of the central Sesia Zone (western Italian Alps). Solid Earth, 9, 167–189

Griffiths, T.A., Habler, G., Rhede, D., Wirth, R., Ram, F., Abart, R., 2014. Localization of submicron inclusion re-equil-

ibration at healed fractures in host garnet. Contributions to Mineralogy and Petrology, 168, 1077

Groppo, C., Beltrando, M., Compagnoni, R., 2009. The *P-T* path of the ultra-high pressure Lago di Cignana and adjoining high-pressure meta-ophiolitic units: insights into the evolution of the subducting Tethyan slab. Journal of Metamorphic Geology, 27, 207–231

Hadjzobir, S., Altenberger, U., Günter, C., 2017. The Edough Massif garnetites: evidence for a metamorphised paleo-garnet beach-sand placer (Cap de Garde, Annaba, Northeast Algeria). Journal of Mediterranean Earth Sciences, 9, 1–13

Halama, R., Konrad-Schmolke, M., De Hoog, J.C.M., 2020. Boron isotope record of peak metamorphic ultrahigh-pressure and retrograde fluid-rock interaction in white mica (Lago di Cignana, Western Alps). Contributions to Mineralogy and Petrology, 175, 20 DOI: 10.1007/s00410-020-1661-8

Hawkins, A.T., Selverstone, J., King, P.L., Frezzotti, M.L., 2009. H*P*/UH*P* fluids preserved in Mn-rich garnets from Lago di Cignana, Italy. Geological Society of America Abstracts with Programs. 41(7), 238

Hay, R.S., Evans, B., 1987. Chemically induced grain boundary migration in calcite: temperature dependence, phenomenology, and possible applications to geologic systems. Contributions to Mineralogy and Petrology, 97, 127–141

Hermann, J., Spandler, C., Hack, A., Korsakov, A.V., 2006. Aqueous fluids and hydrous melts in high-pressure and ultra-high pressure rocks: Implications for element transfer in subduction zones. Lithos, 92, 399–417

Herms, P., John, T., Bakker, R.J., Schenk, V., 2012. Evidence for channelized external fluid flow and element transfer in subducting slabs (Raspas Complex, Ecuador). Chemical Geology, 310–311, 79–96

Kirst, F., Leiss, B., 2017. Kinematics of syn- and post-exhumational shear zones at Lago di Cignana (Western Alps, Italy): constraints on the exhumation of Zermatt-Saas (ultra)high-pressure rocks and deformation along the Combin Fault and Dent Blanche Basal Thrust. International Journal of Earth Sciences, 106, 215–236. DOI: 10.1007/s00531-016-1316-1

Kuzmany, H., 2009. Light Scattering Spectroscopy. In: Solid-State Spectroscopy. Springer, Berlin, Heidelberg

Massey, M.A., Prior, D.J., Moecher, D.P., 2011. Microstructure and crystallographic preferred orientation of polycrystalline microgarnet aggregates developed during progressive creep, recovery, and grain boundary sliding. Journal of Structural Geology, 33, 713–730

Mazzucchelli, M.L., Burnley, P., Angel, R.J., Morganti, S., Domeneghetti, M.C., Nestola, F., Alvaro, M., 2018. Elastic geothermobarometry: Corrections for the geometry of the host-inclusion system. Geology, 46(3), 231–234

Murri, M., Mazzucchelli, M.L., Campomenosi, N., Korsakov, A.V., Prencipe, M., Mihailova, B.D., Scambelluri, M., Angel, R.J., Alvaro, M., 2018. Raman elastic geobarometry for anisotropic mineral inclusions. American Mineralogist, 103(11), 1869–1872

Murri, M., Alvaro, M., Angel, R.J., Prencipe, M., Mihailova, B.D., 2019. The effects of non-hydrostatic stress on the structure and properties of alpha-quartz. Physics and Chemistry of Minerals, 46, 487–499 DOI: 10.1007/s00269-018-01018-6

Peacock, S.M. (1990). Fluid Processes in Subduction Zones. Science, 248, 329–337

Plümper, O., John, T., Podladchikov, Y.Y., Vrijmoed, J.C., Scambelluri, M., 2017. Fluid escape from subduction zones controlled by channel-forming reactive porosity. Nature geoscience, 10, 150–158 DOI: 10.1038/NGEO2865

Reddy, S.M., Wheeler, J., Cliff, R.A., 1999. The geometry and timing of orogenic extension: an example from the Western Italian Alps. Journal of Metamorphic Geology, 17, 573–589

Reinecke, T., 1991. Very-high-pressure metamorphism and uplift of coesite-bearing metasediments from the Zermatt-Saas zone, Western Alps. European Journal of Mineralogy, 3, 7–17

Reinecke, T., 1998. Prograde high- to ultahigh-pressure metamorphism and exhumation of oceanic sediments at Lago di Cignana, Zermatt-Saas Zone, western Alps. Lithos. 42, 147–189

Rimša, A., Whitehouse, M.J., Johansson, L., Piazolo, S., 2007. Brittle fracturing and fracture healing of zircon: An integrated cathodoluminescence, EBSD, U-Th-Pb, and REE study. American Mineralogist, 92, 1213–1224

Rubatto, D., Burger, M., Lanari, P., Hattendorrf, B., Schwarz, G., Neff, C., Schmidt, P.K., Hermann, J., Vho, A., Günther, D., 2020. Identification of growth mechanisms in metamorphic garnet by high-resolution trace element mapping with LA-ICP-TOFMS. Contributions to Mineralogy and Petrology, 175:61. DOI: 10.1007/s00410-020-01700-5

Scambelluri, M., Philippot, P., 2001. Deep fluids in subduction zones. Lithos. 55, 213–227

Skora, S., Mahlen, N.J., Johnson, C.M., Baumgartner, L.P., Lapen, T.J., Beard, B.L., Szilvagyi, E.T. (2015). Evidence

for protracted prograde metamorphism followed by rapid exhumation of the Zermatt-Saas Fee ophiolite. Journal of Metamorphic Geology, 33, 711–734

Smit, M.A., Scherer, E.E., John, T., Janssen, A., 2011. Creep of garnet in eclogite: Mechanisms and implications. Earth and Planetary Science Letters, 311, 411–419

Spandler, C., Pirard, C., 2013. Element recycling from subducting slabs to arc crust: A review. Lithos, 170-171, 208–223

Spry, P.G., Peter, J.M., Slack, J.F., 2000. Meta-Exhalites as Exploration Guides to Ore. Geological Survey of Canada, Contribution no. 1997162, 163–201

Taetz, S., John, T., Bröcker, M., Spandler, C., Stracke, A., 2018. Fast intraslab fluid-flow events linked to pulses of high pore fluid pressure at the subducted plate interface. Earth and Planetary Science Letters, 482, 33–43

Tumiati, S., Martin, S., Godard, G., 2010. Hydrothermal origin of manganese in the high-pressure ophiolite metasediments of Praborna ore deposit (Aosta Valley, Western Alps). European Journal of Mineralogy, 22, 577–594

Van der Molen, I., Van Roermund, H.L.M., 1986. The pressure path of solid inclusions in minerals: the retention of coesite inclusions during uplift. Lithos, 19, 317–324

Van Keken, P.E., Hacker, B.R., Syracuse, E.M., Abers, G.A., 2011. Subduction factory: 4. Depth-dependent flux of H2O from subducting slabs worldwide. Journal of Geophysical Research, 116 DOI: 10.1029/2010JB007922

Vernon, R.H., Flood, R.H., D'Arcy, W.F., 1987. Sillimanite and andalusite produced by base-cation leaching and contact metamorphism of felsic igneous rocks. Journal of Metamorphic Geology, 5, 439–450

Voegelé, V., Cordier, P., Sautter, V., Sharp, T.G., Lardeaux, J.M., Marques, F.O., 1998. Plastic deformation of silicate garnets II. Deformation microstructures in natural samples. Physics of the Earth and Planetary Interiors, 108, 319–338

Vrijmoed, J.C., Van Roermund, H.L.M., Davies, G.R., 2006. Evidence for diamond-grade ultra-high pressure metamorphism and fluid interaction in the Svartberget Fe-Ti garnet peridotite-websterite body, Western Gneiss Region, Norway. Mineralogy and Petrology, 88, 381–405

Wassmann, S., Stöckhert, B., Trepmann, C.A., 2011. Dissolution precipitation creep versus crystalline plasticity in high-pressure metamorphic serpentinites. Geological Society, London, Special Publications, 360, 129–149

Wassmann, S., Stöckhert, B., 2013a. Low stress deformation of garnet by incongruent dissolution precipitation creep. Journal of Structural Geology, 46, 200–219

Wassmann, S., Stöckhert, B., 2013b. Rheology of the plate interface - Dissolution precipitation creep in high pressure metamorphic rocks. Tectonophysics, 608, 1–29

Weber, S., Sandmann, S., Miladinova, I., Fonseca, R.O.C., Froitzheim, N., Münker, C., Bucher, K., 2015. Dating the initiation of Piemonte-Liguria Ocean subduction: Lu-Hf garnet chronometry of eclogites from the Theodul Glacier Unit (Zermatt-Saas zone, Switzerland). Swiss Journal of Geosciences, 108, 183–199. DOI: 10.1007/s00015-015-0180-5

Whitney, D.L., 1996. Garnets as open systems during regional metamorphism. Geology, 24(2), 147–150

Whitney, D.L., Evans, B.W., 2010. Abbreviations for names of rock-forming minerals. American Mineralogist, 95, 185-187

Zaffiro, G., 2020. Constraints on the Equations of State of rutile and zircon: implications for elastic geothermobarometry. PhD Thesis, Cycle XXXII, University of Pavia

Zhang, Y.,1998. Mechanical and phase equilibria in inclusion-host systems. Earth and Planetary Science Letters, 157, 209–222

Zhong, X., Moulas, E., Tajčmanová, L., 2020. Post-entrapment modification of residual inclusion pressure and its implications for Raman elastic thermobarometry. Solid Earth, 11, 223–240

CHAPTER 5

Garnet deformation and recrystallization at (U)H*P*-L*T* conditions: pressure solution and grain-boundary migration

5.1 Introduction

The previous chapter outlined the extensive nature of fluid-rock interaction in quartzite and garnetite, including the observation of microstructures consistent with the operation of intergranular pressure solution (IPS) and grain-boundary migration (GBM) in garnet. Such evidence is observed only rarely in garnet, and this thesis provides the first reports of GBM in garnet, and IPS altogether, at ultrahigh-pressure conditions. Despite the potential of IPS to be a commonplace mechanism in fluid-rich environments and cold subducting slabs, it is only studied rarely in this system. GBM in garnet has never been described in detail. This chapter utilises the common occurrence of garnetite in the LCU that was formerly fluid-rich and at the brittle-ductile transition during peak metamorphism, to study IPS and GBM by focusing on the microstructural aspects. The aim of this chapter is to characterize the role of IPS in garnet in the rheology of subducting metasediments, and the significance and driving force behind GBM in garnet.

5.2 Background

5.2.1 Garnet deformation

The brittle-ductile transition in garnet typically occurs at temperatures of approximately 600 °C, the temperature interval over which the strong lattice friction of dislocations progressively ceases to be a barrier for generating significant strain rates (Voegelé et al., 1998). Plastic deformation in garnet most commonly occurs by dislocation glide, with or without climb (Prior et al., 2000; Kleinschrodt & Duyster, 2002; Storey & Prior, 2005). At high strain, subgrain rotation can lead to dynamic recrystallization and a polygonal microstructure. Grain-boundary sliding is also inferred to operate in garnet undergoing high strain, particularly in fine-grained aggregates, where intercrystalline deformation overtakes intracrystalline deformation (Terry & Heidelbach, 2004; Storey & Prior, 2005).

Intracrystalline deformation deformation by dislocation creep occurs through formation and mobilization of dislocations. Assuming that annealing did not erase this evidence, plastic deformation is easily recognized by the formation of subgrains and other intracrystalline distortions, with misorientations across these boundaries that generally increase with strain (Storey & Prior, 2005). However, coalescence between garnet crystals that come into contact during growth can result in an alignment to very similar orientations, often resulting in low-angle grain boundaries that can be mistakenly identified as subgrain boundaries with low misorientation (Spiess et al., 2001; Prior et al., 2002). The distinction can be made from orientation differences with other neighbouring crystals, and compositional zoning, which should match across the boundaries in the case that the misorientation is not related to deformation but rather from crystals coming into contact during growth (Smit et al., 2011).

The identification of diffusion-accommodated grain-boundary sliding in the ductile regime relies on intercrystalline features, because intracrystalline distortion plays as minor to no role in this mechanism. The characteristics for diffusion-accommodated grain-boundary sliding in garnet are a very fine grain size, curved grain boundaries, shape preferred orientation (SPO) at low strain and no crystallographic preferred orientation (CPO), in layers that deform without necking (Terry & Heidelbach, 2004; 2006). Grain-boundary sliding has not been described in garnet in the brittle regime.

Below 600 °C, plastic deformation in garnet is ineffective and, given that garnet is normally a stiff and minor component in most garnet-bearing rocks, it will only rarely undergo deformation

at those conditions. Exceptions come in the form of discrete fracturing (Prior, 1994; Austrheim et al., 2017; Papa et al., 2017; Yamato et al., 2019), cataclasis (Trepmann & Stöckhert, 2002), and pressure-solution creep (Smit et al., 2011; Wassmann & Stöckhert, 2013; Chapter 4). However, fracturing and cataclasis can occur over a large range of stresses, strain rates, and temperatures including in the otherwise ductile regime and are therefore not indicative of specific conditions except for a high strain rate.

The majority of these processes lead to gradual flattening of garnet grains, with the exception of high-strain grain-boundary sliding and dynamic recrystallization by subgrain rotation (Terry & Heidelbach, 2004; Storey & Prior, 2005). Studying the effect of grain flattening on internal compositional zoning aids in distinguishing intracrystalline and intercrystalline deformation mechanisms. Additionally, grain flattening can be quantified to reconstruct the strain ellipse and quantify the total strain from garnet deformation.

5.2.2 Pressure solution

Stöckhert (2002) predicted the prevalence of pressure solution creep at (ultra)high-pressure-low-temperature ((U)H*P*-L*T*) conditions, based on the lack of dislocation-accommodated deformation in rocks exhumed from these metamorphic conditions, with the exception of eclogite. The vast amounts of silica-undersaturated fluids produced by the dehydration of hydrous lithologies in the slab (Van Keken et al., 2011) support the possibility of strong deformation by fluid-mediated diffusion, however evidence for pressure solution has only been observed in one UH*P*M unit so far (the LCU; Chapter 4). Other systems in which IPS in garnet has been described are a garnet-rich eclogite mylonite (Smit et al., 2011) and between colliding garnets during retrogression of a schist (Wassmann & Stöckhert, 2013). When interacting with enough fluids to efficiently drive intergranular pressure solution (IPS), garnet can undergo significant strains without activating dislocation glide (Smit et al., 2011).

Characteristics for the identification of congruent IPS in garnet were compiled by Smit et al. (2011). Garnet that was deformed by IPS should exhibit SPO, as grains become flattened by localized dissolution and reprecipitation, but lack CPO as it has no effect on, and is not affected by, IPS. The original compositional zonation of the deformed garnets should also be unaffected internally, yet be truncated at garnet-garnet contacts where material is dissolved. Further distinctions between garnet deformed by IPS and clusters of undeformed garnets, are that the latter exhibit equilibrium triple junctions, mostly straight grain boundaries, and identical compositions on both sides of a grain boundary (Smit et al., 2011). The incongruent IPS described by Wassmann & Stöckhert (2013) resulted in the enrichment of minerals that were previously inclusions in garnet, at the contact of the two garnet crystals. Based on a lack of plastic deformation in aggregates of white mica and graphite, the incongruent IPS in garnet in this system is interpreted to have operated at low differential stress.

5.2.3 Grain-boundary migration

Grain-boundary migration (GBM) is a mechanism of recrystallization where a grain boundary migrates over the less stable grain, recrystallizing the material as part of the more stable grain. GBM has been observed as a common mechanism in numerous minerals, such as calcite (Vernon, 1981), halite (Piazolo et al., 2006), quartz (Knipe & Law, 1987), olivine (Toriumi, 1982), orthopyroxene (Drury & Van Roermund, 1988), in many cases as a key mechanism of dynamic recrystallization (Stünitz, 1998 and references therein). However, GBM in garnet is only rarely described. In one case, the exposure of YAG (Yttrium-Aluminium-Garnet) to Yb along grain

boundaries in experiments resulted in local GBM (Marquardt et al., 2011). Superplastic behaviour of fine-grained garnet in a coronitic gabbro is inferred to have occurred by GBM in combination with grain-boundary sliding (Terry & Heidelbach, 2004). GBM is also briefly mentioned in a study on garnet fragmentation by seismic events with high shear heating (Austrheim et al., 2017). The discovery of GBM in garnetite from the LCU (Chapter 2) concerns a different setting than other occurrences of GBM in garnet recognized so far.

For GBM to occur, the migration of the grain boundary must result in a reduction of free energy of the system. In metals, several driving forces can result in an energy contrast sufficient to make GBM feasible: a contrast in stored deformation energy (dislocations), energy of a high-angle grain boundary, surface energy, a chemical driving force, magnetic field, elastic energy, or a temperature gradient (Gottstein & Shvindlerman, 2010). The estimated driving force of dislocations and a chemical contrast are up to several orders of magnitude higher than the other driving forces (Gottstein & Shvindlerman, 2010). GBM is driven by dislocations in the majority of geological materials that can undergo this mechanism under natural conditions (e.g., Toriumi, 1982; Piazolo et al., 2006). However, this driving force may not be sufficient for GBM in garnet in the brittle regime, as the garnet will lack the dislocation density necessary to result in a sufficient energy difference between neighbouring grains. Chemically-induced GBM (CIGM; also diffusion-induced GBM, DIGM), mostly known to operate in metal alloys (Hillert & Purdy, 1977; Chongmo & Hillert, 1981; Liu et al., 1989), has also been inferred for calcite (Evans et al., 1986; Hay & Evans, 1987; Hay & Evans, 1992; McCaig et al., 2007). Contrasts in chemical composition between two adjacent grains (e.g., Chongmo & Hillert, 1981), or between grains and a fluid within the grain boundary (Hay & Evans, 1987) are capable of driving CIGM due to the difference in chemical potential (Gottstein, Shvindlerman, 2010). Experiments performed in studies on CIGM exposed calcite to a melt rich in $SrCO_3$ or $BaCO_3$, observing that GBM is more efficient at forming solid solutions than volume diffusion (Hay & Evans, 1987). During these experiments, the calcite-calcite grain boundary developed lobate, interlocking microstructures (Evans et al., 1986; Hay & Evans, 1987).

5.3 LCU garnetites

Garnetite lenses and layers are a common occurrence within eclogite and various metasediments of the LCU. Most work was performed on sample EC5_1A-1, a garnetite hosted by a garnet-phengite quartzite, previously studied in Chapter 4. For comparison and as test for the consistency of the microstructures in other lithologies in the LCU, garnetites were also sampled from other quartz-rich metasediments and eclogite. Within all studied outcrops (Figure 2.5), the structural relations between host rock and garnetite indicate that garnetite is the more competent lithology, occurring as boudinaged layers or as thickened and in some cases rootless fold hinges. Internally, garnetite is structurally complex and heterogeneous (Figure 5.1). Garnet chain microstructures are locally preserved (Figure 5.1a,b), and internal layering within garnetite is commonly present, exhibiting differences in grain size and layer thickness (Figure 5.1c). Some garnet-garnet grain boundaries retain fluid inclusions (Figure 5.1d).

Certain garnetite microstructures are best emphasized by compositional zonation of the garnet (Figure 5.2). The distribution of Mn in a close-up of layers of different grain sizes (Figure 5.1c; Figure 5.2a) gives this area the appearance of rounded grains compacted together, whereas Ca-richer zones appear as infill with a slight preferred orientation at the top-left and bottom-right parts of grains. Opposing Ca zones across grain boundaries in garnetite C18-6-1 do not always match, and Fe is seen filling in an array of cracks radiating inwards from the grain boundaries (Figure 5.2c,d). These cracks are not visible in the map of Ca distribution. The Mg distribution in two

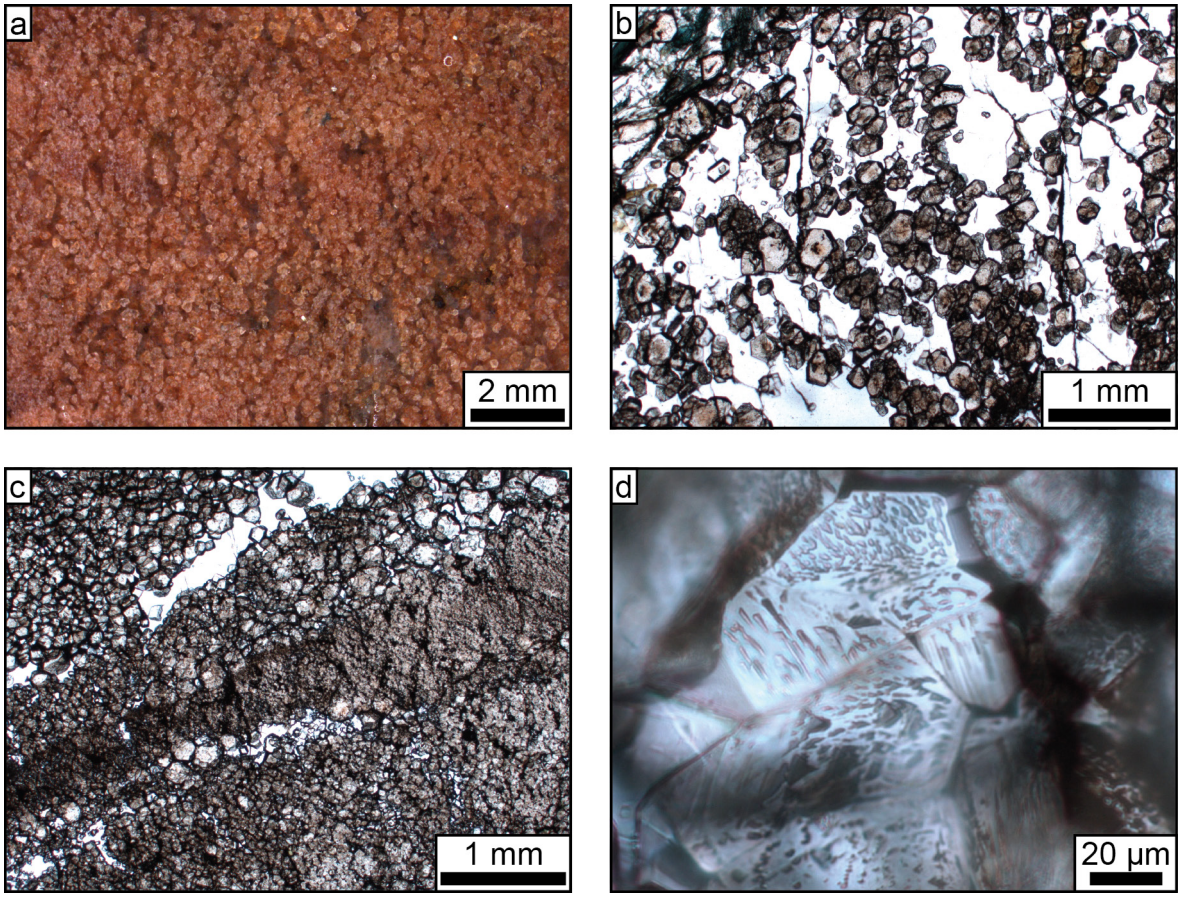

Figure 5.1: Close-up of hand specimen (a) and optical micrographs (b-d) of internal microstructures of garnetite in plane-polarised light. (a) Densely stacked garnet chain microstructures. (b) More widely spaced garnet chain microstructure, separated by quartz. (c) Layering in garnetite defined by grain size variations. (d) Fluid inclusions trapped along garnet-garnet grain boundaries.

different parts of garnet chains in the quartz-richer domain of garnetite EC5_1A-1 (Figure 5.2e,f) highlights how sets of garnets are deformed in different styles. In one case (Figure 5.2e), compositional zones are truncated and mismatching at the grain boundary and the core of a smaller garnet is exposed at the grain contact, however there is no strong interlocking of adjacent garnet grains. In the second case (Figure 5.2f), several grains are strongly interlocked to the point where the rim of one grain is mostly within the largest garnet in the map. In this case, the cores of both garnets are exposed by, and to, the adjacent interlocked grain.

5.4 Results

5.4.1 Subgrains

Subgrains formed by the concentration of dislocations into boundaries, resulting in a slight misorientation of the crystal lattice, are observed in ~5% of the garnet grains in only one garnetite (C18-6-1; Figure 5.3a,b). None of the areas analysed with EBSD exhibit a CPO (representative diagram in Figure 5.3c). Clusters of points represent slightly deformed garnets exhibiting subgrains.

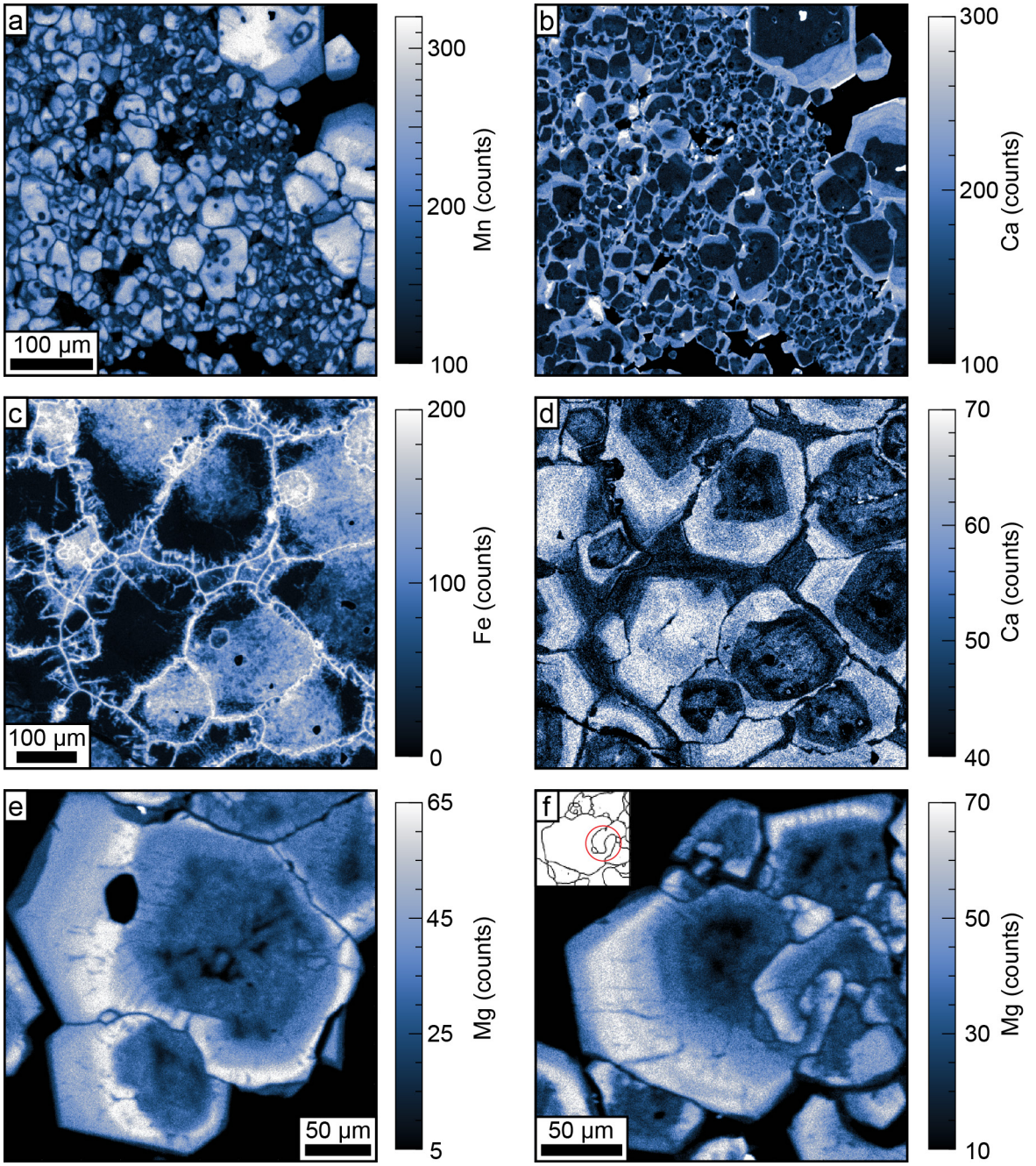

Figure 5.2: EMPA element distribution maps. (a) and (b) are Mn and Ca maps respectively of a layered zone in garnetite EC5_1A-1 consisting of various grain sizes. (c) and (d) are Fe and Ca maps respectively of garnetite C18-6-1, displaying cracked grains and a related garnet-replacement process along the fractures. (e) and (f) are Mg maps of garnets within garnet chains in the quartz-rich domain of garnetite EC5_1A-1. (f) contains an overview map of boundaries obtained by EBSD to clarify the grain structure around the interlocking section. The red circle indicates the interlocking lobes.

5.4.2 Grain-boundary migration

Grain-boundary migration (GBM) affects the morphology of garnet grains, and therefore is inspected before analysing grain shape for the purpose of studying pressure solution. All garnetite samples studied here exhibit interlocking structures that are significantly more interlocking those generated by IPS (Figure 5.4). Recrystallization by GBM is generally also marked by a change in garnet composition (Figure 5.4b,e,f). This change in garnet composition, for example the lack of

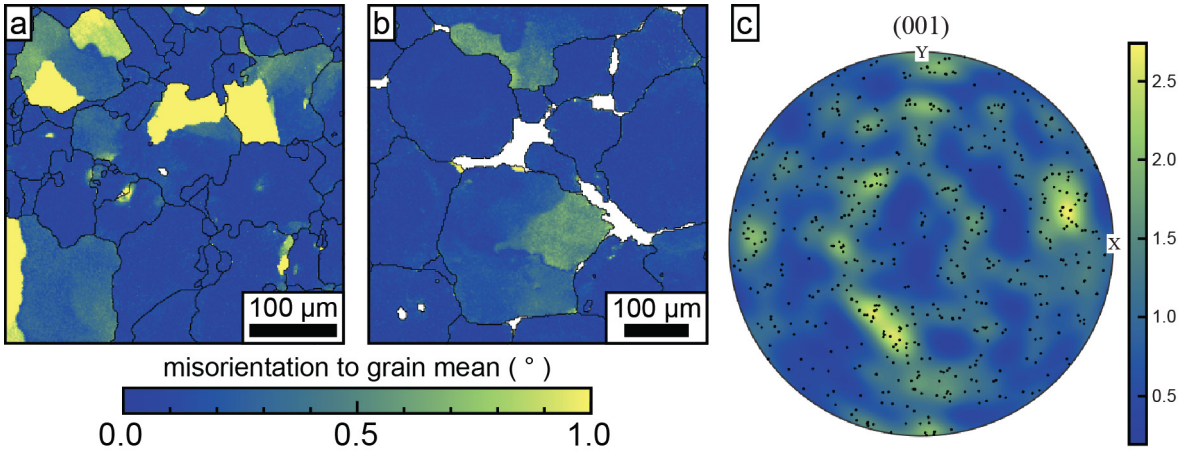

Figure 5.3: (a,b) Maps of garnet misorientations relative to the mean orientation of the grain determined from EBSD maps of two areas of sample C18-6-1. Black lines indicate grain boundaries, other minerals are displayed in white. (c) Crystal orientation plot based on an area of sample C18-6-1 that includes the area displayed in (b). Colour indicates the density of data points as multiples of uniform distribution.

Ti in otherwise Ti-bearing garnet in EC5_1A-1 (Figure 5.4f), allows for GBM-recrystallized garnet to be distinguished from original garnet and helps to highlight the morphology of lobes associated with GBM.

The degree of GBM, and the size of the GBM lobes relative to the garnet crystals, varies by sample and also within samples. The GBM lobes rarely exceed 20 µm, thus their size relative to the garnet crystals depends mostly on the garnet crystal size. In the inner garnetite of EC5_1A-1, grains are ~50 µm on average and therefore, interlocking lobes strongly distort the grain shape. In the inner garnetite of sample EC5_1A-1 (Figure 5.5d), many small grains are found to have the same orientation as a nearby larger garnet grain, both separated from one another by a different garnet grain. The small grains are often entirely embedded within a different garnet, likely cuts through a GBM lobe attached to a larger grain on a different plane than the section. Although a link to GBM is not obvious, quadruple junctions are common in dense garnetite zones (Figure 5.4c,d).

5.4.3 Pressure solution

5.4.3.1 Aspect ratio

The degree of pressure solution is studied by analysis of grain shape and orientation. For this purpose, EBSD maps were obtained for sample E5_1A-1 (16 maps), C18-6-1 (5 maps) and C18-10-1 (1 map). The heterogeneous structure of EC5_1A-1 allows for comparisons between different degrees of deformation. Figure 5.5 displays EBSD maps of quartz-rich outer garnetite where garnets are aligned into chains (Figure 5.5a), and a fine-grained zone within the inner garnetite (Figure 5.6b). Ellipses fit to grain shapes provide the long and short axis necessary to calculate the aspect ratio and long axis orientation of grains. This approach is problematic for more complex grain morphologies, especially when altered by GBM (see complex grain morphologies in Figure 5.4).

Before SPO analysis can be performed, the aspect ratio of garnet must be investigated to find the boundary between undeformed and deformed garnet, and thus reduce noise from undeformed garnet crystals. Table 5.1 contains the total number of grains for each EBSD map in bins of aspect ratio that are 0.2 in width, and the total number of grains reconstructed from the EBSD data.

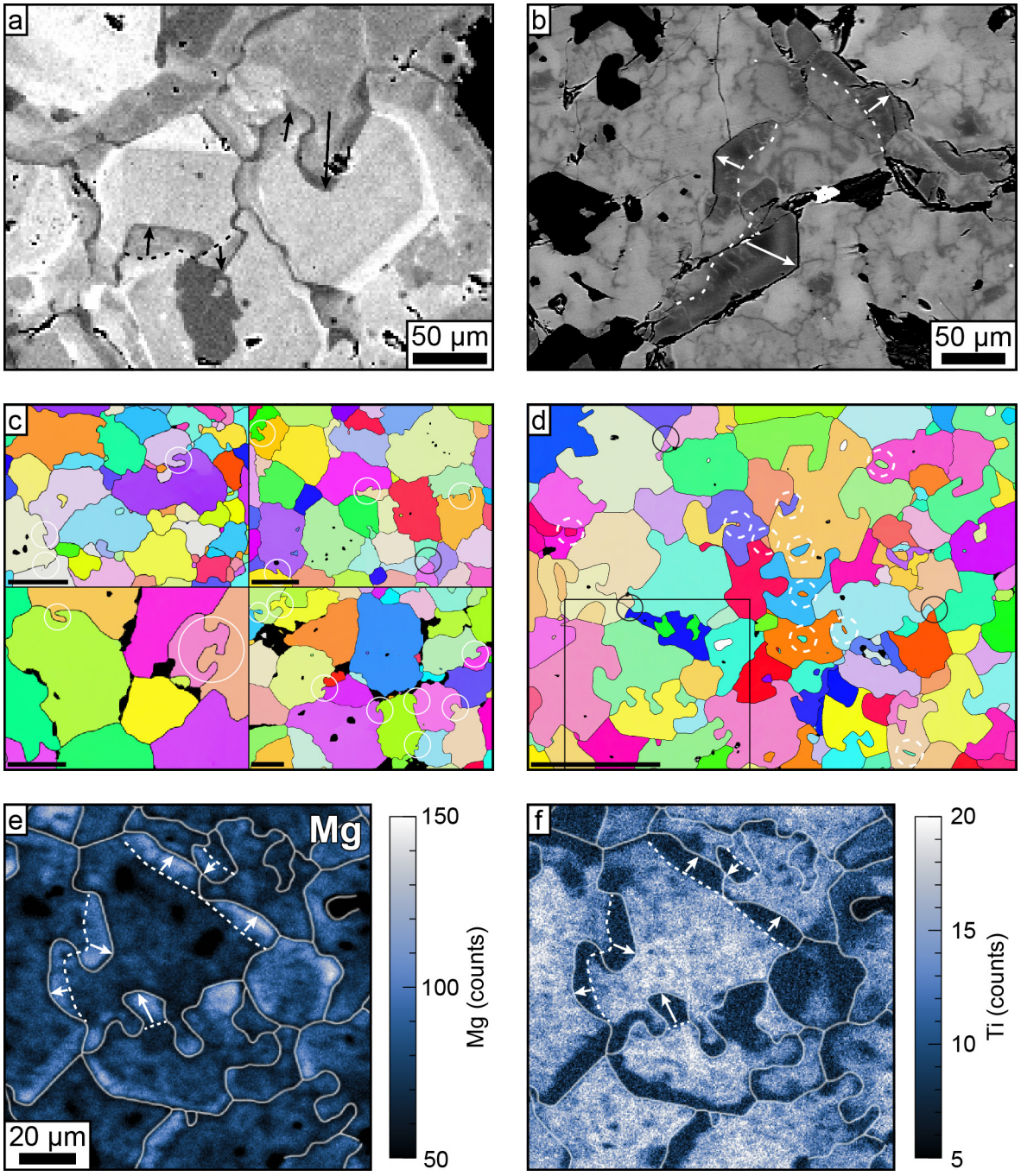

Figure 5.4: Overview of GBM microstructures in garnet from various samples. (a) BSE image of interlocking grains in metasedimentary garnetite C18-10-1. Grain boundaries appear darker in contrast to the main garnet crystals. Black arrows indicate the direction of GBM, the dashed black line marks the estimated initial grain boundary position. (b) BSE image of interlocking grains in eclogitic garnetite C19-08. Note the strong contrast between GBM-recrystallized garnet (dark) and original garnet (lighter, fractured) and similarity in microstructure to (e,f). White arrows indicate the direction of GBM, the dashed white line marks the estimated initial grain boundary position. (c) Maps of crystal orientation coloured based on the Euler angles for four locations in sample C18-6-1. Although grain orientation is not significant for the purpose of this figure and rather a tool of grain separation, the Euler angle colour bar is given in Appendix B Figure B3. White circles indicate interlocking structures. The black circle marks a quadruple junction. (d) Maps of crystal orientation coloured based on the Euler angles for dense inner garnetite in sample EC5_1A-1. Dark circles indicate quadruple junctions. Interlocking structures are too commonplace for marking. White dashed circles indicate small grains with the same orientation as a nearby larger grain that is separated by another grain. The black rectangle marks the area of (e,f). (e,f) EPMA element distribution maps for Mg and Ti respectively for dense inner garnetite in sample E5_1A-1. White arrows indicate the direction of GBM, the dashed white line marks the estimated initial grain-boundary position. All scale bars are 100 µm unless indicated otherwise.

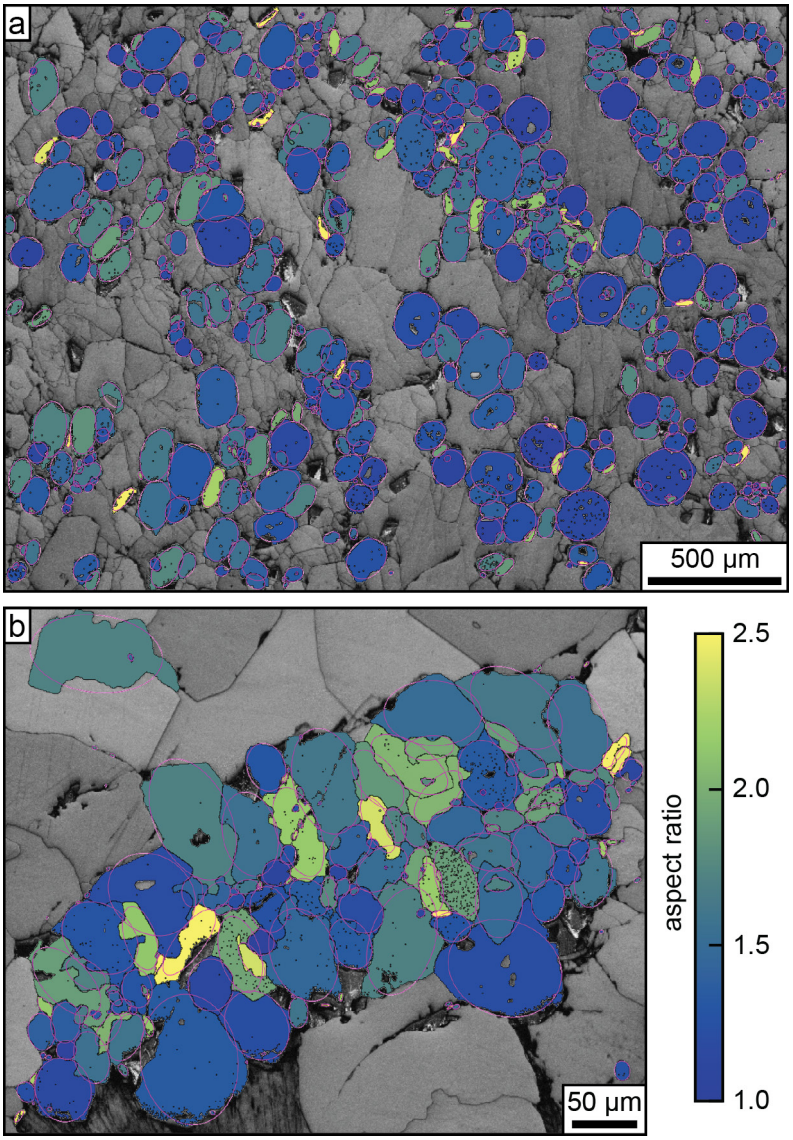

Figure 5.5: EBSD maps M8 and M11 of sample EC5_1A-1. Grains are coloured by their aspect ratio, and the fitted ellipses used to calculate the aspect ratio are superimposed on the respective grains.

In figure 5.7a–c, the data from Table 5.1 for each section are plotted as the percentage of grains in each aspect-ratio bin. With an increase in deformation, grain flattening will increase, causing a shift from low aspect ratios to high aspect ratios. This shift is observed in Figure 5.7a, where map M2 contains the highest percentages of grains in the first two bins (aspect ratio 1.0–1.4), and the lowest percentages in the next three bins. Most analysed maps adhere to this trend and thus the aspect ratio of 1.4 appears to be a boundary between undeformed and deformed grains.
To test whether or not grain flattening depends on various grain size, the data are plotted as aspect ratio against grain area for two representative analysed areas in Figure 5.7d,e. These distributions display a trend in which higher aspect ratios tend to be limited to smaller grains. Several relationship baselines are given as reference for the behaviour of aspect ratio versus cross-sectional area. To determine how the cross-sectional area responds to simplified mass removal, akin to flattening of grains by incongruent IPS, the following formula was derived for the cross-sectional area of a sphere that is flattened by dissolution on two sides:

Table 5.1: EBSD maps with >100 grains not intersecting the edge of the map, and the distribution of grains by aspect ratio in bins of 0.2, up to 3.0.

	EC5-1A													
asp. ratio	M1	M2	M3	M4	M5	M6	M7	M8	M9	M10	M11	M12	M13	2M3
1.0-1.2	63	28	116	209	153	25	146	98	203	127	16	27	230	113
1.2-1.4	106	44	241	361	245	31	287	163	349	184	45	55	354	198
1.4-1.6	77	18	163	322	202	20	180	133	270	119	40	58	250	160
1.6-1.8	49	15	103	192	132	14	111	87	187	61	31	36	130	104
1.8-2.0	25	7	62	104	82	13	59	46	111	27	22	22	62	58
2.0-2.2	18	6	33	71	53	4	44	27	88	20	17	6	35	29
2.2-2.4	12	2	20	35	34	4	21	10	57	9	9	8	16	12
2.4-2.6	5	1	9	25	23	2	7	6	30	5	5	3	9	16
2.6-2.8	5	0	4	15	7	1	3	5	19	5	2	3	4	3
2.8-3.0	2	1	4	7	6	0	2	3	14	1	1	0	0	7
> 3.0	6	2	7	11	15	0	4	2	26	4	2	0	2	10
n	367	124	762	1352	952	114	864	580	1354	562	190	218	1092	710

	C18-6-1					C18-10-1
asp. ratio	M1	M3	M4	M5	M9	M1
1.0-1.2	44	30	47	25	71	472
1.2-1.4	79	80	82	34	99	850
1.4-1.6	67	55	55	20	64	655
1.6-1.8	47	30	45	19	30	372
1.8-2.0	22	17	23	11	15	189
2.0-2.2	14	10	20	3	13	106
2.2-2.4	11	3	1	3	4	50
2.4-2.6	6	3	3	2	6	33
2.6-2.8	3	3	1	1	2	15

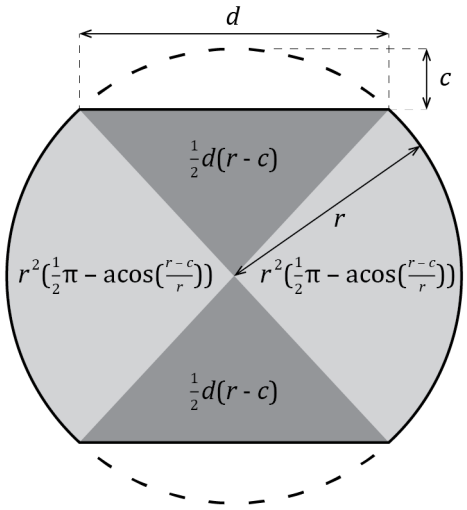

Figure 5.6: Schematic diagram of a spherical grain being dissolved on two sides simultaneously. Shaded sectors of the grain contain the formula for the area of those sectors, combined to calculate the cross-section area of grains.

$$A = d(r - c) + 2r^2(\frac{1}{2}\pi - \text{acos}(\frac{r-c}{r}))$$

Where r is radius, c is the total thickness of material removed parallel to the grain radius, and d is the diameter of the dissolution surfaces (Figure 5.6). Parameter d can be calculated as:

$$d = 2\sqrt{r^2 - (r - c)^2}$$

This approach assumes that all dissolved material exits the system. While it is not known whether this is an accurate description of the pressure solution in these garnetites, the pressure solution observed is at least partially incongruent based on garnet growth not matching the composition of dissolved garnet (Figure 5.2; Chapter 4).

With an increasing amount of material reprecipitating on the long axis of the garnet grains, area decrease with an increase of aspect ratio is reduced compared to the purely incongruent mechanism plotted in Figure 5.7d,e, steepening the associated curves. Completely congruent IPS

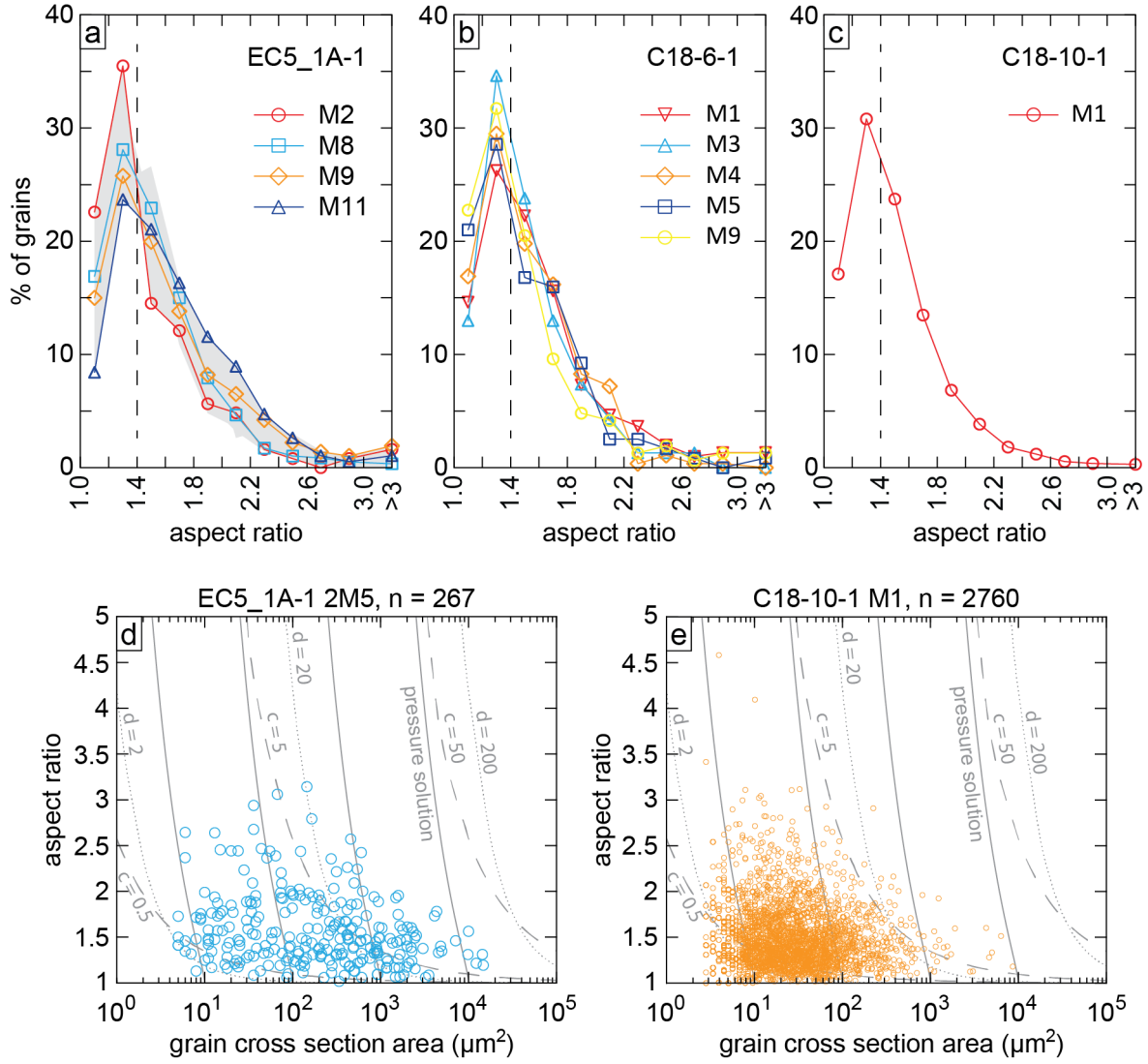

Figure 5.7: (a–c) Distribution of grains with certain aspect ratios, divided into bins 0.2 in width, for (a) EC5_1A-1, (b) C18-6-1 and (c) C18-10-1. Not all maps of EC5_1A-1 are displayed in (a), but the full range of data is given by the grey shaded area. Maps C18-6-1 M3 and M4 have a low resolution thus the uncertainty on reconstructed grain size is relatively high. (d,e) Scatter diagrams of aspect ratio versus cross-sectional area ratio for two EBSD maps. Grey lines indicate the calculated trends of constant dissolution surface diameter d (stippled lines), constant total thickness of material removed parallel to the grain radius c (dashed lines), and the trend for ideal pressure solution (full lines). See main text for calculations.

results in vertical lines. Also given in Figure 5.7d,e are the lines in aspect ratio versus cross-sectional area space that indicate a constant value for *c* and *d* assuming the same process of incongruent IPS. The data do not adhere to any of the given relations.

5.4.3.2 Shape-preferred orientation

With the established cutoff aspect ratio of 1.4 for undeformed versus deformed garnet grains, shape-orientation analysis can be performed. Figure 5.8 presents a polar histogram of long-axis orientations for map E5_1A-1 M4 and strain-ellipse analysis by plotting all long and short axis apexes of the fitted ellipses with their respective orientations for the same map, including a fitted strain ellipse. The polar histogram exhibits a broad peak in long axis orientations around 50-90°, and that the distribution is not perfectly smooth. The garnets in the plotted map (Appendix B Figure B13) exhibit little to no GBM.

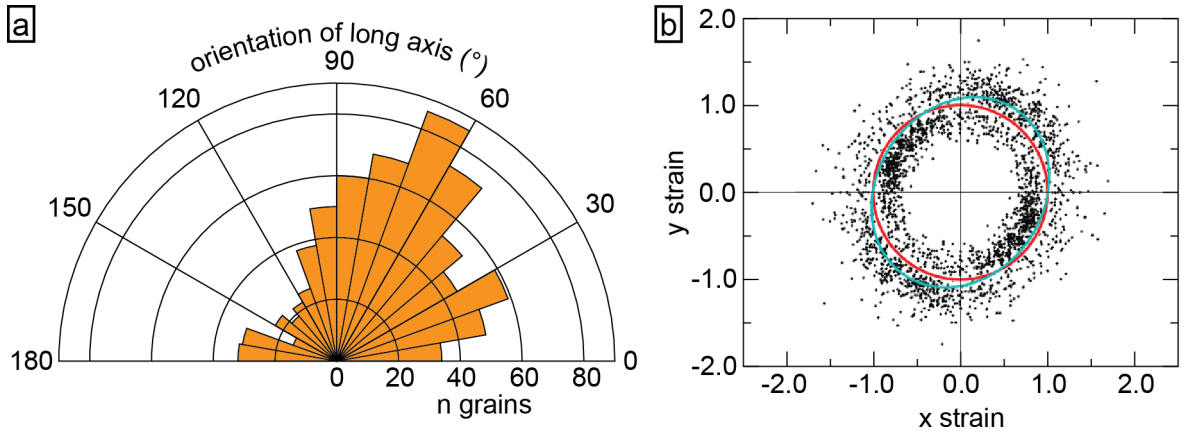

Figure 5.8: (a) Polar histogram of long-axis orientations for ellipses fitted to grains in EBSD map EC5_1A-1 M4. (b) Long and short axes for grains in the same EBSD map as in (a) plotted with their orientation, normalized to the same area as a circle with r = 1, given in red. Long axis apexes plot outside the red circle, short axis apexes plot within the red circle. A strain ellipse, shown in blue, was fitted to the data points.

Further SPO analysis is performed with polar histograms to test for the occurrence of multiple preferential orientations. Polar histograms are constructed of grains with aspect ratios > 1.4 in all EBSD maps of sample EC5_1A-1 for which more than 100 grains were reconstructed (Figure 5.9).

There is no uniform SPO throughout the section. The spread of SPO appears more ordered when the EBSD maps are subdivided into several types based on their larger scale microstructural setting and degree of GBM. Maps strongly affected by GBM, generally those with a small garnet size and consistent GBM at grain boundaries (Figure 5.4d–f), do not exhibit a clear SPO. Maps of the fine-grained zones exhibit an SPO near-perpendicular to the orientation of the fine-grained zone, with the exception of map 2M5, which is grouped with other maps affected strongly by GBM. Map M5 is also not included with other maps on fine-grained zones, as the majority of this map constitutes regular inner garnetite. Maps located in outer garnetite, characterized by layering with distinct grain sizes or by garnet chains, both preserved and deformed, exhibit SPO that correlates with the orientation of those larger scale microstructures. In the case of layering, the SPO is subparallel to this layering. SPO in maps in which garnet chains were identified is at an angle of 45°–90° with the chains. This angle is largest in the map with the best preserved chains (M8). Map M13 is an exception amongst the zone defined by layering, as it exhibits two distinct main orientations (horizontal and at ~70° according to axis numbering in Figure 5.8). Two maps,

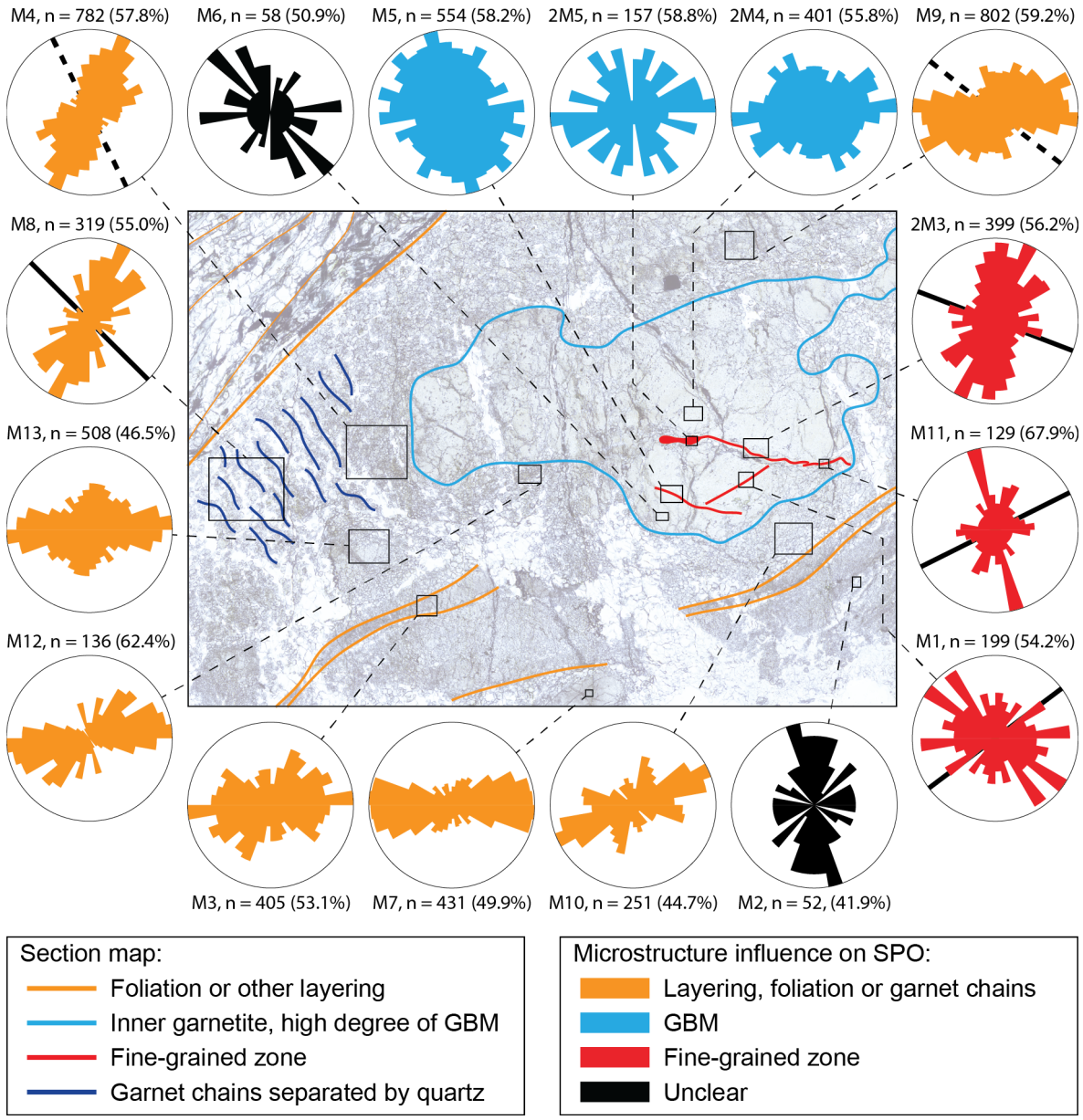

Figure 5.9: Radial shape-orientation histograms (bin size relative to largest bin) for all EBSD maps of section EC5_1A-1 with a total amount of grains over 100, labelled with map name, number of grains and percentage of grains with an aspect ratio of 1.4 or higher. These histograms are linked to their location within an annotated scan of the section. Structural aspects are highlighted to indicate how they related to SPO, and where possible, the visually estimated orientation of structures within EBSD maps is added as a black line to the histograms (garnet chains for orange SPO diagrams, dashed when partially dismembered and not separated by quartz; fine-grained zone for red SPO diagrams). Reference frame for orientations is 0° at east, counting counterclockwise.

M2 and M6, were not grouped with any of the mentioned map types as these maps contain less than 60 grains with aspect ratio > 1.4 and the resulting SPO is unclear.

5.5 Discussion

5.5.1 Plastic deformation and CPO

In garnetite C18-6-1, a minor degree of misorientation, on the order of 1°, is present within a small percentage of the garnet crystals. Based on the sharp boundaries that divide sectors of different orientation within a garnet crystal, and their geometry, which is morphologically unlike grain boundaries (particularly in Figure 5.3b), these are identified as subgrains. Minor misorientations from crystal alignment by coalescence can be excluded due to a lack of CPO covering a larger number of grains (Spiess et al., 2001). As subgrains are only present in few grains, it can be deduced that plastic deformation operated locally and to a minor degree. The low misorientation at the subgrain boundaries is also consistent with low accumulated strain by dislocation creep (Storey & Prior, 2005). Therefore, any significant strain observed in garnet across areas larger than those displaying evidence for dislocation activity must have resulted primarily from a different mechanism.

5.5.2 Grain-boundary migration

Evidence for GBM is present in garnet within all studied garnetites. The distinction between GBM and pressure solution is made based on the degree of interlocking structures, which exceed what is known from pressure solution (Smit et al., 2011), and the change in composition of the lobes (Figure 5.4b,e,f). Within sample EC5_1-A1, the occurrence of evidence for GBM varies strongly between garnetite domains, being most widespread in the dense inner garnetite, where garnet cores are more readily exposed (see Chapter 4). Most lobes formed by GBM do not exceed 20 μm, regardless of grain size, and therefore the finer-grained zones where GBM occurred are affected by the resulting recrystallization grain-shape modification to a higher degree.

The lobate structures formed by GBM at the grain contacts strongly complicate the grain shape to the point where their shape cannot be approximated by an ellipse and so the shape analysis is less effective. The change in composition between the old garnet and new garnet recrystallized by GBM garnet could allow for grain reconstruction in a future work, however grain analysis will have to be performed on element distribution maps rather than EBSD data. This approach will not counterbalance complications caused by grains that are connected in a different plane than the thin section, but appear separated in the data (Figure 5.4d). The issues mentioned here result in no significant SPO being revealed by analysis of zones strongly affected by GBM, particularly when garnet grains are relatively small in comparison to the GBM lobes (Figure 5.9).

Due to a general lack of dislocations formed by plastic deformation, strain is excluded as the primary driving force for GBM in the LCU garnetites. Instead, the strong changes in composition between original and recrystallized garnet observed particularly in the eclogite garnetite (Figure 5.4b) and in EC5_1A-1 (Figure 5.4e,f) suggests a chemical driving force. Additionally, GBM localizing at contact between garnet cores (Chapter 4; Figure 5.2e,f) indicates that a specific range of initial garnet compositions is required to result in GBM. However, two garnet zones of similar composition alone cannot provide the driving force for this mechanism as there is no energy difference between the two. Also, given how the composition of the garnet lobes is not an intermediate of precursor garnet, an external chemical component is required. Therefore, the driving force must be the result of a fluid in the grain boundary that is in disequilibrium with the garnet cores.

Rather than dissolution, however, the disequilibrium between fluid and contact between garnet cores resulted in a (near-) equal volume ratio of the destruction of garnet as the growth of

new garnet in place, and not isochemically. The evidence that GBM only took place when garnet cores came into contact with other garnet cores suggests that the original composition of the cores was more soluble than other parts of the garnet, but it is not clear why GBM lobes also only nucleate from cores. This peculiar behaviour is not observed in other garnetites displaying GBM. The sometimes euhedral GBM-lobes could be consistent with a less soluble garnet penetrating more soluble garnet interiors by pressure solution. However, as GBM appears to have affected boundaries of all orientations, non-isochemical congruent IPS is an unlikely mechanism for formation of the lobes.

In the rare case where IPS could potentially lead to strong interlocking of grains (Figure 5.2f could be IPS or GBM), it still appears that the interlocking structures in the inner garnetite (Figure 5.4e,f) formed by GBM as the original grain boundary, indicated by the boundary between Ti-rich and Ti-poor garnet, is continuous across lobes indicating no movement of lobes into the cores of the other garnets.

The lobate microstructure propagating in both directions from the original grain boundary as observed in garnetite here, is highly similar to the microstructures in calcite that underwent GBM by exposure to a melt in grain boundaries (Hay & Evans, 1987). Although there are no constraints on the fluid in the grain boundaries that drove GBM in garnet in the LCU garnetites, CIGM is the most likely mechanism here.

5.5.3 Pressure solution

The deformed garnet grains in this study exhibit all the characteristic textural observations for pressure solution in garnet as proposed by Smit et al. (2011). Most importantly for the recognition of pressure solution instead of other deformation mechanisms that can also result in flattened grains, is the undistorted preservation and truncation of compositional zones, which also do not match up at opposite sides of grain boundaries (Figure 5.2b,d–f). Equilibrium grain-boundary triple junctions are also not observed, notably highlighted by the presence of quadruple junctions (Figure 5.4c,d).

The garnetite domain displayed in Figure 5.2a,b is relatively unaffected by other mechanisms like fracturing and related selective replacement of garnet, and GBM. Halite deformed by IPS creep exhibits similar patterns (Figure 14c in Závada et al., 2012), although the halite was strained to a far higher degree than the garnet in Figure 5.2a,b. The similarity stems from the style of reprecipitation, indicating that the IPS in garnet is at least partially linked to reprecipitation with an increase in Ca at the expense of Mn concentration in garnet.

The comparison of aspect ratio versus cross section area (Figure 5.7) demonstrates that smaller grains exhibit higher aspect ratios. Several models were compared to the observed trend, such as incongruent pressure solution at a constant dissolution surface diameter or a constant maximum distance of dissolution perpendicular to the grain surface. As pressure solution relies on the localization of high stresses at grain contacts, the expectation is that a progression of compaction leads to a larger surface area of grain contact and thus lower stresses, limiting further IPS. However, none of these approaches fit the observed trend. Therefore, it appears that IPS localizes in smaller grains. The comparison between aspect ratio and cross section area also suggests that IPS tends to localize in general, leading to a limited number of grains at high aspect ratios, even when only considering the smaller grains. This localization of IPS is also apparent from the distribution of aspect ratios across grains, as even the most deformed domains within the garnetite contain > 30% grains with an aspect ratio below 1.4, deemed undeformed for SPO analysis.

Strain ellipses obtained from the EBSD maps that also exhibit a significant SPO (Figure 5.8), do not indicate a high amount of strain within the bulk of the garnet. Although the strain

cannot be accurately quantified due to unknown amounts of reprecipitation, it likely does not exceed the 15% maximum shortening of grains determined by Smit et al., (2011). This observation combined with the low amount of grains at higher aspect ratios, suggests that the majority of grains undergo low oriented strain from pressure solution, and only few grains undergo high strain. The localization of pressure solution into a small percentage of the grains allows for several stages of pressure solution under a different orientation of σ_1 to be recorded and not completely overprinting older phases. The presence of several stages of pressure solution may however reduce the apparent strain from the calculation of strain ellipses that take into account grains with any long axis orientation.

The SPOs within garnetite EC5_1A-1 are distributed in a complex fashion, and appear locally controlled (Figure 5.9). Areas that are strongly affected by GBM cannot be used in this analysis as any possible SPO before GBM is now obscured by the complex nature of the grain morphology. Within EBSD maps where the SPO is related to larger scale microstructures such as layering or garnet chains, two populations can be distinguished. The areas within the layered domain of the garnetite exhibit subhorizontal SPOs, whereas garnet chain domains, most notably M4 and M8, feature a dominant SPO around ~70 °. It is interpreted that these SPOs are (near-) perpendicular to σ1 during accretion (Chapter 4) and deformation of the garnets in that specific zone of garnetite. The occurrence of two discrete common SPO orientations suggests that the two zones were deformed under different stress regimes. Hybrid area M13 displays components of both populations, although it does not exhibit any remnants of garnet chains. This is interpreted as the result of an initial stage of garnet IPS under a subvertical σ_1, leading to a subhorizontal SPO. During a later stage, garnets accreted to the garnetite forming chains (similar to Massey et al., 2011) under a different stress regime, resulting in a different SPO in these domains. Hybrid area M13, being at the outside of the layered domain of the garnetite, experienced both phases of IPS and its SPO was partially overprinted by the second phase. IPS localizing within part of the grains allowed for both orientations to be recorded. Garnet chain map M9 is on the other side of the dense inner garnetite compared to M4 and M8, and its SPO is more subhorizontal. This suggests that internal rotations could have taken place within the garnetite, also supported by the observation of folding of garnetite (Figure 2.5a,b), or that local stress variations resulted in a heterogeneous SPO distribution for the same generation of IPS-deformed garnet.

EBSD maps where the SPO is related to the orientation of the fine-grained zones within the inner garnetite, significantly differ in SPO from the maps where SPO is related to larger scale microstructures. These fine-grained zones are proposed in Chapter 4 to have formed internal fluid pathways within the inner garnetite, during a stage of the evolution of this system where fluid flow elsewhere within the inner garnetite was sparse. Although there is no known analog for this, it is proposed that a gradient in fluid pressure within the fine-grained zone could drive IPS with an unexpected SPO as result.

This study only analysed the garnet grains in 2D, under the assumption that the axes of ε1 and ε3 lie within the plane of the section. Under a flattening regime for compaction suggested in Chapter 4, it is expected that ε2 and ε3 are similar. 3D analysis of grain shape in a near monomineralic system is challenging, but future studies attempting this may yield further details on the relative principal stress orientations leading to the formation of SPOs by IPS.

5.5.4 Reconstruction and implications

The garnetites studied here exhibit microstructures indicating a variety of degrees and styles of IPS and GBM. A reconstruction for one garnetite, also studied in Chapter 4, is made to summarise the operation of these mechanisms during the evolution of the garnetite (Figure 5.10). Overall,

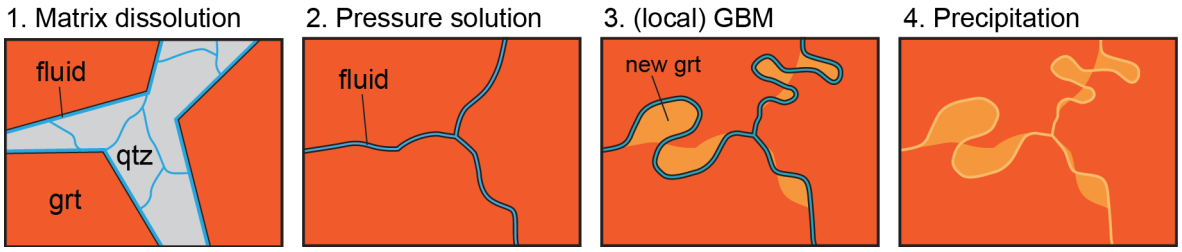

Figure 5.10: Schematic representation of the structural evolution of dense garnetite in sample EC5_1A-1. Stages correspond approximately to those presented in Figure 4.10.

IPS in the studied garnetites resulted in a low mean strain, only localizing to high strain in a few grains with an affinity or smaller grains. The low achieved strain is however well-oriented on a local scale, and can be linked to larger scale microstructures like foliation, garnet chains and local fluid pathways. Several generations of IPS throughout the evolution of the garnetite can be recognized in SPO. To get a better view of the deformation history and stress regime linked to IPS, 3D grain analysis is required.

GBM, driven by a chemical disequilibrium between garnet cores and a grain-boundary fluid, resulted in interlocking lobes of recrystallized garnet, strongly complicating the grain morphology and overwriting any pre-existing SPO.

Grain analysis does not provide any insight in garnet dissolution that is not oriented, such as the garnet dissolution observed in garnet porphyroblasts in the host-rock quartzite, linked to fluid pulses. Despite the fluid-rich environment and the potential for IPS in garnet to operate at low stresses, garnetite was not strongly deformed by IPS, as supported by outcrop-scale microstructures that support garnet as more competent lithology. Thus IPS in garnet plays a minor role in the rheology of garnet-rich systems.

References

Austrheim, H., Dunkel, K.G., Plümper, O., Ildefonse, B., Liu, Y., Jamtveit, B., 2017. Fragmentation of wall rock garnets during deep crustal earthquakes. Science Advances, 3, e1602067

Chongmo, L., Hillert, M., 1981. A metallographic study of diffusion-induced grain boundary migration in the Fe-Zn system. Acta Metallurgica, 29, 1949–1960

Drury, M.R., Van Roermund, H.L.M., 1988. Fluid Assisted Recrystallization in Upper Mantle Peridotite Xenoliths from Kimberlites. Journal of Petrology, 30, 133–152

Evans, B., Hay, R.S., Shimizu, N., 1986. Diffusion-induced grain-boundary migration in calcite. Geology, 14, 60–63

Gottstein, G., Shvindlerman, L.S., 2010. Grain boundary migration in metals: thermodynamics, kinetics, applications. CRC series in materials science and technology (Taylor & Francis, Boca Raton, 2nd edition)

Hay, R.S., Evans, B., 1987. Chemically induced grain boundary migration in calcite: temperature dependence, phenomenology, and possible applications to geologic systems. Contrib Mineral Petrol vol. 97 pp. 127–141

Hay, R.S., Evans, B., 1992. The coherency strain driving force for CIGM in non-cubic crystals: comparison with in situ observations in calcite. Acta Metallurgica et Materialia, 40(10), 2581–2593

Hillert, M., Purdy, G.R., 1977. Chemically induced grain boundary migration. Acta Metallurgica, 26, 333–340

Kleinschrodt, R., Duyster, J.P., 2002. HT-deformation of garnet: an EBSD study on granulites from Sri Lanka, India and the Ivrea Zone. Journal of Structural Geology, 24, 1829–1844

Knipe, R.J., Law, R.D., 1987. The influence of crystallographic orientation and grain boundary migration on microstructural and textural evolution in an S-C mylonite. In: H.J. Zwart, M. Martens, I. van der Molen, C.W. Passchier, C. Spiers and R.L.M. Vissers (Editors), Tectonic and Structural Processes on a Macro-, Meso- and Micro-scale. Tectonophysics, 135: 155–169

Liu, D., Miller, W.A., Aust, K.T., 1989. Diffusion induced grain boundary migration in Ni-Cu diffusion couples. Acta

Metallurgica, 37(12), 3367–3378

Marquardt, K., Petrischcheva, E., Gardés, E., Wirth, R., Abart, R., Heinrich, W., 2011. Grain boundary and volume diffusion experiments in yttrium aluminium garnet bicrystals at 1,723 K: a miniaturized study. Contrib Mineral Petrol 162 739–749

Massey, M.A., Prior, D.J., Moecher, D.P., 2011. Microstructure and crystallographic preferred orientation of polycrystalline microgarnet aggregates developed during progressive creep, recovery, and grain boundary sliding. Journal of Structural Geology, 33, 713–730

McCaig, A., Covey-Crump, S.J., Ismaïl, W.B., Lloyd, G.E., 2007. Fast diffusion along mobile grain boundaries in calcite. Contributions to Mineralogy and Petrology, 153, 159–175

Papa, S., Pennacchioni, G., Angel, R.J., Faccenda, M., 2018. The fate of garnet during (deep-seated) coseismic frictional heating: The role of thermal shock. Geology, 46(5), 471–474

Piazolo, S., Bestmann, M., Prior, D.J., Spiers, C.J., 2006. Temperature dependent grain boundary migration in deformed-then-annealed material: Observations from experimentally deformed synthetic rocksalt. Tectonophysics, 427, 55–71

Prior, D.J., 1994. Sub-critical fracture and associated retrogression of garnet during mylonitic deformation. Contributions to Mineralogy and Petrology, 113(4), 545–556

Prior, D.J., Wheeler, J., Brenker, F.E., Harte, B., Matthews, M., 2000. Crystal plasticity of natural garnet: New microstructural evidence. Geology, 28(11), 1003–1006

Prior, D.J., Wheeler, J., Peruzzo, L., Spiess, R., Storey, C., 2002. Some garnet microstructures: an illustration of the potential of orientation maps and misorientation analysis in microstructural studies. Journal of Structural Geology, 24, 999–1011

Rubatto, D., Burger, M., Lanari, P., Hattendorf, B., Schwarz, G., Neff, C., Schmidt, P.K., Hermann, J., Vho, A., Günther, D., 2020. Identification of growth mechanisms in metamorphic garnet by high-resolution trace element mapping with LA-ICP-TOFMS. Contributions to Mineralogy and Petrology 175:61, https://doi.org/10.1007/s00410-020-01700-5

Smit, M.A., Scherer, E.E., John, T., Janssen, A., 2011. Creep of garnet in eclogite: Mechanisms and implications. Earth and Planetary Science Letters. 311, 411–419

Spiess, R., Peruzzo, L., Prior, D.J., Wheeler, J., 2001. Development of garnet porphyroblasts by multiple nucleation, coalescence and boundary misorientation-driven rotations. J. metamorphic Geol., 19, 259–290

Stöckhert, B., 2002. Stress and deformation in subduction zones: insight from the record of exhumed metamorphic rocks. Geological Society, London, Special Publications, 200, 255–274

Storey, C.D., Prior, D.J., 2005. Plastic Deformation and Recrystallization of Garnet: A Mechanism to Facilitate Diffusion Creep. Journal of Petrlogy, 46(12), 2593–2613

Stünitz, H., 1998. Syndeformational recrystallization - dynamic or compositionally induced? Contributions to Mineralogy and Petrology, 131, 219–236

Terry, M.P., Heidelbach, F., 2004. Superplasticity in garnet from eclogite facies shear zones in the Haram Gabbro, Haramsøya, Norway. Geology, 32(4), 281–284 doi: 10.1130/G20157.1

Terry, M.P., Heidelbach, F., 2006. Deformation-enhanced metamorphic reactions and the rheology of high-pressure shear zones, Western Gneiss Region, Norway. Journal of Metamorphic Geology, 24, 3–18

Toriumi, M., 1982. Grain boundary migration in olivine at atmospheric pressure. Physics of the Earth and Planetary Interiors 30, 26–35

Trepmann, C.A., Stöckhert, B., 2002. Cataclastic deformation of garnet: a record of synseismic loading and postseismic creep. Journal of Structural Geology, 24, 1845–1856

Van Keken, P.E., Hacker, B.R., Syracuse, E.M., Abers, G.A., 2011. Subduction factory: 4. Depth-dependent flux of H2O from subducting slabs worldwide. Journal of Geophysical Research, 116

Vernon, R.H., 1981. Optical microstructure of partly recrystallized calcite in some naturally deformed marbles. Tectonophysics, 78, 601–612

Wassmann, S., Stöckhert, B., 2013. Low stress deformation of garnet by incongruent dissolution precipitation creep. Journal of Structural Geology. 46, 200–219

Voegelé, V, Cordier, P., Sautter, V., Sharp, T.G., Lardeaux, J.M., Marques, F.O., 1998. Plastic deformation of silicate garnets II. Deformation microstructures in natural samples. Physics of the Earth and Planetary Interiors, 108, 319–338

Yamato, P., Duretz, T., Angiboust, S., 2019. Brittle/Ductile Deformation of Eclogites: Insights From Numerical Models. Geochemistry, Geophysics, Geosystems, 20, 3116–3133

Závada, Prokop, Desbois, G, Schwedt, A., Lexa, O., Urai, J.L., 2012. Extreme ductile deformation of fine-grained salt by coupled solution-precipitation creep and microcracking: Microstructural evidence from perennial Zechstein sequence (Neuhof salt mine, Germany). Journal of Structural Geology, 37, 89–104

CHAPTER 6

Elastic geothermobarometry on zircon in garnet: resetting of a host-inclusion system by fracturing and sealing, and the preservation of metastable inclusions

6.1 Introduction

The petrological and microstructural analysis of garnets from the garnet quartzite in Chapter 4 outlined the heavily fractured nature of the garnet porphyroblasts (Figure 6.1a). The garnet composition linked to the selective garnet replacement as result of fracturing, is the same composition as the outermost retrograde rim. Quartz inclusions in this outer garnet zone support the retrograde nature of both this rim and the fracturing and replacement of garnet. Fractures commonly connect to coesite inclusions (arrow markers in Figure 6.1a), leading to the question of how coesite is preserved during a fracturing event in the quartz stability field and at a high enough temperature for garnet to grow. To approach this issue, zircon inclusions in the same UHPM zone in garnet (Figure 6.1b) are studied with Raman spectroscopy to determine elastic strains and apply elastic geothermobarometry. The expectation is that the fracturing event effectively reset the host-inclusion system, and thus the elastic strains of zircon inclusions should reflect the *P-T* conditions of fracturing. The conditions of this event can also help understand how coesite was preserved despite being exposed to conditions in which it is unstable.

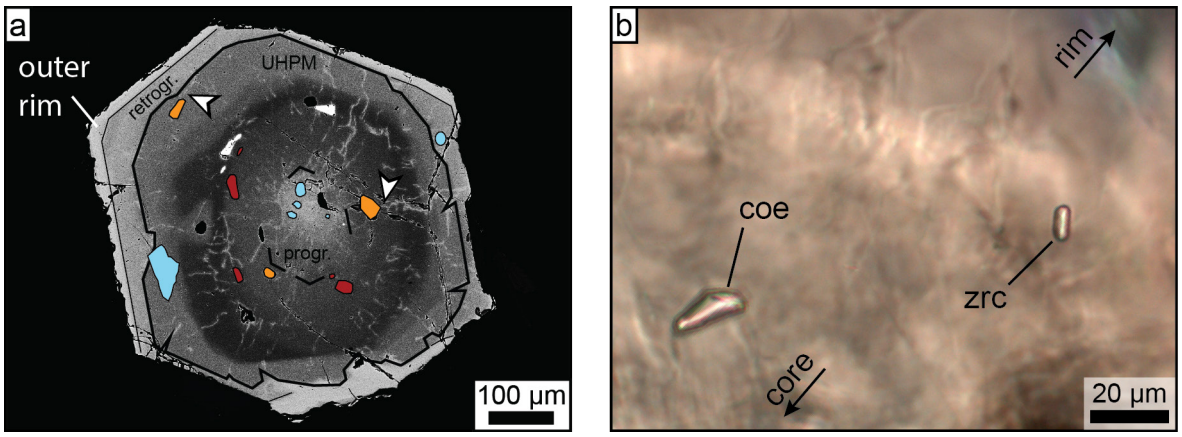

Figure 6.1: (a) BSE image of a garnet from the E5.3.2 quartzite. The locations of quartz (light blue) and coesite (red, orange) within the garnet have been marked. Coesite inclusions marked in orange are at the surface of the section. The arrow markers indicate sealed fractures that connect with coesite inclusions at the surface. An outer rim of the same chemical composition as fracture-sealing garnet is indicated. (b) Micrograph of the mantle of a different garnet from this quartzite, in which inclusions of coesite and zircon are visible. Visible irregularities in the garnet are the result of the sealed fractures. Note the elongated shape of the zircon and slight faceting.

6.2 Results

6.2.1 Data control

To test the suitability of the zircon inclusions, the ω and Full width at half maximum (FWHM) of the 1009 mode for zircon inclusions and the zircon reference crystal are compared (Figure 6.2). Included are the trends established by Campomenosi et al. (2020) of 1) decrease in Raman shift with increasing FWHM as result of metamictization, and 2) increase in Raman shift as result of increasing strain.

The zircon reference crystal yields a range of peak positions of ~1006-1007 cm^{-1} and roughly adheres to trend 1, although well below the limit for the FWHM of 5 cm-1. The buried zircon inclusions consistently yield peak positions of above 1009 cm^{-1}, but trend 1 cannot be clearly distinguished amongst them, although this does not indicate that metamictization has no effect on the position of the 1009 mode. The majority of the inclusions cluster between peak positions

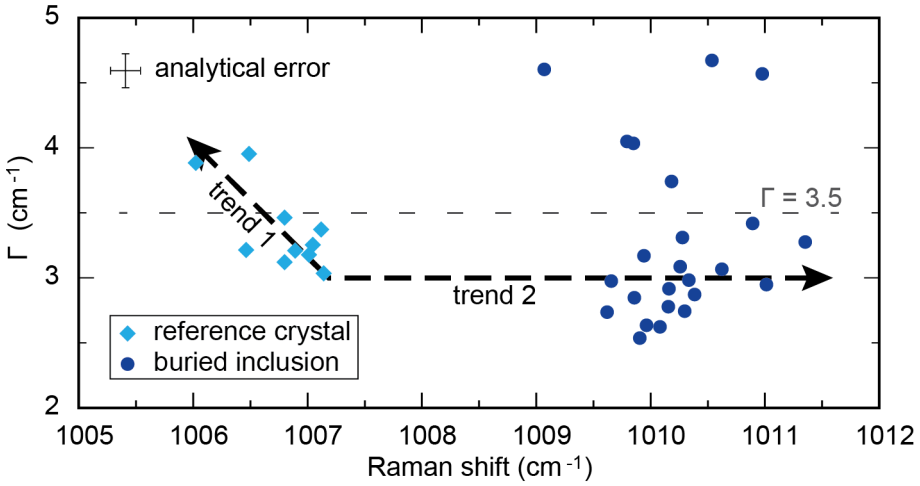

Figure 6.2: Comparison between the peak position and FWHM (*Γ*) of Raman mode B_{1g} (~1009 cm^{-1}) for zircon inclusions and the reference crystal.

Table 6.1: Peak shifts of all studied Raman modes for buried inclusions. Red values are below the propagated analytical error of 0.37 cm^{-1} or have a fitting error above 0.1 cm^{-1}. Two missing values for 213 concern spectra where the 213 peaks were of too low intensity to fit properly.

id	inclusion	201	213	224	356	439	975	1009
1	g996i02	-0.072	0.800	0.236	1.929	0.798	2.344	2.821
2	g996i04	0.142	0.955	0.348	1.256	0.886	2.487	3.107
3	g996i07	-0.053	0.548	0.248	2.188	0.799	2.691	3.166
4	g795i01	-0.166	0.117	-0.164	1.177	2.667	1.338	2.271
5	g795i02	-0.128	0.686	0.124	1.962	0.974	2.499	2.994
6	g717i03	-0.354	0.647	-0.105	1.891	0.614	2.914	3.358
7	g717i04	-0.427	0.672	0.060	2.322	0.660	2.623	3.059
8	g040i02	-0.321	0.608	-0.157	2.195	0.676	2.734	2.987
9	g040i03	-0.277	0.499	-0.078	2.689	0.552	3.006	3.275
10	g077i01	-0.205	0.859	0.162	3.634	1.359	4.488	4.698
11	g096i01	-0.431	0.877	-0.089	3.180	0.911	3.904	4.243
12	g112i01	-0.008		0.229	1.988	1.056	2.894	3.202
13	g212i01	-0.113	0.893	0.133	2.722	0.772	3.258	3.692
14	g425i01	-0.217	1.744	0.177	2.554	1.126	3.200	3.621
15	g302i03	0.202	1.027	0.433	2.198	1.150	2.840	3.273
16	g314i01	0.086	0.987	0.261	2.579	0.754	2.943	3.190
17	g565i01	-0.236	0.919	0.089	2.084	0.968	2.660	3.173
18	g544i01	0.015	1.382	0.506	2.088	1.258	3.079	3.911
19	g548i03	-0.056	0.536	0.116	3.290	0.606	2.817	3.071
20	g548i05	-0.044	0.780	0.366	2.846	0.848	2.663	2.998
21	g591i01	-0.250	0.522	0.004	1.410	1.318	2.648	3.111
22	g668i01	0.080		0.422	1.774	1.907	2.191	3.912
23	g668i02	-0.148	0.698	0.275	2.133	1.399	2.655	3.476
24	g644i01	0.345	1.149	0.514	2.187	1.132	2.893	3.570

of 1009.5 and 1010.5 cm^{-1}, and 2.5 and 3.5 cm^{-1} FWHM. To prevent any possible effect of metamictization within the buried inclusions, all inclusions with a FWHM over 3.5 cm^{-1} were excluded from strain calculations. Fitting errors were normally at least an order of magnitude lower than the instrumental error, unless reported otherwise.

Table 6.1 presents the peak shift of all studied Raman modes of zircon, where all shifts with a fitting error over 0.1 cm^{-1} or an absolute shift lower than the propagated analytical error of 0.37 cm^{-1} are marked (Full data in Appendix C). Only the Raman mode at 356 cm^{-1} consistently overlaps with a peak of the host garnet at a Raman shift of approximately 352 cm^{-1}, resulting in a relatively large fitting error. The Raman modes at approximately 201, 213 and 224 cm^{-1} have a similar issue as they overlap with one another, and their intensity is rather sensitive to the orientation of the zircon crystal. The majority of spectra yield peak shifts of the 201 and 224 modes below the propagated analytical error. The 213 mode also commonly has shifted within the analytical error. None of these issues occur for the 439, 975 and 1009 modes, and the 356 mode only yielded a few problematic measurements due to interference with garnet.

6.2.2 Elastic strains

The state of strain was calculated using EntraPT (Mazzuchelli et al., 2021) for the zircon inclusions that yielded spectra of sufficient quality (Table 6.2; Figure 6.3). Due to the apparent random nature of the 356 mode, the calculations were done using modes 213, 439, 975 and 1009. Calculated values for $\varepsilon_1+\varepsilon_2$ range from -0.0013 to -0.0032, ε_3 ranges from $-6.4*10^{-5}$ to -0.0014. Present-day inclusion pressures for these inclusions are calculated between 0.47 and 0.85 GPa. The majority of inclusions fall within 1σ of strain states corresponding to zircon under hydrostatic stress, and also within isotropic states of strain.

Table 6.2: Strain components with estimated standard deviations, covariance, correlation, χ^2 and inclusion pressure Pinc with estimated standard deviations for all zircon inclusions that were used for strain calculation. Pinc is given in GPa.

Incl.	$\varepsilon_1+\varepsilon_2$	esd	ε_3	esd	Covar	corr%	χ^2	P_{inc}	esd
1	-0.0013	0.0007	-0.00072	0.00047	-3E-07	-94.4	0.05	0.474	0.05
2	-0.0013	0.0007	-0.00089	0.00047	-3E-07	-94.4	0.07	0.512	0.05
3	-0.0020	0.0007	-0.00047	0.00047	-3E-07	-94.4	0.48	0.540	0.05
6	-0.0024	0.0007	-0.00028	0.00047	-3E-07	-94.4	0.28	0.583	0.05
7	-0.0019	0.0007	-0.00042	0.00047	-3E-07	-94.4	0.17	0.526	0.05
8	-0.0021	0.0007	-0.00032	0.00047	-3E-07	-94.4	0.15	0.532	0.05
9	-0.0027	0.0007	-0.00006	0.00047	-3E-07	-94.4	0.33	0.587	0.05
10	-0.0032	0.0007	-0.00062	0.00050	-3E-07	-94.4	1.12	0.851	0.05
11	-0.0031	0.0007	-0.00040	0.00047	-3E-07	-94.4	0.23	0.758	0.05
13	-0.0024	0.0007	-0.00048	0.00047	-3E-07	-94.4	0.1	0.645	0.05
14	-0.0013	0.0007	-0.00135	0.00047	-3E-07	-94.4	0.88	0.628	0.05
15	-0.0013	0.0007	-0.00104	0.00047	-3E-07	-94.4	0.07	0.559	0.05
16	-0.0020	0.0007	-0.00056	0.00047	-3E-07	-94.4	0.02	0.570	0.05
17	-0.0014	0.0007	-0.00087	0.00047	-3E-07	-94.4	0.05	0.534	0.05
18	-0.0013	0.0007	-0.00139	0.00047	-3E-07	-94.4	0.06	0.636	0.05
19	-0.0023	0.0007	-0.00019	0.00047	-3E-07	-94.4	0.23	0.549	0.05
20	-0.0017	0.0007	-0.00063	0.00047	-3E-07	-94.4	0.07	0.522	0.05
24	-0.0014	0.0007	-0.00114	0.00047	-3E-07	-94.4	0.03	0.590	0.05

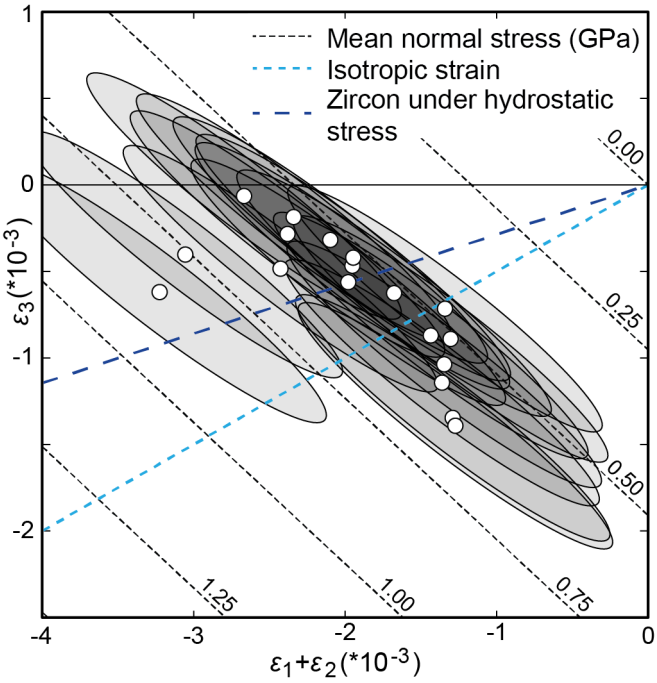

Figure 6.3: Strain diagram of zircon inclusions, comparing $\varepsilon_1+\varepsilon_2$ with ε_3. The 1σ variance-covariance ellipsoids are also provided, and lines of constant mean normal stress including their value in GPa.

6.2.3 P-T results

Isomekes for the zircon inclusions were calculated with EntraPT using two different garnet end-members as host (Figure 6.4). The majority of isomekes per endmember fall in a 100 °C range, similar to the uncertainty of these isomekes. A pyrope host for a zircon inclusion with a certain inclusion pressure Pinc results in an entrapment temperature of approximately 100 °C lower than a zircon inclusion with that same Pinc in a grossular host. As the elastic properties of spessartine fall in between pyrope and grossular (see Chapter 2), the entrapment *P-T* conditions must fall in the range of the highest density of isomekes for both endmembers, which is 450–600 °C at 0 GPa to 830–1000 °C at 3 GPa.

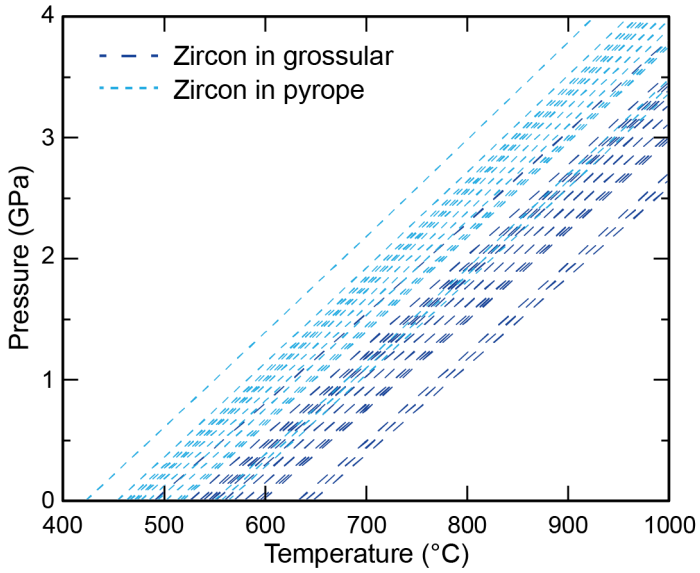

Figure 6.4: Isomekes (lines of constant P_{inc}) for zircon inclusions. Both grossular and pyrope were used and plotted as host garnet composition. The uncertainty on the isomekes is approximately 100 °C.

6.3 Discussion

6.3.1 Elastic strains in zircon inclusions

A total of seven Raman modes were considered for strain calculations (201,213, 224, 356, 439, 975, 1009; Figure 3.2), however only four were used. Modes 201 and 224 exhibit too low shifts in peak position compared to the analytical error to yield any additional value to the other peaks (Table 6.1, and mode 356 suffers from interference with a peak from the host garnet. From the four used modes, strong correlations are found between 213 and 439, and between 975 and 1009. This is the result of the strong similarity of the slope of lines of the same shift in peak position in a $\varepsilon_1+\varepsilon_2$ vs. ε_3 diagram (Figure 3.2).

Zircon inclusions entrapped in pyrope along the retrograde path of the LCU are expected to exhibit ε_3- ε_1 values up to 0.002 near peak *P-T* conditions, down to 0.001 at 1.0 GPa and 500 °C (see Figure 6a of Mazzucchelli et al., 2019). Values of ε_3- ε_1 for the inclusions studied here range from -0.0008 to 0.0013, at an average of 0.0003. Lines of equal ε_3- ε_1 are parallel to the line of isotropic strain in Fiure 6.3, and because of the orientation of the 1σ variance-covariance ellipsoids of the strains, the error on ε_3- ε_1 is large. Although the slope of ε_3- ε_1 compared to isomekes could make it a powerful addition to elastic geothermobarometry, it cannot be used for this purpose due to the uncertainty. Additionally, the average ε_3- ε_1 is low compared to the expected values and therefore the strains may not accurately reflect expected re-entrapment conditions.

Two inclusions yielded Pinc values of > 0.75 GPa, significantly higher than the mean value (Figure 6.3). Metamictization is not responsible for this as any potentially metamict zircons were filtered out using the FWHM analysis using the 1009 peak (Figure 6.2). An explanation for these anomalous inclusion pressures is the presence of soft inclusions within the zircon that were not noticed, and have since entrapment become strained, increasing the inclusion pressure above that for inclusion-free zircon inclusions.

One aspect that was not tested in this study and would provide more certainty on the validity of obtained inclusion pressures, is the composition of the zircon inclusions. The composition of zircon, most notably Hf and REEs, can have a significant effect on its Raman spectrum and can subsequently influence obtained Pinc values if the inclusions compositionally deviate from the reference crystal (Hoskin & Rodgers, 1996; Campomenosi et al., 2020).

6.3.2 *P-T* results

Currently, EntraPT (Mazzucchelli et al., 2021) is only able to perform strain and *P-T* calculations on spherical inclusions, yet the majority of the studied zircon inclusions are elongated (Figure 6.1b). For stiff inclusions in a softer host like zircon in garnet, deviation from a spherical inclusion geometry will result in a higher Pinc (Mazzucchelli et al., 2018). However, as the bulk modulus of zircon and garnet are similar, the Pinc will not deviate much. For a zircon with a long axis five times longer than the other axes, Pinc will be 0.5% higher than a spherical zircon when the c-axis is parallel to the long axis (Mazzucchelli, pers. comm.). As inclusions are commonly slightly faceted (Figure 6.1b), it is a reasonable assumption that the long axis of elongated zircons corresponds to the c-axis (Vavra, 1993; Vavra, 1994). Therefore, the slight elongation of the studied zircon inclusions should not significantly impact the obtained P_{inc} values.

A comparison between isomekes for zircon inclusions and the *P-T* paths for the LCU from literature (Figure 6.5) reveals that the isomekes don't intersect with the exhumation *P-T* path from Van der Klauw et al. (1997). Even the isomekes based on pyrope as host, which yield the lowest temperatures, are generally at least 50 °C higher than the LCU *P-T* path at any point. This means

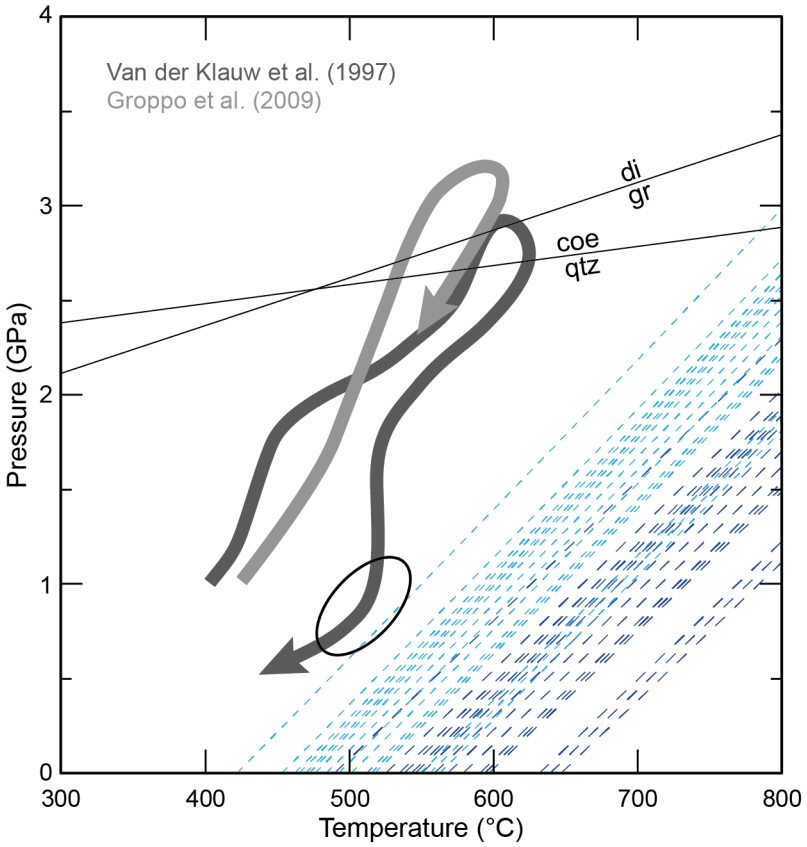

Figure 6.5: Isomekes from zircon inclusions (pyrope host in light blue, grossular host in dark blue) compared to the *P-T* paths for the LCU from literature. Graphite-diamond and quartz-coesite transitions are given for context. The most likely *P-T* range for the resetting of zircon inclusions is circled.

that either the geothermobarometer for zircon in garnet is not calibrated or performed correctly (e.g., inaccurate equations of state or a reference crystal that is too dissimilar to the inclusions) or that the inclusion pressure is higher than expected due to a factor that was not taken into accounted. The garnet that hosts these zircon inclusions is strongly heterogeneous in composition. Local compositional contrasts and therefore variations in unit cell size and elastic properties could result in interferences like coherency strain or what is effectively a garnet-garnet host-inclusion system. The potential effect of these issues on inclusions in garnet has not been studied and no estimate is made regarding if it can significantly affect the inclusion pressure.

From the available evidence and data, the circled area in Figure 6.5 is considered as most likely *P-T* range for fracturing and sealing. First off, the quartz inclusions in the outer garnet rim that corresponds to fracture-sealing garnet indicates conditions in the quartz stability field. The suggested range of *P-T* conditions also requires the least amount of overestimation from the zircon inclusion geothermobarometry. Secondly, mineral inclusions that expand more than their host during exhumation commonly result in radial fracturing of the host surrounding the inclusion (Van der Molen & Van Roermund, 1986; Whitney, 1996). Along this point in the *P-T* path, inclusions entrapped during prograde to peak garnet growth had already built up an inclusion pressure higher than the external pressure, providing a more likely scenario for radial fracturing. As fracture patterns are radial for the whole grain rather than per inclusion, a combined stress field is proposed as driving factor behind fracturing. Finally, at these conditions, the inclusion pressure of coesite inclusions (buffered along the coesite-quartz transition conditions) approaches three times the external pressure, a ratio established by Parkinson (2000) as the point where fracturing of the host garnet occurs.

6.3.3 Coesite preservation

The zircon inclusions investigated here, but also the quartz inclusions in the outermost garnet rim related to sealing of the fractures, suggest that fracture sealing occurred during exhumation at pressures well below the metamorphic pressure peak. Fractures are observed connecting to coesite inclusions, so the coesite was subject to external pressures well within the quartz stability field. If kinetics are the key aspect of coesite breakdown to quartz, a rough number can be applied to the time between fracturing and sealing of garnet. In this case, the rate of dry coesite breakdown at 1.0 GPa and 500 °C is in the order of 10^{-10} ms^{-1}, and changes with roughly three orders of magnitude for every 200 °C in temperature difference (Perrillat et al., 2003). Based on this rate of breakdown, a coesite inclusion of 10 μm diameter should break down in 105 s, or just under 28 hours. The presence of 105 ppm OH within coesite can increase the breakdown rate by more than an order of magnitude compared to dry (10 ppm) coesite (Lathe et al., 2005).

Further investigation is required on the breakdown reaction and the inclusion pressures of coesite to establish the implications of the preservation of the coesite despite exposure to relatively low pressures. Due to the complex crystal symmetry of coesite in comparison to quartz and zircon, it is currently not yet possible to calculate how stress and strain of coesite inclusions in garnet relate, and no Grüneisen tensor is available either.

References

Campomenosi, N., Rubatto, D., Hermann, J., Mihailova, B., Scambelluri, M., Alvaro, M., 2020. Establishing a protocol for the selection of zircon inclusions in garnet for Raman thermobarometry. American Mineralogist 105 992–1001

Hoskin, P.W.O., Rodgers, K.A., 1996. Raman spectral shift in the isomorphous series $(Zr_{1-x}Hf_x)SiO_4$. European Journal of Solid State and Inorganic Chemistry, 33, 1111–1121

Lathe, C., Koch-Müller, M., Wirth, R., Van Westrenen, W., Mueller, H.-J., Schilling, F., Lauterjung, J., 2005. The influence of OH in coesite on the kinetics of the coesite-quartz phase transition. American Mineralogist, 90, 36–43

Mazzucchelli, M.L., Burnley, P., Angel, R.J., Morganti, S., Domeneghetti, M.C., Nestola, F., Alvaro, M., 2018. Elastic geothermobarometry: Corrections for the geometry of the host-inclusion system. Geology, 46(3), 231–234

Mazzucchelli, M.L., Reali, A., Morganti, S., Angel, R.J., Alvaro, M., 2019. Elastic geobarometry for anisotropic inclusions in cubic hosts. Lithos, 350–351, 105281

Mazzucchelli, M.L., Angel, R.J., Alvaro, M., 2021. EntraPT: an online platform for elastic geothermobarometry. American Mineralogist, in press. DOI: https://doi.org/10.2138/am-2021-7693CCBYNCND

Parkinson, C.D., 2000. Coesite inclusions and prograde compositional zonation of garnet in whiteschist of the HP-UHPM Kokchetav massif, Kazakhstan: a record of progressive UHP metamorphism. Lithos, 52, 215–233

Perrillat, J.P., Daniel, I., Lardeaux, J.M., Cardon, H., 2003. Kinetics of the Coesite-Quartz Transition: Application to the Exhumation of Ultrahigh-Pressure Rocks. Journal of Petrology, 44(4), 773–788

Van der Klauw, S.N.G.C., Reinecke, T., Stöckhert, B., 1997. Exhumation of ultrahigh-pressure metamorphic oceanic crust from Lago di Cignana, Piemontese zone, western Alps: the structural record in metabasites. Lithos, 41, 79–102

Vavra, G., 1993. A guide to quantitative morphology of accessory zircon. Chemical Geology, 110, 15–28

Vavra, G., 1994. Systematics of internal zircon morphology in major Variscan granitoid types. Contributions to Mineralogy and Petrology, 117, 331–344

CHAPTER 7

Trace element analysis of garnet and its inclusions: separating contamination from mineral composition

7.1 Introduction

Major element composition of garnet zoning presented in Chapter 4 revealed a spatiotemporal link between garnetite and its quartzite host rock. Intense fluid-rock interaction modified this metasedimentary system that formed a major pathway for external, serpentinite-derived fluids. Most evidence of metamorphic processes and initial bulk chemical composition was overprinted or erased due to the intensity of the fluid-rock interaction, the strong retrograde overprinting on the matrix of the quartzite, and fluid-assisted alteration and recrystallization of garnet. The key to understanding the metamorphic processes and protolith composition lies in the trace elements, notably rare earth elements (REE), within garnet and its inclusions.

This chapter focuses on the trace elements of garnet in quartzite and garnetite, and how we can use those elements to answer several questions about the metamorphic and metasomatic processes that occurred during subduction and exhumation. The link between the two lithologies is studied to test their origin and evolution using REE patterns, and the effect of commonplace contamination by rutile and zircon on the REE concentrations is tested. Furthermore, the composition of contaminant inclusions that are over an order of magnitude smaller than the spot size of LA-ICP-MS is approximated and used for Zr-in-rutile thermometry. I also investigate if the origin of the abundant rutile inclusions is related to the garnet growth mechanism, or if it is related to alteration.

7.2 Background

7.2.1 Trace elements in garnet and rutile

REEs generally occur in garnet in quantities that can be measured by LA-ICP-MS. HREEs (heavy REE) in particular are compatible in garnet, resulting in REE patterns that increase in concentration towards HREEs. Rayleigh fractioning normally results in a decrease of HREE concentration from core to rim in garnet (Hickmott et al., 1987; Otamendi et al., 2002). However, the zoning pattern can deviate from this expectation by the timing of REE release from mineral breakdown (Konrad-Schmolke et al., 2008), and/or limited diffusion (Skora et al., 2006). It is the combination of zoning effects and different compatibility with garnet that results in contrasting ages obtained from Sm/Nd and Lu/Hf geochronology for whole crystal garnet dating (Skora et al., 2009). Another common trend in garnet REE patterns, is the change in slope of the HREE section of this pattern, and eventually the relative decrease in concentration of HREE versus MREE (mid REE; e.g. Konrad-Schmolke et al., 2008; Rubatto et al., 2020). This decrease is defined by the decrease of the ratios YB/Er and Yb/Dy from > 1 in garnet cores to < 1 in garnet rims (Otamendi et al., 2002).

Rutile does not contain measurable REEs, instead incorporating ions with a similar ionic charge (Th, U, Zr, Hf, Sn, Mo) or ionic radius (Fe, V, Cr, Al) as Ti, and several other HFSEs (High field strength elements; Nb, Ta, Sb, W; Zack et al., 2002). When rutile is in equilibrium with zircon and quartz/coesite, its Zr content is controlled by crystallization temperature, providing a reliable geothermometer (Zack et al., 2004; Kohn, 2020).

7.2.2 Petrology of studied garnet

The outcrop studied here is described in detail in Chapter 4; this section builds on the previous description of the host rock and garnetite. An overview of major elements in garnet (Figures 4.7,

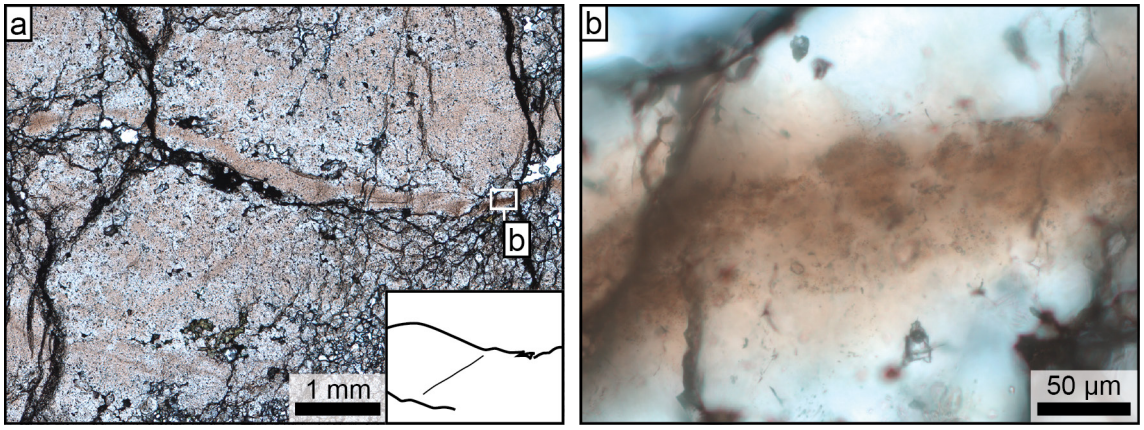

Figure 7.1: Micrographs of host rock and garnetite, taken with plane-polarized transmitted light. (a) Inner garnetite, consisting of "welded" garnets. Darker brown zones are of a finer grainsize and contain more sub-micron rutile inclusions. Location of (b) is given. The inset provides a schematic structure of these zones. (b) Close-up of a fine-grained, rutile-rich zone. The rutile inclusions form a cloud around the centre of the zone.

4.8) highlights the strong similarity of the compositional zonation between the various domains. In the inner garnetite, the garnet core represents a relatively large volume of the entire garnet. The garnet core in all rock domains is strongly affected by a poorly understood type of recrystallization, potentially linked to the recrystallization that is linked to radial fracturing (most visible in Figure 4.7b). All garnet types in this system exhibit a Ti enrichment in the garnet core, as a result of contamination of sub-micron sized rutile inclusions. (Figure 4.9). Within fine-grained zones in the inner garnetite, it appears that these inclusions are enriched in the central part of the zone, giving it a darker brown hue (Figure 7.1). However, the colour of the inner garnetite also varies locally and some patches appear similarly saturated in rutile inclusions as the fine-grained zones (Figure 7.1a).

The metamorphic evolution quartzite-garnetite system (see Chapter 4) was dominated by fluid-rock interaction and subsequent mineral dissolution. Garnet as one of the less soluble minerals was concentrated and underwent pressure solution as crystals came into contact. The fine-grained zones in the inner garnetite are interpreted as internal fluid pathways along which a higher degree of garnet dissolution occurred. Irregularities in compositional zonation in the mantle of garnets in the outer garnetite and host rock is suggested as the result of fluid pulses, inducing phases of garnet dissolution that interrupt the metamorphic growth. Radial fracturing and related alteration and/or crack sealing is a retrograde, late-stage event based on quartz inclusions in the outermost rim (in contrast to coesite in the host-rock garnet mantle) and the cracks cross cutting all other compositional zones.

7.3 Results

7.3.1 Garnet trace elements

Garnets in the host rock exhibit REE patterns with high HREE+Y and low LREE (light REE; Figure 7.2). There is no decrease in HREE+Y from core to rim in host-rock garnet, and the cores contain less MREE (Sm to Tb) than the rims. Yb/Er and Yb/Dy values are < 1 with the exception of several core analyses. Contaminated core analyses (orange open circles in Figure 7.2b) contain higher concentrations of LREE, and a strong positive Ce anomaly. HREE+Y concentrations in host rock garnets are high enough to provide a weak signal for EPMA element distribution mapping (Figure 7.3). A few zones of relatively high Y are observed in the garnet mantle, and a strong Y enrichment is present in the outermost rim. The Y-richer mantle zones coincide with higher concentrations of Mn.

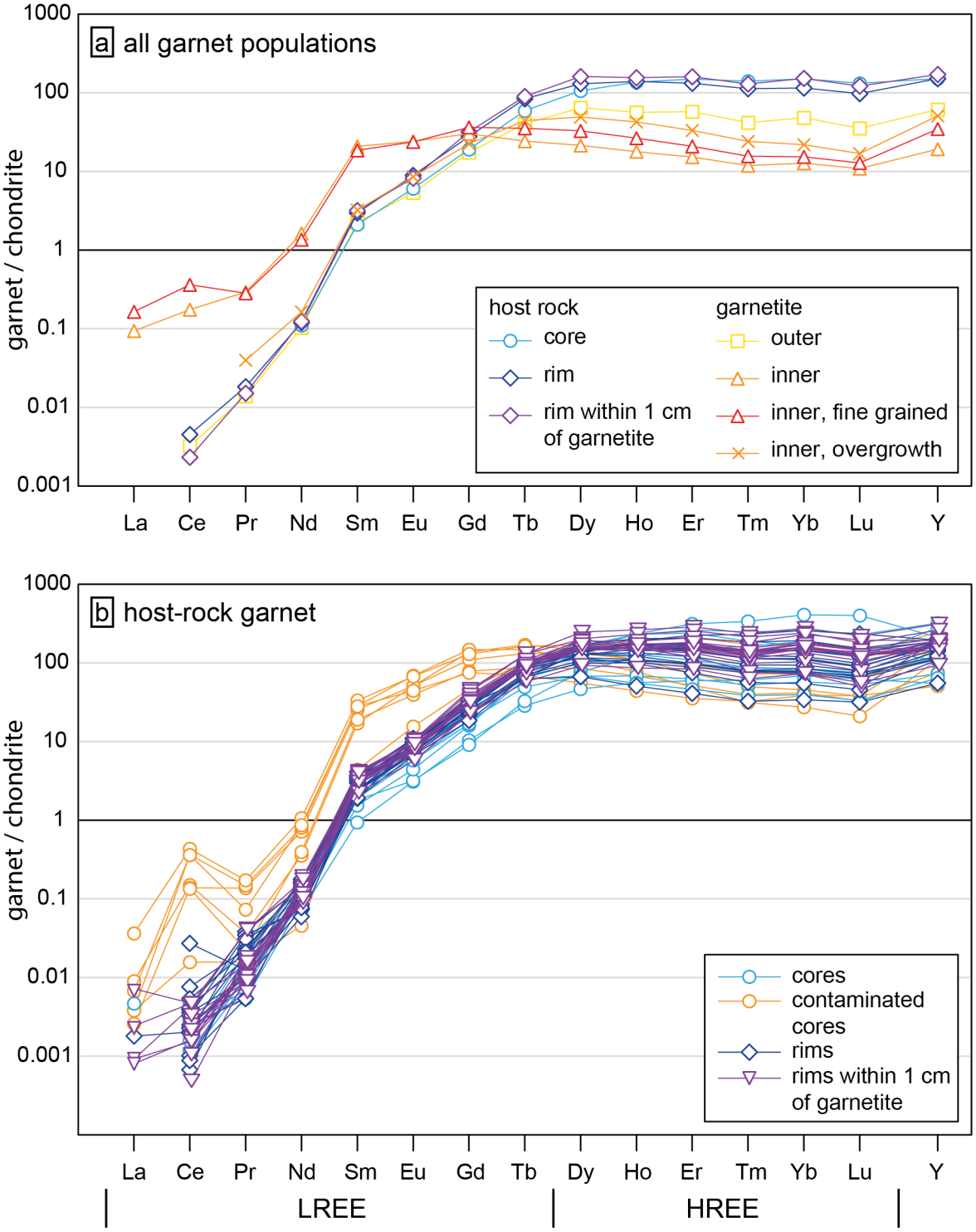

Figure 7.2: Chondrite-normalized REE+Y garnet profiles. (a) Overview of the average composition per analysed garnet population. (b) Individual measurements for the garnet populations from the host rock, including core analyses that are contaminated with rutile. Y is added on the right side of the diagram for comparison to HREEs.

The HREE+Y concentration in garnetite garnets is lower than in host-rock garnets, and given the intermediate concentrations in the outer garnetite, it appears that HREE+Y concentration inversely relates to modal garnet. LREEs up to Gd occur in higher concentrations in the garnetite, and in similar concentrations as contaminated host-rock garnet core analyses. The fine grained zones are slightly richer in La, Ce and HREE+Y compared to the regular inner garnetite. Strongly contaminated garnetite analyses (excluded when contamination could be identified as peak during

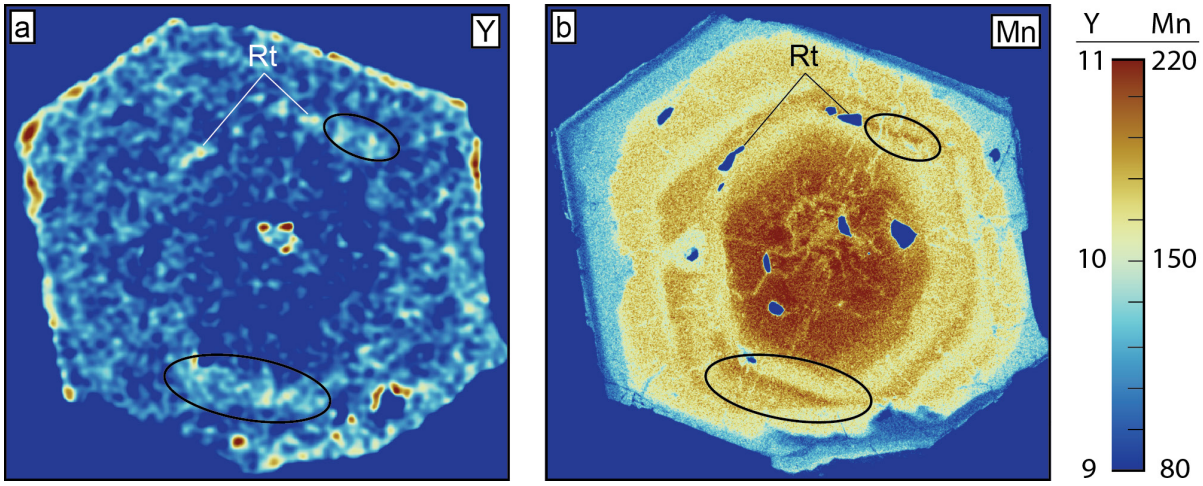

Figure 7.3: Element distribution maps of a garnet from quartzite EC5.3.2, for Y (a) and Mn (b). Smoothing was applied to the Y map. Particularly visible enrichments of Y and Mn that coincide are circled in black. Values plotted are in counts.

the measurement) contain up to 1.8 ppm La and 4.7 ppm Ce. The overgrowth of euhedral garnets on the outer margin of the inner garnetite contains higher concentrations of HREE than the inner garnetite, yet similar LREE as the host rock garnets. Garnets from all analysed rock types exhibit a slight positive Sm anomaly.

7.3.2 Contamination by rutile and zircon inclusions

EPMA element distribution mapping reveals that Ti is mostly enriched in the core of the garnets, and in the majority for the garnets in the case of the inner garnetite (Figure 7.4a–c). In case of the host-rock garnet and outer-garnetite garnet, individual rutile inclusions can be distinguished within a diffuse elevated Ti signal. Within the diffuse Ti-enriched zone, sub-micron inclusions were identified as rutile by Raman spectroscopy. This part of the garnet exhibits a highly irregular compositional zonation, considering zon ing in Mn (Figure 7.4d–f), Mg, and Fe. Ca does not seem strongly affected by this alteration with exception of the inner garnetite (Figure 7.4g–i). In the outer garnetite and in the host rock, the Ti-rich zone corresponds to a euhedrally-shaped Ca-rich zone, which does not always morphologically match the garnet habit (Figure 7.4g).

Practically all analyses on the inner garnetite exhibit some degree of contamination from rutile and/or zircon inclusions (Figure 7.5). Ti concentrations obtained from LA-ICP-MS vary between 47 and 2279 ppm, Zr between 0.2 and 247 ppm. This compares to TiO_2 values in contaminated garnet measured with EPMA of > 0.3 wt%, and > 0.020 ppm assuming incorporation in garnet (see Appendix A). The concentrations of Ti and Zr are a combination of the possible contamination from rutile and zircon, and the Ti and Zr that is accommodated within the garnet. The majority of analyses on host-rock garnet cluster at low concentrations, providing a base line of uncontaminated garnet. Note that the fine-grained inner garnetite contains significantly higher amounts of Zr than the average inner garnetite, and that the overgrowth over the inner garnetite contains Ti and Zr concentrations that fit both the host-rock garnet concentrations and the regular inner garnetite concentrations.

Comparisons of Ti vs. Nb and Zi vs. Hf (Fig. 7.6) should provide examples of how an enrichment of a certain element is the result of contamination, as Nb and Hf are common components of rutile and zircon respectively. Overall, Ti vs. Nb does not follow a fixed ratio as should be the case if the majority of these elements occur within rutile of the same composition throughout the system. Within the analyses of the fine-grained bands within the inner garnetite, the concen-

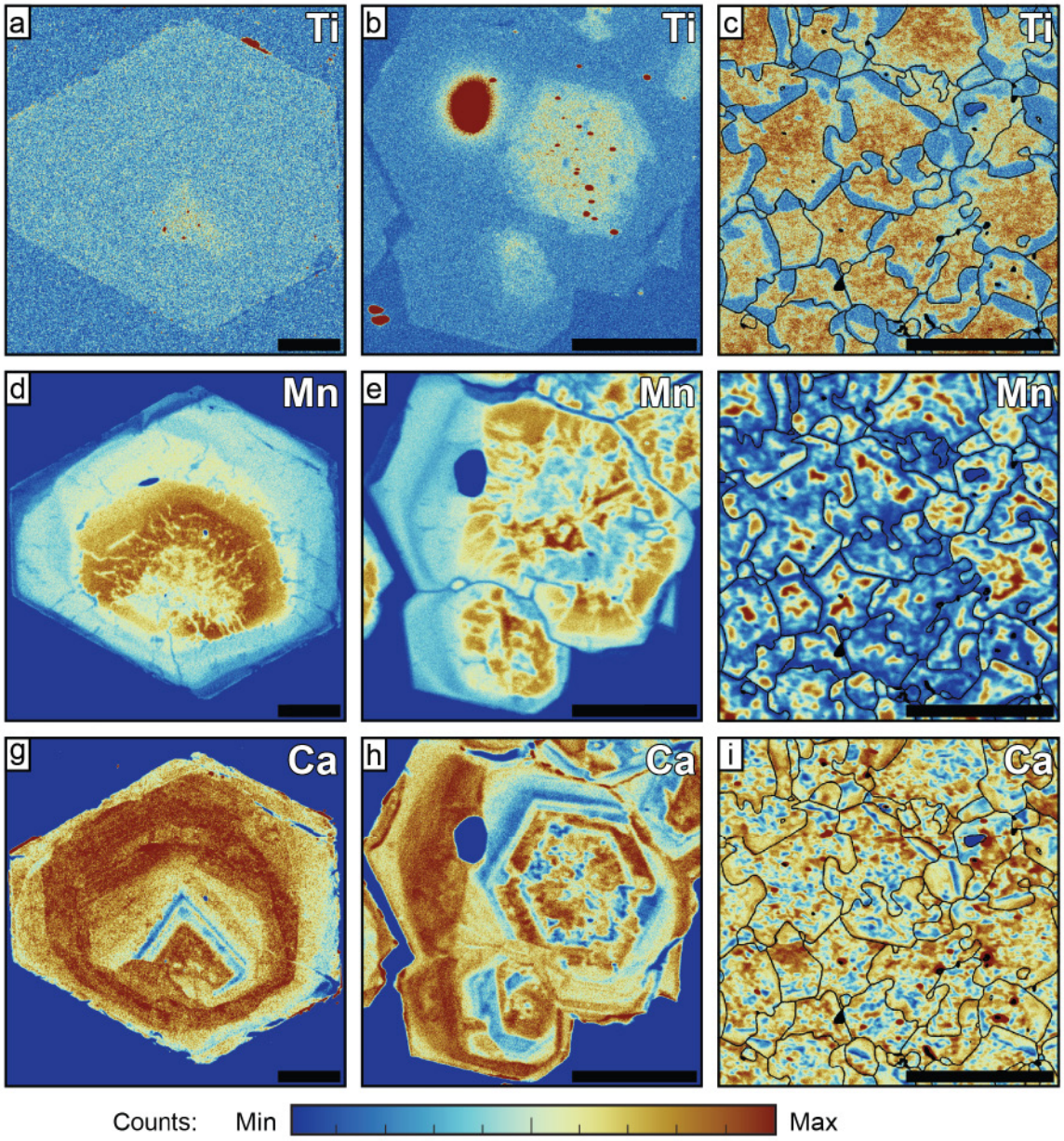

Figure 7.4: EPMA element distribution maps for Ti (a–c), Mn (d–f) and Ca (g–i) of garnet from three different zones: a host-rock garnet (a, d, g), the outer garnetite zone (b, e, h), and inner garnetite (c, f, i), the latter corresponds to Figure 4.7c. Grain boundaries are obtained by EBSD (Chapter 4). Areas that were not indexed are indicated in black. Count intensity is not consistent across the various maps. Black scale bars represent 100 μm.

trations do adhere to this fixed ratio, but not within other datasets of a single garnet population. Rather, Nb concentration increases exponentially with an increase of Ti, a trend that also holds up for Ta. V exhibits an opposite behaviour, as the trend has a shallower slope than lines of an equal ratio. For full analyses including these elements, see Appendix D. Hf in zircon matches the fixed ratio with exception of analyses where both occur in low concentrations, so with a relatively high analytical error.

7.3.3 Inclusion composition: U, Th

Determining the concentration of inclusions within a larger measured area requires knowledge on the composition of the host mineral. Ideally this is achieved by measuring the host without

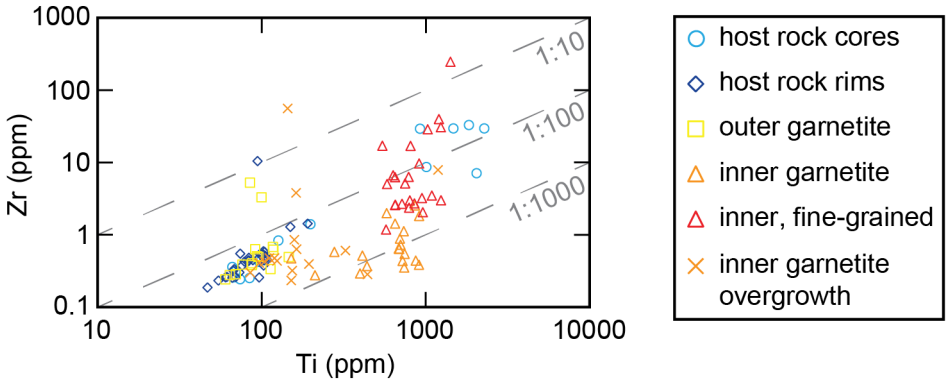

Figure 7.5: Ti vs Zr plot for all garnet analyses, including analyses that were discarded for the REE diagram in Figure 7.xa due to contamination.

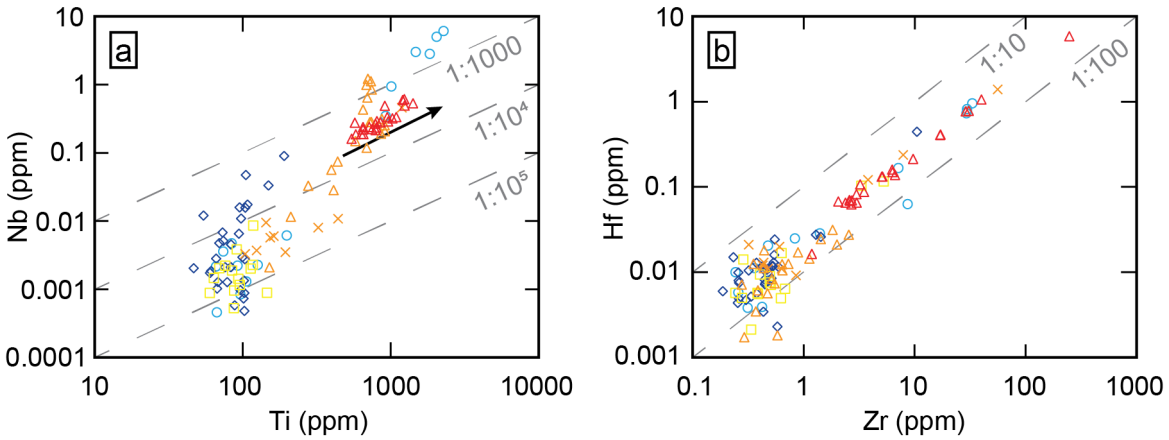

Figure 7.6: Plots of (a) Ti vs. Nb and (b) Zr vs. Hf concentrations. The black arrow in a) indicates the approximate compositional trend within the fine-grained zones of the inner garnetite. See the legend of Figure 7.5. Dashed grey lines correspond to the given Nb:Ti and Hf:Zr ratios.

inclusions. However, in the case of the garnets studied here, all cores contain numerous inclusions and it is not possible to directly measure the uncontaminated garnet. However, if the amount of contamination varies between analyses, it is possible to establish how certain element concentrations relate to known contaminant elements, and obtaining a ratio from the slope of this relation.

U is a complicated element to study in contaminant inclusions, as it can occur in both zircon and rutile (Figure 7.7). Th is also studied, which should be preferentially incorporated into zircon and not in rutile. Th and U exhibit a strong relationship to Zr, as indicated by their linear relationship (Figure 7.7b,d). However, in particular the U vs. Zr concentrations do not follow a fixed ratio. Note the great similarity between Figure 7.7a,c and the Ti vs. Zr diagram of Figure 7.5. The main difference is in the slope at the lower limit of the concentrations, caused by a relationship between the concentrations of Th and U versus Ti from rutile. From the high-Ti end of this slope, the ratios to Ti can be estimated to be 1:106 and 1:105 for Th and U respectively. The higher concentration of U related to rutile is also reflected in the compositional trend that U vs. Zr displays, which exhibits a shallower slope than the fixed ratio. From the high-Zr end of the compositional trends of Th vs. Zr and U vs. Zr, the average ratios to Zr are estimated at 1:100 and 1:500 respectively. Converting these ratios to ppm in rutile and zircon, assuming 99 wt% TiO2 in rutile and 58.3 wt% ZrO2 in zircon, yields concentrations of 0.6 ppm Th and 5.9 ppm U in rutile, and 4300 ppm Th and 860 ppm U in zircon.

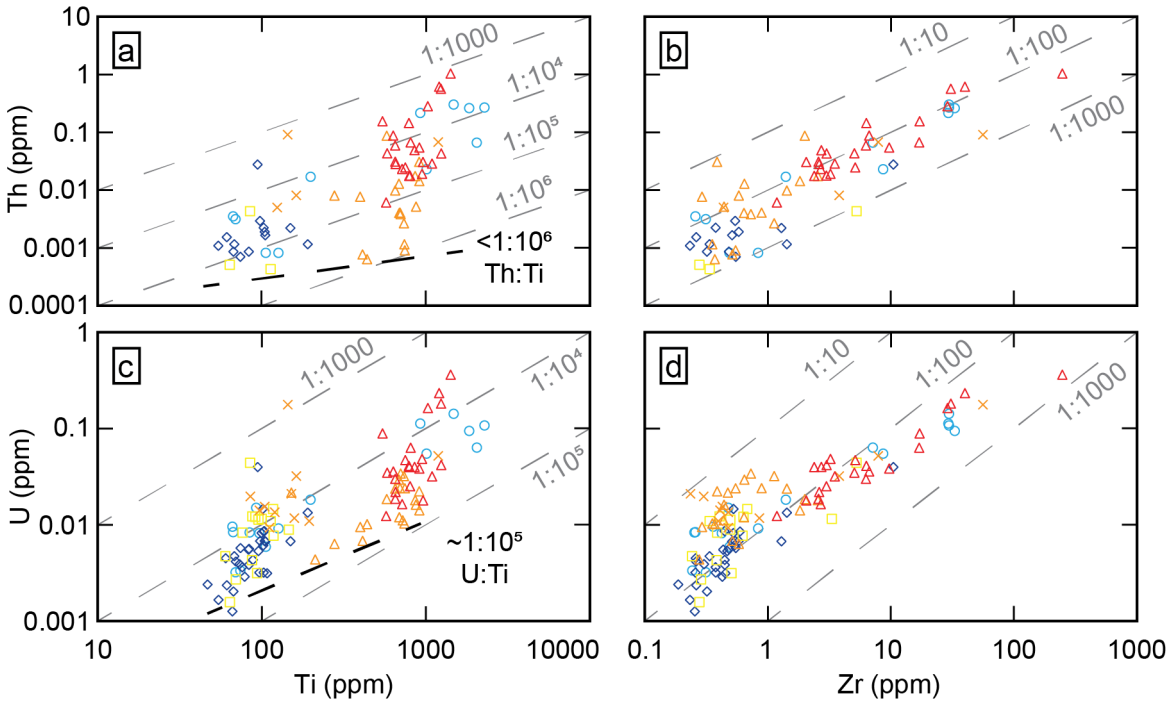

Figure 7.7: Plots of (a) Th vs. Ti, (b) Th vs Zr, (c) Ti vs U, and (d) Zr vs U. Several analyses resulted in Th below the detection limit and are not plotted. See Figure 7.5 for the legend. Dashed grey lines correspond to the given y:x element ratios.

7.3.4 Zr concentration in rutile

The majority of the analyses fall within an envelope defined by two Zr:Ti ratios (Figure 7.8). Inner garnetite measurements mostly plot at or just above the lower ratio, with the exception of fine-grained zones in the inner garnetite. The majority of measurements from the host rock and outer garnetite plot at the higher ratio. The intersection between these ratios indicates the composition where contamination has no effect, and therefore represents an approximation of the garnet composition at 47 ppm Ti and 0.22 ppm Zr. The slopes of the ratios are determined by the range of Zr content in contaminant rutile; any increase in Zr beyond this envelope is the result of zircon contamination. From the ratio of Zr:Ti (1:6000 to 1:125), 98.9 ppm and 4747 ppm Zr in rutile respectively are obtained assuming rutile that is 99 wt% TiO_2.

The garnet analyses span a wide range of apparent Zr-in-rutile concentrations. However a significant part of the higher values are the result of zircon contamination, indicated by Hf exhibiting a linear relationship with Zr (Figure 7.6b). Figure 7.9 compares Hf to Zr/Ti to provide insight in how dependent the Zr concentration in rutile is on zircon contamination. For low Hf values, it is problematic to distinguish between a small volume of zircon and the base concentration of Hf in garnet. Additionally, the error will be relatively large at those concentrations. In general, from Hf > 0.05 ppm, an increase in Zr/Ti appears linked to an increase in Hf. Host-rock garnet analyses also exhibit a rough positive correlation between Zr/Ti and Hf down to Hf = 5 ppb. The analyses from regular inner garnetite and the inner garnetite overgrowth that define the lower ratio of the envelope in Figure 7.8 all fall below Hf = 0.02 ppm. The two analyses from the overgrowth even resulted in Hf below the detection limit (<0.00000 ppm). However, a low amount of 0.01 ppm Hf can even indicate the presence of 0.5 ppm Zr from zircon contamination assuming a 1:50 Hf:Zr ratio (Figure 7.6b), higher than the Zr concentration of the analyses used to define the lower envelope in Figure 7.8. Note that there is no positive trend between Hf concentration and Zr/Ti for these analyses.

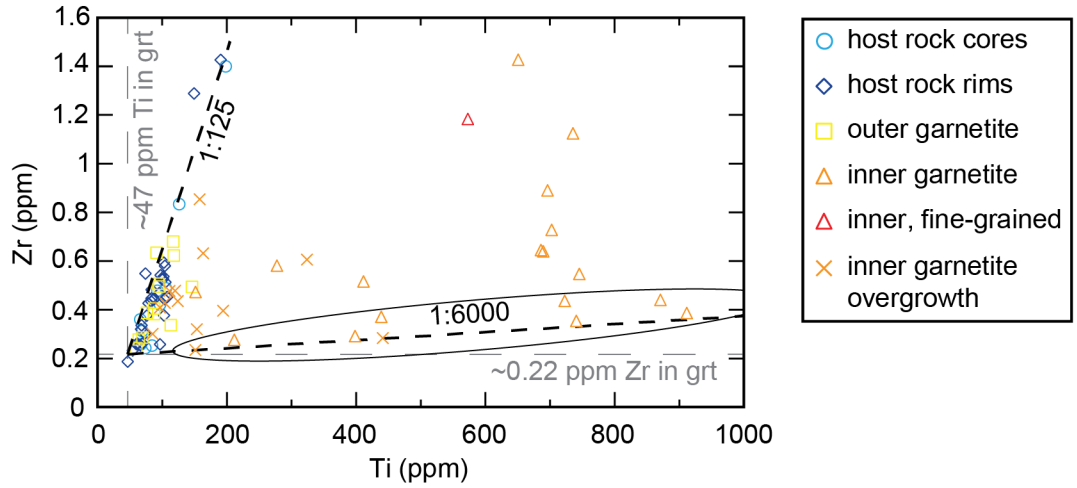

Figure 7.8: Ti vs Zr plot with the estimated Ti and Zr contents of garnet, and the ratios of Zr:Ti that define the envelope within which the majority of the measurements lie. Measurements that define the lower ratio are circled. A linear scale is chosen over logarithmic as only the lower values of the data set are of interest, and these do not span more orders of magnitude than can be displayed properly with a linear scale.

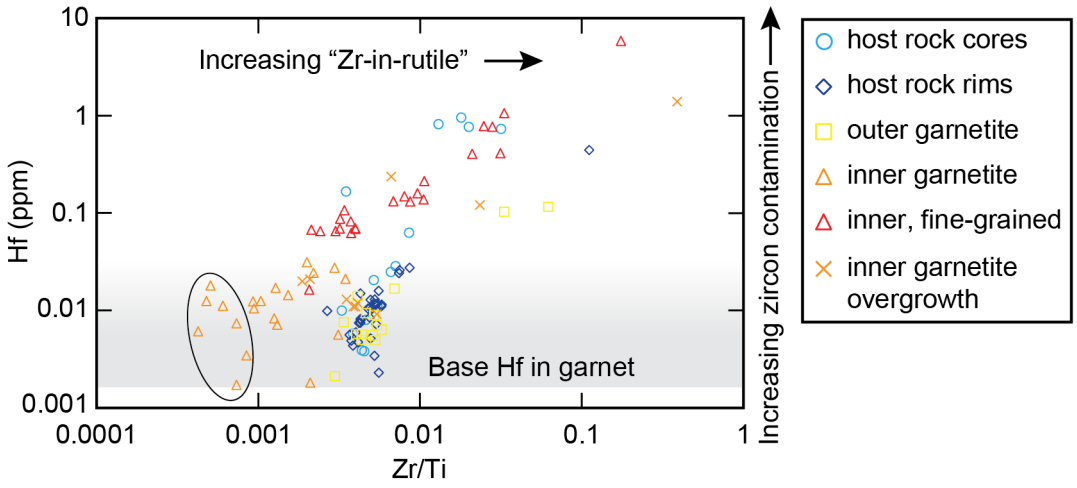

Figure 7.9: Comparison of Zr/Ti vs Hf to understand the effect of zircon contamination on Zr-in-rutile. Circled measurements are the same as are circled in Figure 7.8, except the two analyses of the inner garnetite overgrowth, both of which resulted in below detection limit amounts of Hf.

7.3.5 Reference rutile compositions

To compare calculated concentrations for inclusions, large rutile grains in a different garnetite (C18-3) from the same host rock lithology, and an omphacite vein were also analysed (both from the LCU; see Chapter 8 for the omphacite vein). In this other garnetite, the following concentrations were measured in rutile: Zr from 29.1 to 51.0 ppm; Th from below detection limit to 0.23 ppm; U from 5.66 to 13.8 ppm. In the omphacite vein, the measured concentrations are: Zr from 32.9 to 50.5 ppm; Th from below detection limit to 0.03; U from 0.08 to 0.69. Comparing these concentrations to those obtained from the contaminated analyses suggests that the inclusions are more similar to the large rutile grains in the other garnetite, overlapping the lower range of U yet resulting in higher Th concentrations. The Zr concentrations within the contaminant inclusions are significantly higher than in the large rutile grains.

7.3.6 LREE versus contamination

The inner garnetite and contaminated host-rock garnet core analyses contain higher concentrations of LREE than uncontaminated analyses of host-rock garnet, so to test if this is due to contamination from rutile and zircon, the concentrations of Ti and Zr are compared to Ce and Sm (Figure 7.10). Generally, high Ce and Sm concentrations correspond to high Ti concentrations, whereas high Ce and Sm concentrations can also occur at low Zr concentrations. Note that low Ce and Sm concentrations mostly occur at low Zr. In Ti vs. Sm (Figure 7.10c), it is notable that the fine-grained inner garnetite and host-rock cores behave differently than regular inner garnetite. In the latter, Sm and Ti increase linearly until a Ti of ~900 ppm, where Sm drastically increases (trend 2). In the other two high-Ti domains, the linear trend (1) continues. The correlations exhibited by the other comparisons made in Figure 7.10 are weaker than that of Sm vs. Ti.

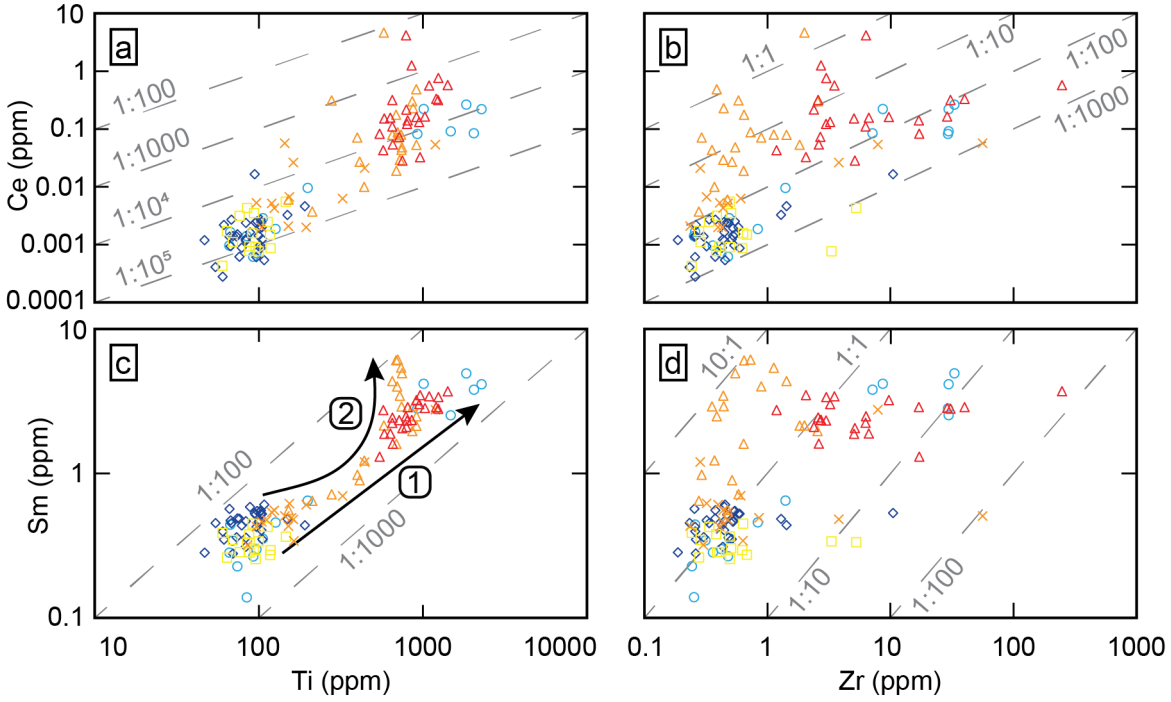

Figure 7.10: Plots of Ce vs (a) Ti and (b) Zr, and Sm vs (c) Ti and (d) Zr. See Figure 7.9 for legend. Dashed grey lines correspond to the given y:x element ratios. Numbered arrows in (c) indicate the trend for 1) fine-grained zones in inner garnetite and contaminated host-rock garnet cores, and 2) regular inner garnetite.

7.4 Discussion

7.4.1 REE behaviour in garnet

REE patterns for uncontaminated host-rock garnets are near identical to those of a high-pressure quartz-phengite schist reported by Spandler et al. (2003), including a slight enrichment in MREE. This enrichment is attributed to the breakdown of MREE-rich titanite to form rutile, which contains no measurable REEs. In contrast with other high pressure garnets (e.g. Konrad-Schmolke et al., 2008; Rubatto et al., 2020), the garnets studied here do not show a significant decrease in HREE from core to rim. The ratios Yb/Er or Yb/Dy proposed by Otamendi et al. (2002), used to test the change in HREE profile slope, only rarely are > 1, and don't fall far below 1 either. Thus, it appears that REE patterns for garnet correspond to a sort of intermediate stage of growth.

The Y-enriched zones in host-rock garnet mantles, suggesting resorption similar to Mn (Figure 4.7a, 7.3, Chapter 4), indicate that Y and the similarly behaving HREEs were redistributed during garnet growth. Given the radial fracturing and subsequent exposure of the inner garnet to fluids (see Chapter 4 for more details), further redistribution of these elements is possible. In this case, fluid-assisted processes involving garnet dissolution and growth played a role in the averaging of garnet profiles between garnet and core, obscuring any HREE fractionation during metamorphic growth.

The HREE pattern slope is the most negative in contaminated host-rock garnet cores, and inner garnetite which is composed mostly of garnet that is equivalent to host-rock cores. Normally this slope becomes more negative as the system evolves further during metamorphic evolution (e.g., Otamendi et al., 2002; Konrad-Schmolke et al., 2008; Rubatto et al., 2020). Finding a REE pattern similar to normally well evolved garnet within the garnet core indicates that the recrystallization that has occurred there also adjusted the REE composition, supporting the fluid-assisted redistribution of elements. However, this argument assumes that the deviation in REE content is not the result of contamination.

The concentration of HREE+Y in garnet decreases with modal garnet content. This is expected when a fixed REE budget is divided over varying amounts of garnet. However, the relative volume within garnet of the recrystallized garnet core is strongly different per zone. Furthermore, localized dissolution occurred preferentially in the garnetite during prograde metamorphism (Chapter 4). Thus, a proper reconstruction of the REE budget for each zone is unfeasible.

7.4.2 Rutile and zircon composition

The concentrations of Th, U, and Zr were approximated for rutile, plus Th and U for zircon, based on contaminated LA-ICP-MS analyses where the majority of the measured volume constituted garnet. The comparison to two populations of large rutile grains in different samples from the LCU results in a reasonable match for U with rutile from a different garnetite. Th and Zr estimated for the contaminant inclusions is higher than concentrations from the large rutile grains. The apparent presence of Th in rutile is unexpected, as it is not an element that is commonly incorporated into rutile (Zack et al., 2002). It is possible that all rutile-contaminated measurements contain a minimum degree of zircon contamination, in which case there are no analyses contaminated by rutile but not by zircon. Concentrations of Th and U are significantly lower in rutile from the omphacite vein, most likely a bulk chemical effect, as the large rutile grains from the reference garnetite and omphacite vein contain similar concentrations of Zr.

7.4.3 Origin of rutile

Several origins of the rutile inclusions are considered: precipitation after re-equilibration of a Ti-richer garnet core (Proyer et al., 2013; Hwang et al., 2019), precipitation from a Ti-mobilizing infiltrating fluid (Scambelluri & Philippot, 2001) during fracturing, or remnants of a Ti-bearing precursor mineral. The euhedral-shaped zone of diffuse Ti-enrichment (most notable in Figure 7.4b) suggests that the presence of Ti is related to garnet growth rather than a post-growth fluid source. There are several candidates for a precursor mineral containing minor Ti, notably mica minerals which commonly incorporate a low concentration of Ti (Chambers & Kohn, 2012). However, the geometry of the Ti-enriched zone being congruent with that of the garnet (Figure 7.4b) poses an issue for this mechanism, and points towards Ti not being inherited.

Interpreting the difference in Ti (and Zr?) concentrations between the hypothetical original garnet core and the Ti-poorer UHPM zone is difficult due to the complex solubility of Ti in

garnet (Ackerson et al., 2017). It is often suggested that Ti is more readily incorporated in garnet at high *P* and/or *T* (Hwang et al., 2019 and references therein). The geological setting of the LCU as Jurassic ophiolite (Rubatto et al., 1998) with no known pre-Alpine metamorphism denies the possibility of a previously unknown precursor garnet that formed at higher *P-T* conditions than during Alpine metamorphism. Additionally, no reports indicate the presence of hydrothermal garnet before subduction metamorphism in hydrothermally Mn-enriched oceanic metasediments such as the likely protolith of the investigated samples (Tumiati et al., 2010). However, there are several substitution mechanisms for Ti, and currently there is no accurate way of calculating its solubility. If Ti concentration in garnet is simply a matter of *P-T* conditions, it is expected that the UHPM zone contains more Ti, especially since it also contains rutile inclusions (Figure 7.4b). Ackerson et al. (2017) suggest that Ti incorporation is correlated with major element composition of garnet, so a Ti-richer core without Ti inherited from a precursor cannot be excluded, and is the most likely scenario of all considered mechanisms.

7.4.4 Zr-in-rutile thermometry

Zr-in-rutile thermometry is applied to the rutile contamination using the calibration of Kohn (2020) for α-quartz and coesite, using the Zr concentration obtained from the lower ratio of the envelope in Figure 7.8 and a pressure range relevant to the LCU of 0 to 3.5 GPa (Figure 7.11). This approach results in temperatures between 500 and 630 ± 15 (2σ) °C. This approach does not take into account the possibility that all rutile contamination occurs alongside a minimum amount of zircon contamination. A second Zr-in-rutile concentration is obtained under the assumption that all Th (1:106 ratio Th:Ti) is the result of zircon contamination (1:100 ratio Th:Zr), and removing the corresponding Zr from the Ti:Zr ratio. This results in a concentration of 40 ppm Zr in rutile using the same method as used for the original concentration, and a corresponding Zr-in-rutile temperature range of 440 to 560 ± 15 (2σ) °C (Figure 7.10). The obtained Zr concentrations in rutile rely on low concentrations in the analyses, however even at these concentrations, the uncertainty is approximately at a σ1 of 10% the concentration. Furthermore, numerous analyses were used to construct both the baseline for Zr in garnet and the ratio if Zr vs. Ti.

The higher temperature results from the contaminant rutile inclusions suggests that the Zr concentration was re-equilibrated during radial fracturing and related garnet recrystallization and re-equilibration, and thus reflect the conditions of resetting rather than the prograde growth *P-T* of the large rutile grains (Figure 7.10). The temperature range between the Zr-in-rutile values with and without zircon contamination correction represents reasonable *P-T* conditions within the metamorphic history of the LCU, covering almost the entire near-isothermal decompression path (Figure 7.10). This range includes the part of the *P-T* path that is suggested as most likely for radial fracturing based on elastic geothermometry on zircon inclusions that were reset as result of the radial fracturing (approx. 1.0 GPa, >500 °C; see Chapter 6).

The validity of the obtained temperatures depends on the activity of a phase of SiO_2. Quartz is identified as inclusion in garnet cores, although its presence is not confirmed for every analysed garnet. The almost ubiquitous occurrence of zircon as contaminant inclusion indicates that equilibrium with zircon occurred, and that the system is at or close to the necessary SiO_2 activity.

The upper values that constrain the envelope in Figure 7.8 result in temperatures exceeding 900 °C. These values involve a high degree of zircon contamination, or come from rutile that was not in equilibrium with SiO_2, leading to a higher Zr concentration and thus a temperature overestimation (Ferry & Watson, 2007). Figure 7.9 uses Hf to demonstrate that zircon contamination is re-

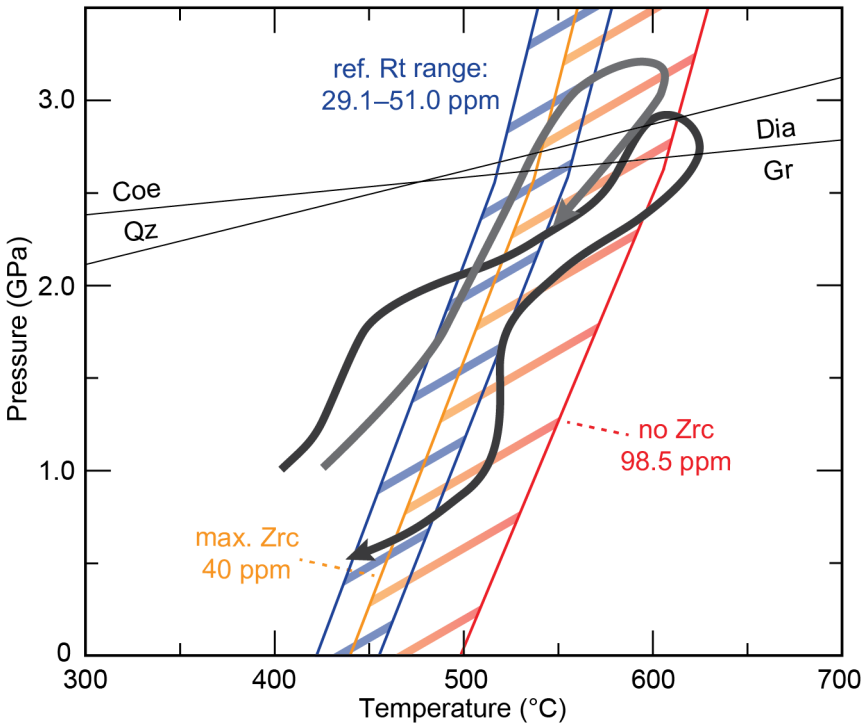

Figure 7.10: results for Zr-in-rutile thermometry based on the calibration of Kohn (2020) using the lower Zr to Ti value of the envelope in Figure 7.8, both without and with correction for possible zircon contamination. These results are compared to the Zr-in-rutile concentrations from large rutile grains in a different garnetite, and *P-T* paths of the LCU (dark grey: Reinecke, 1998; medium grey: Groppo et al., 2009). The upper concentration of 4747 Zr-in-rutile, which assumes no zircon contamination, is not displayed but results in temperatures over 900 °C.

sponsible for high Zr/Ti values, but it is not clear why this contamination is limited by a maximum ratio between Zr and Ti for host-rock garnets (Figure 7.8).

7.4.5 Fine-grained zone in inner garnetite

The visible difference between the regular inner garnetite and the fine-grained zones (Figure 4.6) is the grain size. In Chapter 4, this difference is explained as a grain size reduction by dissolution along preferential fluid pathways within the garnetite. Additionally, the apparent enrichment of rutile in these zones is suggested to be the result of liberation of rutile from dissolved garnet, or the influx of Ti from a fluid. However, the LA-ICP-MS data indicates only a slight enrichment in Ti (Figure 7.5). Zr, La, Ce, HREE+Y are enriched more strongly than Ti in the fine-grained zones. Currently no explanation is found for this behaviour.

7.4.6 Contamination versus fluid enrichment

Based on a lack of strong linear trends for Ce and Sm related to Zr (Figure 7.10b,d), in contrast to what is observed for Hr and Zr (Figure 7.6), the enrichment of LREEs in contaminated analyses is not the result of incorporation in contaminant zircon inclusions. However, the comparison between Ti and Sm yields a remarkable difference between regular inner garnetite and the fine-grained zones (Figure 7.10c). Sm is incompatible with rutile (Zack et al., 2002), and should not result in Sm:Ti ratios of 1:100 to 1:1000. The sudden increase in Sm from Ti > 800 ppm for the regular inner garnetite analyses also indicates that a different mechanism causes this enrichment. Rather, it appears that all garnet of this particular composition is contaminated to such a degree

that uncontaminated analyses are not possible at the used spot size. The abundance of rutile appears to correspond to the volume of recrystallized garnet core within the analysed spot, as this part of the garnet is most strongly affected by recrystallization (Figure 7.4). The LREE could signify the composition of the fluid that assisted this recrystallization, transported into the garnet along fractures. It is unclear why this trend is not as strong with Ce, another element that is enriched in contaminated analyses.

References

Ackerson, M.R., Watson, E.B., Tailby, N.D., Spear, F.S., 2017. Experimental investigation into the substitution mechanisms and solubility of Ti in garnet. American Mineralogist, 102(1), 158–172

Chambers, J.A., Kohn, M.J., 2012. Titanium in muscovite, biotite, and hornblende: Modeling, thermometry, and rutile activities of metapelites and amphibolites. American Mineralogist, 97(4), 543–555

Ferry, J.M., Watson, E.B., 2007. New thermodynamic models and revised calibrations for the Ti-in-zircon and Zr-in-rutile thermometers. Contributions to Mineralogy and Petrology, 154, 429–437 DOI: 10.1007/s00410-007-0201-0

Groppo, C., Beltrando, M., Compagnoni, R., 2009. The *P-T* path of the ultra-high pressure Lago di Cignana and adjoining high-pressure meta-ophiolitic units: insights into the evolution of the subducting Tethyan slab. Journal of Metamorphic Geology, 27, 207–231

Hickmott, D.D., Shimizu, N., Spear, F.S., Selverstone, J., 1987. Trace-element zoning in a metamorphic garnet. Geology, 15, 573–576

Hwang, S.-L., Shen, P., Chu, H.-T., Yui, T.-F., Iizuka, Y., Schertl, H.-P., 2019. Rutile inclusions in garnet from a dissolution-reprecipitation mechanism. Journal of Metamorphic Geology, 37, 1079–1098

Kohn, M. J., 2020. A refined zirconium-in-rutile thermometer. American Mineralogist, 105(6), 963–971

Konrad-Schmolke, M., Zack, T., O'Brien, P.J., Jacob, D.E., 2008. Combined thermodynamic and rare earth element modelling of garnet growth during subduction: Examples from ultrahigh-pressure eclogite of the Western Gneiss Region, Norway. Earth and Planetary Science Letters, 272, 488–498

Otamendi, J.E., De la Rosa, J.D., Patiño Douce, A.E., Castro, A., 2002. Rayleigh fractionation of heavy rare earths and yttrium during metamorphic garnet growth. Geology, 30(2), 159–162

Proyer, A., Habler, G., Abart, R., Wirth, R., Krenn, K., Hoinkes, G., 2013. TiO_2 exsolution from garnet by open-system precipitation: evidence from crystallographic and shape preferred orientation of rutile inclusions. Contributions to Mineralogy an Petrology, 166, 211–234

Reinecke, T. (1998). Prograde high- to ultahigh-pressure metamorphism and exhumation of oceanic sediments at Lago di Cignana, Zermatt-Saas Zone, western Alps. Lithos, 42, 147–189

Rubatto, D., Gebauer, D., Fanning, M., 1998. Jurassic formation and Eocene subduction of the Zermatt-Saas-Fee ophiolites: implications for the geodynamic evolution of the Central and Western Alps. Contributions to Mineralogy and Petrology, 132, 269–287

Rubatto, D., Burger, M., Lanari, P., Hattendorf, B., Schwarz, G., Neff, C., Schmidt, P.K., Hermann, J., Vho, A., Günther, D., 2020. Identification of growth mechanisms in metamorphic garnet by high-resolution trace element mapping with LA-ICP-TOFMS. Contributions to Mineralogy and Petrology, 175:61, https://doi.org/10.1007/s00410-020-01700-5

Scambelluri, M., Philippot, P., 2001. Deep fluids in subduction zones. Lithos. 55, 213–227

Skora, S., Baumgartner, L.P., Mahlen, N.J., Johnson, C.M., Pilet, S., Hellebrand, E., 2006. Diffusion-limited REE uptake by eclogite garnets and its consequences for Lu–Hf and Sm–Nd geochronology. Contributions to Mineralogy and Petrology, 152, 703–720

Skora, S., Lapen, T.J., Baumgartner, L.P., Johnson, C.M., Hellebrand, E., Mahlen, N.J., 2009. The duration of prograde garnet crystallization in the UHP eclogites at Lago di Cignana, Italy. Earth and Planetary Science Letters, 287, 402–411

Spandler, C., Hermann, J., Arculus, R., Mavrogenes, J., 2003. Redistribution of trace elements during prograde metamorphism from lawsonite blueschist to eclogite facies; implications for deep subduction zone processes. Contributions to Mineralogy and Petrology, 146, 205–222

Zack, T., Kronz, A., Foley, S.F., Rivers, T., 2002. Trace element abundances in rutiles from eclogites and associated garnet mica schists. Chemical Geology, 184, 97–122

Zack, T., Moraes, R., Kronz, A., 2004. Temperature dependence of Zr in rutile: empirical calibration of a rutile thermometer. Contributions to Mineralogy and Petrology, 148, 471–488

CHAPTER 8

Increased trace-element migration in crystal-plastically deformed UH*P* rutile: dislocations in low-angle boundaries as high-diffusivity pathways

Abstract

The trace-element composition of rutile is commonly used to constrain *P-T-t* conditions for a wide range of metamorphic systems. Recent studies have highlighted the importance of micro- and nanostructures in the redistribution of trace elements in rutile, high-diffusivity pathways, and dislocation-impurity associations. Deformation of rutile and its effect on composition are studied by combining microstructural and petrological analyses with atom probe tomography on rutile from an omphacite vein of the ultrahigh-pressure metamorphic Lago di Cignana unit (Western Alps, Italy). Zr-in-rutile thermometry and inclusions of quartz in rutile and of coesite in omphacite constrain rutile deformation to around the prograde H*P*-UH*P* boundary at 500–550 °C. Crystal-plastic deformation of a large rutile grain resulted in low-angle boundaries that generate a total misorientation of ~25°. Dislocations constituting the low-angle boundary are enriched in common and uncommon trace elements including Fe and Ca, providing evidence for diffusion of trace elements along the dislocation cores. The role of dislocation microstructures as fast diffusion pathways must be evaluated when applying high-resolution analytical procedures as compositional disturbances might lead to erroneous interpretations.

To be submitted as: Verberne, R., Van Schrojenstein Lantman, H.W., Reddy, S.M., Alvaro, M., Wallis, D., Fougerouse, D., Langone, A., Saxey, D.W., Rickard, W.D.A.: Increased trace-element migration in crystal-plastically deformed UH*P* rutile: dislocations in low-angle boundaries as high-diffusivity pathways.

8.1 Introduction

Rutile is a common accessory mineral formed at mid- to lower-crustal metamorphic conditions (Dachille et al., 1968) and stable in ultra-high temperature (UH*T*) and pressure (UH*P*) environments (Jamieson and Olinger, 1969; Mei et al., 2014; Withers et al., 2003). The trace-element and isotopic compositions of rutile are routinely analysed to constrain the timing and conditions of geological events. Two of the most used applications of rutile composition are U-Pb geochronology (Mezger et al., 1989; Zack et al., 2004b) and Zr-in-rutile thermometry (Kohn, 2020; Zack et al., 2004a). These applications are a significant addition to the traditional options for geothermobarometry and geochronology in the often-restrictive mineral assemblages of UHP metamorphic rocks (Cutts and Smit, 2018; DesOrmeau et al., 2017; Gao et al., 2014; Zack and Luvizotto, 2006). Furthermore, rutile has the capacity to retain information about the *P-T-t* path by preserving mineral and fluid inclusions (Hart et al., 2016; Hart et al., 2018; Ni et al., 2008).

The use of rutile is underpinned by the assumption that the element mobility during subsequent geological events is well understood and inclusions remain shielded from chemical interaction with the host-grain exterior. However, whereas Ti is generally considered immobile in aqueous fluids, its mobility can drastically increase with changes in fluid composition (Antignano and Manning, 2008; Gao et al., 2007; Rapp et al., 2010; Scambelluri and Philippot, 2001) and many studies regularly report disturbances in trace-element distribution and isotopic compositions (Kohn, 2020; Kooijman et al., 2010; Kooijman et al., 2012; Smye and Stockli, 2014; Zhou et al., 2020). These effects have generally been attributed to trace-element migration via volume diffusion. More recently, the presence of twin boundaries, low-angle boundaries (i.e., subgrain boundaries), and high-angle grain boundaries have been proposed to affect the distribution and mobility of trace elements in natural rutile (Moore et al., 2020; Zack and Kooijman, 2017).

The diffusion of trace elements is element-specific and is controlled by the temperature, pressure, fluid activity and type of active diffusion pathway. Volume diffusion in larger rutile grains is ineffective below approximately 600 °C for Pb and 650 °C for Zr (Cherniak, 2000; Cherniak et al., 2007). Grain boundaries form fast pathways for intergranular diffusion (Klinger and Rabkin, 1999), particularly when wetted by a fluid.

Intragranular diffusion can be enhanced beyond volume diffusion through microstructures in the form of dislocation-impurity pair migration (Imai and Sumino, 1983; Petukhov and Klyuchnik, 2012) and high-diffusivity pathways (Love, 1964; Sutton et al., 1995). Trace-element migration by dislocation-impurity associations relies on the coupled migration of dislocations and trace elements trapped in and around them (Imai and Sumino, 1983; Petukhov and Klyuchnik, 2012). This mechanism can lead to removal of trace elements into the grain boundary network. Alternatively, the increasing concentration of solutes can immobilise the migrating dislocation leading to a localised trace element enrichment (Dubosq et al., 2019; Imai and Sumino, 1983; Petukhov and Klyuchnik, 2012). High-diffusivity pathways can form along microstructures related to growth and deformation, such as dislocations, low- and high-angle boundaries, or twin boundaries (Keller et al., 2006; Love, 1964; Plümper et al., 2012; Reddy et al., 2007; Sutton et al., 1995; Timms et al., 2006; Vukmanovic et al., 2014).

Identifying these effects in geological materials has remained challenging due to limitations in the spatial resolutions of techniques capable of measuring chemical and isotopic composition (Reddy et al., 2007; Timms et al., 2006). Advances in analytical techniques allow for correlation between high-spatial resolution chemical and isotopic data with micro- and nanoscale structures. Atom probe tomography (APT) is one such technique with high spatial resolution providing chemical and isotopic information in three dimensions (Gault et al., 2012; Larson et al; 2013). Over the last five years, this technique has proven to be a powerful tool within the field of earth

sciences (Reddy et al., 2020; Saxey et al., 2018). The combination of APT with analytical techniques employing larger spot sizes (e.g. LA-ICP-MS or SIMS) allows for correlation of geochronological data (Peterman et al., 2019; Peterman et al., 2016; Valley et al., 2014; Valley et al., 2015; Seydoux-Guillaume et al., 2019, Verberne et al., 2020). Furthermore, APT can reveal a structural-chemical relationship down to the nanoscale when applied in combination with high-resolution structural imaging techniques like electron backscatter diffraction (EBSD), transmission Kikuchi diffraction (TKD) or transmission electron microscopy (TEM) (Fougerouse et al., 2019; Fougerouse et al., 2018; Kirkland et al., 2018; Montalvo et al., 2019; Piazolo et al., 2016; Reddy et al., 2016; Reddy et al., 2020).

This contribution investigates trace-element migration via dislocations in low-angle boundaries related to the plastic deformation of rutile. The rutile is located within deformed omphacite veins from the UH*P*-low-temperature (L*T*) metamorphic Lago di Cignana unit (LCU). The LCU provides an excellent opportunity for studying the effect of diffusion along dislocations. The minerals were strained during H*P* deformation resulting in dislocation microstructures whilst the low temperatures ensured that volume diffusion was ineffective and thus did not obscure the effect of dislocations. Instead, the structure and properties of the dislocations resulted in the capture of trace elements due to the strain field around the dislocation core (Cottrell and Bilby, 1949) and the changes in inter-atomic spacing and charge state (Kuzmina et al., 2015, and references therein). By the combination of a range of analytical techniques, the study first constrains the growth and deformation history of rutile in relation to *P-T* conditions. Then, micro- and nanoscale analytical techniques are applied to investigate the relation between plastic deformation of rutile and segregation of trace elements. This study highlights the complexity that can arise from the interplay between different structural features, and how these structures correlate with nanoscale chemical heterogeneities. The presence of dislocations will affect the diffusion characteristics along the boundary, which will not necessarily match those as expected by volume diffusion models alone.

8.2 Geological setting and sample description

8.2.1 Geological overview

The Lago di Cignana unit is a lens of UH*P* metabasic and metasedimentary rocks within the Zermatt-Saas unit (ZSU), an ophiolitic nappe of generally H*P*-metamorphic grade (Figure 8.1a). The ZSU was subducted and underwent eclogite-facies metamorphism during the Alpine orogeny (Rubatto et al., 1998), reaching peak metamorphic conditions of 600–630 °C, 2.7–2.9 GPa determined for metasediments (Reinecke, 1998) and 590–605 °C, > 3.2 GPa based on eclogites (Groppo et al., 2009). Subsequently, the LCU was exhumed and juxtaposed with the overlying lower-grade (greenschist-amphibolite facies) Combin zone (Figure 8.1a) (Kirst and Leiss, 2017; Amato et al., 1999; Reddy et al., 2003). As one of few exposed ophiolitic units exhumed after Alpine UH*P* metamorphism, the LCU provides unique insights into fluid-rock interaction at great depth in subduction zones (Frezzotti et al., 2011; Halama et al., 2020; Van Schrojenstein Lantman et al., 2021).

The LCU has been the topic of numerous geochronological studies aimed at pinpointing the timing of formation and subduction of the Piemonte-Ligurian oceanic crust. U-Pb dating of magmatic zircon derived from lithologies within the ZSU resulted in formation ages of the oceanic crust of 164–153 Ma, and metamorphic ages of 44 Ma (Rubatto et al., 1998). Garnet Sm-Nd and Rb-Sr dating yielded ages of 39–42 Ma (Amato et al., 1999; Skora et al., 2015). Rb-Sr white-mica ages of 39–36 Ma for the Combin Fault represent the exhumation leading to emplacement of the ZSU below the Combin Zone, in agreement with rapid exhumation after peak metamorphism (Kirst and Leiss, 2017; Reddy et al., 1999, Reddy et al., 2003).

8.2.2 LCU eclogite

The main lithologies of the LCU are quartzite and schist locally bearing garnetite lenses, calc-schist, marble, and eclogite (Forster et al., 2004). Garnet- and glaucophane-rich zones in the eclogite are suggested to reflect compositional differences due to fluid-rock interaction (Van Schrojenstein Lantman et al., 2021) or related to pillow basalts (Van der Klauw et al., 1997). The peak metamorphic assemblage consists of garnet, omphacite, glaucophane, lawsonite, phengite, rutile and minor coesite and zircon. The latter two are also present as inclusions in omphacite and garnet (Groppo et al., 2009; King et al., 2004). Lawsonite has broken down to pseudomorphs of epidote and paragonite. Titanite, ilmenite, Ca-amphibole, and biotite preserved as inclusions in garnet cores represent an early prograde metamorphic mineral assemblage. The eclogite is rich in TiO_2 (> 2 wt. %), resulting in an abundance of rutile (Groppo et al., 2009). A multitude of veins has been identified in the LCU eclogites, consisting of, for example, omphacite, glaucophane, quartz (potentially after coesite), epidote/clinozoisite and retrogressed lawsonite (Borghini et al., 2015). The relative timings of vein formation range from UH*P* metamorphism to retrograde metamorphic stages during exhumation.

The LCU eclogites were pervasively deformed by dislocation creep of pyroxene with dynamic recrystallisation resulting from grain boundary migration. At the onset of extension, the deformation became localized leading to the formation of shear bands. (Van der Klauw et al., 1997). Little to no deformation took place in the eclogites during the first 40 km of exhumation, down to *P-T* conditions of < 1.5 GPa, 500–550 °C (Van der Klauw et al., 1997). Following this part of exhumation, further deformation within eclogites is associated with a retrograde mineral assemblage of hornblende, albite, and epidote (Kirst and Leiss, 2017).

8.2.3 Sample description

The studied sample, obtained at 45°52'42.5"N 7°35'33.3"E (Figure. 8.1a) is an eclogite cross-cut by a network of omphacite-glaucophane-apatite-rutile veins up to approximately 1 cm in width (Figure 8.1b,c). The omphacite crystals in these veins exhibit a strong shape preferred orientation and are up to 1 mm in length. Apatite and rutile in the veins occur as millimetre-size crystals (Figure 8.1c,d). In contrast, glaucophane rarely exceeds a grain size of a 100 μm. Garnet is only present in the wall rock. Rutile within the wall rock occurs as grains smaller than 100 μm, which is significantly smaller than rutile in the veins. No deformation features in the vein are visible in the hand specimen or thick section.

8.3 Methods

This contribution is a collaboration between the Geoscience Atom Probe group, Curtin University, and University of Pavia, where measurements were performed concurrently. To ensure that the obtained data represent equivalent material, two near-identical thick sections of 100 μm thickness were prepared from the same chip of the hand specimen (Figure 8.1b,c). Work conducted at the University of Pavia focused on multiple grains of a variety of minerals with data acquisition at scales of 1–50 μm, while the complementary work at Curtin University focused on the micro and nanoscale characterisation of a single large rutile crystal (Figure 8.1c,d; 8.2a).

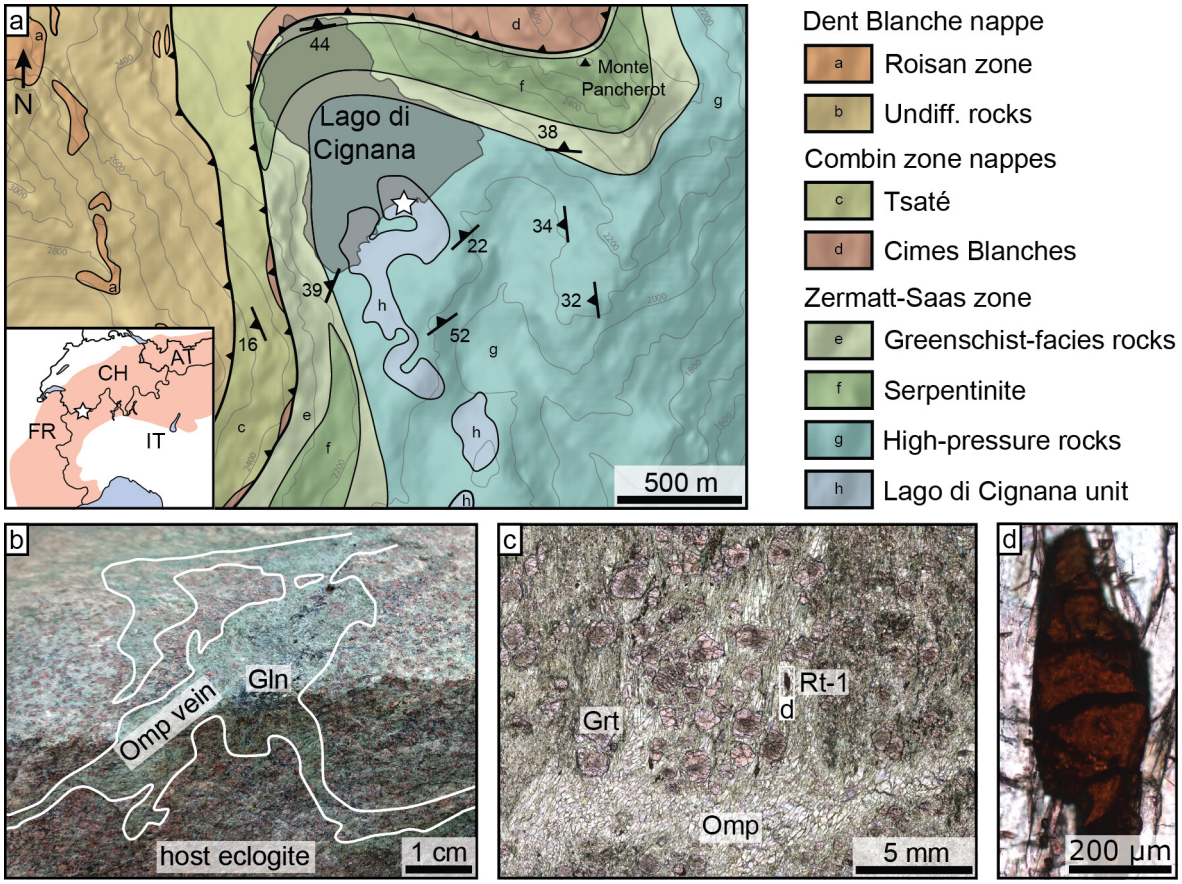

Figure 8.1: (a) Simplified geological map of the sample area around Lago di Cignana, modified after Kirst & Leiss (2017) and references therein. (b) Outcrop photograph of eclogite containing an omphacite-glaucophane vein. (c–d) plain polarized photomicrographs of the thick section analysed at Curtin and the selected rutile for nanoscale analyses (see Figure 8.2). In (c), several large rutile grains are clearly visible as well as the omphacite vein. Rt = rutile, Omp = omphacite, Grt = garnet.

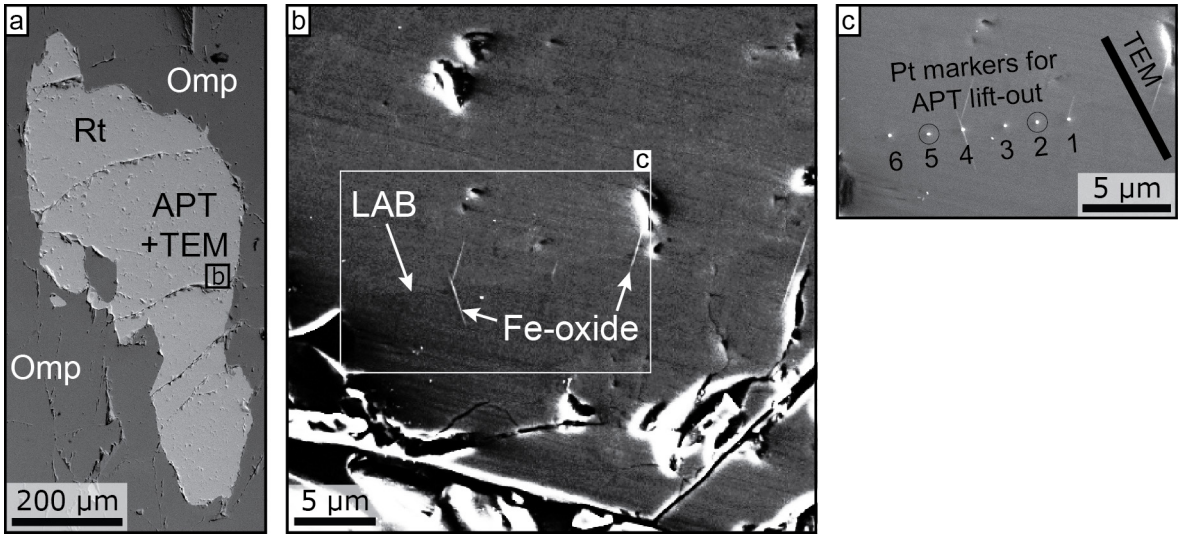

Figure 8.2: (a) Backscatter Electron image of the rutile grain Rt-1 highlighting the APT and TEM lift-out area and showing the rutile grain is completely surrounded by omphacite. (b) close-up secondary electron image of the lift-out site. The low-angle boundary is made visible via the electron tunneling effect. Fe-oxide exsolutions clearly intersect this boundary. (c): Deposited Pt-buttons that assist during the APT specimen preparation. The TEM section was taken to the right-hand side of APT spec. 1.

8.3.1 Raman Spectroscopy

Raman spectroscopy for the purpose of the identification of mineral inclusions was conducted at the University of Pavia using a Horiba LabRam HR Evolution spectrometer with a holographic grating of 1800 grooves/mm. The Horiba is equipped with an Olympus BX41 confocal microscope and operated at a constant temperature of 20 ± 1 °C. Raman spectra were excited using the 514.532 nm line of a solid-state (YAG) laser. The laser power on the sample surface was approximately 1–2 mW. The spectrometer was calibrated by matching the Raman spectrum to the silicon peak at 520.5 cm^{-1}.

8.3.2 LA-ICP-MS

Trace element mineral composition of rutile was determined by laser ablation inductively coupled plasma mass spectrometry (LA-ICP-MS) at the IGG-CNR (Istituto di Geoscienze e Georisorse of the National Research Council) in Pavia. The instrument couples an Excimer Laser 193 nm ArF (GeoLas200 Microlas) with a Triple Quadrupole (8900 QQQ from Agilent). Elements that were measured are: 7Li, 9Be, 11B, 23Na, 25Mg, 27Al, 29Si, 39K, 43Ca, 44Ca, 45Sc, 47Ti, 51V, 53Cr, 55Mn, 57Fe, 59Co, 60Ni, 63Cu, 66Zn, 75As, 85Rb, 88Sr, 89Y, 90Zr, 93Nb, 95Mo, 118Sn, 121Sb, 133Cs, 138Ba, 139La, 140Ce, 141Pr, 146Nd, 149Sm, 151Eu, 157Gd, 159Tb, 163Dy, 165Ho, 167Er, 169Tm, 173Yb, 175Lu, 177Hf, 181Ta, 182W, 208Pb, 232Th and 238U. NIST-SRM610 was used as an external standard, whereas Ti was adopted as an internal standard for rutile. In each analytical run, the USGS reference samples BCR2 and NIST612 (Norman et al., 1996; Pearce et al., 1997; Rocholl et al., 1997) were analysed together with the unknowns for quality control. Precision and accuracy are better than 5% and 10%, respectively. Data reduction was performed using the Glitter software package (Van Achterbergh, 2001). A laser beam, 50 μm in diameter, was employed to analyse 16 spots over six rutile grains, measuring core and rim separately when grain size allowed, and using an average TiO_2 content of 99 wt. % as an internal standard.

8.3.3 Scanning Electron Microscopy

Rutile was characterised by using the TESCAN MIRA3 field-emission scanning electron microscope at the John de Laeter Centre (JdLC), Curtin University, Perth, Australia. BSE images were collected at a working distance of 15 mm and an accelerating voltage of 20 kV. For combined electron backscatter diffraction (EBSD) and energy dispersive x-ray spectroscopy (EDS) imaging the SEM was operated at a working distance of 15 mm with the stage tilted to 70°. An accelerating voltage of 20 kV was applied with a beam intensity of 17, yielding a beam current of 3 nA. EBSD data were acquired at a step size of 1 μm and the match units for rutile (Swope et al., 1995) and omphacite (Oberti and Caporuscio, 1991) were obtained from the American Mineralogist crystallography database (801 448-45x).

Transmission Kikuchi Diffraction (TKD) was performed on the APT specimens to assist with targeting the low-angle boundaries during sample preparation for ATP and to provide correlation with APT data. TKD was performed with a step size of 15 nm and at a working distance of 9 mm, 90° tilt, an accelerating voltage of 30 kV, and a beam intensity of 15, yielding a beam current of 2 nA.

Post-processing of EBSD and TKD data was performed in Matlab®, version R2019a, using the free toolbox MTEX Version 5.3 (Bachmann et al., 2010). Images were plotted using the colourblind friend colourkey of Crameri (2018). Post-processing involved a noise reduction procedure by applying a wildspike correction and removal of 'grains' < 5 pixels. The procedure was followed

by applying a 5x5 pixel Median Filter, part of the MTEX toolbox. The function works similar to a nearest-neighbour extrapolation in for example Channel5. The filter smooths the EBSD data and is designed to preserve subgrain boundaries in the process. Full scripts can be found in supplementary material.

8.3.4 Focussed-Ion-Beam SEM

Specimen preparation for transmission electron microscopy (TEM) and atom probe tomography (APT) was conducted on the Tescan Lyra Ga+ Focused Ion Beam Scanning Electron Microscope (FIB-SEM) (Figure 8.2), which is part of the Advanced Resource Characterization Facility (ARCF) within the JdLC. The FIB-SEM was operated at an accelerating voltage of 30 kV. TEM and APT specimens were extracted from one low-angle boundary in a single grain. The TEM foil was mounted on a copper half-grid and thinned to < 100 nm followed by a 2 kV cleaning routine to remove damage induced by 30 kV specimen preparation. APT specimens were precisely targeted using electron-beam deposited markers and followed by the standard lift-out and sharpening procedures and 2 kV clean up routine (Rickard et al., 2020). TKD imaging ensured the LAB was present close to the apex of the tip after final sample preparation and consequently within the field-of-view for APT analysis. Final secondary electron (SE) imaging was performed in SEM-mode only at a working distance of 6 mm and an accelerating voltage of 10 kV.

8.3.5 Transmission Electron Microscopy

TEM analysis was performed on the FEI Talos FS200X Field Emission Gun TEM equipped with a Super-X EDS detector housed in the John de Laeter Centre, Curtin University, Australia. The TEM was operated at 200 kV. TEM imaging was conducted in both bright- and dark-field (BF and DF) modes. The TEM diffraction investigation was conducted with the assistance of Kikuchi patterns that were generated by convergent beam electron diffraction (CBED). A small spot was used to minimize the beam-related damage to the sample, and the sample was tilted to align a zone axis or meet a two-beam condition to acquire selected area diffraction (SAD) patterns. Both BF and DF TEM imaging were undertaken with the objective apertures after tilting the sample to a diffraction condition within 20°.
Chemical analysis was conducted using the attached two pairs of Super-X detectors. The TEM is fitted with four scanning transmission electron microscopy (S/TEM) detection systems: High Angle Annular Dark Field (HAADF), upper Dark Field (DF4), lower Dark Field (DF2), and Bright Field (BF). The contrast in HAADF images results predominantly from chemical/phase differences and the contrast in BF images results predominantly from orientation differences. The DF4 and DF2 detectors reveal both chemical and orientation contrasts at different angles. TEM, S/TEM, and EDS data acquisition were conducted with the Velox software.

8.3.6 Atom Probe Tomography

APT analyses were performed on a Cameca Local Electrode Atom Probe (LEAP) 4000X HR that is part of the ARCF in the JdlC. The LEAP was operated in laser-assisted mode at a pulse rate of 200 kHz, a laser pulse energy of 50 pJ, a base temperature of 50 K and a detection rate of 0.8% (1600 ions s^{-1}) based on recommendations by Verberne et al. (2019). Five needle-shaped specimens were run in the atom probe yielding 38×106–95×106 ion counts. All specimens remained intact after the run. Post-processing was performed using Cameca's Integrated Visualization and Analysis Software (IVAS) 3.8.0. Peaks in the mass spectra were labelled per individual element for

specific ionization states and ranged with a constant width of 0.2 Da unless clearly resulting in the measurement of background signals. Detailed information about acquisition and post-processing is provided in Appendix E based on Blum et al. (2018). For visualization and compositional analyses, isoconcentration surfaces were computed in 3D using IVAS, with error bars on the proximity histograms given in 1σ) (Hellman et al., 2000).

8.4 RESULTS

8.4.1 Inclusion characterization

The majority of the vein network consists of omphacite, locally containing mineral and fluid inclusions. The identification of inclusions and particularly differentiation between quartz and coesite is limited to Raman spectroscopy as these inclusions are commonly buried below the surface of the section. Coesite, apatite and zircon are found within omphacite, the latter being the most abundant (Figure 8.3a,c,d). Calcite is also present, although only as daughter crystals in primary fluid inclusions. Zircon, omphacite, and rutile were identified as inclusions in garnet. Inclusions hosted in rutile are difficult to identify due to the strong Raman signal of rutile. Nevertheless, quartz inclusions were identified in rutile (Figure 8.3b,d). No radial fractures were observed around these inclusions. Fe-exsolution platelets that are ubiquitous in rutile (Figure 8.3b) could not be identified using Raman spectroscopy.

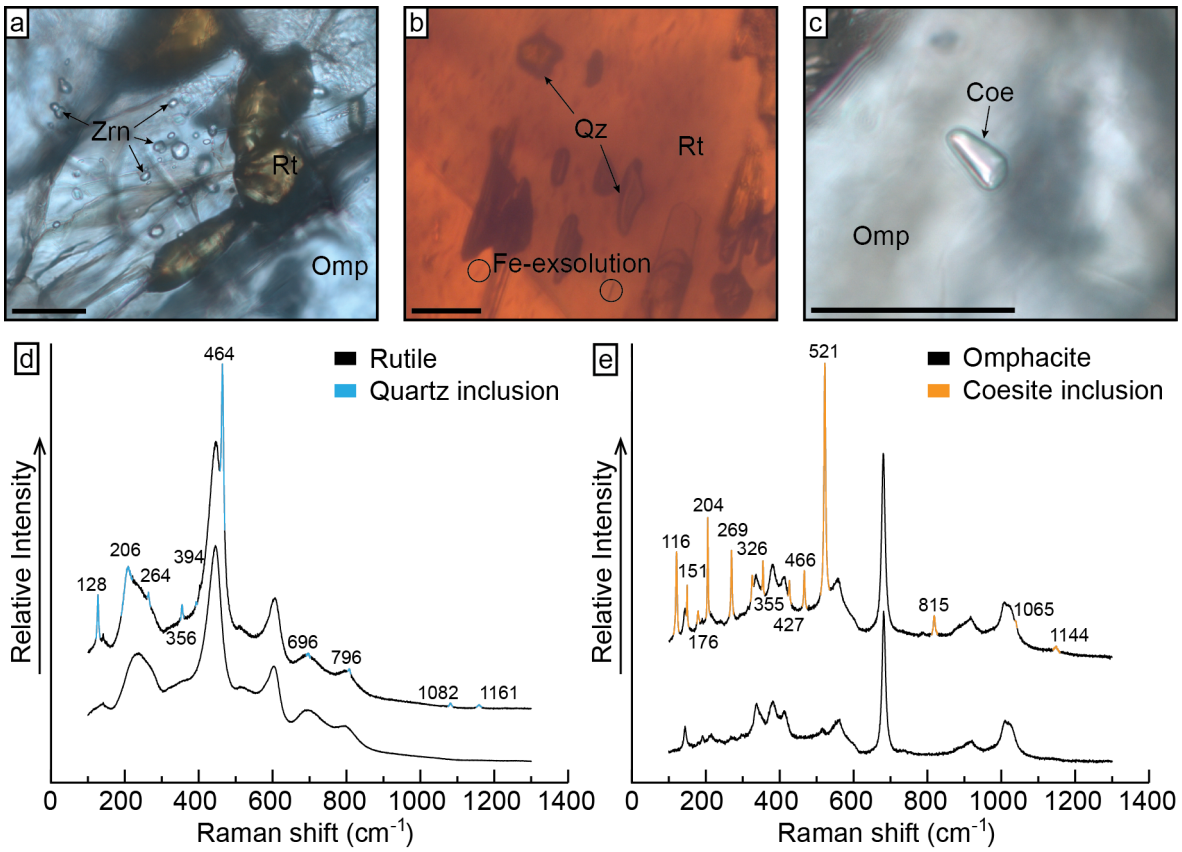

Figure 8.3: (a–c) Optical micrographs revealing the presence of zircon inclusions in omphacite (a), quartz and Fe-rich inclusions in rutile (b), and coesite in omphacite. Scale bars indicate 50 µm. (d–e) Representative Raman spectra confirming the presence of quartz in rutile (d) and coesite in omphacite (e). Peaks belonging to quartz and coesite respectively have been marked within the spectra. Zrn = zircon, Omp = omphacite, Rt = rutile, Qz = quartz, Coe = coesite.

8.4.2 Rutile geochemistry

Table 1 presents representative measurements and average compositions for rutile. Additionally, the concentrations of all elements in rutile that consistently yielded concentrations above the detection limit are displayed in Figure 8.4a. Measured Zr concentrations in rutile, taking into account 1σ, are in the range of 31.47 to 52.55 ppm. Most rutile cores contain higher Zr concentrations than their respective rims, and overall differences in Zr concentration exist between grains beyond the uncertainty of the measurements As a result, the Zr-in-rutile thermometry does not result in a single temperature. Using the full range of Zr concentrations including analytical uncertainty, Zr-in-rutile thermometry results in a range of 500–550 ± 15 (2σ) °C based on the pressure-sensitive thermometer of Kohn (2020) using the "combined" calibration for quartz and coesite (Figure 8.4b).

8.4.3 Structural analysis of rutile

The various substructures within rutile are characterized by different analytical techniques. The images in Figure 8.2b,c reveal a low-angle boundary due to subtle orientation-contrast effects and show the presence of Fe-rich exsolution platelets crosscutting the low-angle boundary. These thin, Fe-rich platelets are visible throughout the entire grain and have apparent acute angles of 35° between two platelets, intersecting the LAB at apparent angles of 69° and 78° in Figure 8.2b,c. Note that the images only show the 2D geometry and therefore the apparent angles likely deviate from the true angles. Furthermore, the direction of the LAB varies slightly along its length so that the angular relationships are not constant. Other rutile grains within the section also contain Fe-rich platelets, yielding two different orientations although intersecting at different apparent angles.

The EBSD maps reveal that rutile, present within the omphacite vein, is deformed (Figure 8.5a). However, the extent of deformation within the omphacite is harder to resolve. The omphacite vein displays a strong shape preferred orientation (SPO) (Figure 8.1c).

Rutile exhibits a total misorientation of approximately 25° (Figure 8.5b) across the grain, which results from the presence of low-angle boundaries (LABs). The individual LABs have misorientation angles of up to 2° (Figure 8.5b,d). The most common misorientation axis is <100> (Figure 8.5c,e). However, the misorientation shows a dispersion in two directions in the pole figures (Figure 8.6). On the (001) pole figure the data points spread about ~18° in the longitudinal direction and ~9° in the latitudinal direction. This is indicative of more than one active operating slip system. TKD maps of the APT specimens revealed that two specimens contain LABs with a dip of approximately 60° relative to the surface of the thin section (Figure 8.5d). The two specimens come from the same crystal approximately 5 μm apart, however the boundary dip in opposite directions.

8.4.4 Nanoscale structure and composition

The TEM HAADF and dark-field images indicate that the LAB is composed of approximately parallel dislocations aligned along the boundaries (Figure 8.7b,c). The separation of two dislocations varies in the range of ~5–35 nm (Figure 8.7c,d). The LABs are not planar, but instead exhibit an irregular pattern and are offset by ~10 nm steps (Figure 8.7b, white arrow).

The interactions and overlaps between different features in the TEM image complicate the extraction of all information captured within a single frame. The APT data yields the same level of complexity with overlapping dislocations. However, the 3D digital reconstruction allows for clearer visualization and separation based on chemical heterogeneities.

Table 8.1: Six representative LA-ICP-MS analyses of rutile and the average of all measurements (see Appendix D Table D7 for full data set, errors, and detection limits). Measurements below detection limit were not taken into account for the calculation of average values. B.D.L. = below detection limit.

Element	*1.3 (core)*	*2.1 (rim)*	*3.2 (rim)*	*4.1 (rim)*	*6.3 (rim)*	*8.2 (core)*	*Average*
	006SMPL	008SMPL	012SMPL	013SMPL	017SMPL	019SMPL	
Li7	B.D.L.	B.D.L.	B.D.L.	B.D.L.	B.D.L.	B.D.L.	
Be9	B.D.L.	B.D.L.	B.D.L.	B.D.L.	B.D.L.	B.D.L.	
B11	14.49	20.88	14.64	9.6	13.32	15.2	16.0
Na23	9.41	10.9	11.26	11.05	13.19	11.37	11.0
Mg25	116.55	106.91	104.67	108.21	112.32	107.46	107.9
Al27	54.56	27.17	50.87	70.31	107.75	28.6	60.5
Si29	2270.42	1428.97	1334.5	1680.39	1828.16	1472.15	1736.4
K39	14.6	6.91	B.D.L.	B.D.L.	B.D.L.	B.D.L.	11.9
Ca43	B.D.L.	B.D.L.	B.D.L.	B.D.L.	B.D.L.	B.D.L.	
Ca44	B.D.L.	B.D.L.	46.44	B.D.L.	B.D.L.	77.14	58.6
Sc45	0.744	0.483	0.555	0.651	0.21	0.787	0.6
V51	1138.59	1066.48	1029.4	936.02	965.48	1045.44	1043.2
Cr53	200.65	259.59	297.71	244.83	205.25	217.37	233.0
Mn55	B.D.L.	1.08	B.D.L.	B.D.L.	B.D.L.	B.D.L.	1.0
Fe57	5923.42	6143.26	5050.25	6477.72	5357.42	7015.43	6056.3
Co59	B.D.L.	B.D.L.	0.0104	B.D.L.	B.D.L.	B.D.L.	0.0
Ni60	0.095	0.118	B.D.L.	0.14	B.D.L.	B.D.L.	0.1
Cu63	4.79	5.75	4.07	3.81	4.01	3.26	4.5
Zn66	32.03	32.43	26.22	22.97	22.39	21.23	27.6
As75	B.D.L.	B.D.L.	B.D.L.	B.D.L.	B.D.L.	B.D.L.	
Rb85	B.D.L.	B.D.L.	B.D.L.	B.D.L.	B.D.L.	B.D.L.	
Sr88	1.971	2.11	B.D.L.	1.826	1.81	1.684	1.9
Y89	0.147	0.212	0.131	0.154	0.128	0.127	0.2
Zr90	50.45	32.94	40.66	37.81	49.86	44	41.7
Nb93	280.92	298.94	292.25	299.37	268.81	281.15	285.7
Mo95	10.78	7.07	8.84	8.07	9.72	9.57	8.9
Sn118	58.73	51.54	65.29	53.62	56.23	54.97	56.9
Sb121	1.23	0.9	1.47	1.09	0.99	1.24	1.2
Cs133	B.D.L.	B.D.L.	B.D.L.	B.D.L.	B.D.L.	B.D.L.	
Ba138	0.0027	0.45	B.D.L.	0.0097	B.D.L.	0.0112	0.1
La139	B.D.L.	B.D.L.	B.D.L.	B.D.L.	B.D.L.	0.0031	0.0
Ce140	B.D.L.	0.0123	0.0214	0.0027	0.0062	0.0093	0.0
Pr141	0.0019	B.D.L.	0.0025	B.D.L.	B.D.L.	0.0026	0.0
Nd146	B.D.L.	B.D.L.	0.014	B.D.L.	B.D.L.	B.D.L.	0.0
Sm149	B.D.L.	B.D.L.	B.D.L.	B.D.L.	B.D.L.	B.D.L.	
Eu151	B.D.L.	B.D.L.	B.D.L.	B.D.L.	B.D.L.	B.D.L.	
Gd157	B.D.L.	0.033	B.D.L.	B.D.L.	B.D.L.	B.D.L.	0.0
Tb159	0.002	0.011	0.0028	B.D.L.	B.D.L.	0.0029	0.0
Dy163	B.D.L.	B.D.L.	B.D.L.	0.0099	B.D.L.	0.012	0.0
Ho165	B.D.L.	0.0116	B.D.L.	B.D.L.	B.D.L.	B.D.L.	0.0
Er167	0.0086	B.D.L.	B.D.L.	0.021	B.D.L.	B.D.L.	0.0

Table 8.1 (cont.):

Element	*1.3 (core)*	*2.1 (rim)*	*3.2 (rim)*	*4.1 (rim)*	*6.3 (rim)*	*8.2 (core)*	*Average*
Tm169	B.D.L.	B.D.L.	B.D.L.	B.D.L.	B.D.L.	B.D.L.	
Yb173	B.D.L.	B.D.L.	B.D.L.	B.D.L.	B.D.L.	0.037	0.0
Lu175	0.0022	B.D.L.	B.D.L.	0.0027	B.D.L.	0.0032	0.0
Hf177	2.15	1.77	2.1	1.58	2.28	1.82	1.9
Ta181	16.2	17.44	17.21	17.08	15.18	16.22	16.5
W182	3.36	3.4	2.69	2.83	2.76	2.5	2.8
Pb208	B.D.L.	B.D.L.	B.D.L.	B.D.L.	0.068	0.02	0.1
Th232	B.D.L.	0.023	B.D.L.	B.D.L.	B.D.L.	0.018	0.0
U238	0.513	0.35	0.309	0.08	0.347	0.689	0.3

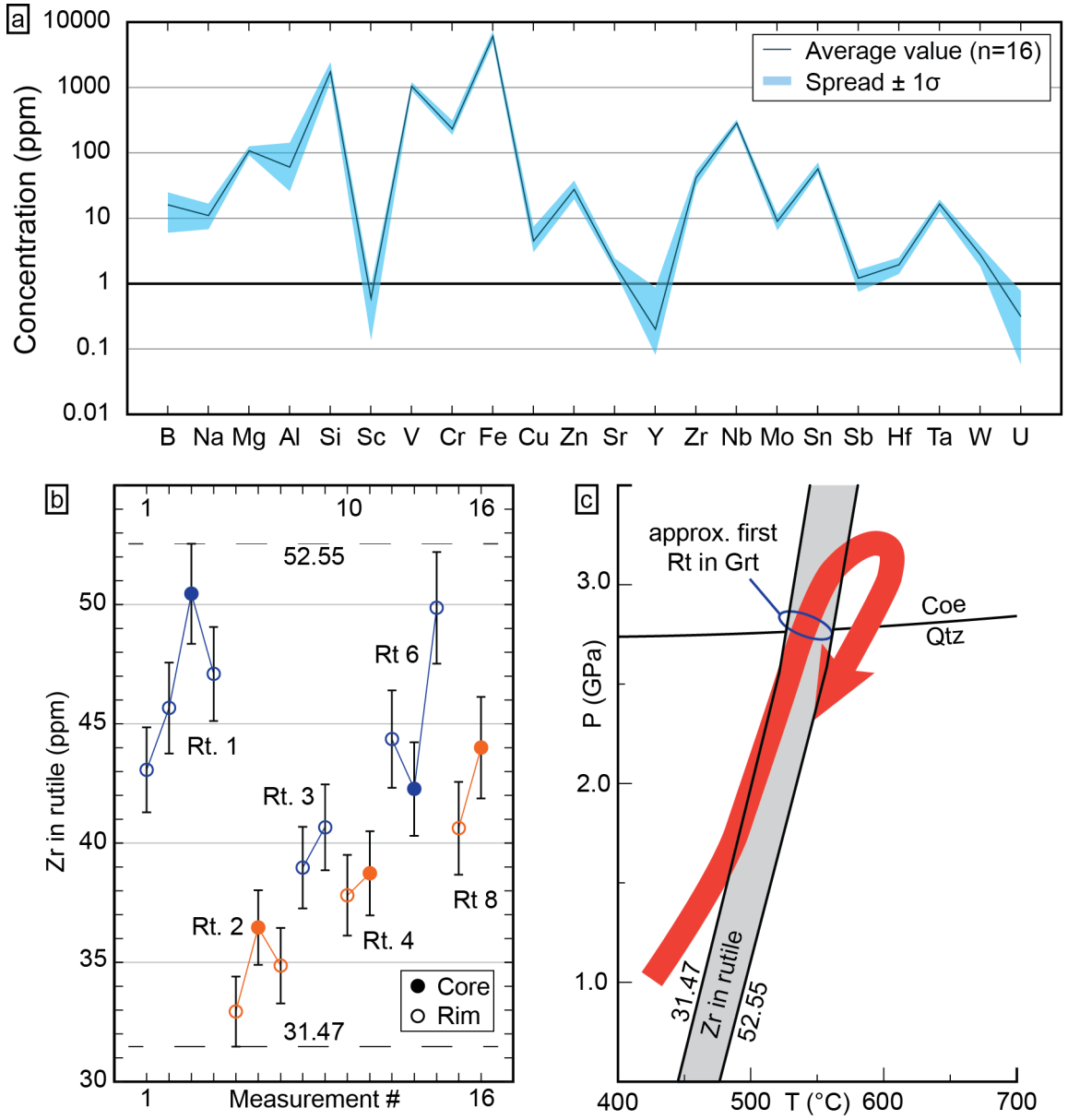

Figure 8.4: (a) Spider diagram of elements measured with LA-ICP-MS, showing the weighted average as a solid line. (b) Detailed diagram for all measured Zr concentrations in rutile. (c) *P-T* diagram illustrating the metamorphic history after Groppo et al. (2009), and how it compares to Zr-in-rutile thermometry for the range of concentrations in (b).

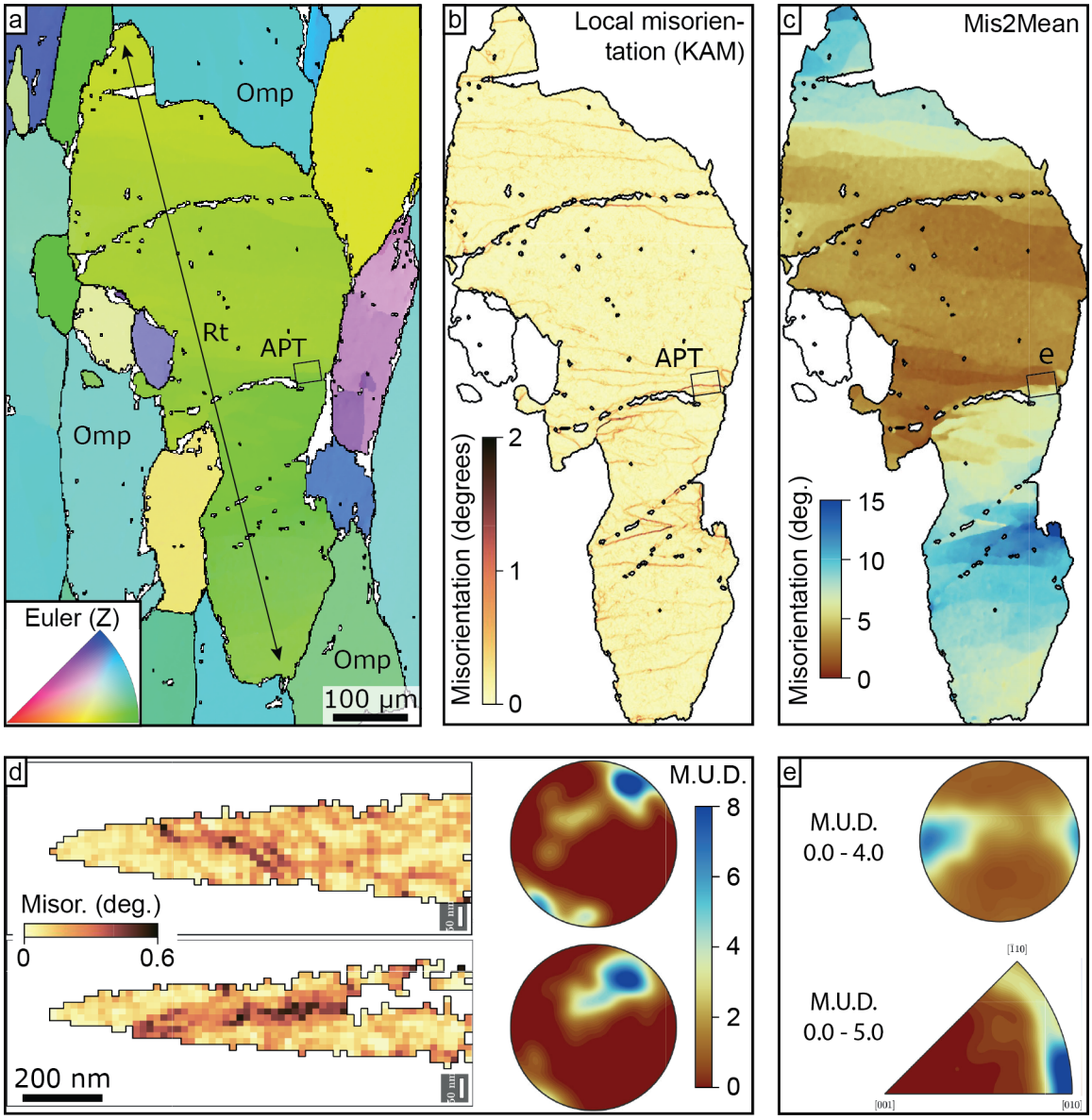

Figure 8.5: (a) EBSD Euler map showing the orientation of rutile and omphacite crystals. (b) EBSD local misorientation map for the same rutile grain as in (a). (c) Map of the rutile grain coloured by the misorientation per pixel relative to the mean orientation. (d) TKD local misorientation maps for two APT specimens taken from the area marked "APT" in (b), revealing the low-angle boundary. (e) Misorientation pole figure (top) and misorientation axes in the crystal reference frame (bottom) for the area marked in (b–c).

As expected from the TKD maps, of the five specimens analysed, two contained a LAB within the field of view. These two specimens, M2 and M5 (Figure 8.2c), are hereafter referred to as Specimen 1 and Specimen 2, respectively. The 3D reconstructions of Specimen 1 (Figure 8.8a) and Specimen 2 (Figure 8.8b) reveal the presence of a mix of chemically distinct linear features that interact and overlap. These are highlighted by contrasting distribution of Fe (red) and Ca (purple) and visualised using Fe isoconcentration surfaces (0.8 at. % Fe) in Figure 8.8, overlain with the Ca distribution. Note that the 2D images of 3D features sometimes create false angles.

APT chemical analysis of the rutile matrix demonstrates a homogeneous distribution of trace elements outside the LAB, with a TiO2 concentration of ~96 at. % and H concentration of 2-3 at. % (1, 2 and 3 Da) (Figure 8.9). Pb is only observed above background as 208Pb++ (104 Da) and is distributed homogeneously.

Chemical heterogeneities are only observed in relation to the LAB in Specimen 1 and

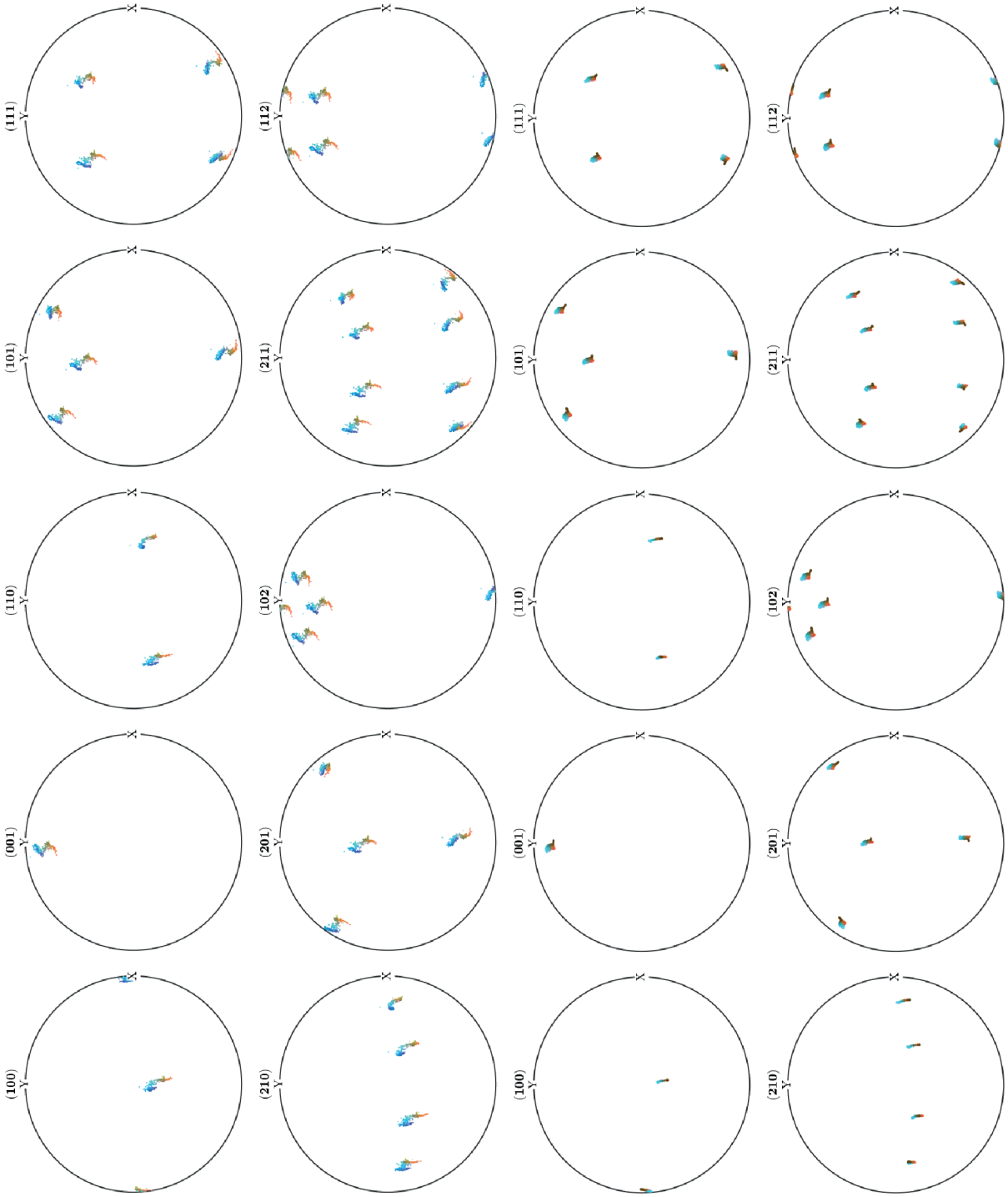

Figure 8.6: Pole plots coloured by orientation for the whole grain region of interest in Figure 8.5b,c.

Specimen 2 and not in the rutile matrix. Sub-horizontal, parallel linear features are observed in these two specimens yielding an orientation parallel to the <100> disorientation axis. These features are interpreted as dislocations (Figure 8.8). The dislocations within a single specimen all lie in the same plane with a spacing of ~10 nm. In both specimens, the dislocations are enriched in trace elements, compensated for by a reduction in Ti (Figures 8.8, 8.9). The increase in H concentration was determined to be caused by the presence of OH-species, while H-species (1, 2 and 3 Da) remain homogeneous. The concentrations are evaluated using a 1D concentration profile. These profiles exhibit Fe concentrations reaching ~1 at. %. Al, Si and Ca concentrations increase from < 0.05 at. % to 0.25 at. %, 0.15 at. % and 0.1 at. %, respectively, across individual structures.

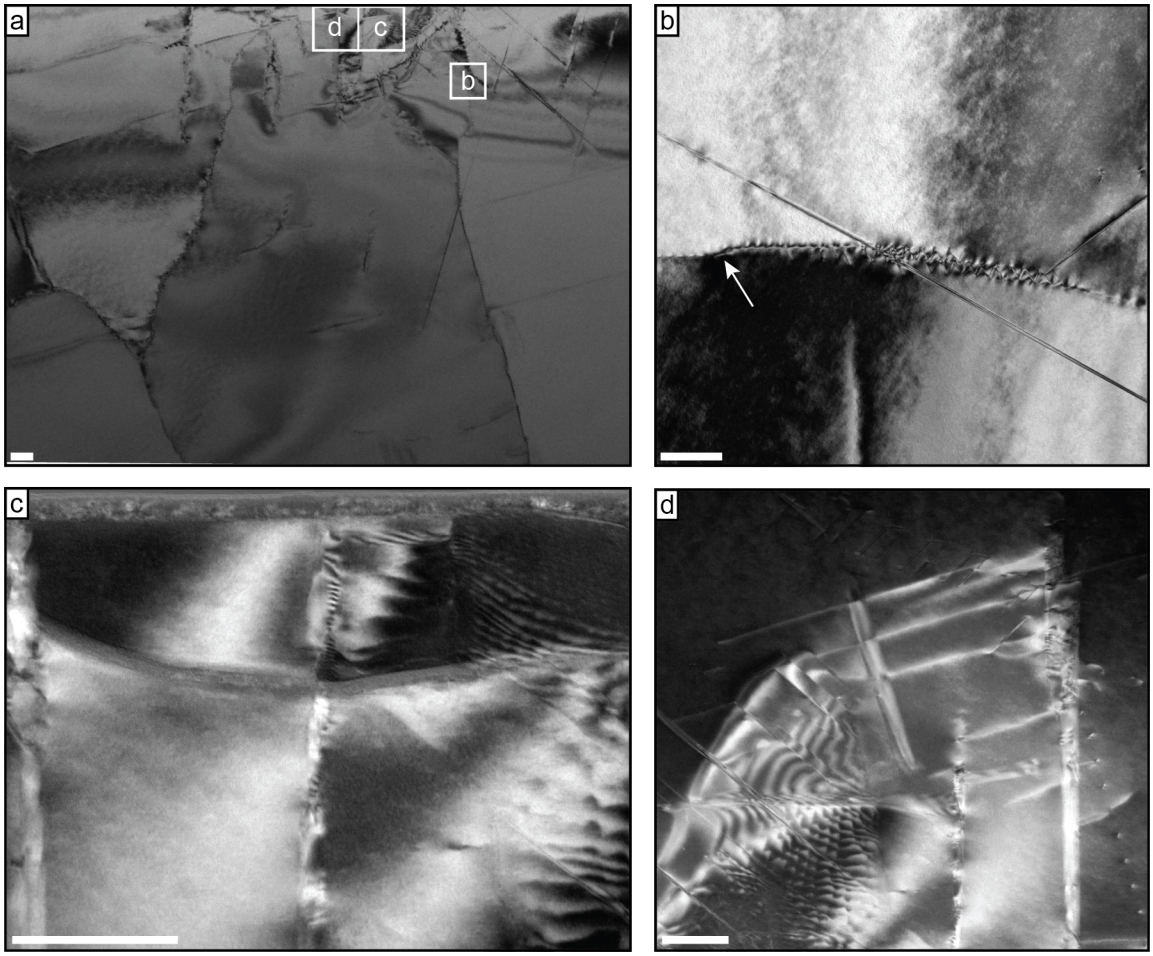

Figure 8.7: (a–d) TEM HAADF image showing the complexity of the microstructures present within deformed rutile. Locations of (b–d) are given. (b) TEM HAADF and (c–d) TEM Dark-field images showing the low-angle boundaries in greater detail. All scale bars indicate 100 nm.

Approximately every 50 nm, the plane in which the dislocations lie is offset by roughly 10 nm (Figure 8.8e). These 'steps' still exhibit the dislocation pattern within their substructure (Figure 8.8f). The dislocations and their spacing contain higher concentrations of trace elements (Figure 8.8c,e). The chemical composition of these steps is displayed as a 1D concentration profile (Figure 8.9). Again, increases in Fe (~0.5 to 4.2 at. %), Al (< 0.05 to 0.45 at. %) and Si (< 0.05 to 0.1 at. %) are observed. In addition, Zr changes to approximately 0.1 at. % up from < 0.05 at. %. The Ca signal is notably low at < 0.05 at. %.

Extending from the dislocations in specimen 2 are two near vertical Fe-enriched features we will refer to as platelets (Figure 8.8b). The acute angle between these two platelets is 58.6° (Figure 8.8c). The platelets intersect the LAB at 60° and 61.4°. The chemistry of these platelets is comparable to the chemistry of the steps but the degree of enrichment for Fe is less and Ca and Si are absent. Fe reaches concentrations of approximately 2 at. % up from 0.5 at. % and H increases from ~2 at. % to 3.5 at. %. The concentration of Zr within the 1D profile is ~0.06 at. % and the concentration of Al is ~0.12 at. %.

Two entangled, sub-vertical, dislocations are present within Specimen 1 and are connected to the previously described horizontal dislocations (Figure 8.8a). Where the two dislocations are separate, they exhibit different chemical signatures. Branch-1, left in Figure 8.8d, exhibits concentrations of Fe and Al of ~1.8 at. % and ~0.15 at. %, respectively. Branch-2 yields a slightly stronger enrichment in Fe 2.1 at. % and higher concentrations of Al 0.42 at. %. Furthermore, this branch also exhibits concentrations of ~0.23 at. % Ca, 0.19 at. % Si and 0.08 at. % Zr.

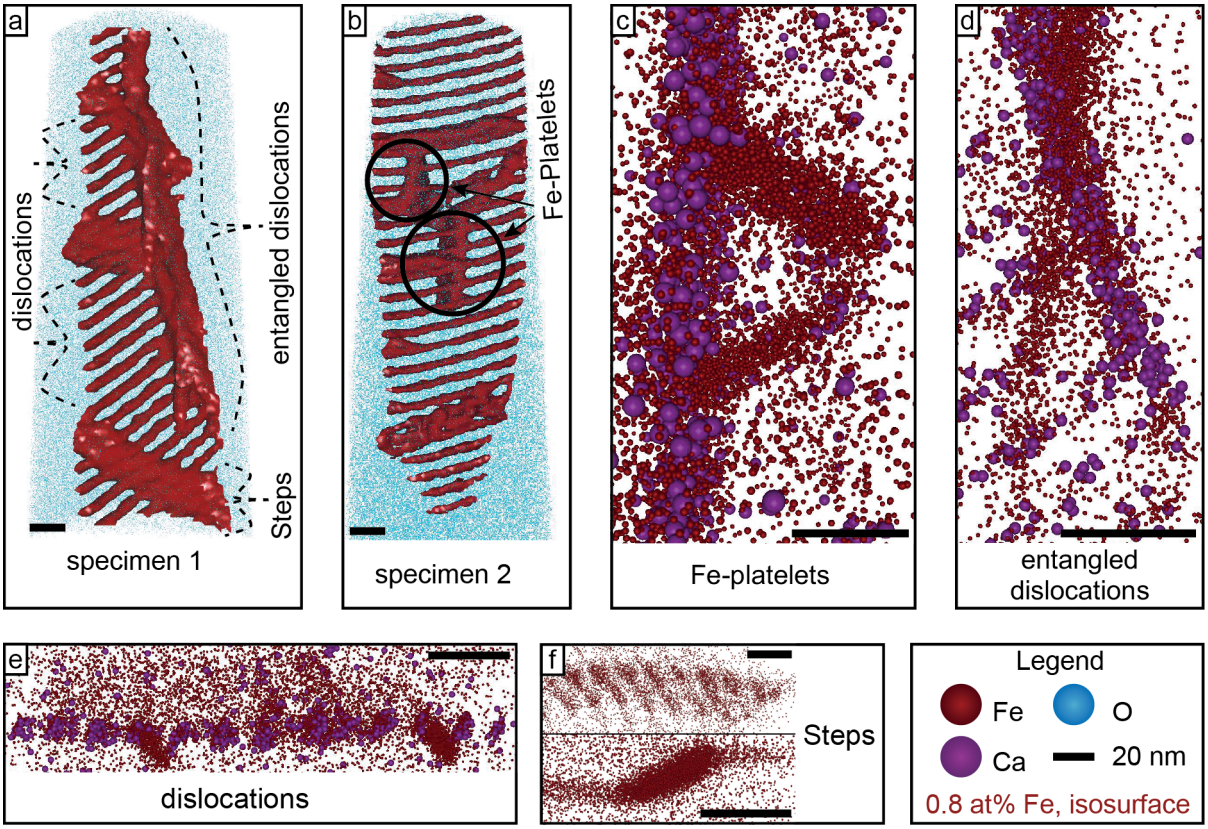

Figure 8.8: 3D digital reconstruction of APT specimen 1 and 2. (a–b) Isoconcentration surfaces for Fe with several substructures labelled. (c) View along the dip of the low-angle boundary in specimen 2 showing the two Fe-platelets extending from the LAB. The angles are ~60°. (d) Two entangled dislocations dislocations, of which one in direct contact with the dislocations that form the LAB. (e) view of the low-angle boundary along the dislocation core showing the distribution of Fe and Ca. (f) Top and side view of the 'steps" showing the resulting offset of ~10 nm. These 'steps' are also visible in (e) where they are free of any Ca enrichment.

Where the two dislocations intersect, the Fe and H increase further relative to the individual branches to approximately 4 at. % and 6 at. %, respectively. Al also increases slightly compared to the individual branches reaching concentrations of ~0.45 at. %, while Ca, Si and Zr remain on the same levels as in Branch-2 (Figure 8.9). Note that all elements have their maximum concentration in the core of the dislocation, no element appears to prefer the core or rim of the dislocation.

Whereas 1D concentration profiles provide insight in the distribution of individual features, proximity histograms (Hellman 2000) are ideal to visualise the overall extent of trace element enrichment as well as providing better statistical insights due to measuring significantly larger volumes. Proximity histograms are measured orthogonally to each point on an isoconcentration surface. The distance is based on the smallest radius of all included features. Here, this radius is 5 nm based on the 1D concentration profile for a dislocation (Figure 8.9a). The proximity histogram (Figure 8.9f, 1s error bars) is based on the 0.8 at. % Fe isoconcentration surface, thus including all the above described features. The TiO_2 concentration is approximately 96 at. % in the matrix, and this decreases by approximately 5 at. % within the substructures. The Fe concentration increases from ~0.1 at. % to ~2.3 at. % and the H signal increases from ~2.3 at. % to ~4.2 at. %, together making up the bulk of trace-element enrichment. Furthermore, V increases from ~0.26 at. % to ~0.45, Cr concentrations increase from ~0.17 at. % to ~0.26 at. %.. Al, Ca, Si, and Sn are present in concentrations of < 0.025 at. % within the matrix but reach concentrations of 0.42, 0.12, 0.12 and 0.07 at. % respectively. Zr, important for temperature estimations, is present in concentrations of < 0.01 at. % in the matrix but increases to 0.025 at. % within features in the LAB.

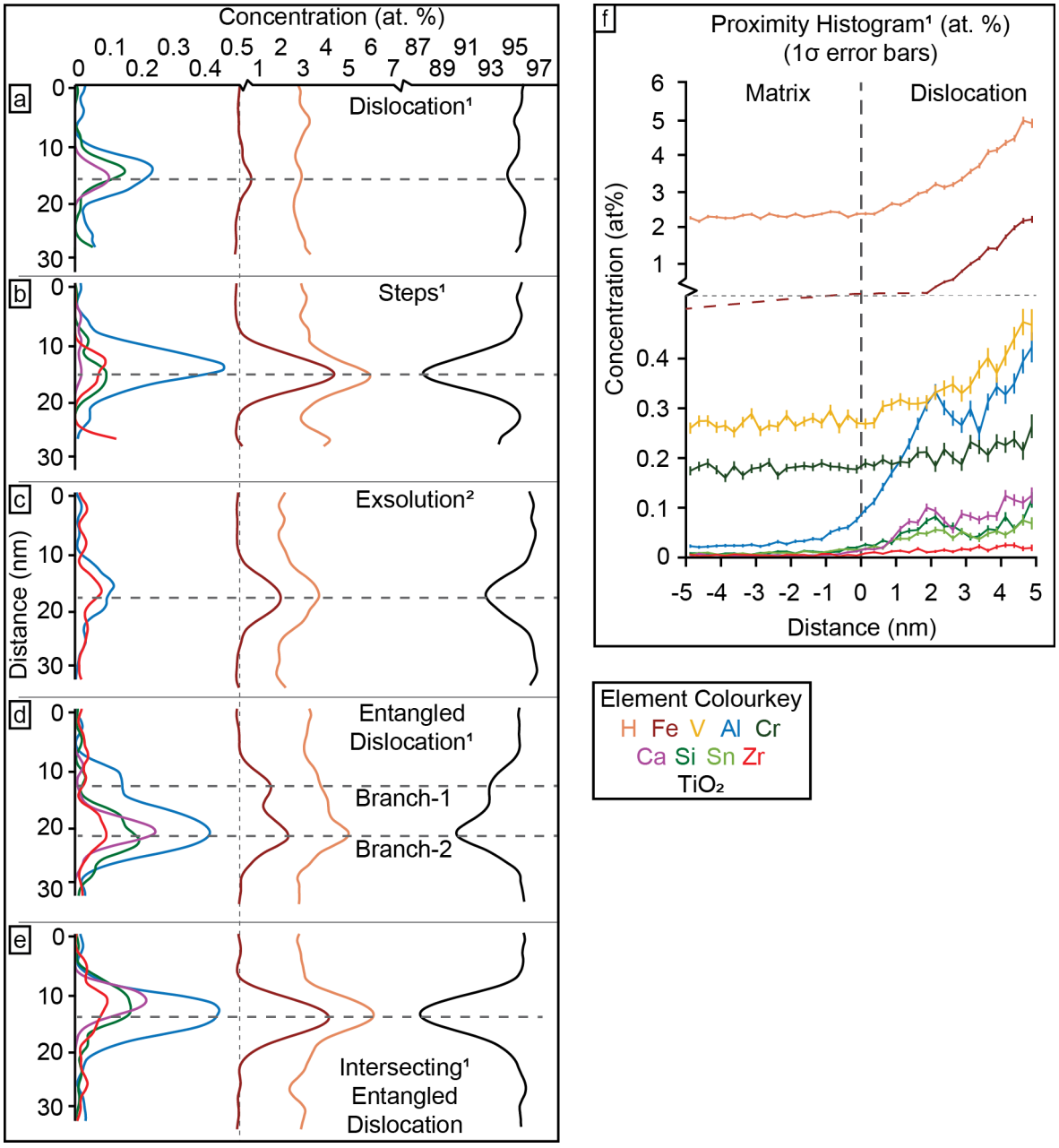

Figure 8.9: (a–e) Concentration profiles for the several substructures observed in the 3D APT reconstruction. The index number refers to the specimen number (1 or 2). (a–e) 1D concentration profile through single substructures observed in APT specimens 1 and 2. The structures exhibit different chemical signatures. All are enriched in Fe and Al, however the degree varies, and some features contain higher amounts of Ca and Si. (f) Proximity histogram for the full low-angle boundary.

8.5 Discussion

8.5.1 Relative timing and conditions of geological events

Before assessing the influence of LABs on rutile geochemistry, the relative timing and the *P-T* conditions experienced during and after growth should be constrained, to obtain the conditions of deformation and potential volume diffusion. Omphacite within the rutile-bearing vein contains coesite inclusions (Figure 8.3b), in contrast to the quartz inclusions preserved inside the investigated rutile grains (Figure 8.3c). This contrast indicates that 1) the vein formed at ultrahigh-pressure

metamorphic conditions, commonly recognized within the study area and 2) Rutile growth took place before (U)H*P* metamorphic conditions.

To further constrain temperatures during rutile growth, Zr-in-rutile thermometry was applied using the *P*-sensitive "Combined" calibration by Kohn (2020). The composition of rutile grown in equilibrium with zircon-quartz/coesite provides temperature estimates that accurately reflect crystallisation temperature and are not over- or underestimates (Zack et al., 2004a). The pressure range of rutile growth was estimated to be 2.3–2.8 GPa based on the quartz-coesite transition as upper limit. The lower limit is based on the timing of rutile growth relative to garnet growth (Groppo et al., 2009). The resulting temperature range of 510–565 (± 20) °C agrees with the prograde *P-T* conditions determined by Groppo et al. (2009). Determining the timing of deformation of rutile and omphacite is problematic due to a lack of constraints. Given the strong deformation in rutile in contrast with the weakly deformed omphacite that forms the vein matrix (Figures 8.1, 8.5a), the rutile was deformed during and/or after its growth in the quartz stability field but before the formation of the omphacite vein. It is this deformation that is linked to the formation of LABs. Onset of extension within the LCU eclogites during UH*P* conditions coincided with the localization of deformation into shear bands (Van der Klauw et al., 1997). The lack of these shear bands and retrograde mineralization that should occur alongside deformation during exhumation, suggests that the majority of deformation in this system occurred at eclogite facies conditions.The formation of the Fe-platelets by exsolution from rutile (Figure 8.2b,c) is an unmixing process that reduces the energy of an oversaturated solution and occurs in response to the cooling (Putnis, 1978). The presence of these Fe-bearing exsolution products is explained by cooling associated the rapid exhumation of this Alpine region after the metamorphic peak at 45–41 Ma (Rubatto et al., 1998; Amato et al., 1999; Reddy et al., 1999; Gouzu et al., 2016).

8.5.2 Crystal-plastic deformation of rutile

Intragranular distortion in rutile occurred via dislocation creep and resulted in the formation of LABs within the crystal. For rutile, only a few studies report on natural deformation microstructures (Moore et al., 2020; Plavsa et al., 2018). However, the activation of the slip systems in rutile has been studied experimentally since the early 1960s. These studies showed activation of {101}<-101> and {110}<001> depending on crystal orientation (Ashbee and Smallman, 1963; Hirthe and BRITTAIN, 1963). Furthermore, Carr and Graham, 1985 (unpublished data) presented evidence for slip on the (100) plane. Later studies reported the activation of the {101}<-101> and {110}<001> slip systems to be temperature dependent with activation occurring at 600 °C and 900 °C, respectively (Blanchin et al., 1990). However, a more recent study on natural samples by Moore et al., (2020) demonstrated that the activation of {110}<001> is unlikely to be temperature dependent, at least to 900°C, given the thermal history of their studied samples.

The microstructural analysis of rutile by EBSD shows the presence of low-angle boundaries determined to have formed on the {101}<-101> slip system, with a rotation around [100]. This is in agreement with experimental results on the effect of indentation on [001], identical to rotation around (100). The UH*P*-L*T* (>2.7 GPA, ~600° C) metamorphic conditions would suggest the temperature threshold of 600°C for this slip system (Blanchin et al., 1990) is lower. This would be in agreement with the conclusion of Moore et al., (2020) on the {110}<001> slip system.

8.5.3 Formation of nanoscale substructures

The low-angle boundaries observed by EBSD were targeted for APT and TEM analyses, which revealed a complex underlying substructure. Evenly spaced linear features lie consistently within

the plane of the LAB. The geometry, size, and spacing of these features suggests that they are dislocations and are therefore intrinsic to the LAB (Hirthe and Balluffi, 1973). APT studies on LABs have previously observed similar features in zircon (Piazolo et al., 2016; Reddy et al., 2016) and titanite (Kirkland et al., 2018). In rutile, the geometry of linear features in the LAB is comparable with dislocations observed in twin boundaries in rutile (Reddy et al., 2020, Verberne et al., under construction). The spacing between dislocations as well as the diameter of the zone of enrichment in trace-elements varies between these studies. The enriched zone consists of the dislocation core and a surrounding area of distorted lattice, elastically strained having a stress field called the Cottrell atmosphere (Cottrell and Bilby, 1949). The capture of trace elements in the Cottrell atmosphere cancels out the stress fields. In minerals, studies by APT show that the enrichment zone extends for approximately 3–5 nm in zircon (Piazolo et al., 2016), compared to 10–24 nm in titanite. In this study, dislocations in rutile have an enriched zone of trace elements of ~8–10 nm in diameter, similar to the dislocations observed in twin boundaries (Reddy et al., 2020; Verberne et al., in prep.). The reason for the discrepancy in diameter of the enriched zone between minerals is not directly clear. In the most basic approach, the burgers vector (b) of the dislocation is equivalent to the interatomic spacing. For rutile, this is ~0.46 nm (a/b) & 0.3 nm (c), for zicon 0.66 & 0.59 nm and 0.71 nm, 0.87 nm and 0.66 nm for titanite. Thus the enriched zones in the rutile are ~17b–33b, zircon 4b–8b and titantie 11b–33b, depending on the axis. Modelling of Cottrell atmospheres in metallic samples (Ni) with hydrogen as solute/trace element yield diameters of ~12b (Sills and Cai 2018). The stress field around dislocations in each mineral and compared to metallics will be different and could cause the discrepancy for how far from the core a Cottrel atmosphere can extend. Furthermore, the difference in electric field around the dislocation and the host material when exposed during APT analysis in each mineral and reconstruction parameters could lead to a magnifying effect on the dislocations radius.

The dislocations that form the LAB lie on a plane that is offset on intervals of approximately 10 nm, referred to as "steps" (Figures 8.7b, 8.8e,f). Such a structure was not observed in previous APT analyses of LABs in minerals (Piazolo et al., 2016; Reddy et al., 2016) and titanite (Kirkland et al., 2018). The dislocations are still visible within these steps (Figure 8.8f), suggesting the steps formed after the dislocations. Whereas the structure itself yields the appearance of dislocations similar to those in titanite (Kirkland 2018), it is unlikely that this feature is a dislocation intersecting the LAB at a different angle. This configuration would not result in the offset of the LAB itself and the dimensions of this feature do not fit with the other dislocations observed in this and previous studies of rutile (Reddy et al., 2020; Verberne et al., 2021; Kuzmina 2015). Instead, this feature is interpreted to reflect a long-period - chemical - stacking order (LPSO) (Inoue et al., 2001). LPSO's are known in the material sciences and are formed as a mechanism for strain accommodation in a chemically enriched region (Abe et al., 2002; Inoue et al., 2001) (Furuhara and Gu, 2013). Nucleation of these structural sites on an existing array of dislocation can therefore be expected and it has been suggested that the local strain field around the dislocations can enhance diffusion of trace elements to achieve chemical ordering (Abe et al., 2002).

BSE images of Fe-rich platelets in rutile consistently show two different orientations of the platelets within a single grain (Figure 8.2b,c). This consistency indicates a structural control on the growth of these platelets. The apparent angles between two sets of platelets change between grains. However, unlike 3D APT data, it is not possible to re-orientate the field of view and therefore it is likely the measured angles provide a false impression due to exposed rutile surface being random. The Fe-rich platelets observed in Specimen 2 are inherently different to the LPSOs. The chemical fingerprint only reflects growth within the same chemical system. The physical phenomena that these platelets reflect remains ambiguous. However, the composition does not reflect formation of a completely new phase, containing only approximately 4 at. % Fe. The angle between

two platelets is 60°, close to the angle of intersection of hematite exsolutions observed by (Recnik et al., 2015; Figure 8.3b).

Given that the platelets observed by APT and BSE imaging both intersect the same LAB it is tempting to relate them to each other. The measured angles in the APT data and the indications of structurally controlled growth based on both APT data and BSE images suggest that the nanoscale platelets in the APT data set record the onset of growth of exsolution structures or potentially the onset of the formation Guinier-Preston zones from which Fe-bearing exsolution structures can form (Putnis, 1978).

8.5.4 Mechanisms for element mobility

Before assessing the role of microstructures in the mobility of trace elements, volume diffusion must be considered as a reference frame. Because the rate bulk/volume diffusion is exponentially temperature-dependent, the majority of diffusion will have taken place at (near-) peak metamorphic temperatures, which is 590–630 °C in the case of the LCU (Groppo et al., 2009; Reinecke, 1998). No precise data are available on the duration of peak temperature of LCU. However, an estimate can be made based on the ages of metamorphism and exhumation. The onset of metamorphic peak temperatures occurred between the 44 Ma U-Pb metamorphic zircon age (Rubatto et al., 1998) and the Sm-Nd garnet age of 42–39 Ma (Amato et al., 1999; Skora et al., 2015). Near-peak temperatures persisted during decompression until amphibolite- to greenschist-facies overprinting. The age of cooling below (near-) peak temperatures is constrained by dates in the range 36–45 Ma from white-mica geochronology (various mica Rb-Sr, Reddy et al., 1999; phengite-(clino)zoisite Rb-Sr, Skora et al., 2015; white mica K-Ar, Gouzu et al., 2016). These ages are generally complicated by recrystallization, excess Ar and compositional zoning, and the age of 36 Ma is considered to be the most reliable constraint on the timing of cessation of exhumation at elevated temperatures (Reddy et al., 2003). These geochronological data suggest a 5–8 Myr duration of (near-) peak temperatures, assuming limited cooling during the initial stages of exhumation.

The diffusion of Zr through rutile parallel to the c-axis, the direction of fastest diffusion, has experimentally been studied at temperatures in the range 750–1100 °C (Cherniak et al., 2007). By extrapolating the Arrhenius equation in Cherniak et al. (2007), the effective diffusion length for Zr in rutile is obtained for Zr at the previously discussed range of temperature and duration representative of the peak metamorphic temperature of the LCU (Figure 8.10). For comparison, the effective diffusion length is also given for Fe parallel and perpendicular to the c-axis based on a temperature-dependent power law of experimentally obtained diffusion coefficients by Sasaki et al. (1985). Fe diffuses several orders of magnitude faster than Zr, and with an effective diffusion length of 0.2–4.5 m, should be homogenized throughout the rutile crystals. Zr is unlikely to have achieved an effective diffusion length of 10–20 μm. Based on the work by Cherniak et al. (2007) and Dohmen et al. (2019), the closure temperature for Zr in rutile studied here should be in the order of 600–650 °C, which is in agreement with the low effective diffusion length for Zr estimated for the LCU. Al and Si, two elements that are enriched within the LABs (Figure 8.9), are experimentally demonstrated to diffuse significantly slower than other elements in rutile at high temperature (Cherniak & Watson, 2019), which also holds up when extrapolating diffusion coefficients to temperatures relevant to the LCU (Figure 8.10).

The presence of nanoscale substructures that are chemically and structurally different from each other suggest that potentially different mechanisms for trace-element mobility were at play. The three main mechanisms that need to be evaluated are the effectiveness of volume diffusion, the potential for fast-diffusion pathways and dislocation-impurity pair migration. Previous APT studies demonstrated that information on the active diffusion mechanisms could be derived

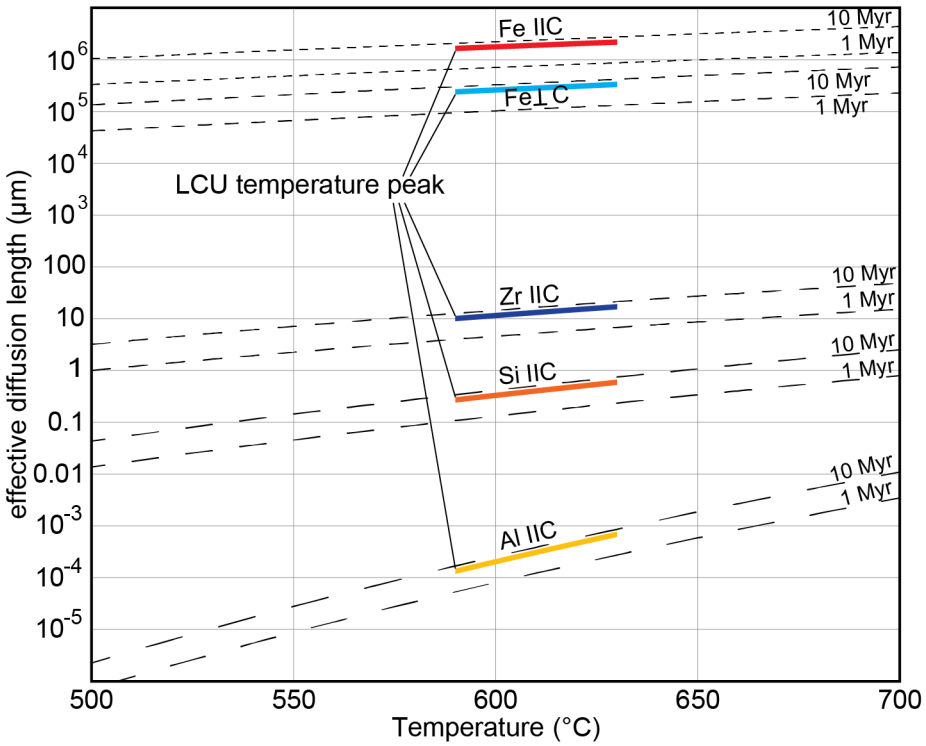

Figure 8.10: Effective diffusion length in rutile of Fe, Zr, Al, and Si parallel to the c-axis, and Fe perpendicular to the c-axis, determined for the possible range of the metamorphic temperature peak temperatures and durations for the LCU. Lines of effective diffusion length versus temperature for fixed durations of peak temperature of 1 Myr and 10 Myr are also given.

from the APT datasets and correlative analysis. Volume diffusion in combination with U-decay effects was demonstrated to result in the formation of Pb enriched clusters (Peterman et al., 2019; Peterman et al., 2016; Valley et al., 2014; Valley et al., 2015; Verberne et al., 2020). Fast-diffusion pathways in the form of low- and high-angle and twin boundaries have been argued to allow for element migration (Fougerouse et al., 2019; Fougerouse et al., 2018; Piazolo et al., 2016) and dislocation-impurity pair migration was suggested to lead to trace element enrichment in titanite (Kirkland et al., 2018) and pyrite (Dubosq et al., 2019).

APT revealed that the features associated with the LAB are enriched in common trace elements (e.g., Fe, Zr, Si, Al) and, in the case of the dislocations composing the LAB and one orthogonal dislocation, also uncommon Ca. The presence of Fe and other trace elements with an affinity for rutile in the nanoscale substructure might reflect capture of trace elements in the strain field around dislocations (Cottrell and Bilby, 1949). The models for volume diffusion show that Fe and Zr both could diffuse into the dislocations during peak metamorphism. Subsequent migration of dislocations into the LAB would result in enrichment of the LAB in trace elements (Dubosq et al., 2019; Imai and Sumino, 1983; Petukhov and Klyuchnik, 2012). Alternatively, these elements could be derived from the grain exterior (Fougerouse et al., 2019; Joesten, 1991; Kirkland et al., 2018), which would result in a dichotomy about whether the dislocations behaved as an element trap, as a pathway for diffusion or both. For the dislocations decorating the LAB, it is not possible to discriminate between the active diffusion pathways and potentially a combination of them. However, the trace element composition of other structures, the 'steps' and entangled dislocations allow us to further constrain diffusion pathways for at least these features.

The Fe enrichment of the steps and formation of platelets raise questions about the mobility of Fe and the timing of formation. If these 'steps' are related to the formation of LPSOs and the platelets reflect the onset of the formation of precipitations (Guinier-Preston (GP) zones)

then these features formed at different times. LPSOs are associated with strain accommodation, whereas the GP zones would be associated with decompression during exhumation. While their formation might have been in response to different processes, it is possible that the mechanism facilitating Fe migration was the same. 1D chemical profiles through both features show only enrichment of Fe within these features, with no depletion of Fe in the adjacent material. Continued volume diffusion would have led to a homogenisation of Fe concentration outside the dislocations (Figures 8.8, 8.9). Both structures are in direct contact with the Fe-enriched dislocations in the subgrain boundary. This contact suggests that the formation of Fe-enriched 'steps' and platelets is linked to the presence of the LAB, which may have acted as a high-diffusivity pathway for providing Fe. However, the presence of mainly Fe and Al, over other trace elements also points towards differences in diffusivity between elements. The charge properties of dislocation can play a vital role, resulting in the formation of Ti^{3+} that would allow for enhanced diffusion of these elements.

Besides common rutile trace elements, the dislocations are decorated in Ca. Ca has no affinity for rutile and is not expected to be incorporated within the crystal lattice during growth. Reports on Ca in rutile attributed its apparent presence to potential interference with the surrounding Ca-bearing silicate phases (Zack et al., 2002). Rutile standards for LA-ICP-MS, such as R10 (Luvizotto et al., 2009), also lack values for Ca calibration. LA-ICP-MS data in this study (Table 1) did not indicate Ca in rutile above detection limits. The rutile grain resides within an omphacite vein also including apatite, glaucophane, and calcite as daughter crystals within primary fluid inclusions. Consequently, source material for Ca was readily available. However, the lack of Ca in the rutile matrix rules out volume-diffusion and dislocation-impurity pair diffusion as mechanisms for Ca enrichment in dislocations. Besides Ca enrichment around dislocations, volume diffusion would have resulted in enrichment of the rutile matrix, and without Ca in the matrix no ions can be captured in the strain field of the dislocations. The ionic size of elemental species in part control element migration, it can be questioned whether large cations such as Ca can migrate into the region of elastic strain around a dislocation (Cottrell and Bilby, 1949; Kirkland et al., 2018; Shannon, 1976).

Si and Al are enriched in the LABs alongside Ca, but are more readily incorporated in rutile and thus don't require an external source (Figure 8.4a). However, Si and Al are known to diffuse at significantly lower rates in rutile than other elements (Figure 8.10; Cherniak and Watson, 2019). The affinity of these elements for LABs without the possibility for their enrichment through volume diffusion at the temperature and timescale of the LCU, indicates a different mechanism of incorporation similarly to Ca.

Trace-element enrichment by fast diffusion along dislocations, or "pipe" diffusion (Love, 1964), has been suggested in previous APT studies on minerals to facilitate the removal of Pb in zircon (Piazolo et al., 2016) or allow for the incorporation of potassium, a large cation, in titanite (Kirkland et al., 2018). Therefore, we interpret the Ca decorating the dislocations in rutile as externally derived and to have been incorporated into the low-angle boundary by enhanced diffusivity along dislocations.

The lack of Ca in one of the vertically orientated dislocations, the steps, and Fe-rich platelets (Figures 8.8, 8.9), further suggests that Ca incorporation predated these dislocations or was energetically unfavourable. Migrating dislocations can be entangled resulting in a core-core overlap leading to enrichment in trace elements, as demonstrated for pyrite (Fougerouse et al., 2019). Here, the simplest explanation would be that a migrating dislocation becomes entangled and pinned on the pre-existing Ca-rich dislocations. The diffusion for large cations like Ca along the dislocation core would have become ineffective before this entanglement as otherwise Ca would have diffused into the Ca-free branch.

Trace element enrichment is highest in the core with lower concentrations of solutes further away

from the dislocation core. This is consistent with observation of the aforementioned hydrogen in Ni (Sills and Cai, 2018). Mainly in the 'steps' and where the entangled dislocations intersect the difference in concentration between the rutile matrix and features is ~6 at. %. While not matching a known different mineral phase, a 6 at. % difference in composition raises the question whether these features should be considered rutile or a discrete, thermodynamically stable phase? Similar features, though in higher concentrations have been described as linear complexions (Kuzmina 2015).

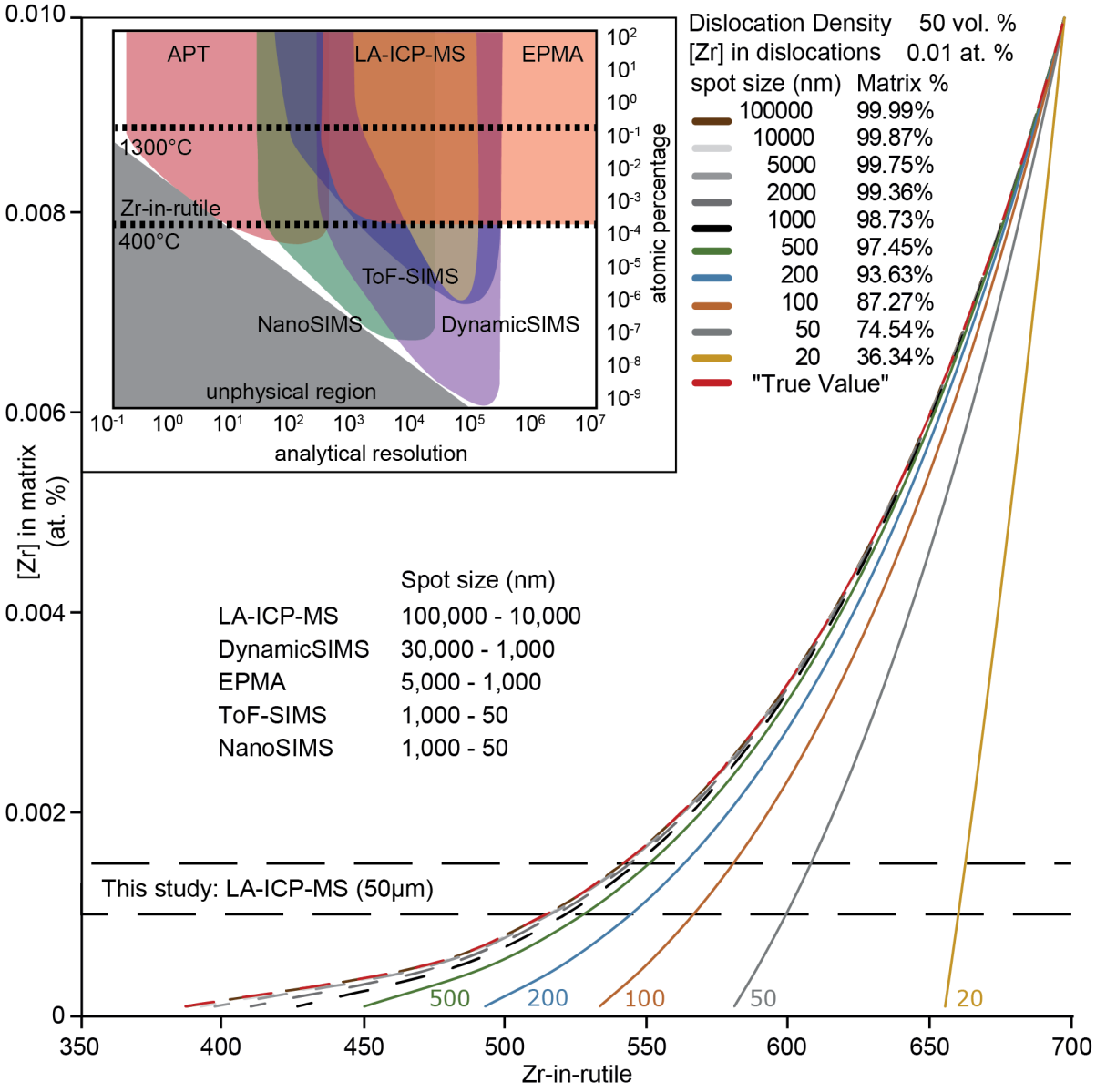

Figure 8.11: Temperatures obtained by Zr-in-rutile thermometry, and how these are affected by Zr-enriched LABs, as a function of Zr in the rutile matrix. Several spot sizes of the hypothetical chemical analysis are displayed. The inset is a diagram of the range of analytical resolution and detection limit for chemical analysis techniques used in Earth sciences. Element concentrations corresponding to two extreme temperatures for the application of Zr-in-rutile are given as context. Zr-in-rutile temperatures and concentrations are obtained using the calibration of Kohn (2020) at a pressure of 2.0 GPa.

8.5.5 Implications for Zr-in-rutile geothermometry

Accurate results from Zr-in-rutile geothermometry require constraints on the activities of Zr (a_{Zr}) and Si (a_{Si}) (Kohn, 2020; Tomkins et al., 2007; Watson et al., 2006; Zack et al., 2004a). In cases where a_{Si} and/or $a_{Zr} < 1$, the Zr-in-rutile geothermometer will provide over- or underestimates of the temperature. It is assumed that $a_{Si} = a_{Zr} = 1$ if Zr- and Si-bearing phases (e.g. zircon and quartz) are in equilibrium with rutile (Zack et al., 2004a). Here, quartz is present as inclusions in rutile and both zircon and coesite are present as inclusions within the surrounding omphacite grains (Figure 8.3), thereby satisfying the requirements for accurate Zr-in-rutile thermometry.

The impact of intragranular substructure on rates of diffusion needs to be considered as dislocations can act as fast diffusion pathways or traps for trace elements. An effective diffusion length of 10 µm (Figure 8.10) allows for the mobilization of Zr into the LAB network for vast regions of the grain interior (Figure 8.5b). The question becomes whether Zr is retained or mobilized along the dislocations. Recent APT studies on rutile have argued that while Zr might be able to migrate along dislocations, the diffusivity of Zr along dislocations is still several orders slower than Fe. It was therefore suggested that dislocations mainly act as a trap for mobile Zr, thus preserving bulk Zr concentrations, albeit in a more localised form.

Whereas it remains an open question as to whether Zr is retained or migrates along dislocations, the influence of Zr present within a LAB on composition measurements can be tested. Zr-in-rutile thermometry is calibrated for the Zr concentration in weight percentages. Thus, the substitution of Ti and O for any other element will barely affect the measured Zr concentration. Here, it is shown that dislocations and other substructures linked to the LAB can result in the exchange of 1–8 at. % Ti for other trace elements (Figure 8.9). However, this compositional modification is very localised. As a consequence, the spatial resolution of the analytical technique used for measuring Zr concentration may play a critical role in determining the measured concentrations. We can assess the influence of the spatial resolutions of different techniques on Zr-in-rutile thermometry under the following assumptions:

1. The chemical system is simplified assuming a composition of $Ti_{1-x}O_2$, where x is only Zr.
2. The Zr concentration in the LAB is based on the proximity diagram of this study (0.01 at. %)
3. "Measurements" are acquired on surfaces perpendicular to the LAB and are centred on the LAB.
4. The length and depth of the LAB are equal to the spot size (d) diameters and analytical depth. The width of the LAB is equal to the diameter of the zone of chemical enrichment around dislocations (y) visualized by APT.
5. The volume of the LAB within the spot analysis is simplified to be length (l)*width (w)*depth (d), ignoring the curvature at the edges.
6. The composition of the LAB is a mix between the dislocations and the remaining volume in the LAB assumed to have the composition of the matrix. The contributions of dislocations and matrix to the LAB composition is set to 50% each based on the isoconcentration profiles of Specimens 1 and 2 (Figure 8.8).

From the above assumptions the proportion of matrix sampled by a given spot size is:
with the concentration afterwards corrected for the proportion of dislocations within the LAB.

$$(1 - \frac{4y}{\pi \times d}) \times 100\%$$

For the measurements performed in this study, it can be shown that Zr-in-rutile temperatures calculated from analyses performed with a spot size >1 µm are not influenced by the Zr enrichment of the LAB, assuming the matrix represents the "true value" (Figure 8.11). Naturally, the temperature profiles converge to the point where the concentration of Zr in dislocations matches the con-

centration of Zr concentration in a matrix. Lower Zr concentration in the LAB compared to the matrix naturally leads to an underestimation of the temperature. If it is assumed Zr was removed from the rutile via the LAB network, spot sizes < 1 μm might provide more accurate Zr-in-rutile temperatures, however current models are not calibrated for the properties of dislocations.

8.6 Summary

This study demonstrates that LABs can act as diffusion pathways for trace elements in rutile. The influence on measurements will be technique- and element-dependent and requires knowledge about the geological history. Especially when working with high-resolution analytical techniques, a good understanding of the presence of intragranular microstructures and their relation to the pressure and temperature history is crucial for correct interpretation.

Acknowledgements

Work was conducted within the Geoscience Atom Probe Facility at Curtin University and part of the Advanced Resource Characterisation Facility (ARCF). The ARCF, under the auspices of the National Resource Sciences Precinct (NRSP) - a collaboration between CSIRO, Curtin University, and The University of Western Australia - is supported by the Science and Industry Endowment Fund (SIEF). The authors gratefully acknowledge support of Curtin University's Microscopy & Microanalysis Facility and the John de Laeter Centre, whose instrumentation has been supported by University, State and Commonwealth Government funding. H.W. v.S.L. and M. A. acknowledge funding received from the European Research Council under the European Union's Horizon 2020 research and innovation program grant agreement 714936 to M. Alvaro.

References

Abe, E., Kawamura, Y., Hayashi, K., and Inoue, A., 2002, Long-period ordered structure in a high-strength nanocrystalline Mg-1 at. % Zn-2 at. % Y alloy studied by atomic-resolution Z-contrast STEM: Acta Materialia, v. 50, no. 15, p. 3845-3857.

Antignano, A., and Manning, C. E., 2008, Rutile solubility in H_2O, H_2O–SiO_2, and H_2O–$NaAlSi_3O_8$ fluids at 0.7–2.0 GPa and 700–1000 C: implications for mobility of nominally insoluble elements: Chemical Geology, v. 255, no. 1-2, p. 283-293.

Ashbee, K., and Smallman, R. E., 1963, The plastic deformation of titanium dioxide single crystals: Proceedings of the Royal Society of London. Series A. Mathematical and Physical Sciences, v. 274, no. 1357, p. 195-205.

Bachmann, F., Hielscher, R., and Schaeben, H., Texture analysis with MTEX–free and open source software toolbox, in Proceedings Solid State Phenomena2010, Volume 160, Trans Tech Publ, p. 63-68.

Basu, S., Elshrief, O. A., Coward, R., Anasori, B., and Barsoum, M. W., 2012, Microscale deformation of (001) and (100) rutile single crystals under spherical nanoindentation: Journal of Materials Research, v. 27, no. 1, p. 53.

Blanchin, M., Bursill, L., and Lafage, C., 1990, Deformation and microstructure of rutile: Proceedings of the Royal Society of London. A. Mathematical and Physical Sciences, v. 429, no. 1876, p. 175-202.

Blum, T.B., Darling, J.R., Kelly, T.F., Larson, D.J., Moser, D.E., Perez-Huerta, A., Prosa, T.J., Reddy, S.M., Reinhard, D.A., Saxey, D.W., Ulfig, R.M., and Valley, J.W., 2018, Best Practices for Reporting Atom Probe Analysis of Geological Materials: In D.E. Moser, F. Corfu, J.R. Darling, S.M. Reddy, and K. Tait, Eds., Microstructural Geochronology: Planetary records down to atom scale, p. 369-373. Wiley.

Borghini, A., Ferrando, S., Groppo, C.T., 2015. Geologic and petrographic study of the veins in the metabasites of the ultra-high pressure Lago di Cignana Unit (upper Valtournenche, western Alps). Congresso SGI-SIMP Florence, abstract. http://hdl.handle.net/2318/1524973

Cherniak, D., 2000, Pb diffusion in rutile: Contributions to Mineralogy and Petrology, v. 139, no. 2, p. 198-207.

Cherniak, D. J., Manchester, J., and Watson, E. B., 2007, Zr and Hf diffusion in rutile: Earth and Planetary Science Letters, v. 261, no. 1-2, p. 267-279.

Cherniak, D.J., and Watson, E.B., 2019, Al and Si diffusion in rutile: American Mineralogist, v. 104, n. 11, p. 1638-1649.

Cottrell, A. H., and Bilby, B., 1949, Dislocation theory of yielding and strain ageing of iron: Proceedings of the Physical Society. Section A, v. 62, no. 1, p. 49.

Crameri, F., 2018. Scientific colour-maps. Zenodo. http://doi.org/10.5281/zenodo.1243862

Cutts, J., and Smit, M., 2018, Rates of deep continental burial from Lu-Hf garnet chronology and Zr-in-rutile thermometry on (ultra) high-pressure rocks: Tectonics, v. 37, no. 1, p. 71-88.

Dachille, F., Simons, P., and Roy, R., 1968, Pressure-temperature studies of anatase, brookite, rutile and TiO_2-II: Am Mineral, v. 53, p. 1929-1939.

DesOrmeau, J. W., Gordon, S. M., Little, T. A., Bowring, S. A., and Chatterjee, N., 2017, Rapid time scale of Earth's youngest known ultrahigh-pressure metamorphic event, Papua New Guinea: Geology, v. 45, no. 9, p. 795-798.

Dohmen, R., Marschall, H. R., Ludwig, T., and Polednia, J., 2019, Diffusion of Zr, Hf, Nb and Ta in rutile: effects of temperature, oxygen fugacity, and doping level, and relation to rutile point defect chemistry: Physics and Chemistry of Minerals, v. 46, no. 3, p. 311-332.

Dubosq, R., Rogowitz, A., Schweinar, K., Gault, B., and Schneider, D. A., 2019, A 2D and 3D nanostructural study of naturally deformed pyrite: assessing the links between trace element mobility and defect structures: Contributions to Mineralogy and Petrology, v. 174, no. 9, p. 72.

Forster, M., Lister, G., Compagnoni, R., Giles, D., Hills, Q., Betts, P., Beltrando, M., and Tamagno, E., 2004, Mapping of oceanic crust with "H*P*" to" UH*P*" metamorphism: The Lago di Cignana Unit,(Western Alps), Mapping geology in Italy, Geological Society of London.

Fougerouse, D., Reddy, S. M., Kirkland, C. L., Saxey, D. W., Rickard, W. D., and Hough, R. M., 2019, Time-resolved, defect-hosted, trace element mobility in deformed Witwatersrand pyrite: Geoscience Frontiers, v. 10(1), p. 55-63.

Fougerouse, D., Reddy, S. M., Saxey, D. W., Erickson, T. M., Kirkland, C. L., Rickard, W. D. A., Seydoux-Guillaume, A. M., Clark, C., and Buick, I. S., 2018, Nanoscale distribution of Pb in monazite revealed by atom probe microscopy: Chemical Geology, v. 479, p. 251-258.

Frezzotti, M., Selverstone, J., Sharp, Z., and Compagnoni, R., 2011, Carbonate dissolution during subduction revealed by diamond-bearing rocks from the Alps: Nature Geoscience, v. 4, no. 10, p. 703-706.

Furuhara, T., and Gu, X., 2013, Discussion on strain accommodation associated with formation of LPSO Structure: Materials Transactions, v. 54, no. 5, p. 675-679.

Gao, J., John, T., Klemd, R., and Xiong, X., 2007, Mobilization of Ti–Nb–Ta during subduction: evidence from rutile-bearing dehydration segregations and veins hosted in eclogite, Tianshan, NW China: Geochimica et Cosmochimica Acta, v. 71, no. 20, p. 4974-4996.

Gao, X. Y., Zheng, Y. F., Xia, X. P., and Chen, Y. X., 2014, U-Pb ages and trace elements of metamorphic rutile from ultrahigh-pressure quartzite in the Sulu orogen: Geochimica Et Cosmochimica Acta, v. 143, p. 87-114.

Gouzu, C., Yagi, K., Thanh, N. X., Itaya, T., and Compagnoni, R., 2016, White mica K–Ar geochronology of H*P*–UH*P* units in the Lago di Cignana area, western Alps, Italy: tectonic implications for exhumation: Lithos, v. 248, p. 109-118.

Groppo, C., Beltrando, M., and Compagnoni, R., 2009, The *P–T* path of the ultra-high pressure Lago Di Cignana and adjoining high-pressure meta-ophiolitic units: insights into the evolution of the subducting Tethyan slab: Journal of Metamorphic Geology, v. 27, no. 3, p. 207-231.

Halama, R., Konrad-Schmolke, M., and De Hoog, J. C., 2020, Boron isotope record of peak metamorphic ultrahigh-pressure and retrograde fluid–rock interaction in white mica (Lago di Cignana, Western Alps): Contributions to Mineralogy and Petrology, v. 175, no. 3, p. 20.

Hart, E., Storey, C., Bruand, E., Schertl, H. P., and Alexander, B. D., 2016, Mineral inclusions in rutile: A novel recorder of H*P*-UH*P* metamorphism: Earth and Planetary Science Letters, v. 446, p. 137-148.

Hart, E., Storey, C., Harley, S. L., and Fowler, M., 2018, A window into the lower crust: Trace element systematics and the occurrence of inclusions/intergrowths in granulite-facies rutile: Gondwana Research, v. 59, p. 76-86.

Hellman, O. C., Vandenbroucke, J. A., Rusing, J., Isheim, D., and Seidman, D. N., 2000, Analysis of Three-dimensional

Atom probe Data by the Proximity Histogram: Microsc Microanal, v. 6, no. 5, p. 437-444.

Hirthe, W. M., and BRITTAIN, J. O., 1963, High-Temperature Steady-State Creep in Rutile: Journal of the American Ceramic Society, v. 46, no. 9, p. 411-417.

Imai, M., and Sumino, K., 1983, In situ X-ray topographic study of the dislocation mobility in high-purity and impurity-doped silicon crystals: Philosophical Magazine A, v. 47, no. 4, p. 599-621.

Inoue, A., Kawamura, Y., Matsushita, M., Hayashi, K., and Koike, J., 2001, Novel hexagonal structure and ultrahigh strength of magnesium solid solution in the Mg–Zn–Y system: Journal of Materials Research, v. 16, no. 7, p. 1894-1900.

Jamieson, J. C., and Olinger, B., 1969, Pressure-temperature studies of anatase, brookite rutile, and TiO_2 (II): A discussion: American Mineralogist: Journal of Earth and Planetary Materials, v. 54, no. 9-10, p. 1477-1481.

Joesten, R., 1991, Grain-boundary diffusion kinetics in silicate and oxide minerals, Diffusion, atomic ordering, and mass transport, Springer, p. 345-395.

Keller, L. M., Abart, R., Wirth, R., Schmid, D. W., and Kunze, K., 2006, Enhanced mass transfer through short-circuit diffusion: growth of garnet reaction rims at eclogite facies conditions: American Mineralogist, v. 91, no. 7, p. 1024-1038.

King, R. L., Bebout, G. E., Kobayashi, K., Nakamura, E., and Van Der Klauw, S. N., 2004, Ultrahigh-pressure metabasaltic garnets as probes into deep subduction zone chemical cycling: Geochemistry, Geophysics, Geosystems, v. 5, no. 12.

Kirkland, C., Fougerouse, D., Reddy, S., Hollis, J., and Saxey, D., 2018, Assessing the mechanisms of common Pb incorporation into titanite: Chemical Geology, v. 483, p. 558-566.

Kirst, F., and Leiss, B., 2017, Kinematics of syn-and post-exhumational shear zones at Lago di Cignana (Western Alps, Italy): constraints on the exhumation of Zermatt–Saas (ultra) high-pressure rocks and deformation along the Combin Fault and Dent Blanche Basal Thrust: International Journal of Earth Sciences, v. 106, no. 1, p. 215-236.

Klinger, L., and Rabkin, E., 1999, Beyond the Fisher model of grain boundary diffusion: effect of structural inhomogeneity in the bulk: Acta Materialia, v. 47, no. 3, p. 725-734.

Kohn, M. J., 2020, A refined zirconium-in-rutile thermometer: American Mineralogist: Journal of Earth and Planetary Materials, v. 105, no. 6, p. 963-971.

Kooijman, E., Mezger, K., and Berndt, J., 2010, Constraints on the U-Pb systematics of metamorphic rutile from in situ LA-ICP-MS analysis: Earth and Planetary Science Letters, v. 293, no. 3-4, p. 321-330.

Kooijman, E., Smit, M. A., Mezger, K., and Berndt, J., 2012, Trace element systematics in granulite facies rutile: implications for Zr geothermometry and provenance studies: Journal of Metamorphic Geology, v. 30, no. 4, p. 397-412.

Kuzmina, M., Herbig, M., Ponge, D., Sandlöbes, S., and Raabe, D., 2015, Linear complexions: confined chemical and structural states at dislocations: Science, v. 349, no. 6252, p. 1080-1083.

Love, G., 1964, Dislocation pipe diffusion: Acta Metallurgica, v. 12, no. 6, p. 731-737.

Luvizotto, G. L., Zack, T., Meyer, H. P., Ludwig, T., Triebold, S., Kronz, A., Munker, C., Stockli, D. F., Prowatke, S., Klemme, S., Jacob, D. E., and von Eynatten, H., 2009, Rutile crystals as potential trace element and isotope mineral standards for microanalysis: Chemical Geology, v. 261, no. 3-4, p. 346-369.

Mei, Z. G., Wang, Y., Shang, S. L., and Liu, Z. K., 2014, First-principles study of the mechanical properties and phase stability of TiO2: Computational Materials Science, v. 83, p. 114-119.

Mezger, K., Hanson, G., and Bohlen, S., 1989, High-precision UPb ages of metamorphic rutile: application to the cooling history of high-grade terranes: Earth and Planetary Science Letters, v. 96, no. 1-2, p. 106-118.

Montalvo, S. D., Reddy, S. M., Saxey, D. W., Rickard, W. D. A., Fougerouse, D., Quadir, Z., and Johnson, T. E., 2019, Nanoscale constraints on the shock-induced transformation of zircon to reidite: Chemical Geology, v. 507, p. 85-95.

Moore, J., Beinlich, A., Porter, J. K., Talavera, C., Berndt, J., Piazolo, S., Austrheim, H., and Putnis, A., 2020, Microstructurally controlled trace element (Zr, U–Pb) concentrations in metamorphic rutile: An example from the amphibolites of the Bergen Arcs: Journal of Metamorphic Geology, v. 38, no. 1, p. 103-127.

Müller, W. F., and Compagnoni, R., 2009, Eclogite from the ultrahigh-pressure metamorphic unit at Lago di Cignana, Western Alps: A process-oriented transmission electron microscope study: Lithos, v. 109, no. 3-4, p. 323-332.

Nakayama, T., and Sasaki, T., 1963, The Diffusion of Ba in a Rutile Single Crystal: Bulletin of the Chemical Society of Japan, v. 36, n. 5, p. 569-574.

Ni, P., Zhu, X., Wang, R., Shen, K., Zhang, Z., Qiu, J., and Huang, J., 2008, Constraining ultrahigh-pressure (UH*P*) metamorphism and titanium ore formation from an infrared microthermometric study of fluid inclusions in rutile from Donghai UHP eclogites, eastern China: Geological Society of America Bulletin, v. 120, no. 9-10, p. 1296-1304.

Norman, M., Pearson, N., Sharma, A., and Griffin, W., 1996, Quantitative analysis of trace elements in geological materials by laser ablation ICPMS: instrumental operating conditions and calibration values of NIST glasses: Geostandards Newsletter, v. 20, no. 2, p. 247-261.

Oberti, R., and Caporuscio, F. A., 1991, Crystal chemistry of clinopyroxenes from mantle eclogites: a study of the key role of the M2 site population by means of crystal-structure refinement: American Mineralogist, v. 76, no. 7-8, p. 1141-1152.

Pearce, N. J., Perkins, W. T., Westgate, J. A., Gorton, M. P., Jackson, S. E., Neal, C. R., and Chenery, S. P., 1997, A compilation of new and published major and trace element data for NIST SRM 610 and NIST SRM 612 glass reference materials: Geostandards newsletter, v. 21, no. 1, p. 115-144.

Peterman, E., Reddy, S. M., Saxey, D., Fougerouse, D., Snoeyenbos, D., and Rickard, W., 2019, Nanoscale processes of trace element mobility in metamorphosed zircon: Contributions to Mineralogy and Petrology, v. 174, no. 11, p. 92.

Peterman, E. M., Reddy, S. M., Saxey, D. W., Snoeyenbos, D. R., Rickard, W. D., Fougerouse, D., and Kylander-Clark, A. R., 2016, Nanogeochronology of discordant zircon measured by atom probe microscopy of Pb-enriched dislocation loops: Sci Adv, v. 2, no. 9, p. e1601318.

Petukhov, B., and Klyuchnik, P., 2012, Dynamic interaction of dislocations with impurity subsystem in crystalline materials: Crystallography Reports, v. 57, no. 3, p. 388-392.

Piazolo, S., La Fontaine, A., Trimby, P., Harley, S., Yang, L., Armstrong, R., and Cairney, J. M., 2016, Deformation-induced trace element redistribution in zircon revealed using atom probe tomography: Nature communications, v. 7, no. 1, p. 1-7.

Plavsa, D., Reddy, S. M., Clark, C., and Agangi, A., 2018, Capricorn Orogen rutile study, a combined electron backscatter diffracction (EBSD) and laser ablation split stream (LASS) analytical approach, Record 2018/12, 54p.

Plümper, O., King, H. E., Vollmer, C., Ramasse, Q., Jung, H., and Austrheim, H., 2012, The legacy of crystal-plastic deformation in olivine: high-diffusivity pathways during serpentinization: Contributions to Mineralogy and Petrology, v. 163, no. 4, p. 701-724.

Putnis, A., 1978, The mechanism of exsolution of hematite from iron-bearing rutile: Physics and Chemistry of Minerals, v. 3, no. 2, p. 183-197.

Rapp, J. F., Klemme, S., Butler, I. B., and Harley, S. L., 2010, Extremely high solubility of rutile in chloride and fluoride-bearing metamorphic fluids: An experimental investigation: Geology, v. 38, no. 4, p. 323-326.

Recnik, A., Stankovic, N., and Daneu, N., 2015, Topotaxial reactions during the genesis of oriented rutile/hematite intergrowths from Mwinilunga (Zambia): Contributions to Mineralogy and Petrology, v. 169, no. 2.

Reddy, S., Wheeler, J., and Cliff, R., 1999, The geometry and timing of orogenic extension: an example from the Western Italian Alps: Journal of Metamorphic Geology, v. 17, p. 573-590.

Reddy, S. M., Saxey, D. W., Rickard, W. D., Fougerouse, D., Montalvo, S. D., Verberne, R., and Van Riessen, A., 2020, Atom Probe Tomography: Development and Application to the Geosciences: Geostandards and Geoanalytical Research, v. 44, no. 1, p. 5-50.

Reddy, S. M., Timms, N. E., Pantleon, W., and Trimby, P., 2007, Quantitative characterization of plastic deformation of zircon and geological implications: Contributions to Mineralogy and Petrology, v. 153, no. 6, p. 625-645.

Reddy, S. M., van Riessen, A., Saxey, D. W., Johnson, T. E., Rickard, W. D. A., Fougerouse, D., Fischer, S., Prosa, T. J., Katherine, P. R. E., Reinhard, D. A., Chen, Y. M., and Olson, D., 2016, Mechanisms of deformation-induced trace element migration in zircon resolved by atom probe and correlative microscopy: Geochimica Et Cosmochimica Acta, v. 195, p. 158-170.

Reinecke, T., 1998, Prograde high-to ultrahigh-pressure metamorphism and exhumation of oceanic sediments at Lago di Cignana, Zermatt-Saas Zone, western Alps: Lithos, v. 42, no. 3-4, p. 147-189.

Rickard, W. D., Reddy, S. M., Saxey, D. W., Fougerouse, D., Timms, N. E., Daly, L., Peterman, E., Cavosie, A. J., and Jourdan, F., 2020, Novel Applications of FIB-SEM-Based ToF-SIMS in Atom Probe Tomography Workflows: Microscopy and Microanalysis, p. 1-8.

Rocholl, A. B., Simon, K., Jochum, K. P., Bruhn, F., Gehann, R., Kramar, U., Luecke, W., Molzahn, M., Pernicka, E., and Seufert, M., 1997, Chemical Characterisation of NIST Silicate Glass Certified Reference Material SRM 610 by

ICP-MS, TIMS, LIMS, SSMS, INAA, AAS and PIXE: Geostandards Newsletter, v. 21, no. 1, p. 101-114.

Rubatto, D., Gebauer, D., and Fanning, M., 1998, Jurassic formation and Eocene subduction of the Zermatt–Saas-Fee ophiolites: implications for the geodynamic evolution of the Central and Western Alps: Contributions to Mineralogy and Petrology, v. 132, no. 3, p. 269-287.

Sasaki, J., Peterson, N.L., and Hoshino, K., 1985, Tracer impurity diffusion in single-crystal rutile (TiO_{2-x}): Journal of Physics and Chemistry of Solids, v. 46, no. 11, p. 1267-1283.

Saxey, D., Moser, D., Piazolo, S., Reddy, S., and Valley, J., 2018, Atomic worlds: Current state and future of atom probe tomography in geoscience: Scripta Materialia, v. 148, p. 115-121.

Scambelluri, M., and Philippot, P., 2001, Deep fluids in subduction zones: Lithos, v. 55, no. 1-4, p. 213-227.

Shannon, R. D., 1976, Revised effective ionic radii and systematic studies of interatomic distances in halides and chalcogenides: Acta crystallographica section A: crystal physics, diffraction, theoretical and general crystallography, v. 32, no. 5, p. 751-767.

Skora, S., Lapen, T.J., Baungartner, L.P., Johnson, C.M., Hellebrand, E., and Mahlen, N.J, 2009, The duration of prograde garnet crystallization in the UH*P* eclogites at Lago di Cignana, Italy: Earth and Planetary Science Letters, v. 287, p. 402-411

Skora, S., Mahlen, N., Johnson, C. M., Baumgartner, L. P., Lapen, T., Beard, B. L., and Szilvagyi, E., 2015, Evidence for protracted prograde metamorphism followed by rapid exhumation of the Zermatt-Saas Fee ophiolite: Journal of Metamorphic Geology, v. 33, no. 7, p. 711-734.

Smye, A. J., and Stockli, D. F., 2014, Rutile U-Pb age depth profiling: A continuous record of lithospheric thermal evolution: Earth and Planetary Science Letters, v. 408, p. 171-182.

Sutton, A. P., Balluffi, R. W., and Sutton, A., 1995, Interfaces in crystalline materials.

Swope, R. J., Smyth, J. R., and Larson, A. C., 1995, H in rutile-type compounds: I. Single-crystal neutron and X-ray diffraction study of H in rutile: American Mineralogist, v. 80, no. 5-6, p. 448-453.

Timms, N. E., Kinny, P. D., and Reddy, S. M., 2006, Enhanced diffusion of uranium and thorium linked to crystal plasticity in zircon: Geochemical Transactions, v. 7, no. 1, p. 10.

Tomkins, H. S., Powell, R., and Ellis, D. J., 2007, The pressure dependence of the zirconium-in-rutile thermometer: Journal of Metamorphic Geology, v. 25, no. 6, p. 703-713.

Valley, J. W., Cavosie, A. J., Ushikubo, T., Reinhard, D. A., Lawrence, D. F., Larson, D. J., Clifton, P. H., Kelly, T. F., Wilde, S. A., and Moser, D. E., 2014, Hadean age for a post-magma-ocean zircon confirmed by atom-probe tomography: Nature Geoscience, v. 7, no. 3, p. 219-223.

Valley, J. W., Reinhard, D. A., Cavosie, A. J., Ushikubo, T., Lawrence, D. F., Larson, D. J., Kelly, T. F., Snoeyenbos, D. R., and Strickland, A., 2015, Nano- and micro-geochronology in Hadean and Archean zircons by atom-probe tomography and SIMS: New tools for old minerals: American Mineralogist, v. 100, no. 7, p. 1355-1377.

Van Achterbergh, E., 2001, Data reduction software for LA-ICP-MS: Laser Ablation-ICP-mass spectrometry in the earth sciences: principles and applications, p. 239-243.

Van der Klauw, S., Reinecke, T., and Stöckhert, B., 1997, Exhumation of ultrahigh-pressure metamorphic oceanic crust from Lago di Cignana, Piemontese zone, western Alps: the structural record in metabasites: Lithos, v. 41, no. 1-3, p. 79-102.

Van Schrojenstein Lantman, H.W., Scambelluri, M., Gilio, M., Wallis, D., and Alvaro, M., 2021, Extensive fluid–rock interaction and pressure solution in a UHP fluid pathway recorded by garnetite, Lago di Cignana, Western Alps: Journal of Metamorphic Geology, v. 00, p. 1-18. DOI: 10.1111/jmg.12585

Verberne, R., Reddy, S., Saxey, D., Fougerouse, D., Rickard, W., Plavsa, D., Agangi, A., and Kylander-Clark, A., 2020, The geochemical and geochronological implications of nanoscale trace-element clusters in rutile: Geology.

Verberne, R., Saxey, D. W., Reddy, S. M., Rickard, W. D., Fougerouse, D., and Clark, C., 2019, Analysis of Natural Rutile (TiO2) by Laser-assisted Atom Probe Tomography: Microscopy and Microanalysis, p. 1-8.

Vukmanovic, Z., Reddy, S. M., Godel, B., Barnes, S. J., Fiorentini, M. L., Barnes, S. J., and Kilburn, M. R., 2014, Relationship between microstructures and grain-scale trace element distribution in komatiite-hosted magmatic sulphide ores: Lithos, v. 184, p. 42-61.

Watson, E. B., Wark, D. A., and Thomas, J. B., 2006, Crystallization thermometers for zircon and rutile: Contributions to Mineralogy and Petrology, v. 151, no. 4, p. 413-433.

Withers, A. C., Essene, E. J., and Zhang, Y. X., 2003, Rutile/TiO2II phase equilibria: Contributions to Mineralogy and Petrology, v. 145, no. 2, p. 199-204.

Zack, T., and Kooijman, E., 2017, Petrology and geochronology of rutile: Reviews in Mineralogy and Geochemistry, v. 83, no. 1, p. 443-467.

Zack, T., Kronz, A., Foley, S. F., and Rivers, T., 2002, Trace element abundances in rutiles from eclogites and associated garnet mica schists: Chemical Geology, v. 184, no. 1-2, p. 97-122.

Zack, T., and Luvizottow, G., 2006, Application of rutile thermometry to eclogites: Mineralogy and Petrology, v. 88, no. 1-2, p. 69-85.

Zack, T., Moraes, R., and Kronz, A., 2004a, Temperature dependence of Zr in rutile: empirical calibration of a rutile thermometer: Contributions to Mineralogy and Petrology, v. 148, no. 4, p. 471-488.

Zack, T., von Eynatten, H., and Kronz, A., 2004b, Rutile geochemistry and its potential use in quantitative provenance studies: Sedimentary Geology, v. 171, no. 1-4, p. 37-58.

Zhou, T., Li, Q., Klemd, R., Shi, Y., Tang, X., Li, C., and Liu, Y., 2020, Multi-system geochronology of North Dabie eclogite: Ineffective garnet 'shielding' on rutile inclusions under multi-thermal conditions: Lithos, v. 368-369, 105573

CHAPTER 9
Conclusions and future prospects

9.1 Conclusions

The understanding of deep subduction processes is still challenged by complicating factors such as limited and biased exhumation, dismemberment of exhuming ultrahigh-pressure (UH*P)* units, retrograde overprinting, and limitations of current techniques for interrogating minerals for their geological record. This thesis provides a multi-disciplinary look into the interaction of fluids, stress, deformation, and metamorphism at high- to ultrahigh-pressure metamorphic conditions. In lithologies challenged by metamorphic overprinting during retrogression, valuable information was retrieved from garnet and inclusions preserved therein. The result is a comprehensive overview of metamorphism, deformation, and fluid-rock interaction in a garnet-rich environment in a fluid-rich, cold subduction zone setting.

The combination of microstructures, mineral inclusions, and garnet compositions in Chapter 4 provide a record of metamorphism and fluid-rock interaction for the UH*P* garnetite-bearing quartzite of the Lago di Cignana unit (LCU). This fluid-rock interaction record showcases the longevity of this system as a major fluid pathway throughout subduction. The externally derived fluids locally led to a significant compaction and mass removal by intergranular pressure solution (IPS) of minerals such as quartz, carbonates, and garnet. Due to its relatively low solubility, garnet was concentrated into garnetite stylolites, constituting a new potential mechanism for the formation of garnetite. Quartz inclusions entrapped in euhedral garnet overgrowths on garnetite yield strains that indicate near-hydrostatic stress conditions during garnet growth. Considering pressure solution as the main mechanism of mass removal, this fluid-rock interaction also operated as a means of exerting control on deformation during metamorphism.

Based on a compositional link between coesite-bearing garnet in the host quartzite and inclusion-poor garnet in the garnetite, IPS in garnet is found to have operated under UH*P* conditions, the first recognition of this mechanism at such pressure. In Chapter 5, detailed study of microstructures and grain shape of garnet reveals that despite a strong presence of fluids, pressure solution in garnet did not result in high strain, is localized into smaller grains, and in a small amount of grains in general. The degree of strain compared to the heavily deformed quartzite host rock indicates that IPS in garnet does not result in weak garnetite layers. At least two generations of SPO are recorded in various zones of the garnetite, supporting the suggestion that the garnetite formed and deformed in phases by the accretion of garnets from dissolution of interstitial material, followed by IPS in garnet. Evidence for recrystallization of garnet by grain-boundary migration (GBM) is observed in all studied garnetites, both metasedimentary and eclogitic, and this mechanism appears to be driven by a chemical disequilibrium between garnet cores and a grain-boundary fluid. This driving force for GBM in garnet has not been previously recognized, and raises questions about the nature of the fluids the circulated through the LCU.

A process of radial fracturing and subsequent garnet replacement along fractures and in the cores of garnets, is studied by the use of elastic geothermobarometry (Chapter 6) and trace-element analysis of garnet and inclusions in the core (Chapter 7). As expected, the fracturing and sealing of garnets resulted in the resetting of elastic strains in zircon inclusions. Although an unresolved issue regarding the application of geothermobarometry or the host-inclusion system resulted in an overestimation of *P-T* conditions, radial fracturing and garnet replacement are suggested at ~1 GPa and > 500 °C. Coesite inclusions did not break down to quartz despite this fracturing and resetting, with potential implications for the coesite-quartz reaction.

Zr-in-rutile thermometry applied to filtered LA-ICP-MS analyses of garnet contaminated with rutile and zircon, resulted in temperatures that overlap with the majority of the near-isothermal decompression path of the LCU, which is in agreement with the conditions suggested for zircon inclusion resetting. These rutile inclusions originate from re-equilibration of Ti-bearing

garnet as result of the garnet replacement. Neither of the contaminant minerals can be linked to positive anomalies of light to mid rare earth elements (REE), which therefore represent the composition of the fluid that caused the garnet replacement. REE patterns in garnets in the host-rock quartzite, and Y element distribution mapping, suggest that HREEs were redistributed during the metamorphic evolution.

Rutile was the main subject as alternative to garnet in Chapter 8, studied for the effect that deformation has on its composition, using a variety of analytical techniques including Atom Probe tomography (APT). Zr-in-rutile thermometry combined with quartz inclusions in rutile, and coesite inclusions in the host omphacite vein, suggests that rutile grew just before the quartz-coesite transition. Deformation of the rutile formed low-angle boundaries that acted as fast diffusion pathways for various elements, some foreign to rutile. In this case, this diffusion had no significant effect on Zr-in-rutile temperatures, but at higher *T*, longer timescales and/or smaller spot size analyses, this deformation-accommodated diffusion must be taken into account.

This thesis highlights an extreme case of fluid-rock interaction in a long-lived fluid pathway. Fluids derived from dehydrating serpentinites led to high amounts of dissolution of matrix minerals, resulting in the accumulation of garnet. The fluids that circulated through these garnetites resulted in unique microstructures that reveal a history of IPS, GBM, radial fracturing, and partial replacement accommodated by infiltrating fluids. The study of elastic strains in inclusions revealed that garnet growth in this fluid-rich environment occurred at (near-) hydrostatic stresses, and elastic strains in zircon were used to show that host fracturing and resealing results in elastic strain resetting. Overall, the results of this thesis combine new insights into subduction zone deformation and fluid-assisted mass transfer, and the utility of garnet and rutile as hosts to inclusions rich in information. In both cases, deformation needs to be studied in detail to properly utilize the insights into the geological history that is stored in these host minerals, be it chemical, morphological, or from inclusions.

9.2 Future prospects

The extreme nature of fluid-rock interaction uncovered in the LCU, signified by the high degree of dissolution and GBM in garnet, warrants further research into the composition of this fluid. The data presented in this thesis is not sufficient for the quantification of absolute mass or volume loss, which is a further step in understanding mass transfer in subduction zones. Ideally, this concept is also tested in other parts of subduction zones to get a more comprehensive view of fluid-rock interaction and mass transfer rather than only extreme cases.

Elastic strain analysis using Raman spectrometry on inclusions in garnet shows great promise as a tool for the assessment of differential stress during garnet growth and mineral entrapment, albeit only qualitative for the time being. A next step in the development of this tool is to combine it with evidence from the garnet host, its inclusions, and the matrix if preserved, for paleopiezometry and paleo-stress-orientation. Careful inspection of the garnet host is necessary to confirm that garnet growth and deformation represent the same state of stress.

Another step to take in the further development of elastic geothermobarometry is the expansion to more minerals as host and inclusion, currently challenged by characteristics as crystal symmetry and chemically variable compositions. Examples of target minerals are rutile, omphacite, and tourmaline as host; coesite and apatite as inclusions.

The recently developed application of APT on earth materials opens up a new scale of high-quality chemical analysis. At the time of this research, it had not yet been applied to garnet successfully. However, in the future, this application can yield valuable insights regarding garnet growth, alteration, deformation, and the interaction of inclusion and host.

Acknowledgements

This thesis was made possible thanks to the work, support, help, and welcome distractions by many. First of all, a big thank you to Matteo Alvaro, who provided this opportunity, supported my work despite a strong deviation from the initial plan and gave me the freedom to do so while still getting the most out of this PhD. Also many thanks to Marco Scambelluri for helping me stay on the right track, the many discussions and support. I'm also grateful to David Wallis for getting me acquainted with EBSD and MTex, the always thoughtful and in-depth feedback, and the many hours in Utrecht spent at the EBSD-SEM.

The mineralogy research group and everyone involved in it has been of great value thanks to the many interesting and useful discussions and support, most notably Mattia Gilio who assisted with the published paper, Mattia Mazzucchelli for help with elastic geothermobarometry, and Mara Murri for dealing with my nonsense. Also a big thank you to Marta Morana who's always willing to help with just about anything that I can't figure out. But I can't forget the contributions and other support by the rest of the group: my former office mate Gabriele "Paccio" Zaffiro, my new office mate Joseph Gonzalez, Mattia Bonazzi, Anna Barbaro, Nicola Campomenosi, Claudia Stangarone, Kira Musiyachenko, Alice Girani, Giulia Mingardi, Zeno Geddo, Francesca Miozzi, Marco Piazzi, Daria Pasqual, Ross Angel, and Prof. M. Chiara Domeneghetti.

The work on trace elements in this thesis would not have been possible without Antonio Langone, who helped perform analyses, process the data, and interpret them afterwards.

Many thanks to Andrea Risplendente for performing the many EPMA analyses that were used in this thesis, and to the team in the Genova rock lab for most of the sample preparation.

I am grateful to Chris Spiers, Martyn Drury, Oliver Plümper, Leo Kriegsman, and Herman van Roermund for fruitful discussions on topics presented in Chapters 4 and 5, during my visits to Utrecht.

This thesis also benefited from the annual examinations taken care of by Alessio Sanfilippo, and from feedback by Giulio Borghini and Alberto Vitale Brovarone.

This project has received funding from the European Research Council under the European Union's Horizon 2020 research and innovation program grant agreement 714936 to M. Alvaro, and from the Italian MIUR to the PRIN program n. 2017ZE49E7. Part of Chapter 8 was performed at the Geoscience Atom Probe Facility at Curtin University and part of the Advanced Resource Characterisation Facility (ARCF). The ARCF, under the auspices of the National Resource Sciences Precinct (NRSP) - a collaboration between CSIRO, Curtin University, and The University of Western Australia - is supported by the Science and Industry Endowment Fund (SIEF). I gratefully acknowledge support of Curtin University's Microscopy & Microanalysis Facility and the John de Laeter Centre, whose instrumentation has been supported by University, State and Commonwealth Government funding. The research presented in Chapter 8 was carried out in cooperation with Rick Verberne, Steven Reddy, Denis Fougerouse, David Saxey and William Rickard.

Throughout this PhD, I've had the great pleasure of meeting fantastic people from and at all over the world, during courses, workshops, meetings, seminars, field trips, and conferences. There are way too many of you to name but I'm glad I met each and every one of you.

To all my friends and coworkers in Pavia, this experience wouldn't have been the same without you and I'm grateful to you all. Val and Mattia, perhaps it's good that this pandemic happened because otherwise writing my thesis would've been a lot harder. Mazzu and Marta, it was always fun to grab a quick beer or gelato. Joe and Emily, you've arrived only recently and entirely too late, but it's been great fun so far. There are too many of you to mention, but a special thank you to Anna, Stefania, Carlotta, Riccardo, Silvia, Niccolò, Yuri, and Chiara.

Getting through the pandemic was strange, but it was comforting to have friends online, most notably on Twitter and Discord. You know who you are, fellow cycling fans, geology nerds, gaming buddies, old friends, and more.

Mijn vrienden in Nederland, of waar jullie ook heen zijn gegaan sindsdien, zijn van onnoembare waarde voor mij en ik ben jullie allen ontzettend dankbaar. Telkens wanneer ik weer in Nederland ben, of wanneer ik jullie ergens anders ter wereld tegenkom, is het van ouds gezellig. Het vervelendste aan weg van huis gaan is dat jullie niet in de buurt zijn. Ik ben ongetwijfeld een paar mensen vergeten te noemen maar dat maakt jullie niet minder gewaardeerd.
Jaartje '09, in het bijzonder Rick, Jorien, en Robin, het is altijd gezellig met jullie.
Dank jullie wel beste Eindbazen, Martijn, Martijn, Joost, Joost, David, Arne, Oscar, Sietske, en Lisa. Ik kan niet wachten tot we weer samen op avontuur gaan.
Beste ex-Cambridgelaan, al gaat het om een borreltje, een filmavond, of en skivakantie, het is altijd ontzettend leuk en daar ben ik jullie erg dankbaar voor. Remi, Ingrid, Jolien, Eelco, Huub, Inge, Martijn, Roos, en Rick, hopelijk kan ik jullie in de toekomst weer wat vaker opzoeken.
Een speciaal bedankje aan Lisa, Jorien, en Rick. Jullie zijn fantastisch en het was bijzonder om samen de PhD door te komen, en om worstelingen en successen met elkaar te delen.
Sjoerd, ik zal je nooit vergeten.

Evelien, Marnix, en Irene, wat ben ik blij dat we dit allemaal hebben meegemaakt en dat jullie altijd bereid waren om me te steunen, advies en ervaring te delen, wanneer ik het nodig had, of te koppig was om dat toe te geven. Anja, Martijn, en Annet, wat fijn dat jullie ook bij de familie horen, en dat de deur altijd open staat.
Lukas en Maarten, hopelijk mag ik jullie ooit inspireren om ook jullie dromen te achtervolgen, mocht dat in de wetenschap zijn, in de muziek, of elders.
Opa Cossee, jij hebt me altijd geinspireerd, met name voor de natuur en alles eromheen.
Mama en papa, jullie hebben altijd voor mij klaar gestaan door weer en wind.

Appendix A: Supplementary data for Chapter 4

Table A1: EPMA measurements in wt% of transect 1L1, and corresponding calculated garnet composition in atoms per formula unit. Relative molar percentages of Fe vs Mg vs Mn as plotted in Figure 4.8 are also given. These values are plotted in Figure 4.8a. See Figure A1a for the location of the measurements.

1L1	10	11	12	13	14	15	16	17	18	19	20	21	22	23	24	25
SiO2	38.92	38.82	38.77	38.62	38.57	38.94	39.11	39.21	39.48	39.2	39.49	38.77	38.87	38.57	38.52	38.2
TiO2	0.0214	0.0414	0.1432	0.119	0	0.0456	0.094	0	0	0.0433	0.0149	0.0175	0.0175	0	0.063	0.0188
Al2O3	21.6	21.65	20.93	21.5	21.75	21.73	21.9	22.04	21.93	21.99	22.09	21.83	22.02	21.71	21.72	21.81
Cr2O3	0.037	0.0039	0	0	0.0328	0	0.0124	0	0	0.0074	0	0.0581	0.0138	0.0508	0	0
FeOx	10.18	9.22	8.71	11.79	8.88	8.02	8.34	10.75	9.39	9.18	9.44	12.68	12.52	19.83	19.9	22.69
MgO	4.36	3.64	3.15	3.57	4.35	4.5	4.75	4.74	5.73	5.68	5.49	4.11	3.96	3.02	3.12	2.46
MnO	23.61	25.29	24.63	21.83	24.47	24.33	23.35	20.35	19.59	20.38	20.26	18.73	19.11	14.38	14.19	11.6
CaO	3.52	4.41	6	4.9	4.15	4.82	5.15	5.33	6.05	6.2	5.96	6.08	5.92	4.89	4.8	5.4
Na2O	0.0147	0.0081	0	0.0229	0.0158	0.0574	0.0454	0.0328	0.0128	0.0371	0.0525	0.0013	0.0391	0.0412	0.0343	0.0442
K2O	0	0	0	0	0	0	0.0018	0.0021	0	0	0	0.0102	0	0	0	0
Total:	102.26	103.08	102.33	102.35	102.22	102.44	102.75	102.45	102.18	102.72	102.80	102.29	102.47	102.49	102.35	102.22
O	12	12	12	12	12	12	12	12	12	12	12	12	12	12	12	12
SiO2	3.015	2.996	3.017	2.999	2.985	2.999	2.996	3.008	3.013	2.979	3.001	2.991	2.995	3.002	3.001	2.988
TiO2	0.001	0.002	0.008	0.007	0	0.003	0.005	0	0	0.002	0.001	0.001	0.001	0	0.004	0.001
Al2O3	1.973	1.970	1.920	1.968	1.985	1.973	1.978	1.993	1.973	1.970	1.979	1.985	2.000	1.992	1.995	2.011
Cr2O3	0.002	0.000	0	0	0.002	0	0.001	0	0	0.000	0	0.004	0.001	0.003	0	0
Fe2O3	0	0.035	0.029	0.023	0.045	0.032	0.026	0	0.003	0.073	0.025	0.029	0.013	0.007	0.002	0.016
FeO	0.660	0.560	0.537	0.743	0.530	0.484	0.509	0.690	0.596	0.510	0.575	0.789	0.794	1.284	1.295	1.468
MnO	1.549	1.653	1.623	1.436	1.604	1.587	1.515	1.322	1.266	1.312	1.304	1.224	1.247	0.948	0.936	0.769
MgO	0.503	0.419	0.365	0.413	0.502	0.516	0.542	0.542	0.652	0.643	0.622	0.473	0.455	0.350	0.362	0.287
CaO	0.292	0.365	0.500	0.408	0.344	0.398	0.423	0.438	0.495	0.505	0.485	0.503	0.489	0.408	0.401	0.453
Na2O	0.002	0.001	0	0.003	0.002	0.009	0.007	0.005	0.002	0.005	0.008	0.000	0.006	0.006	0.005	0.007
K2O	0	0	0	0	0	0	0.000	0.000	0	0	0	0.001	0	0	0	0
Totals	7.997	8.000	8.000	8.000	8.000	8.000	8.000	7.998	8.000	8.000	8.000	8.000	8.000	8.000	8.000	8.000
FeO*	0.655	0.564	0.511	0.743	0.550	0.499	0.520	0.698	0.587	0.540	0.589	0.801	0.809	1.294	1.301	1.492
Fe	24.20%	21.39%	20.45%	28.67%	20.70%	19.17%	20.18%	27.23%	23.44%	21.65%	23.41%	32.07%	32.23%	49.91%	50.04%	58.57%
Mg	18.59%	15.88%	14.61%	15.94%	18.89%	19.85%	21.04%	21.15%	26.01%	25.78%	24.73%	18.92%	18.11%	13.51%	13.93%	11.26%
Mn	57.21%	62.72%	64.94%	55.39%	60.41%	60.99%	58.78%	51.61%	50.55%	52.57%	51.86%	49.01%	49.66%	36.57%	36.02%	30.17%

Table A1 (cont.):

1L1	1	2	3	4	5	6	7	8	9
SiO2	38.96	38.9	38.71	39.26	39.53	39.53	39	39.14	39.26
TiO2	0.0242	0	0	0.0189	0.0175	0.0271	0.0256	0.0215	0
Al2O3	21.63	22.07	21.81	21.52	21.8	21.83	21.83	22.08	21.83
Cr2O3	0	0	0.0474	0	0.055	0	0	0.0167	0.028
FeOx	18.99	15.38	15.69	13.1	13.94	10.15	10.07	8.66	8.32
MgO	3.28	3.85	3.51	4.43	4.14	5.85	5.33	5.15	4.81
MnO	14.69	17.1	17.43	17.86	18.35	19.25	20.38	22.34	23.8
CaO	4.87	5.09	5.25	6.16	5.83	5.83	5.39	5.15	4.99
Na2O	0.0154	0	0.0035	0.0171	0	0.0229	0	0.0165	0.0335
K2O	0.0006	0	0.005	0.0138	0	0	0.0068	0	0.0049
Total:	102.46	102.39	102.46	102.38	103.66	102.49	102.03	102.57	103.08
O	12	12	12	12	12	12	12	12	12
SiO2	3.023	3.004	3.000	3.021	3.014	3.009	2.995	2.994	2.999
TiO2	0.001	0	0	0.001	0.001	0.002	0.001	0.001	0
Al2O3	1.979	2.010	1.993	1.952	1.960	1.959	1.976	1.991	1.966
Cr2O3	0	0	0.003	0	0.003	0	0	0.001	0.002
Fe2O3	0	0	0.005	0.008	0.006	0.022	0.032	0.019	0.038
FeO	1.232	0.993	1.013	0.835	0.883	0.624	0.615	0.535	0.493
MnO	0.966	1.119	1.144	1.164	1.185	1.241	1.326	1.447	1.540
MgO	0.379	0.443	0.405	0.508	0.471	0.664	0.610	0.587	0.548
CaO	0.405	0.421	0.436	0.508	0.476	0.476	0.444	0.422	0.408
Na2O	0.002	0	0.001	0.003	0	0.003	0	0.002	0.005
K2O	0.000	0	0.000	0.001	0	0	0.001	0	0.000
Totals	7.987	7.991	8.000	8.000	8.000	8.000	8.000	8.000	8.000
FeO*	1.250	1.017	1.014	0.820	0.868	0.619	0.621	0.543	0.504
Fe	48.18%	39.43%	39.56%	32.91%	34.39%	24.54%	24.28%	21.08%	19.44%
Mg	14.62%	17.19%	15.81%	20.38%	18.64%	26.29%	23.86%	22.77%	21.13%
Mn	37.20%	43.38%	44.63%	46.70%	46.97%	49.17%	51.86%	56.15%	59.43%

Table A2: EPMA measurements in wt% of transect 2L1, and corresponding calculated garnet composition in atoms per formula unit. Relative molar percentages of Fe vs Mg vs Mn as plotted in Figure 4.8 are also given. These values are plotted in Figure 4.8a. See Figure A1b for location of the measurements.

2L1	20	21	22	23	24	25
SiO2	38.77	38.59	38.97	39.31	39.06	38.87
TiO2	0.0414	0.0576	0.0418	0.0471	0.0014	0.0067
Al2O3	21.72	21.64	21.86	21.87	22.31	22.28
Cr2O3	0.0389	0	0	0.0024	0.0039	0.0173
FeOx	7.7	7.03	12.8	13.57	14.05	16.64
MgO	3.23	3.93	4.28	4.39	4.26	3.85
MnO	26.16	25.48	18.94	18.08	18.33	16.33
CaO	5.03	5.64	6.06	5.73	5.33	5.04
Na2O	0.0442	0.0191	0	0.0367	0	0.0322
K2O	0.0113	0.0054	0.0052	0	0.0198	0.0009
Total:	102.75	102.39	102.96	103.04	103.37	103.07
O	12	12	12	12	12	12
SiO2	3.001	2.981	2.986	3.008	2.984	2.987
TiO2	0.002	0.003	0.002	0.003	0.000	0.000
Al2O3	1.982	1.971	1.975	1.973	2.009	2.019
Cr2O3	0.002	0	0	0.000	0.000	0.001
Fe2O3	0.016	0.065	0.048	0.011	0.026	0.010
FeO	0.482	0.390	0.772	0.858	0.872	1.060
MnO	1.715	1.667	1.229	1.172	1.186	1.063
MgO	0.373	0.452	0.489	0.501	0.485	0.441
CaO	0.417	0.467	0.498	0.470	0.436	0.415
Na2O	0.007	0.003	0	0.005	0	0.005
K2O	0.001	0.001	0.001	0	0.002	0.000
Totals	8.000	8.000	8.000	8.000	8.000	8.000
FeO rec.	0.495	0.413	0.784	0.858	0.893	1.081
Fe	19.16%	16.32%	31.34%	33.90%	34.82%	41.82%
Mg	14.43%	17.86%	19.53%	19.79%	18.92%	17.06%
Mn	66.42%	65.82%	49.13%	46.32%	46.26%	41.12%

Table A2 (cont.):

2L1	3	4	5	6	7	8	9	10	11	12	13	14	15	16	17	18	19
SiO2	39.02	39.19	39.33	39.57	39.32	39.41	38.57	39.08	38.85	38.84	38.39	38.21	38.16	38.15	38.47	38.62	38.81
TiO2	0.0364	0	0.0135	0	0.0553	0.0216	0.0227	0.0373	0.0254	0.0518	0.0611	0.1144	0.0775	0.0961	0.1066	0.0534	0.0093
Al2O3	21.85	21.95	21.97	22.04	21.91	21.56	21.6	21.53	21.7	21.55	21.65	21.42	20.98	20.86	20.78	21.15	21.5
Cr2O3	0	0.0227	0	0	0	0	0	0	0.0597	0.0146	0.0261	0	0.0136	0	0	0.0414	0
FeOx	13.23	9.96	8.25	8.25	9.09	7.49	6.11	4.67	12.33	9.96	7.48	11.37	11.03	14.56	11.82	14.78	14.24
MgO	4.73	5.4	5.84	5.65	5.41	4.82	3.75	3.18	2.84	2.97	2.76	2.94	2.57	2.26	2.41	2.63	2.76
MnO	18.02	20.01	20.92	21.7	20.55	23.29	26.84	29.36	22.04	25.54	27.54	23.82	23.03	20.74	23.33	20.27	20.44
CaO	5.87	6.1	5.93	5.73	5.89	5.88	5.48	5.26	5.31	4.2	4.76	4.46	5.77	5.75	5.89	5.26	5.4
Na2O	0.0612	0.0655	0.0059	0.0136	0.0273	0	0.035	0.0095	0.0497	0.0709	0.0311	0	0.0408	0.0291	0.0209	0.0261	0
K2O	0	0.0032	0	0	0	0	0.0021	0	0.0054	0	0	0	0.0033	0	0	0	0
Total:	102.82	102.70	102.26	102.95	102.25	102.47	102.41	103.13	103.21	103.20	102.70	102.33	101.68	102.45	102.83	102.83	103.16
O	12	12	12	12	12	12	12	12	12	12	12	12	12	12	12	12	12
SiO2	2.985	2.984	2.998	3.003	3.006	3.022	2.983	3.016	3.003	3.007	2.986	2.985	2.999	2.988	2.998	3.006	3.006
TiO2	0.002	0	0.001	0	0.003	0.001	0.001	0.002	0.001	0.003	0.004	0.007	0.005	0.006	0.006	0.003	0.001
Al2O3	1.970	1.970	1.975	1.972	1.975	1.949	1.970	1.959	1.977	1.967	1.986	1.973	1.944	1.926	1.909	1.941	1.963
Cr2O3	0	0.001	0	0	0	0	0	0	0.004	0.001	0.002	0	0.001	0	0	0.003	0
Fe2O3	0.066	0.070	0.029	0.025	0.010	0.003	0.067	0.006	0.019	0.023	0.037	0.042	0.056	0.092	0.085	0.042	0.023
FeO	0.780	0.564	0.497	0.498	0.572	0.477	0.329	0.295	0.778	0.622	0.449	0.700	0.669	0.862	0.686	0.920	0.900
MnO	1.167	1.290	1.351	1.395	1.331	1.513	1.759	1.919	1.443	1.675	1.815	1.576	1.533	1.376	1.540	1.337	1.341
MgO	0.539	0.613	0.664	0.639	0.616	0.551	0.432	0.366	0.327	0.343	0.320	0.342	0.301	0.264	0.280	0.305	0.319
CaO	0.481	0.498	0.484	0.466	0.483	0.483	0.454	0.435	0.440	0.348	0.397	0.373	0.486	0.483	0.492	0.439	0.448
Na2O	0.009	0.010	0.001	0.002	0.004	0	0.005	0.001	0.007	0.011	0.005	0	0.006	0.004	0.003	0.004	0
K2O	0	0.000	0	0	0	0	0.000	0	0.001	0	0	0	0.000	0	0	0	0
Totals	8.000	8.000	8.000	8.000	8.000	8.000	8.000	8.000	8.000	8.000	8.000	8.000	8.000	8.000	8.000	8.000	8.000
FeO rec.	0.812	0.599	0.501	0.500	0.570	0.453	0.355	0.280	0.790	0.634	0.468	0.708	0.680	0.878	0.688	0.920	0.892
Fe	32.25%	23.94%	19.92%	19.74%	22.64%	18.00%	13.95%	10.92%	30.87%	23.91%	18.00%	26.95%	27.05%	34.87%	27.43%	35.90%	34.96%
Mg	21.40%	24.49%	26.38%	25.21%	24.49%	21.89%	16.98%	14.26%	12.78%	12.92%	12.29%	13.03%	11.97%	10.48%	11.16%	11.91%	12.49%
Mn	46.35%	51.57%	53.70%	55.04%	52.87%	60.11%	69.07%	74.83%	56.36%	63.17%	69.71%	60.02%	60.98%	54.65%	61.41%	52.18%	52.55%

Table A2 (cont.):

2L1	1	2
SiO2	38.27	38.51
TiO2	0	0.0148
Al2O3	21.35	21.82
Cr2O3	0	0.0358
FeOx	22.91	16.23
MgO	1.84	3.74
MnO	12.49	16.67
CaO	5.23	5.4
Na2O	0	0.0617
K2O	0	0
Total:	102.09	102.48
O	12	12
SiO2	3.014	2.978
TiO2	0	0.001
Al2O3	1.982	1.990
Cr2O3	0	0.002
Fe2O3	0	0.058
FeO	1.509	0.992
MnO	0.833	1.092
MgO	0.216	0.431
CaO	0.441	0.447
Na2O	0	0.009
K2O	0	0
Totals	7.995	8.000
FeO rec.	1.510	1.029
Fe	59.00%	40.33%
Mg	8.44%	16.89%
Mn	32.56%	42.78%

Table A3: EPMA measurements in wt% of transect 3L1, and corresponding calculated garnet composition in atoms per formula unit. Relative molar percentages of Fe vs Mg vs Mn as plotted in Figure 4.8 are also given. These values are plotted in Figure 4.8b. See Figure A1c for location of the measurements.

3L1	8	9	10	11	12	13	14	15	16	17	18	19	20
SiO2	37.68	37.5	37.67	37.59	37.6	38.24	37.96	38.12	38.32	38.37	38.07	38.29	38.59
TiO2	0.1682	0.2362	0.2789	0.3183	0.2981	0.1252	0.0459	0.0139	0.0376	0.0599	0	0.0293	0.0517
Al2O3	21.14	20.64	20.81	20.49	20.26	21	21.35	21.46	21.42	21.62	21.31	21.33	21.54
Cr2O3	0.0509	0	0	0	0	0	0	0	0	0	0.003	0.0183	0.0048
FeOx	19.81	16.04	16.81	17.82	17.26	12.41	16.1	18.2	19.44	15.22	20.66	18.38	5.84
MgO	1.97	2.39	2.29	2.24	2.24	2.23	2.53	2.49	2.18	2.54	1.78	2.02	2.92
MnO	16.43	19.46	19.5	17.8	18.97	22.25	18.86	17.63	16.66	19.88	15.38	16.68	28.02
CaO	4.96	5.26	5.2	5.26	4.6	5.57	5.04	4.27	4.84	4.88	4.89	5.53	5.19
Na2O													
K2O	0.0022	0	0	0.0167	0.0038	0	0	0	0.007	0	0.0044	0	0.0091
Total:	102.21	101.53	102.56	101.54	101.23	101.83	101.89	102.18	102.90	102.57	102.10	102.28	102.17
O	12	12	12	12	12	12	12	12	12	12	12	12	12
SiO2	2.970	2.967	2.955	2.979	2.994	3.011	2.984	2.994	2.993	2.995	3.004	3.006	3.009
TiO2	0.010	0.014	0.016	0.019	0.018	0.007	0.003	0.001	0.002	0.004	0	0.002	0.003
Al2O3	1.964	1.925	1.925	1.914	1.902	1.949	1.978	1.987	1.973	1.990	1.982	1.974	1.980
Cr2O3	0.003	0	0	0	0	0	0	0	0	0	0.000	0.001	0.000
Fe2O3	0.074	0.112	0.132	0.092	0.076	0.014	0.048	0.024	0.037	0.013	0.011	0.010	0
FeO	1.232	0.949	0.971	1.088	1.073	0.803	1.010	1.171	1.233	0.981	1.352	1.197	0.381
MnO	1.097	1.304	1.296	1.195	1.279	1.484	1.256	1.173	1.102	1.314	1.028	1.109	1.851
MgO	0.231	0.282	0.268	0.265	0.266	0.262	0.296	0.291	0.254	0.295	0.209	0.236	0.339
CaO	0.419	0.446	0.437	0.447	0.392	0.470	0.424	0.359	0.405	0.408	0.413	0.465	0.434
Na2O	0	0	0	0	0	0	0	0	0	0	0	0	0
K2O	0.000	0	0	0.002	0.000	0	0	0	0.001	0	0.000	0	0.001
Totals	8.000	8.000	8.000	8.000	8.000	8.000	8.000	8.000	8.000	8.000	8.000	8.000	7.998
FeO rec.	1.253	0.968	0.999	1.094	1.063	0.785	1.023	1.177	1.239	0.982	1.349	1.189	0.376
Fe	48.54%	37.90%	38.99%	42.85%	40.75%	31.01%	39.74%	44.55%	47.74%	37.88%	52.17%	46.92%	14.66%
Mg	8.96%	11.03%	10.45%	10.36%	10.19%	10.34%	11.51%	11.04%	9.78%	11.40%	8.09%	9.32%	13.22%
Mn	42.49%	51.07%	50.56%	46.79%	49.06%	58.65%	48.76%	44.41%	42.48%	50.72%	39.74%	43.76%	72.12%

Table A3 (cont.):

3L1	1	2	3	4	5	6	7
SiO2	38.42	37.93	37.6	37.68	37.46	37.22	37.68
TiO2	0.021	0.0726	0.2159	0.1127	0.3282	0.1776	0.3127
Al2O3	21.81	21.51	20.63	21.41	20.57	20.48	20.47
Cr2O3	0.0549	0	0	0	0	0	0
FeOx	12.47	15.28	8.59	13.62	21.23	18.96	20.49
MgO	3.7	2.58	2.07	2.51	1.82	2.05	1.95
MnO	19.94	18.45	26.89	20.71	15.02	17.41	15.87
CaO	5.75	5.97	5.23	5.32	5.61	4.89	5.27
Na2O							
K2O	0	0.0005	0	0.0049	0	0	0.0058
Total:	102.17	101.79	101.23	101.37	102.04	101.19	102.05
O	12	12	12	12	12	12	12
SiO2	2.979	2.975	2.986	2.973	2.963	2.966	2.979
TiO2	0.001	0.004	0.013	0.007	0.020	0.011	0.019
Al2O3	1.993	1.989	1.932	1.992	1.918	1.924	1.908
Cr2O3	0.003	0	0	0	0	0	0
Fe2O3	0.043	0.052	0.070	0.049	0.118	0.123	0.097
FeO	0.765	0.950	0.500	0.850	1.286	1.140	1.258
MnO	1.309	1.226	1.809	1.384	1.006	1.175	1.063
MgO	0.428	0.302	0.245	0.295	0.215	0.243	0.230
CaO	0.478	0.502	0.445	0.450	0.475	0.418	0.446
Na2O	0	0	0	0	0	0	0
K2O	0	0.000	0	0.000	0	0	0.001
Totals	8.000	8.000	8.000	8.000	8.000	8.000	8.000
FeO rec.	0.785	0.971	0.501	0.871	1.304	1.164	1.261
Fe	31.13%	38.86%	19.61%	34.15%	51.65%	45.07%	49.38%
Mg	16.95%	12.07%	9.59%	11.57%	8.50%	9.43%	9.00%
Mn	51.92%	49.07%	70.80%	54.28%	39.85%	45.50%	41.62%

Table A4: EPMA measurements in wt% of transect 3L2 and point measurement 3-3, and corresponding calculated garnet composition in atoms per formula unit. Relative molar percentages of Fe vs Mg vs Mn as plotted in Figure 4.8 are also given. These values are plotted in Figure 4.8b. See Figure A1c for location of the measurements.

3L2	10	11	12	13	14	15	3-3
SiO2	38.79	38.67	38.5	38.67	38.55	37.68	37.58
TiO2	0.1067	0	0.0337	0	0.0561	0.0098	0.0266
Al2O3	21.65	21.95	21.94	21.86	21.83	21.95	21.96
Cr2O3	0	0	0	0	0	0	0.0541
FeOx	8.06	9.68	11.97	13.77	13.88	17.6	24.62
MgO	4.81	4.86	4.25	3.89	3.67	2.71	1.85
MnO	22.63	20.83	19.04	17.52	18.32	16.26	11.16
CaO	5.84	6.04	6.21	6.26	5.83	5.62	5.42
Na2O							
K2O	0.0122	0	0.0137	0	0	0	0.0029
Total:	101.90	102.03	101.96	101.97	102.14	101.83	102.67
O	12	12	12	12	12	12	12.000
SiO2	2.991	2.975	2.975	2.995	2.989	2.952	2.943
TiO2	0.006	0	0.002	0	0.003	0.001	0.002
Al2O3	1.968	1.991	1.999	1.996	1.996	2.027	2.028
Cr2O3	0	0	0	0	0	0	0.003
Fe2O3	0.038	0.060	0.049	0.015	0.019	0.068	0.079
FeO	0.481	0.562	0.724	0.877	0.881	1.085	1.533
MnO	1.478	1.357	1.246	1.149	1.203	1.079	0.740
MgO	0.553	0.557	0.489	0.449	0.424	0.316	0.216
CaO	0.483	0.498	0.514	0.519	0.484	0.472	0.455
Na2O	0	0	0	0	0	0	0.000
K2O	0.001	0	0.001	0	0	0	0.000
Totals	8.000	8.000	8.000	8.000	8.000	8.000	8.000
FeO rec.	0.487	0.588	0.750	0.882	0.888	1.133	1.589
Fe	19.33%	23.49%	30.18%	35.57%	35.31%	44.81%	62.43%
Mg	21.96%	22.27%	19.69%	18.10%	16.86%	12.51%	8.48%
Mn	58.72%	54.24%	50.13%	46.33%	47.83%	42.68%	29.09%

Table A4 (cont.):

3L2	1	2	3	4	5	6	7	8	9
SiO2	37.93	37.94	38.01	38.31	38.07	38.1	38.63	38.49	38.72
TiO2	0.0388	0.0498	0.0458	0.0444	0.0528	0.0515	0.0154	0.028	0
Al2O3	20.95	21.4	21.47	21.45	21.32	21.77	21.53	21.58	21.81
Cr2O3	0	0	0.0305	0.0115	0	0	0	0	0.0135
FeOx	9.27	7.5	5.93	5.66	5.42	6.05	6.67	6.7	8.22
MgO	2.51	2.64	2.51	2.78	2.87	3.6	3.71	4.06	4.86
MnO	26.36	27.93	28.53	28.8	28.45	26.73	25.59	24.57	22.24
CaO	4.78	4.41	5.02	4.88	4.99	5.35	5.69	5.81	5.88
Na2O									
K2O	0.0102	0	0	0	0	0.0058	0.0039	0.0005	0
Total:	101.85	101.87	101.55	101.94	101.17	101.66	101.84	101.24	101.74
O	12	12	12	12	12	12	12	12	12
SiO2	2.986	2.982	2.992	3.001	3.001	2.970	3.003	3.000	2.987
TiO2	0.002	0.003	0.003	0.003	0.003	0.003	0.001	0.002	0
Al2O3	1.945	1.983	1.993	1.981	1.981	2.001	1.973	1.983	1.984
Cr2O3	0	0	0.002	0.001	0	0	0	0	0.001
Fe2O3	0.080	0.048	0.016	0.012	0.012	0.053	0.019	0.014	0.041
FeO	0.531	0.445	0.375	0.358	0.346	0.342	0.414	0.423	0.489
MnO	1.758	1.859	1.902	1.911	1.899	1.765	1.685	1.622	1.453
MgO	0.295	0.309	0.294	0.324	0.337	0.418	0.430	0.472	0.559
CaO	0.403	0.371	0.423	0.410	0.421	0.447	0.474	0.485	0.486
Na2O	0	0	0	0	0	0	0	0	0
K2O	0.001	0	0	0	0	0.001	0.000	0.000	0
Totals	8.000	8.000	8.000	8.000	8.000	8.000	8.000	8.000	8.000
FeO rec.	0.544	0.460	0.380	0.355	0.342	0.369	0.411	0.421	0.502
Fe	20.96%	17.51%	14.74%	13.71%	13.27%	14.47%	16.28%	16.75%	19.96%
Mg	11.34%	11.76%	11.43%	12.53%	13.07%	16.38%	17.02%	18.75%	22.23%
Mn	67.70%	70.73%	73.83%	73.76%	73.66%	69.14%	66.71%	64.50%	57.81%

Table A5: EPMA measurements in wt% of transect 4L1, and corresponding calculated garnet composition in atoms per formula unit. Relative molar percentages of Fe vs Mg vs Mn as plotted in Figure 4.8 are also given. These values are plotted in Figure 4.8c. See Figure A1d for location of the measurements.

4L1	25	26	27	28	29	30
SiO2	38.29	38.37	38.21	38.28	38.34	38.61
TiO2	0.0681	0.0762	0.0294	0.0067	0.0174	0.0148
Al2O3	21.38	21.67	21.85	21.87	21.66	21.65
Cr2O3	0	0.0346	0	0.039	0.0477	0
FeOx	4.59	4.77	5.01	5.3	5.32	5.57
MgO	2.93	3.25	3.44	3.48	3.6	3.82
MnO	29.59	28.87	28.51	28.45	27.74	27.1
CaO	4.97	5.04	5.14	5.01	5.25	5.19
Na2O						
K2O	0.001	0.0055	0.0018	0.0044	0	0
Total:	101.82	102.09	102.19	102.44	101.98	101.95
O	12	12	12	12	12	12
SiO2	2.999	2.989	2.969	2.968	2.982	2.998
TiO2	0.004	0.004	0.002	0.000	0.001	0.001
Al2O3	1.974	1.990	2.001	1.999	1.986	1.982
Cr2O3	0	0.002	0	0.002	0.003	0
Fe2O3	0.020	0.021	0.058	0.063	0.045	0.019
FeO	0.281	0.289	0.268	0.281	0.301	0.343
MnO	1.963	1.905	1.876	1.868	1.827	1.783
MgO	0.342	0.377	0.398	0.402	0.417	0.442
CaO	0.417	0.421	0.428	0.416	0.438	0.432
Na2O	0	0	0	0	0	0
K2O	0.000	0.001	0.000	0.000	0	0
Totals	8.000	8.000	8.000	8.000	8.000	8.000
FeO rec.	0.278	0.297	0.297	0.313	0.318	0.343
Fe	10.76%	11.52%	11.56%	12.13%	12.40%	13.37%
Mg	13.24%	14.63%	15.49%	15.56%	16.28%	17.22%
Mn	76.00%	73.86%	72.95%	72.31%	71.32%	69.42%

Table A5 (cont.):

4L1	7	8	9	10	11	12	13	14	15	16	17	18	19	20	21	22	23	24
SiO2	37.94	37.82	38.28	37.98	37.91	37.48	37.51	37.73	37.99	37.83	37.76	38.21	38.04	37.78	38.1	37.79	38.36	38.15
TiO2	0.0532	0.0146	0.1388	0.1734	0.0613	0.0902	0.065	0.0225	0.0173	0.0292	0	0	0.0267	0.036	0.0881	0	0.0853	0.0066
Al2O3	21.55	21.42	21.29	21.32	21.41	21.43	21.29	21.51	21.52	21.89	21.75	21.67	21.63	21.75	21.77	21.6	21.58	21.56
Cr2O3	0.0064	0.0011	0.0312	0	0.0402	0.0133	0.0478	0.0243	0.0078	0.0284	0.0458	0	0	0	0.0003	0	0	0
FeOx	14.6	15.14	13.98	13.69	11.91	9.81	9.2	9.4	10.74	9.66	6.64	8.2	9.93	7.87	6.26	5.69	4.93	4.61
MgO	2.49	2.23	2.26	2.17	2.37	2.49	2.52	2.44	2.14	2.23	2.44	2.52	2.56	2.69	2.72	2.79	2.68	2.83
MnO	22.55	21.22	22.19	22.16	24.44	27.18	27.69	27.41	25.34	27.14	28.86	26.78	25.19	26.86	27.8	28.72	29.7	30.28
CaO	3.46	4.2	4.81	4.95	4.45	3.63	3.56	3.58	4.46	4.15	4.56	5.25	5.14	4.95	4.93	5.02	5.11	4.54
Na2O																		
K2O	0	0.0077	0	0	0	0	0	0.0002	0	0	0.0092	0.004	0	0	0	0.0008	0	0.005
Total:	102.65	102.05	102.98	102.44	102.59	102.12	101.88	102.12	102.22	102.96	102.06	102.63	102.52	101.94	101.67	101.61	102.45	101.98
O	12	12	12	12	12	12	12	12	12	12	12	12	12	12	12	12	12	12
SiO2	2.972	2.979	2.987	2.979	2.968	2.950	2.959	2.969	2.986	2.952	2.962	2.977	2.968	2.960	2.989	2.967	2.991	2.987
TiO2	0.003	0.001	0.008	0.010	0.004	0.005	0.004	0.001	0.001	0.002	0	0	0.002	0.002	0.005	0	0.005	0.000
Al2O3	1.990	1.989	1.959	1.971	1.976	1.988	1.980	1.995	1.994	2.014	2.012	1.990	1.990	2.009	2.014	2.000	1.983	1.990
Cr2O3	0.000	0.000	0.002	0	0.002	0.001	0.003	0.002	0.000	0.002	0.003	0	0	0	0.000	0	0	0
Fe2O3	0.059	0.051	0.049	0.051	0.079	0.101	0.091	0.063	0.032	0.077	0.062	0.056	0.070	0.066	0	0.066	0.025	0.035
FeO	0.898	0.946	0.863	0.847	0.701	0.545	0.515	0.555	0.674	0.553	0.374	0.478	0.578	0.450	0.411	0.308	0.296	0.267
MnO	1.496	1.416	1.467	1.472	1.621	1.812	1.850	1.827	1.687	1.794	1.918	1.767	1.665	1.783	1.848	1.910	1.961	2.008
MgO	0.291	0.262	0.263	0.254	0.277	0.292	0.296	0.286	0.251	0.259	0.285	0.293	0.298	0.314	0.318	0.327	0.311	0.330
CaO	0.290	0.355	0.402	0.416	0.373	0.306	0.301	0.302	0.376	0.347	0.383	0.438	0.430	0.416	0.414	0.422	0.427	0.381
Na2O	0	0	0	0	0	0	0	0	0	0	0	0	0	0	0	0	0	0
K2O	0	0.001	0	0	0	0	0	0.000	0	0	0.001	0.000	0	0	0	0.000	0	0.000
Totals	8.000	8.000	8.000	8.000	8.000	8.000	8.000	8.000	8.000	8.000	8.000	8.000	8.000	8.000	7.999	8.000	8.000	8.000
FeO rec.	0.922	0.968	0.868	0.858	0.730	0.590	0.553	0.585	0.687	0.600	0.413	0.502	0.608	0.487	0.420	0.341	0.300	0.280
Fe	34.05%	36.58%	33.42%	33.21%	27.77%	21.90%	20.47%	21.69%	26.17%	22.60%	15.80%	19.59%	23.64%	18.86%	16.24%	13.22%	11.68%	10.71%
Mg	10.73%	9.90%	10.12%	9.82%	10.53%	10.84%	10.98%	10.60%	9.55%	9.78%	10.90%	11.42%	11.58%	12.16%	12.30%	12.67%	12.10%	12.61%
Mn	55.23%	53.52%	56.46%	56.97%	61.70%	67.26%	68.55%	67.70%	64.28%	67.62%	73.29%	68.99%	64.78%	68.98%	71.46%	74.11%	76.22%	76.68%

Table A5 (cont.):

4L1	1	2	3	4	5	6
SiO2	37.89	37.97	37.88	37.94	38.21	37.74
TiO2	0.2303	0.0241	0	0.0107	0	0.0319
Al2O3	20.52	21.36	21.67	21.43	21.6	21.79
Cr2O3	0.0055	0	0	0	0	0.0064
FeOx	20.28	19.88	17.38	18.15	18.58	16.31
MgO	1.67	1.86	2.19	2.01	2.06	2.31
MnO	16.07	16.39	18.77	18	19.05	21.43
CaO	5.69	5.02	4.76	4.93	3.83	2.92
Na2O						
K2O	0.0286	0.0412	0.0071	0.0059	0.0183	0.0067
Total:	102.38	102.55	102.66	102.48	103.35	102.55
O	12	12	12	12	12	12
SiO2	2.988	2.981	2.964	2.978	2.981	2.965
TiO2	0.014	0.001	0	0.001	0	0.002
Al2O3	1.908	1.977	1.999	1.983	1.987	2.018
Cr2O3	0.000	0	0	0	0	0.000
Fe2O3	0.092	0.061	0.073	0.060	0.053	0.049
FeO	1.245	1.244	1.064	1.131	1.159	1.023
MnO	1.073	1.090	1.244	1.197	1.259	1.426
MgO	0.196	0.218	0.255	0.235	0.240	0.270
CaO	0.481	0.422	0.399	0.415	0.320	0.246
Na2O	0	0	0	0	0	0
K2O	0.003	0.004	0.001	0.001	0.002	0.001
Totals	8.000	8.000	8.000	8.000	8.000	8.000
FeO rec.	1.250	1.270	1.101	1.154	1.181	1.058
Fe	49.60%	49.26%	42.34%	44.62%	44.09%	38.40%
Mg	7.79%	8.44%	9.82%	9.09%	8.94%	9.82%
Mn	42.61%	42.29%	47.84%	46.29%	46.97%	51.78%

Table A6: EPMA measurements in wt% of transect 5L1, and corresponding calculated garnet composition in atoms per formula unit. Relative molar percentages of Fe vs Mg vs Mn as plotted in Figure 4.8 are also given. These values are plotted in Figure 4.8c. See Figure A1e for location of the measurements.

5L1	12	13	14	15	16	17	18	19	20
SiO2	38.71	39	38.84	39.24	39.08	39.02	38.93	38.19	37.69
TiO2	0.0322	0	0.0094	0	0.0984	0.0513	0.0499	0.0927	0.3635
Al2O3	21.49	21.64	21.81	21.69	21.79	21.91	21.57	21.35	20.72
Cr2O3	0	0.0184	0.002	0.0457	0	0	0	0	0.0135
FeOx	5.64	6.26	6.78	7.03	7.62	8.64	14.55	21.33	21.67
MgO	3.52	3.94	4.3	4.45	4.86	4.45	3.14	1.87	1.87
MnO	27.5	26.45	25.39	23.86	23.76	22.9	18.66	14.58	15.52
CaO	5.12	5.22	5.28	5.64	5.45	5.29	5.76	5.64	4.51
Na2O									
K2O	0.0032	0	0.0083	0.0064	0	0	0	0	0.0007
Total:	102.02	102.53	102.42	101.96	102.66	102.26	102.66	103.05	102.36
O	12	12	12	12	12	12	12	12	12
SiO2	3.012	3.011	2.993	3.025	2.994	3.006	3.016	2.982	2.977
TiO2	0.002	0	0.001	0	0.006	0.003	0.003	0.005	0.022
Al2O3	1.971	1.969	1.981	1.971	1.968	1.990	1.970	1.965	1.929
Cr2O3	0	0.001	0.000	0.003	0	0	0	0	0.001
Fe2O3	0.001	0.008	0.032	0	0.033	0	0	0.059	0.073
FeO	0.366	0.396	0.405	0.453	0.456	0.557	0.943	1.334	1.358
MnO	1.812	1.730	1.657	1.558	1.542	1.494	1.224	0.964	1.038
MgO	0.408	0.453	0.494	0.511	0.555	0.511	0.363	0.218	0.220
CaO	0.427	0.432	0.436	0.466	0.447	0.437	0.478	0.472	0.382
Na2O	0	0	0	0	0	0	0	0	0
K2O	3E-04	0	8E-04	6E-04	0	0	0	0	7E-05
Totals	8.000	8.000	8.000	7.988	8.000	7.997	7.996	8.000	8.000
FeO rec.	0.352	0.385	0.413	0.465	0.456	0.558	0.935	1.346	1.360
Fe	13.70%	15.01%	16.10%	18.34%	17.86%	21.78%	37.07%	53.24%	51.94%
Mg	15.86%	17.65%	19.26%	20.18%	21.74%	19.93%	14.37%	8.61%	8.41%
Mn	70.44%	67.34%	64.64%	61.48%	60.40%	58.29%	48.55%	38.15%	39.66%

Table A6 (cont.):

5L1	1	2	3	4	5	6	7	8	9	10	11
SiO2	37.79	37.93	37.64	38.21	37.97	38.62	38.45	38.8	38.7	38.62	38.46
TiO2	0.3173	0.3246	0.2294	0.1931	0	0.0282	0.0389	0	0.0281	0.0429	0.0214
Al2O3	20.49	21.02	20.68	20.91	21.26	21.38	21.51	21.47	21.54	21.8	21.56
Cr2O3	0.0458	0.007	0.0199	0	0.0251	0	0	0	0.0475	0.0568	0
FeOx	18.33	18.15	17.86	20.35	18.88	14.34	8.72	6.56	5.89	5.52	5.53
MgO	2.07	2.19	2.22	1.96	2.07	2.61	3.03	3.11	3.31	3.38	3.45
MnO	17.86	17.6	17.47	16.1	16.47	20.45	24.97	27.19	27.99	27.7	27.95
CaO	5.36	5.3	5.28	5.19	5.25	4.95	5.01	5.09	5.13	5.25	5.1
Na2O											
K2O	0	0	0.0057	0	0	0.0025	0	0	0.0192	0	0
Total:	102.26	102.52	101.40	102.91	101.93	102.38	101.73	102.22	102.65	102.37	102.07
O	12	12	12	12	12	12	12	12	12	12	12
SiO2	2.978	2.975	2.984	2.993	2.993	3.017	3.009	3.020	2.999	2.996	2.993
TiO2	0.019	0.019	0.014	0.011	0	0.002	0.002	0	0.002	0.003	0.001
Al2O3	1.904	1.944	1.933	1.931	1.975	1.969	1.985	1.970	1.968	1.993	1.978
Cr2O3	0.003	0.000	0.001	0	0.002	0	0	0	0.003	0.003	0
Fe2O3	0.099	0.067	0.072	0.061	0.038	0	0	0	0.030	0.007	0.033
FeO	1.109	1.123	1.112	1.272	1.207	0.937	0.571	0.427	0.351	0.351	0.326
MnO	1.192	1.169	1.173	1.068	1.100	1.353	1.655	1.793	1.837	1.820	1.842
MgO	0.243	0.256	0.262	0.229	0.243	0.304	0.353	0.361	0.382	0.391	0.400
CaO	0.453	0.445	0.448	0.436	0.443	0.414	0.420	0.425	0.426	0.436	0.425
Na2O	0	0	0	0	0	0	0	0	0	0	0
K2O	0	0	6E-04	0	0	2E-04	0	0	2E-03	0	0
Totals	8.000	8.000	8.000	8.000	8.000	7.997	7.996	7.995	8.000	8.000	8.000
FeO rec.	1.112	1.129	1.116	1.268	1.214	0.928	0.571	0.422	0.355	0.353	0.332
Fe	43.65%	44.20%	43.74%	49.43%	47.48%	35.91%	22.13%	16.39%	13.78%	13.77%	12.90%
Mg	9.54%	10.02%	10.28%	8.92%	9.51%	11.75%	13.70%	14.01%	14.85%	15.24%	15.54%
Mn	46.81%	45.78%	45.98%	41.65%	43.01%	52.34%	64.17%	69.60%	71.37%	70.99%	71.56%

Table A7: EPMA measurements in wt% of transect 6L1, and corresponding calculated garnet composition in atoms per formula unit. Relative molar percentages of Fe vs Mg vs Mn as plotted in Figure 4.8 are also given. These values are plotted in Figure 8c. See Figure A1f for location of the measurements.

6L1	1	2	3	4
SiO2	38.59	38.92	38.82	38.69
TiO2	0.0125	0	0.043	0.0248
Al2O3	21.92	22.25	22.07	21.77
Cr2O3	0	0.0604	0	0.03
FeOx	12.83	10.15	7.33	4.73
MgO	3.37	4.84	4.63	3.19
MnO	20.45	20.73	24.25	29.33
CaO	5.67	5.94	5.66	4.82
Na2O	0.0198	0.0396	0.0167	0.0111
K2O	0	0	0.0038	0
Total:	102.86	102.93	102.82	102.60
O	12	12	12	12
SiO2	2.979	2.968	2.971	3.001
TiO2	0.001	0	0.002	0.001
Al2O3	1.995	2.000	1.991	1.991
Cr2O3	0	0.004	0	0.002
Fe2O3	0.048	0.066	0.066	0.004
FeO	0.780	0.582	0.404	0.303
MnO	1.337	1.339	1.572	1.927
MgO	0.388	0.550	0.528	0.369
CaO	0.469	0.485	0.464	0.401
Na2O	0.003	0.006	0.002	0.002
K2O	0	0	0.000	0
Totals	8.000	8.000	8.000	8.000
FeO rec.	0.806	0.625	0.436	0.304
Fe	31.85%	24.87%	17.19%	11.68%
Mg	15.32%	21.88%	20.82%	14.19%
Mn	52.84%	53.25%	61.98%	74.13%

Table A8: Fitted peak positions and uncertainties for Raman spectra of inclusions and standards, given in in cm^{-1}.

Msr.	t (s)	rep.	m128		m206		m265		m393		m403		m464		m1080		m1160	
			value	2σ	value	2σ	value	2σ	value	2σ	value	2σ	value	2σ	value	2σ	value	2σ
i001	10	2	132.6	0.03	224.82	0.08	x	x	x	x	x	x	471.32	0.02	1083.25	1.26	1158.25	0.18
i002	10	2	130.46	0.03	217.91	0.06	266.6	0.18	393.35	0.2	402.9	0.14	468.27	0.02	x	x	1157.83	0.16
i003	10	2	132.48	0.05	223.97	0.1	268.47	0.39	393.66	0.32	403.53	0.27	470.71	0.03	1083.14	0.9	1156.92	0.46
i004	10	2	132.49	0.03	225.88	0.07	269.17	0.19	393.52	0.34	403.05	0.13	471.75	0.02	x	x	1156	0.3
i005	10	2	131.01	0.05	220.37	0.08	267.31	0.19	x	x	x	x	469.5	0.02	x	x	1157.24	0.34
i006	10	2	132.66	0.03	225.73	0.06	268.11	0.31	393.1	0.19	401.27	0.26	471.67	0.05	x	x	1157.27	0.22
i007	15	2	133.61	0.03	228.22	0.07	269.64	0.29	393.3	0.24	403.49	0.18	472.86	0.03	x	x	1156.13	0.28
i008	15	2	133.35	0.04	225.51	0.06	269.63	0.22	x	x	404.15	0.16	471.65	0.02	x	x	1156.09	0.35
i009	15	2	132.3	0.03	223.63	0.05	268.7	0.17	x	x	403.2	0.11	470.88	0.02	x	x	1156.21	0.25
i010	15	2	130.7	0.05	218.11	0.11	266.93	0.56	x	x	x	x	468.64	0.03	x	x	1158.57	0.37
i011	15	2	132.56	0.04	224.1	0.06	267.97	0.19	393.51	0.13	x	x	471.08	0.03	1073.87	1.09	1158.28	0.2
i012	15	2	131.86	0.1	221.5	0.1	267.09	0.27	x	x	x	x	470.17	0.04	x	x	x	x
i013	15	2	131.19	0.05	220.42	0.11	266.6	0.36	x	x	x	x	469.79	0.02	x	x	1158.37	0.12
i014	15	2	127.73	0.09	206.27	0.24	264.1	0.29	x	x	x	x	464.77	0.03	1082.19	0.13	1158.74	0.62
i015	15	2	132.26	0.09	224.37	0.08	267.98	0.26	x	x	401.91	0.44	471.27	0.01	1082.6	0.15	1156.25	0.5
i018	15	2	132	0.03	222.9	0.06	266.61	0.33	x	x	x	x	470.45	0.04	1083.12	0.82	1158.48	0.09
i019	15	2	132.25	0.05	223.99	0.1	x	x	x	x	x	x	471.04	0.03	1083.1	1.08	1158.45	0.15
i020	15	2	127.62	0.05	206.2	0.26	x	x	x	x	x	x	464.66	0.03	x	x	1161.04	0.16
i021	15	2	132.6	0.03	224.82	0.08	x	x	x	x	x	x	471.32	0.02	1083.25	1.26	1158.25	0.18
std1	5	3	127.9	0.02	206.96	0.05	263.71	0.11	393.58	0.11	400.64	0.14	464.67	0.01			1160.38	0.19
std2	30	2	128.12	0.08	207.63	0.05	264.3	0.14	x	x	x	x	464.68	0.02	1081.61	0.17	x	x
std3	30	2	127.88	0.03	206.88	0.05	264.54	0.11	393.53	0.09	402.49	0.24	464.55	0.02	x	x	1160.32	0.24
avg_std			128	0.06	207.26	0.05	264.42	0.13	393.53	0.09	402.49	0.24	464.62	0.02	1081.61	0.17	1160.32	0.24

Table A9: Shifts in peak positions in Raman spectra of quartz inclusions in comparison to an unstrained standard crystal. The shift of inclusions i001 to i006 where obtained by subtracting the value of the standard "std1", while shifts for inclusions i007 to i021 were obtained by subtracting the average of standards "std2" and "std3". The shifts are reported together with the instrumental uncertainty (0.5 cm^{-1}), or the fitting uncertainties if > 0.5 cm^{-1}.

Msr.	m128		m206		m265		m464	
	value	2σ	value	2σ	value	2σ	value	2σ
i001	4.7	0.5	17.86	0.5	x	x	6.65	0.5
i002	2.56	0.5	10.95	0.5	2.89	0.5	3.6	0.5
i003	4.58	0.5	17.01	0.5	4.76	0.5	6.04	0.5
i004	4.59	0.5	18.92	0.5	5.46	0.5	7.08	0.5
i005	3.11	0.5	13.41	0.5	3.6	0.5	4.83	0.5
i006	4.76	0.5	18.77	0.5	4.4	0.5	7	0.5
i007	5.61	0.5	20.96	0.5	5.22	0.5	8.24	0.5
i008	5.35	0.5	18.25	0.5	5.21	0.5	7.03	0.5
i009	4.3	0.5	16.37	0.5	4.28	0.5	6.26	0.5
i010	2.7	0.5	10.85	0.5	2.51	0.56	4.02	0.5
i011	4.56	0.5	16.84	0.5	3.55	0.5	6.46	0.5
i012	3.86	0.5	14.24	0.5	2.67	0.5	5.55	0.5
i013	3.19	0.5	13.16	0.5	2.18	0.5	5.17	0.5
i014	-0.27	0.5	-0.99	0.5	-0.32	0.5	0.15	0.5
i015	4.26	0.5	17.11	0.5	3.56	0.5	6.65	0.5
i018	4	0.5	15.64	0.5	2.19	0.5	5.83	0.5
i019	4.25	0.5	16.73	0.5	x	x	6.42	0.5
i020	-0.38	0.5	-1.06	0.5	x	x	0.04	0.5
i021	4.6	0.5	17.56	0.5	x	x	6.7	0.5

Table A11: *P-T* conditions representing prograde metamorphism of Lago di Cignana, and corresponding strain estimations for quartz inclusions.

		EosFit			unrelaxed	
P (GPa)	T (°C)	eV	e1	e3	e1	e3
1	370	-0.0138	-0.0049	-0.0042	-0.0039	-0.0032
1	470	-0.0118	-0.0040	-0.0039	-0.0032	-0.0029
1.5	400	-0.0220	-0.0079	-0.0064	-0.0064	-0.0048
1.5	500	-0.0203	-0.0071	-0.0062	-0.0058	-0.0047
2	440	-0.0293	-0.0106	-0.0083	-0.0086	-0.0063
2	540	-0.0277	-0.0099	-0.0082	-0.0080	-0.0062
2.5	500	-0.0356	-0.0130	-0.0101	-0.0105	-0.0076
2.5	600	-0.0341	-0.0123	-0.0100	-0.0099	-0.0076
3	530	-0.0418	-0.0154	-0.0117	-0.0124	-0.0088
3	630	-0.0404	-0.0146	-0.0117	-0.0118	-0.0088

Table A10: Calculated strains, estimated standard deviations (esd) and errors for quartz inclusions.

	ε1+ε2	esd	ε3	esd	ε_V	esd	var_x	var_y	cov	corr%	χ2
i001	-0.01833	0.00669	-0.00365	0.00432	-0.02198	0.0024	4.47561E-05	1.86624E-05	-2.86207E-05	-99	2.38
i002	-0.01652	0.00518	0.00129	0.00336	-0.01523	0.0019	2.68324E-05	1.12896E-05	-1.72297E-05	-99	1.47
i003	-0.02066	0.01027	-0.00152	0.00666	-0.02218	0.0037	0.000105473	4.43556E-05	-6.76495E-05	-99	5.78
i004	-0.02365	0.01057	-0.0013	0.00685	-0.02495	0.0039	0.000111725	4.69225E-05	-7.16757E-05	-99	6.13
i005	-0.0181	0.00591	0.00007	0.00383	-0.01804	0.0021	3.49281E-05	1.46689E-05	-2.23951E-05	-99	1.91
i006	-0.02111	0.00577	-0.00271	0.00374	-0.02382	0.0021	3.32929E-05	1.39876E-05	-2.13971E-05	-99	1.83
i007	-0.02025	0.0079	-0.0054	0.00512	-0.02565	0.0029	0.00006241	2.62144E-05	-4.00734E-05	-99	3.42
i008	-0.01716	0.01174	-0.00513	0.00761	-0.02229	0.0043	0.000137828	5.79121E-05	-8.84758E-05	-99	7.56
i009	-0.01748	0.00727	-0.0031	0.00471	-0.02058	0.0026	5.28529E-05	2.21841E-05	-3.39464E-05	-99	2.9
i010	-0.01245	0.00428	-0.00138	0.00277	-0.01382	0.0015	1.83184E-05	7.6729E-06	-1.17614E-05	-99	0.47
i011	-0.01597	0.00455	-0.00441	0.00295	-0.02038	0.0016	2.07025E-05	8.7025E-06	-1.32815E-05	-99	1.14
i012	-0.01251	0.00427	-0.00435	0.00277	-0.01686	0.0015	1.82329E-05	7.6729E-06	-1.17005E-05	-99	0.62
i013	-0.01274	0.00427	-0.00317	0.00277	-0.01591	0.0015	1.82329E-05	7.6729E-06	-1.17005E-05	-99	0.38
i014	0.00403	0.00427	-0.00189	0.00277	0.00214	0.0015	1.82329E-05	7.6729E-06	-1.17005E-05	-99	0.3
i015	-0.01747	0.00427	-0.00362	0.00277	-0.0211	0.0015	1.82329E-05	7.6729E-06	-1.17005E-05	-99	0.36
i018	-0.01529	0.00627	-0.00356	0.00407	-0.01885	0.0023	3.93129E-05	1.65649E-05	-2.52586E-05	-99	2.16
i019	-0.01685	0.00433	-0.00366	0.0028	-0.02051	0.0016	1.87489E-05	0.00000784	-1.20141E-05	-99	0.94
i020	0.00303	0.00433	-0.00116	0.0028	0.00188	0.0016	1.87489E-05	0.00000784	-1.20141E-05	-99	0.63
i021	-0.01722	0.00556	-0.00416	0.00359	-0.02137	0.0020	3.09136E-05	1.28881E-05	-1.97738E-05	-99	1.65

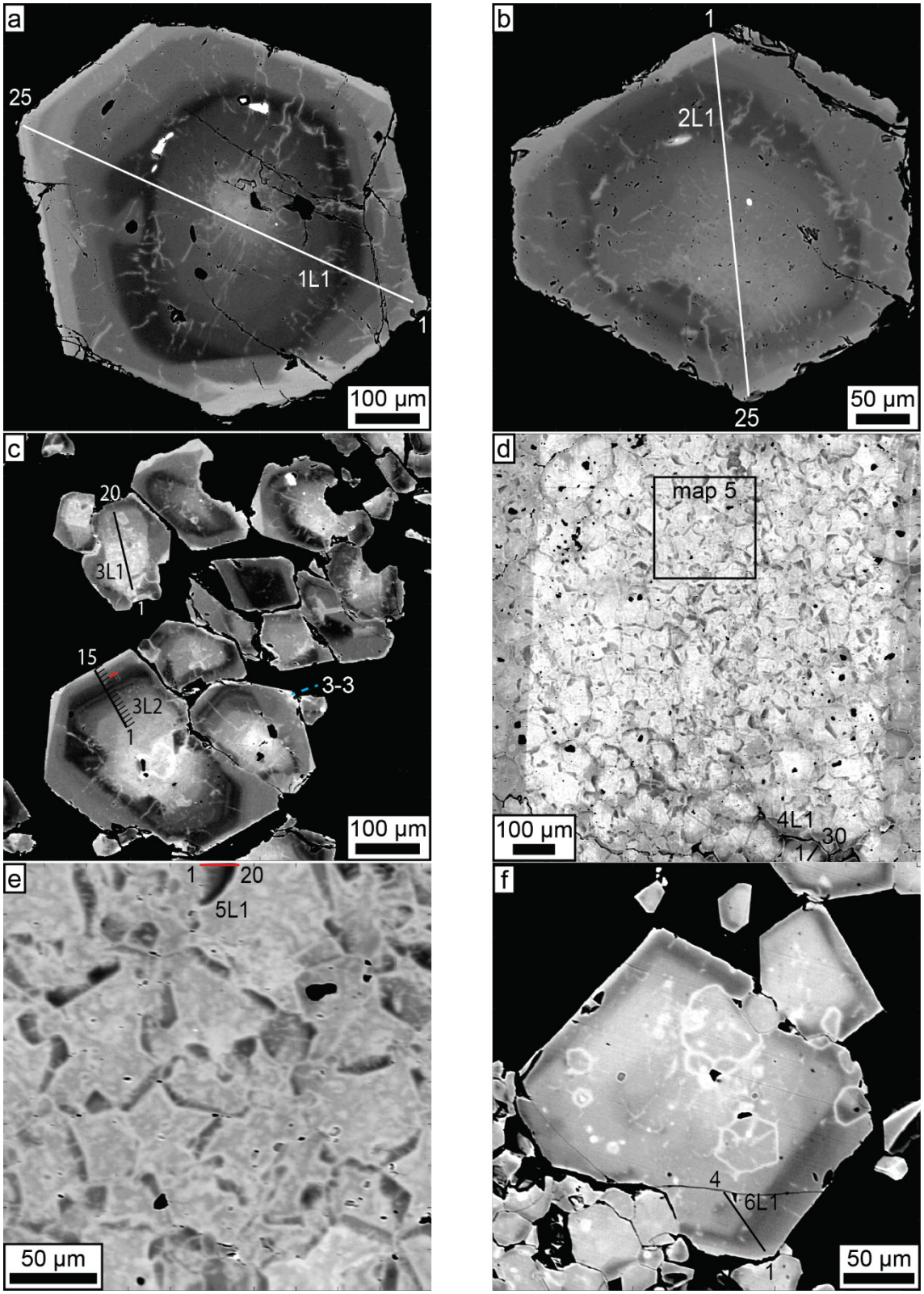

Figure A1: BSE images including the locations of all EPMA measurements, of (a,b) representative host-rock garnets, (c) outer garnetite, (d,e) inner garnetite where (e) is a close-up of the marked area in (d), and (f) euhedral overgrowth on the outer margin of the inner garnetite.

Appendix B: Supplementary data for Chapter 5

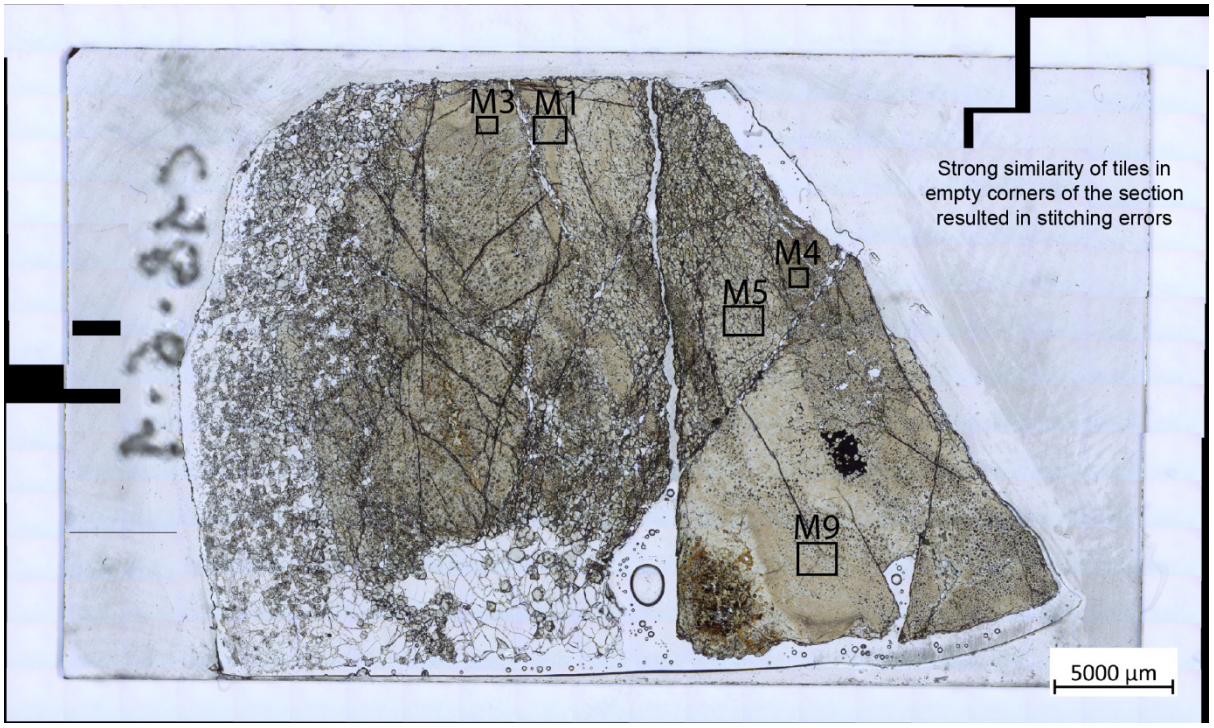

Figure B1: Section C18-6-1 overview with map locations

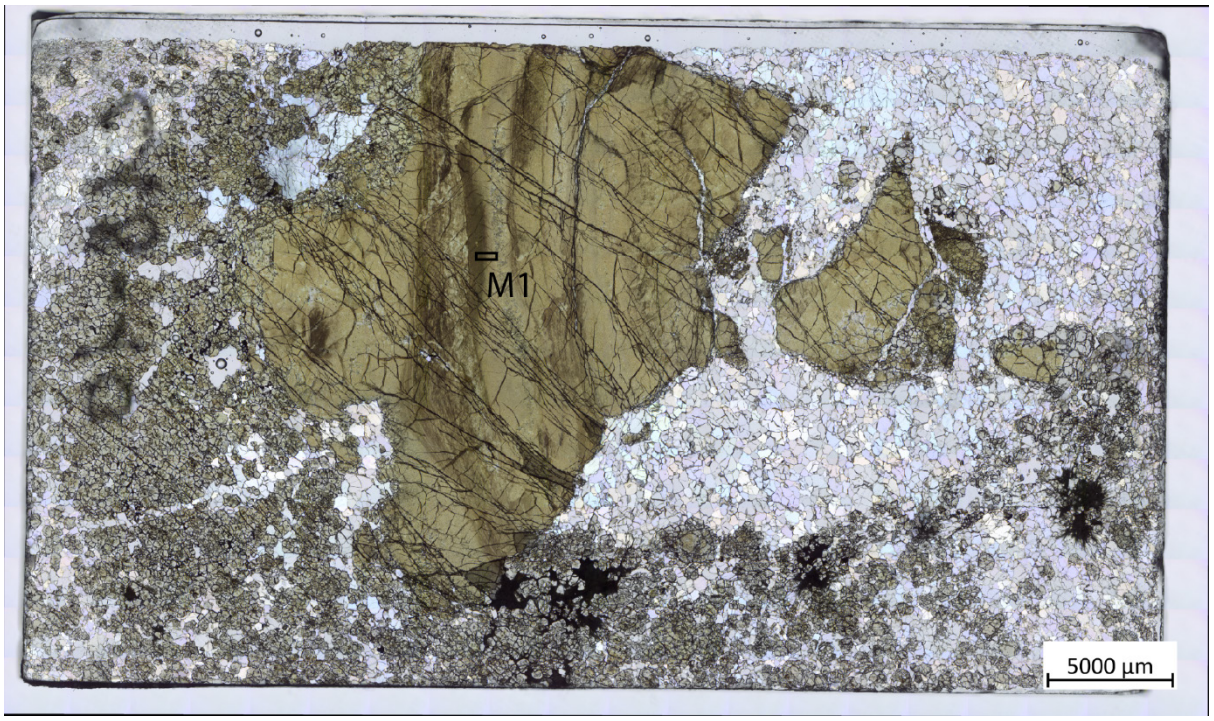

Figure B2: Section C18-10-1 with map location

For locations in EC5_1-A1, see Figure 5.9

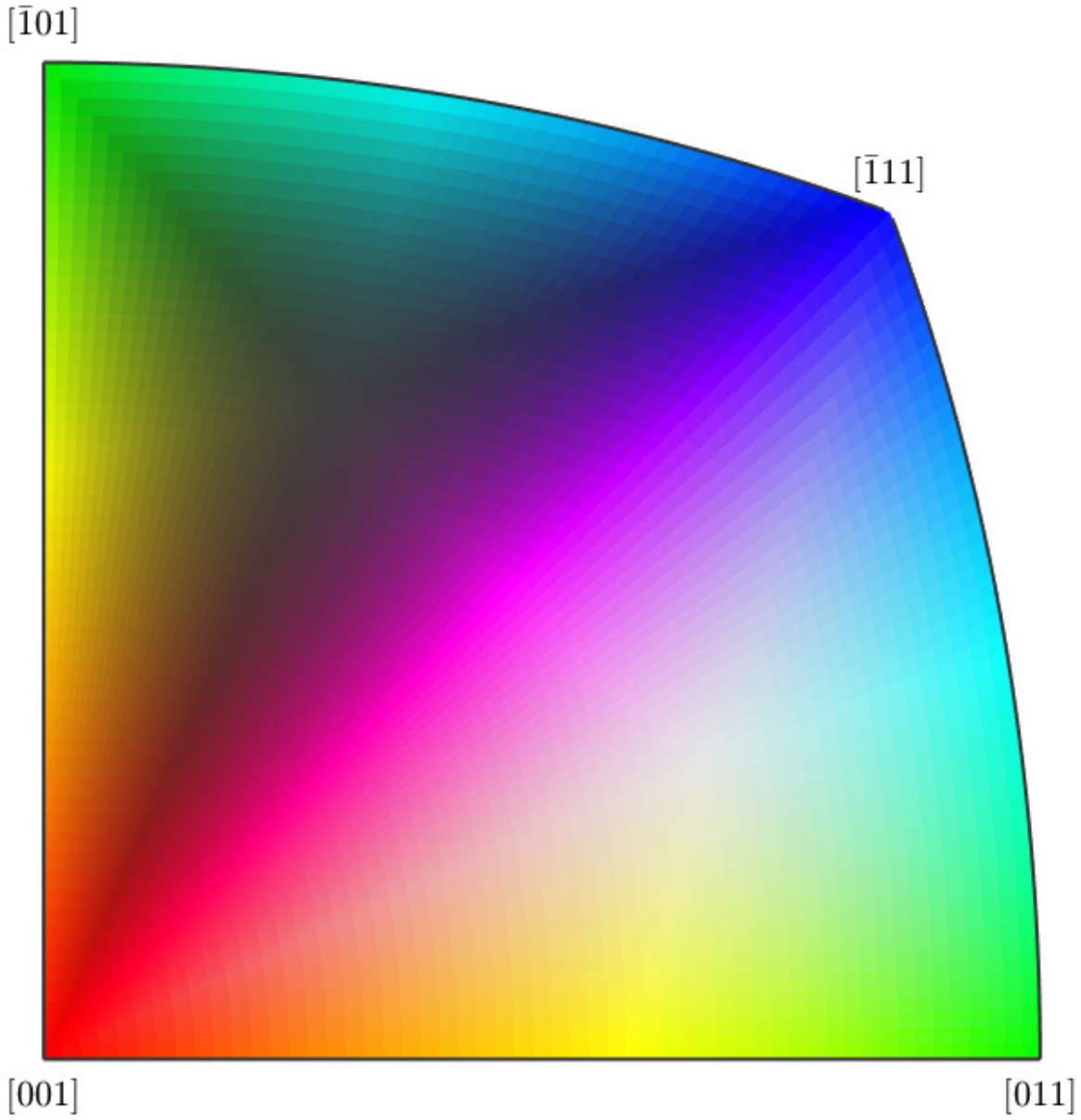

Figure B3: Euler angle colour bar, used in Figure 5.4c,d

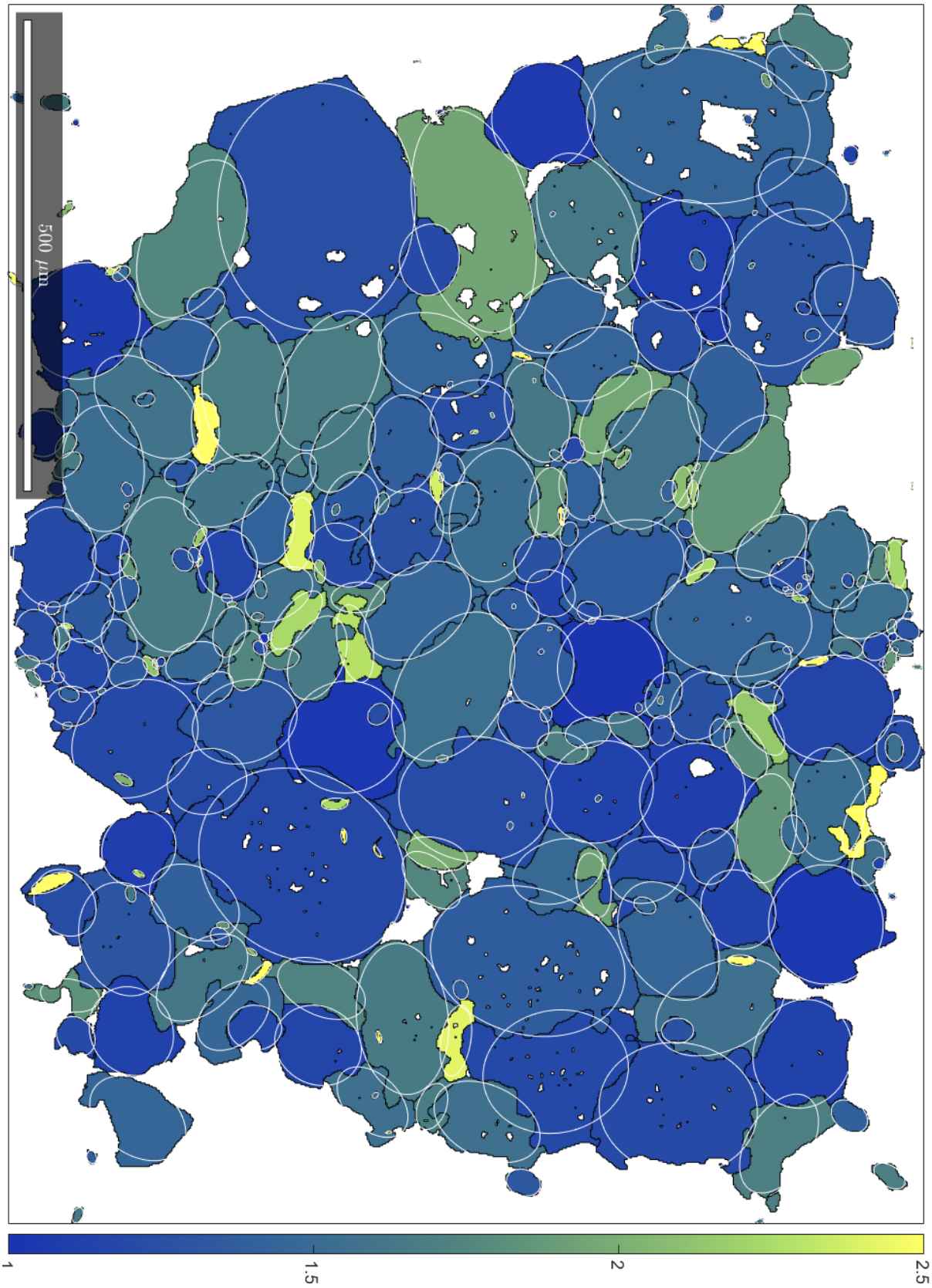

Figure B4: C18-6-1_M1 (900x650, 1.5 μm spacing)

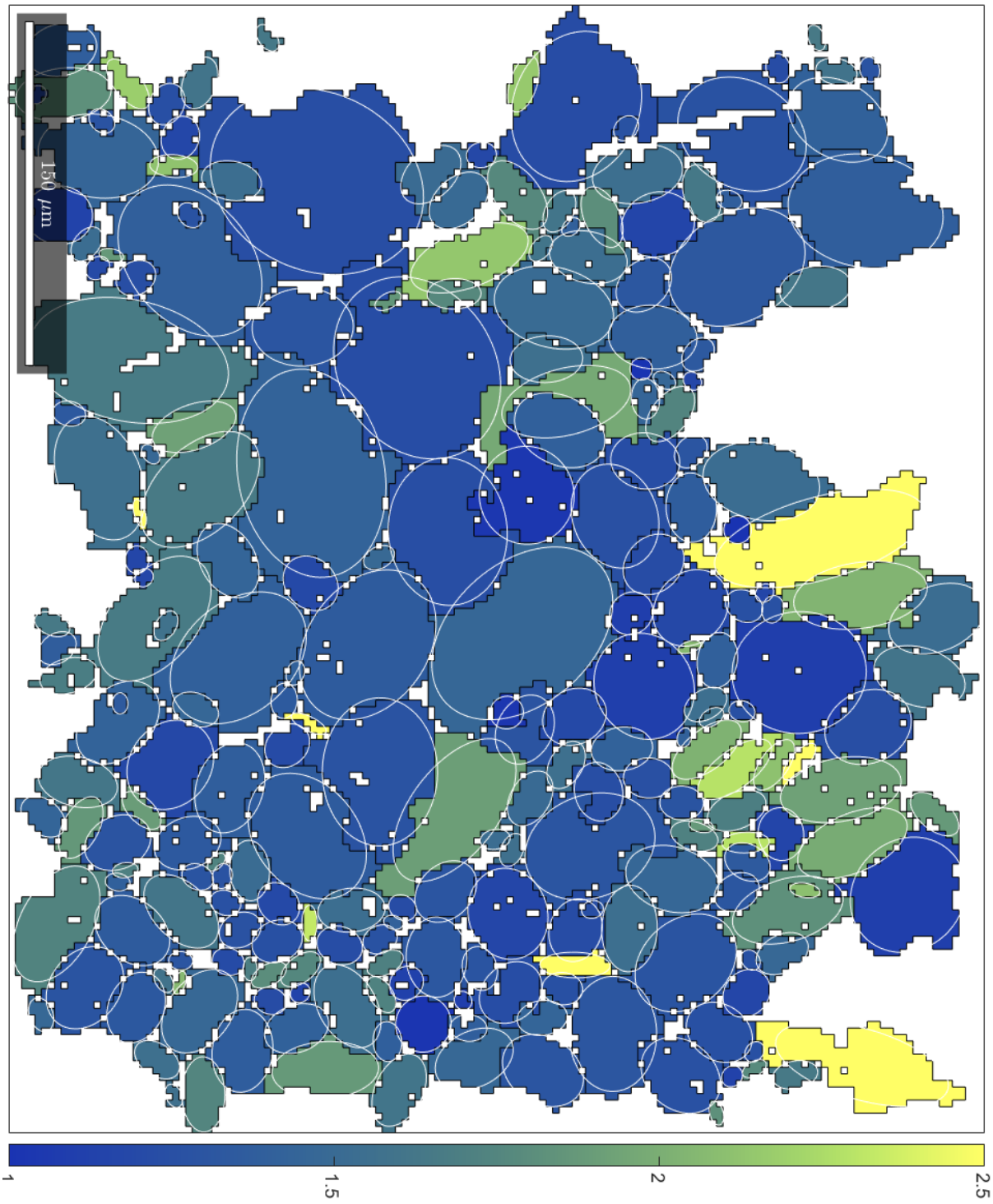

Figure B5: C18-6-1_M3 (175 x 150, 2.86 µm spacing)

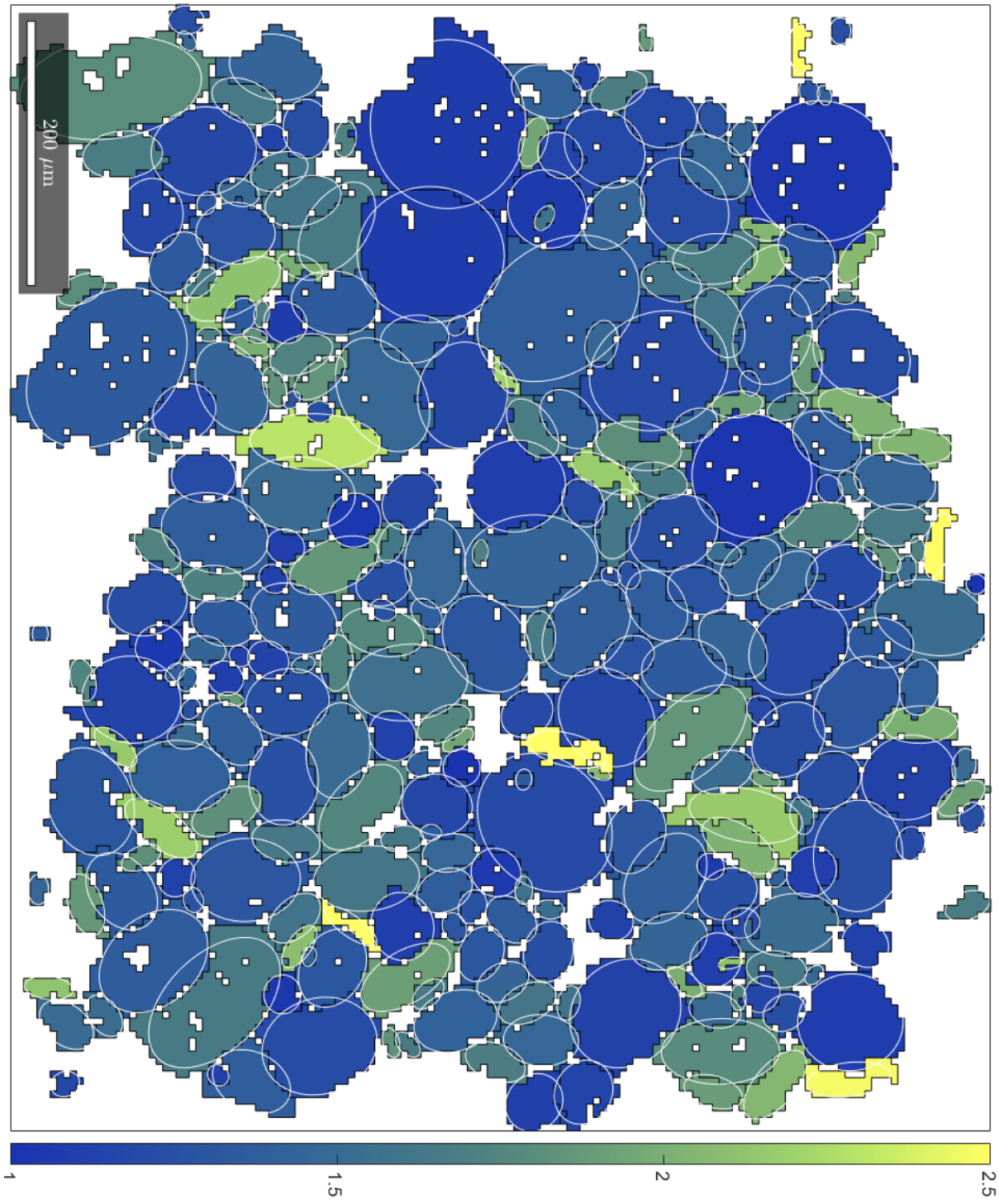

Figure B6: C18-6-1_M4 (175 x 150, 5.01 μm spacing)

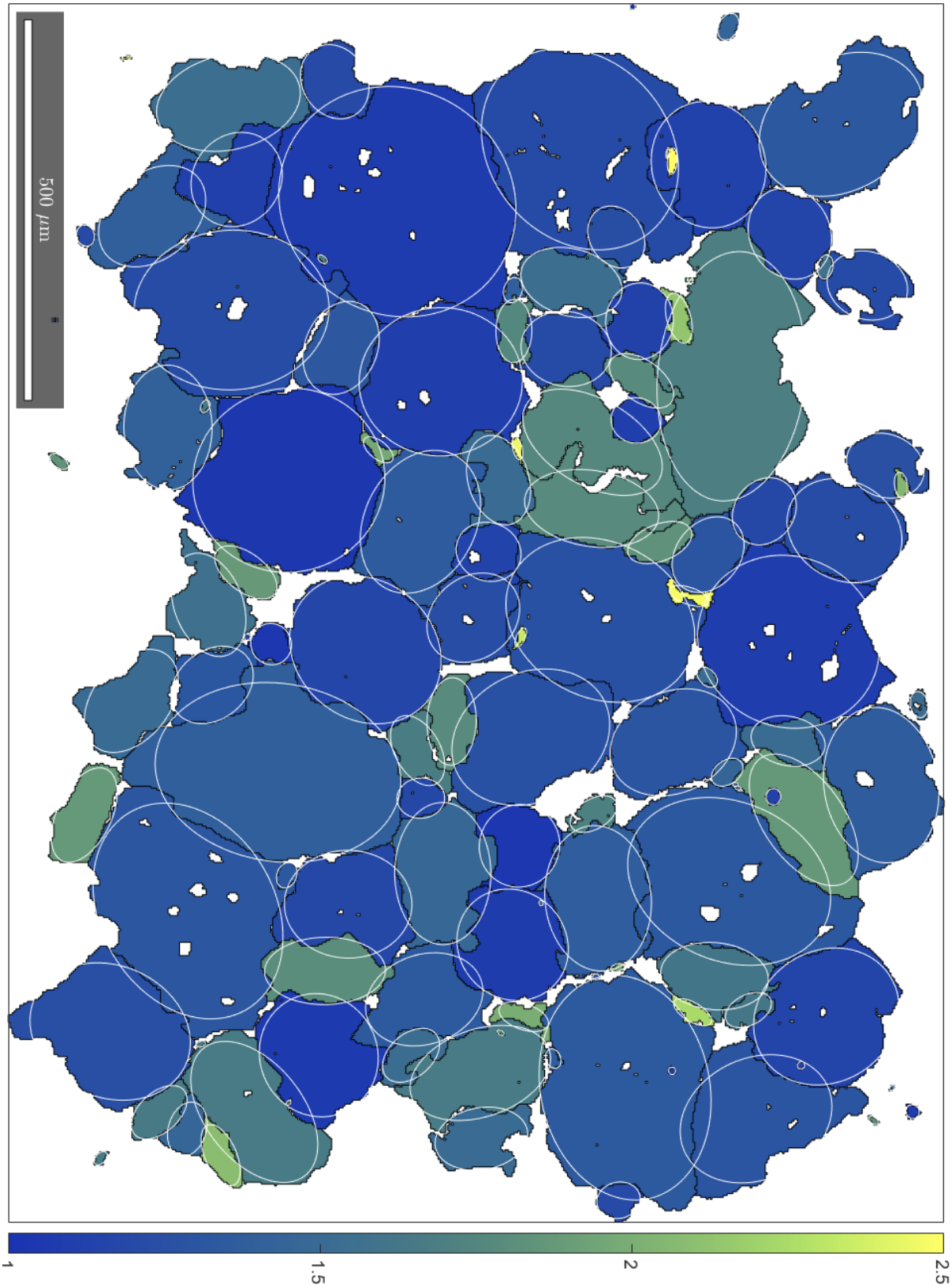

Figure B7: C18-6-1_M5 (650 x 500, 2.5 μm spacing)

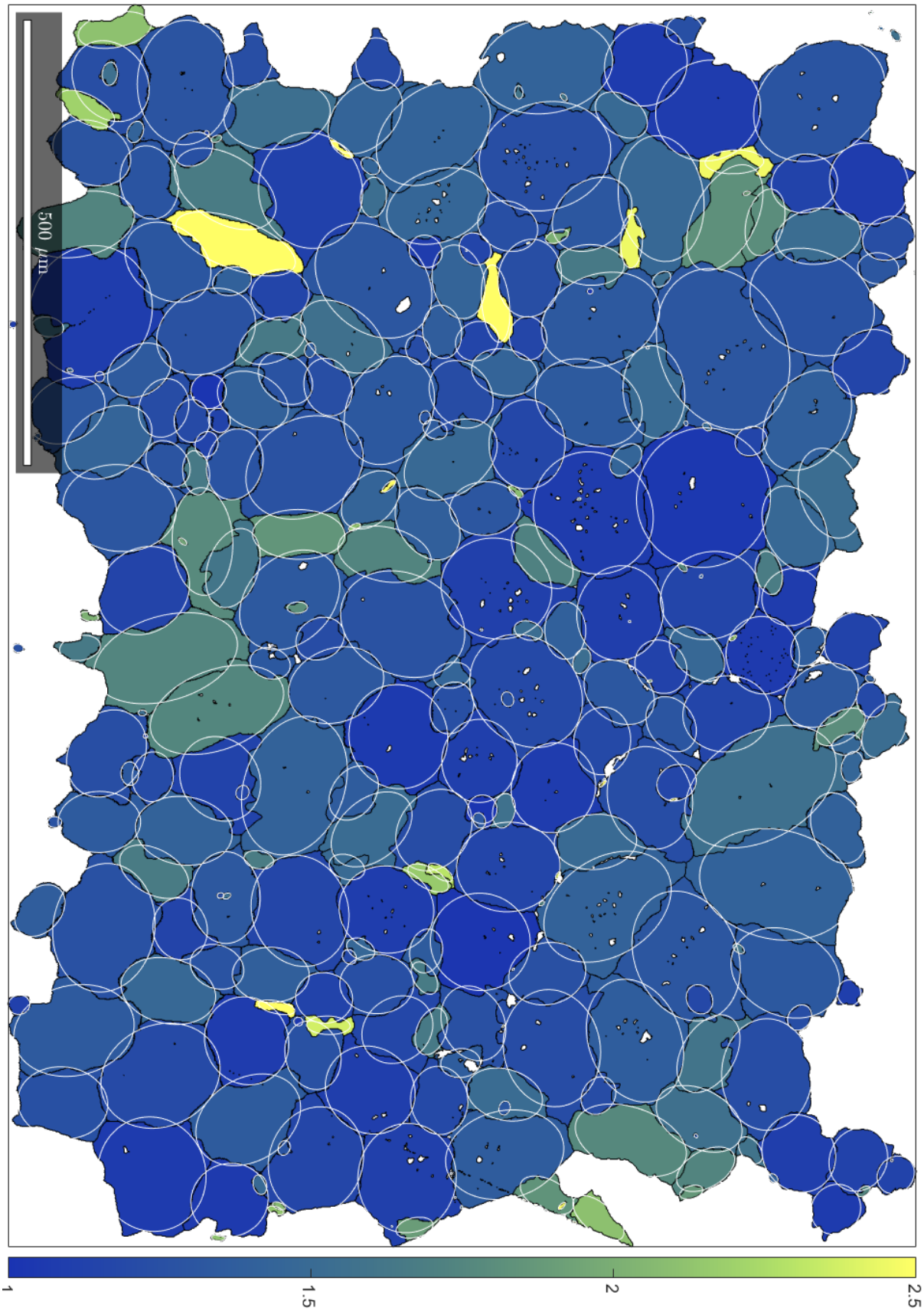

Figure B8: C18-6-1_M9 (1750 x 1280, 0.8 µm spacing)

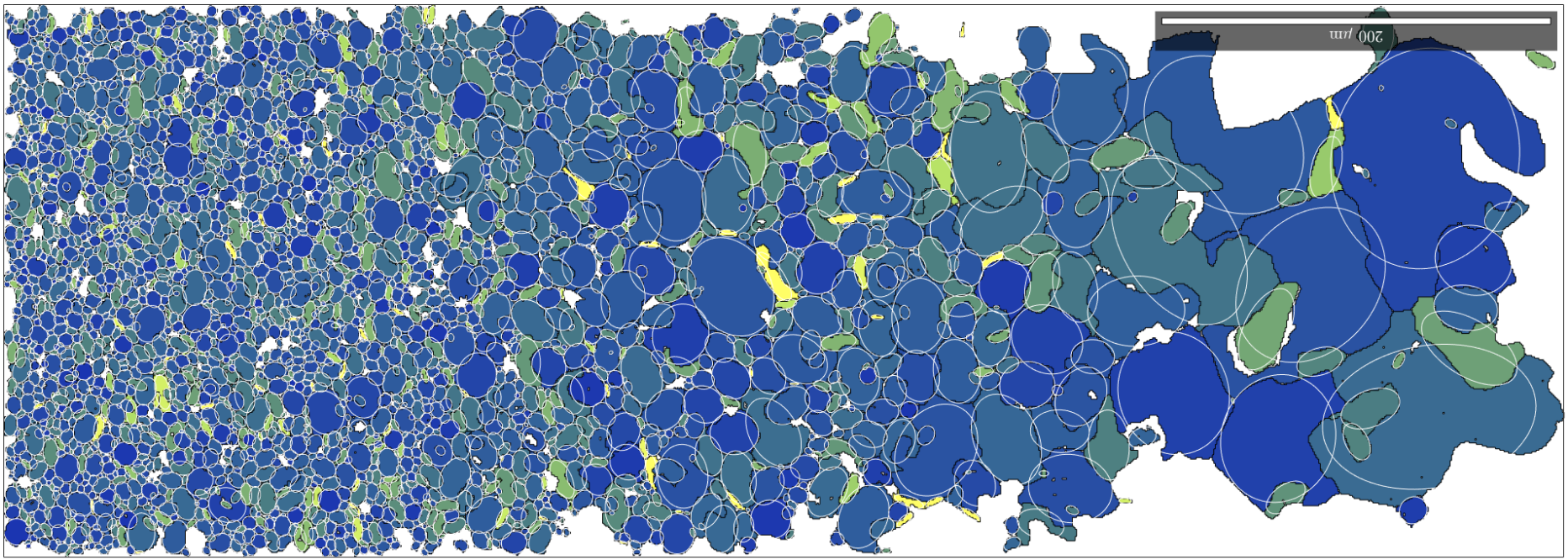

Figure B9: C18-10-1_M1 (1080 x 380, 0.75 μm spacing) – Same color bar and values as Figure B8

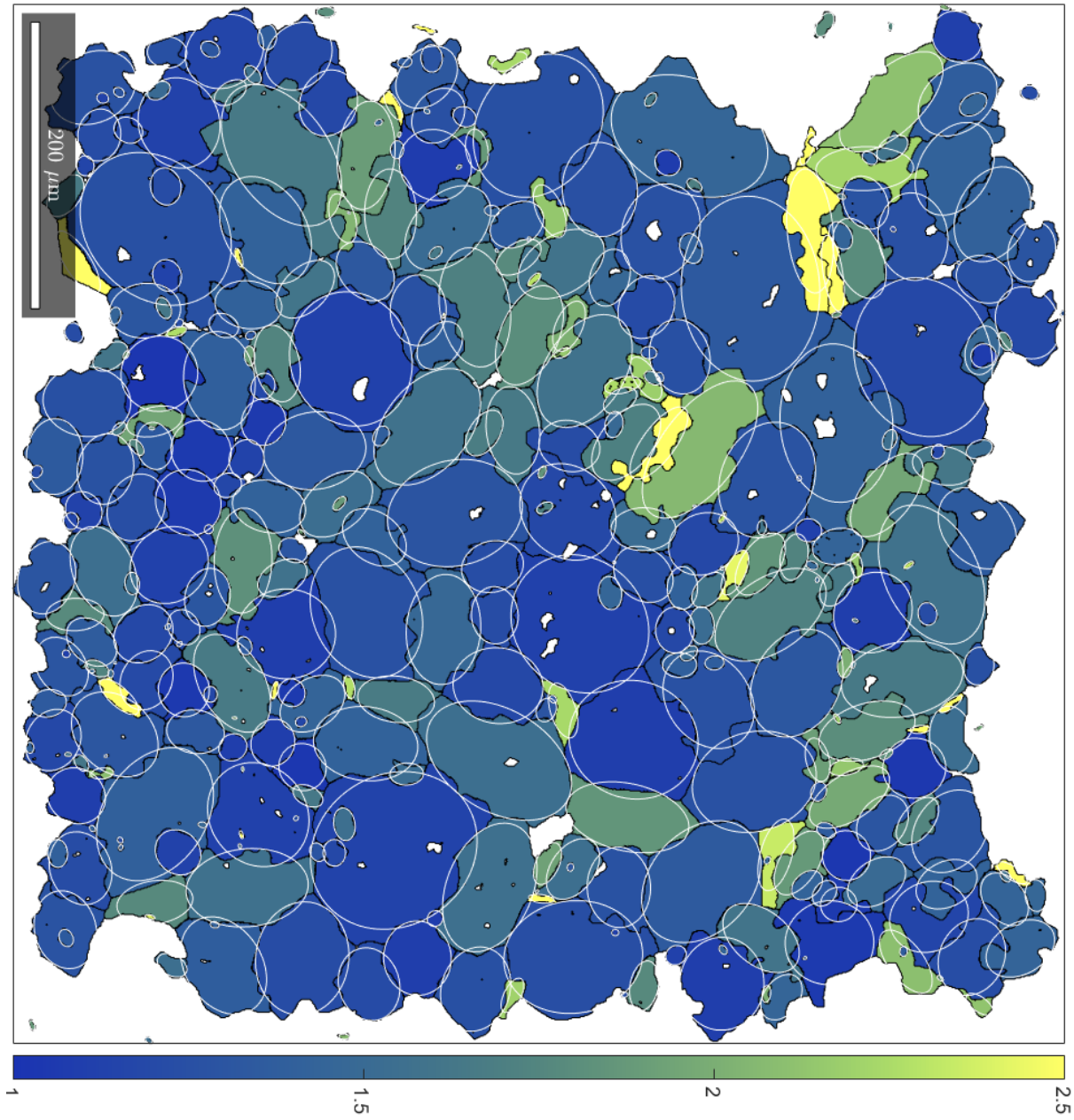

Figure B10: EC5_1A-1_M1 (979 x 984, 0.75 μm spacing)

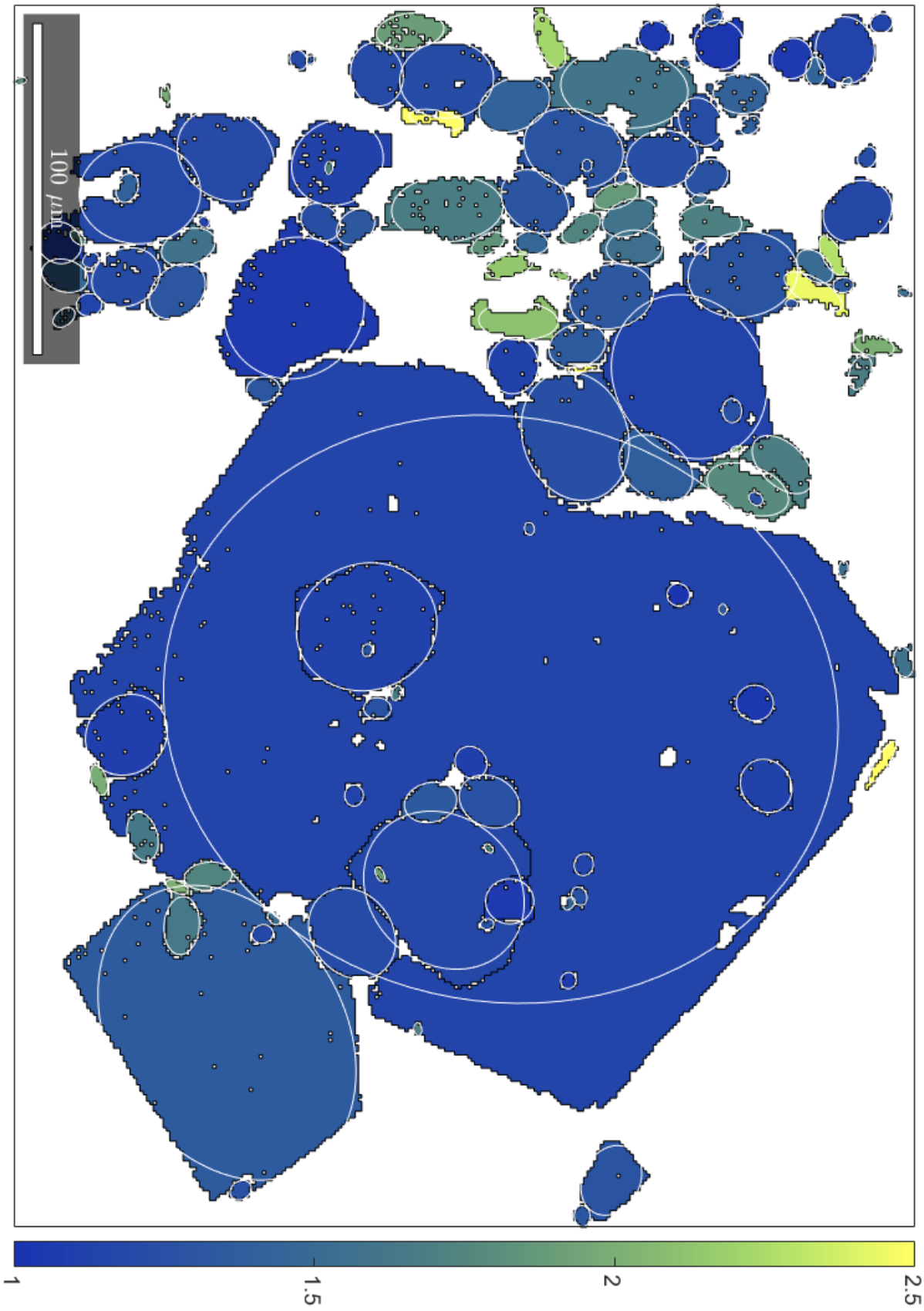

Figure B11: EC5_1A-1_M2 (276 x 372, 1 µm spacing)

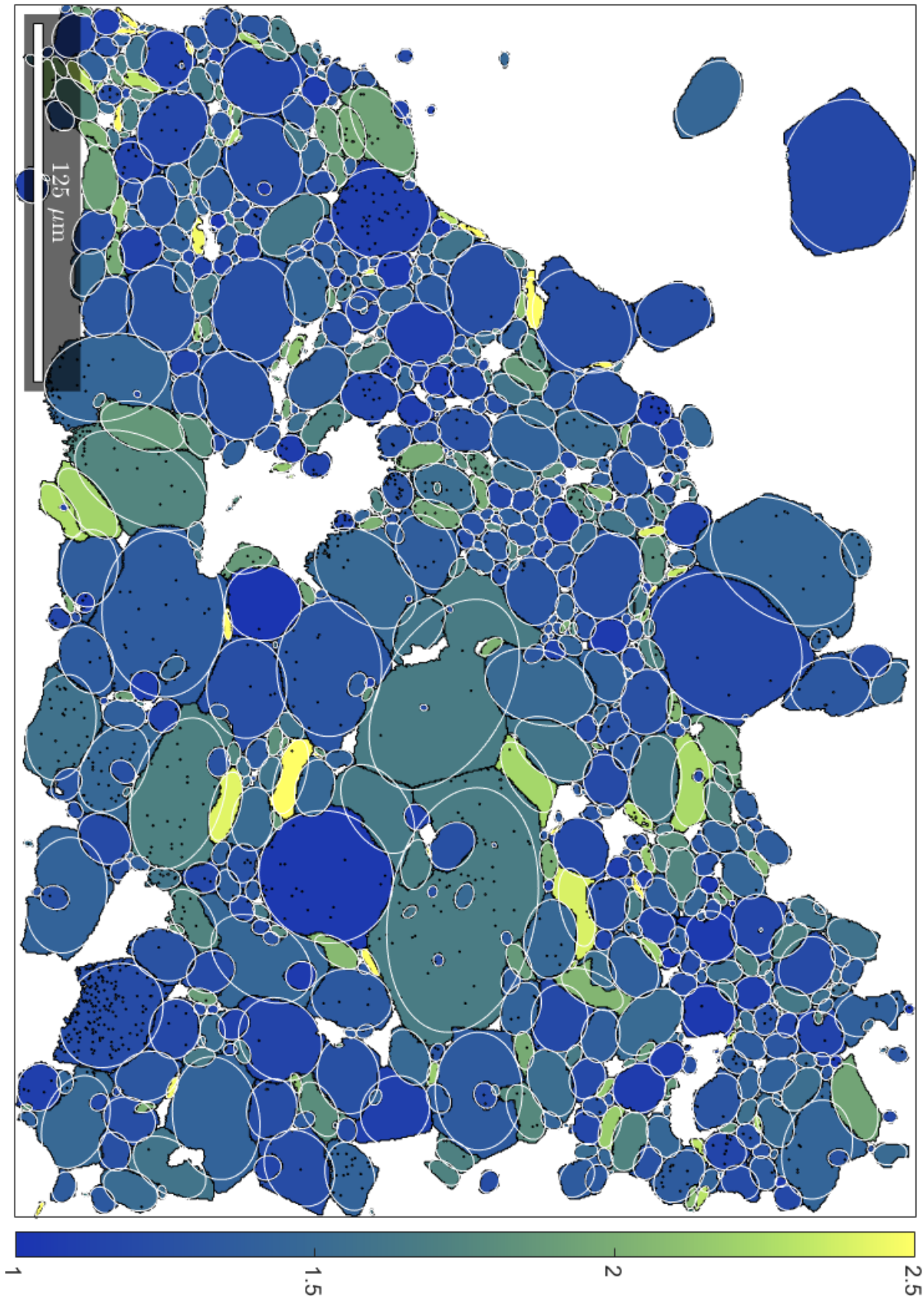

Figure B12: EC5_1A-1_M3 (849 x 639, 0.5 μm spacing)

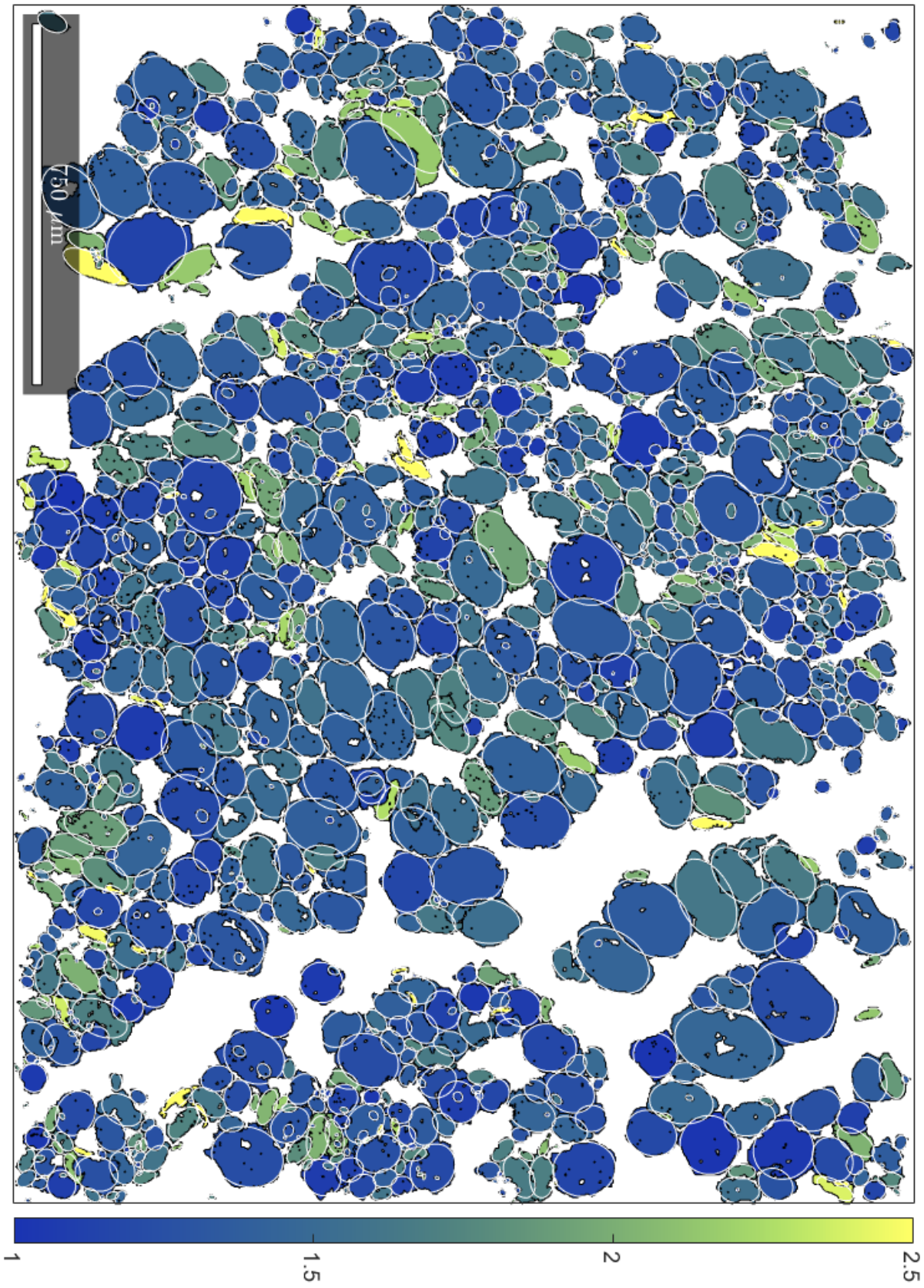

Figure B13: EC5_1A-1_M4 (1000 x 750, 2.5 µm spacing)

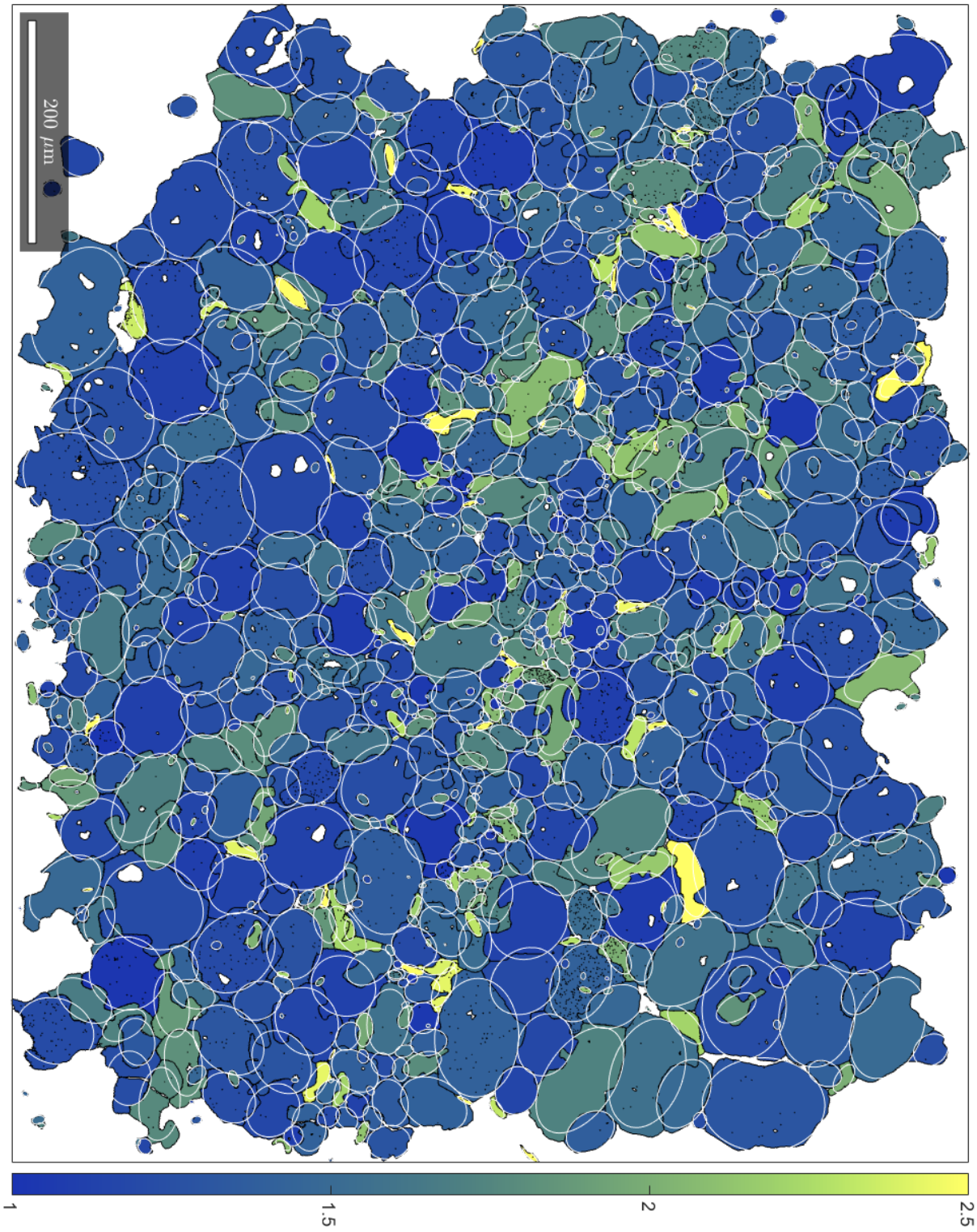

Figure B14: EC5_1A-1_M5 (2090 x 1720, 0.5 μm spacing)

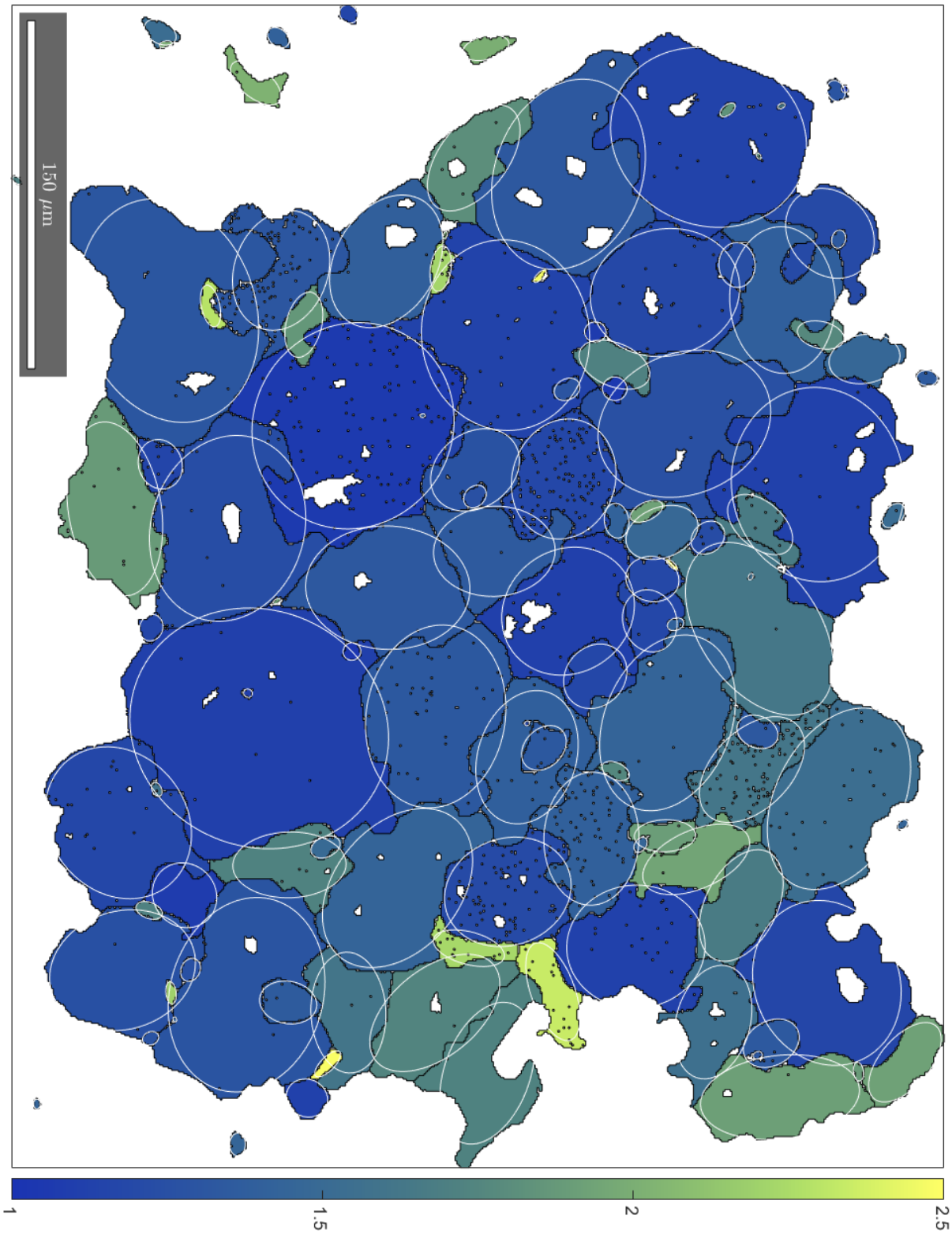

Figure B15: EC5_1A-1_M6 (675 x 550, 0.75 µm spacing)

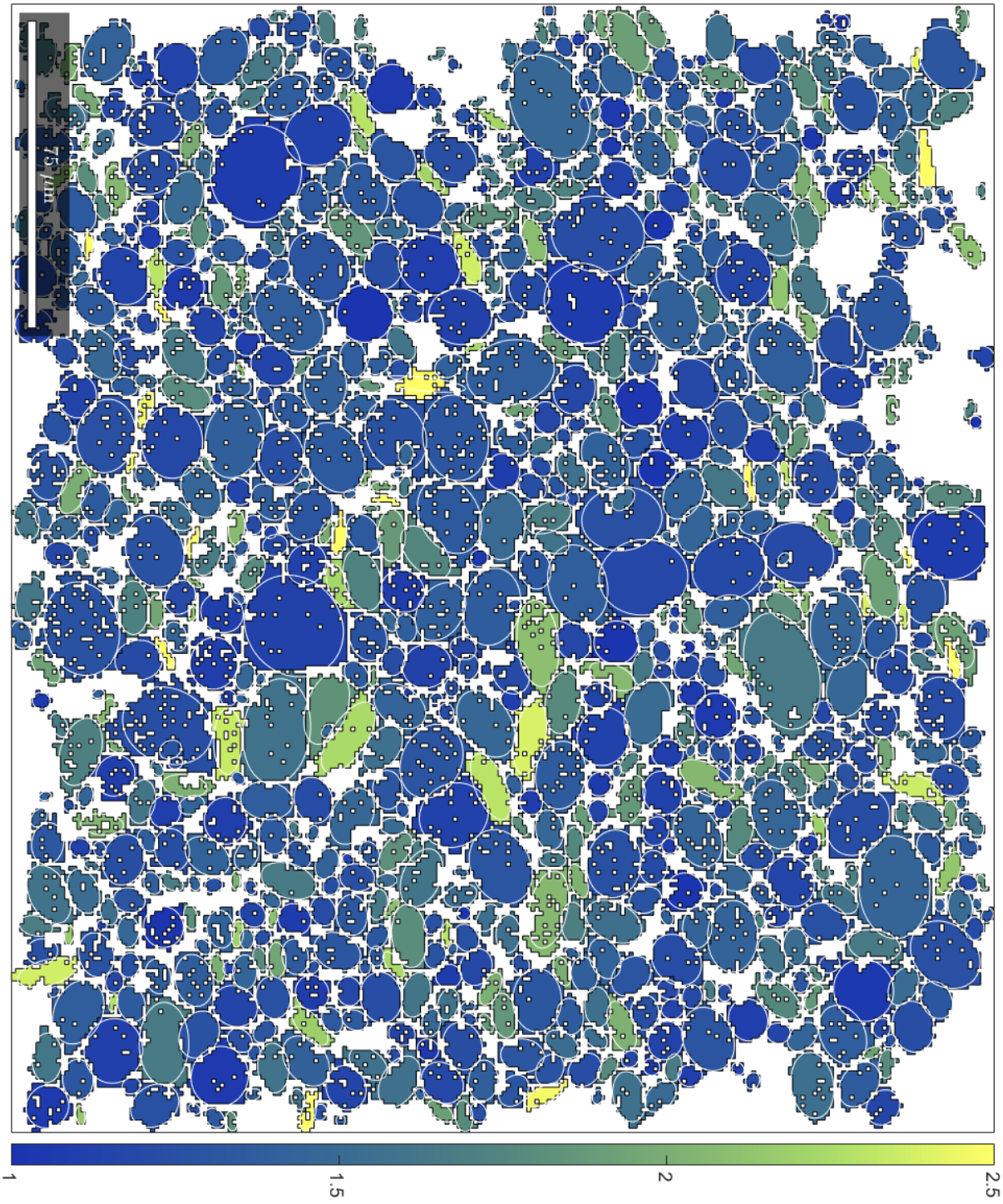

Figure B16: EC5_1A-1_M7 (277 x 242, 1 µm spacing)

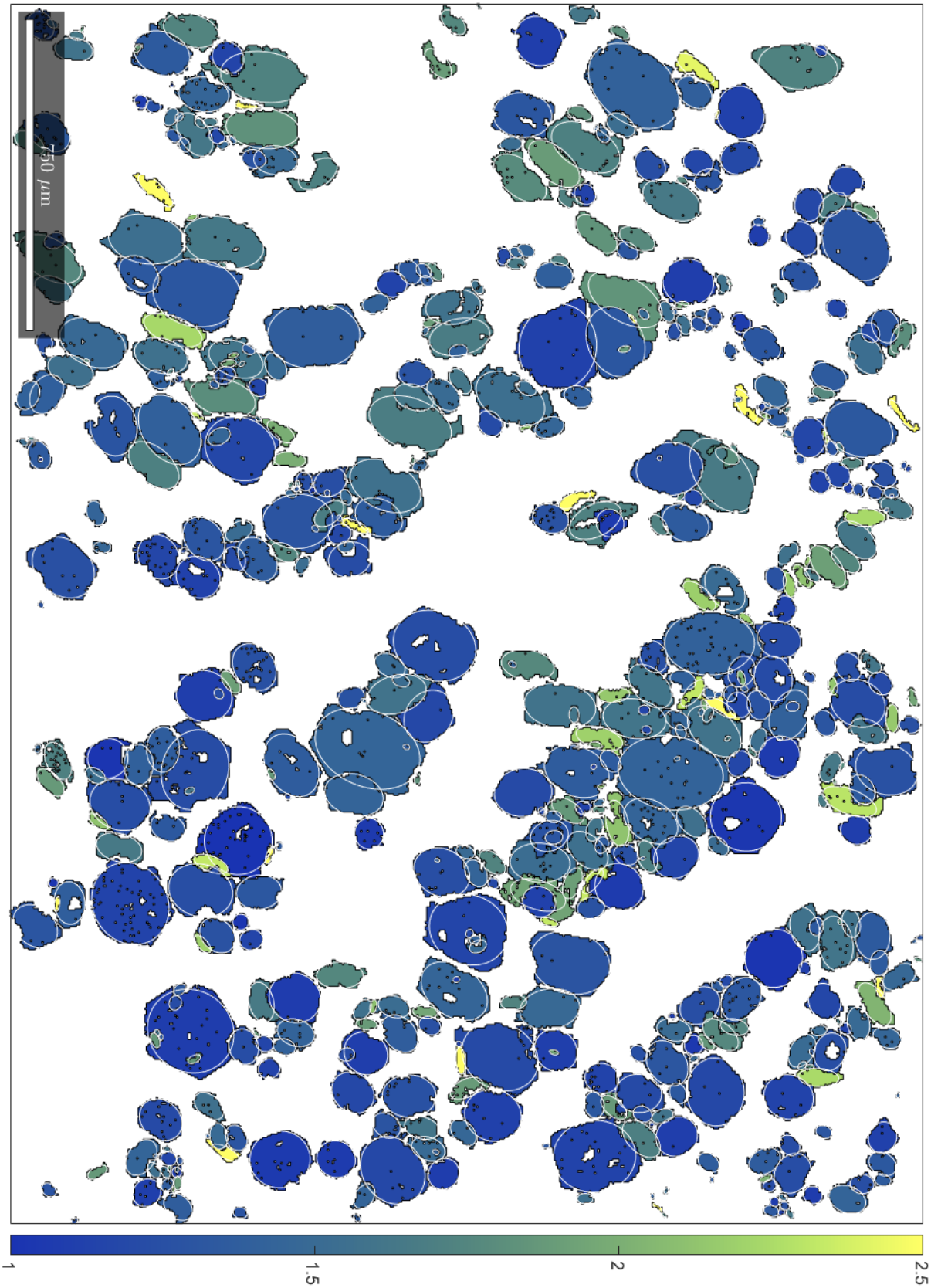

Figure B17: EC5_1A-1_M8 (737 x 552, 4 µm spacing)

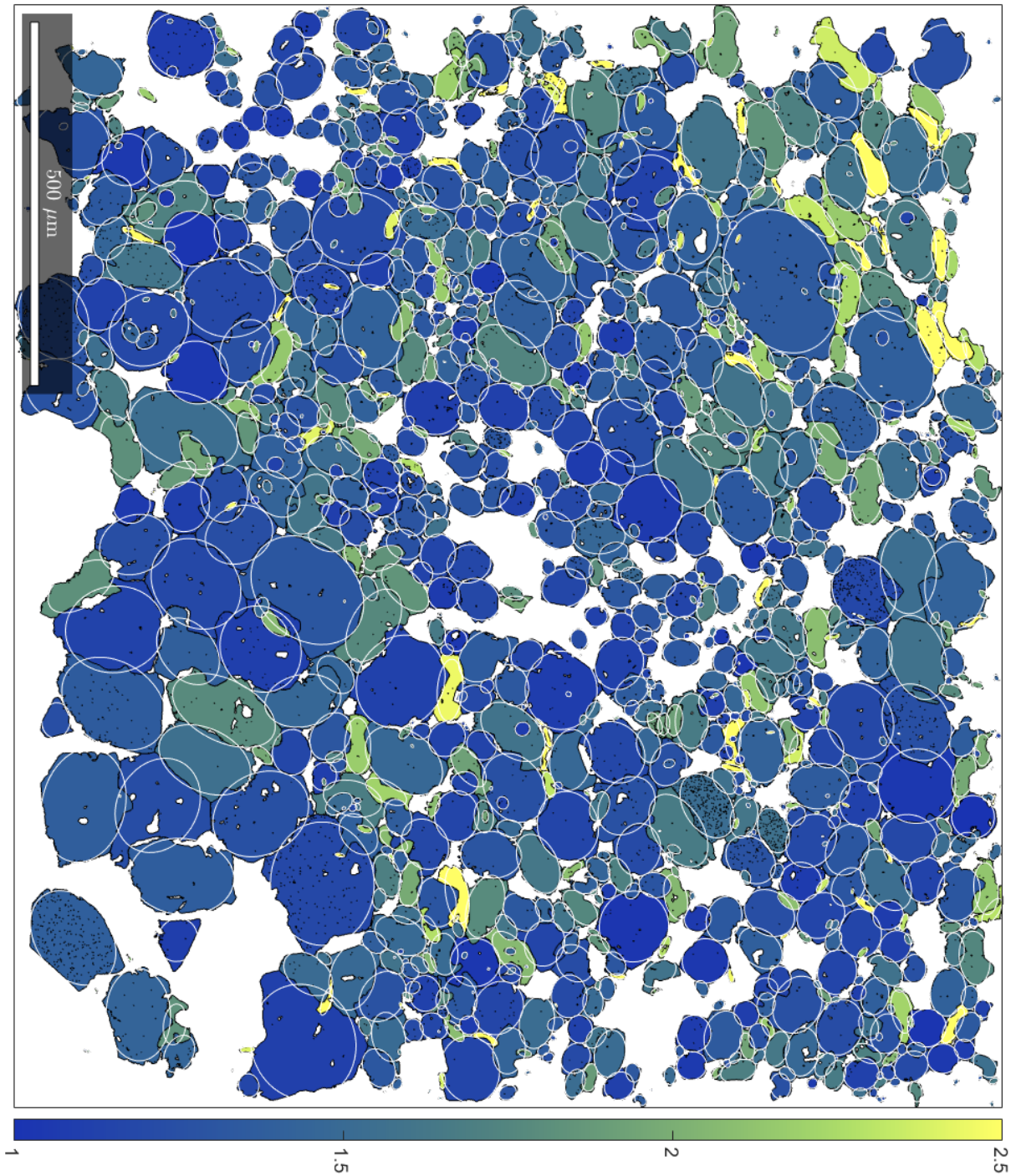

Figure B18: EC5_1A-1_M9 (2025 x 1825, 0.75 μm spacing)

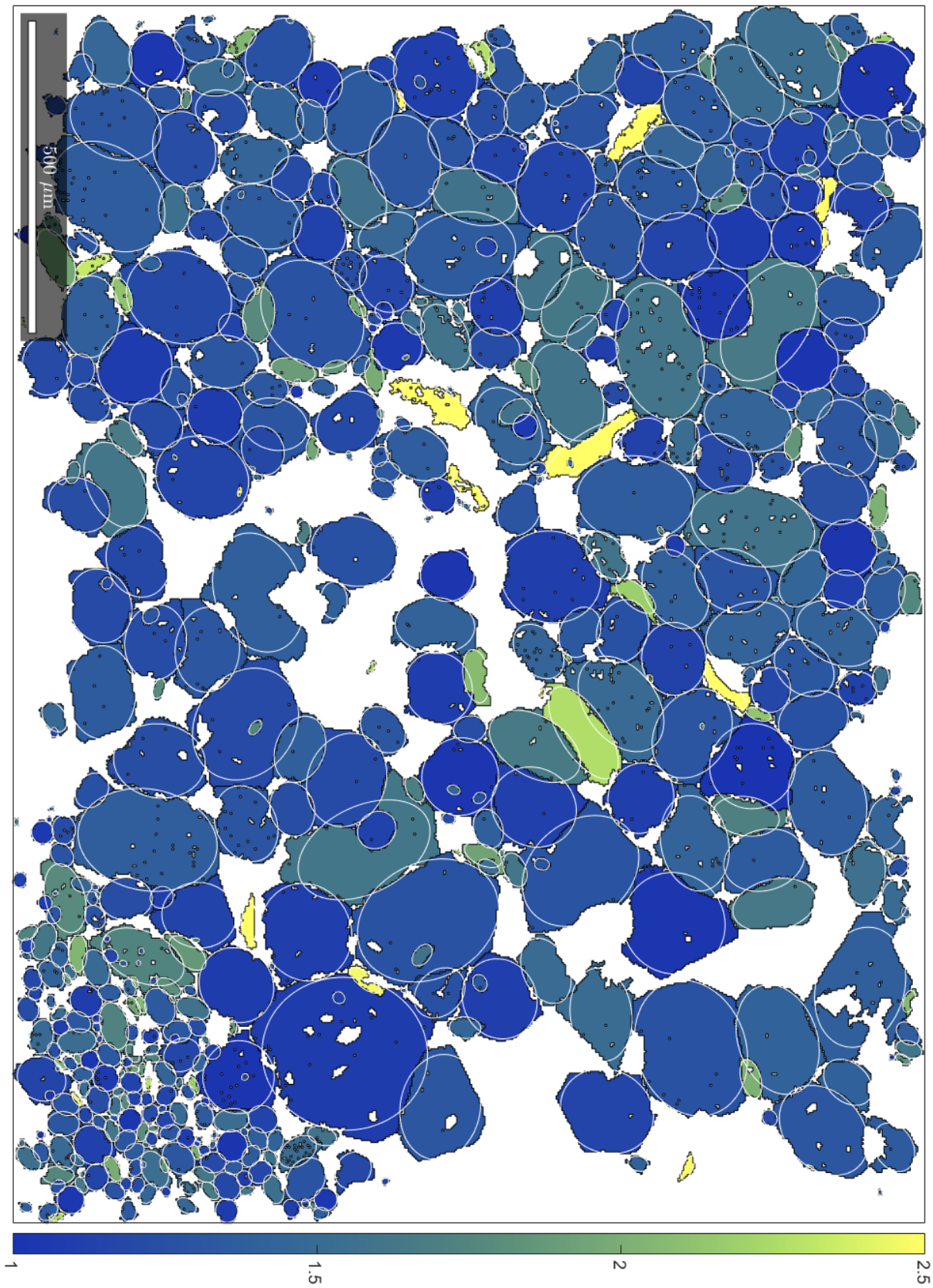

Figure B19: EC5_1A-1_M10 (655 x 491, 3 µm spacing)

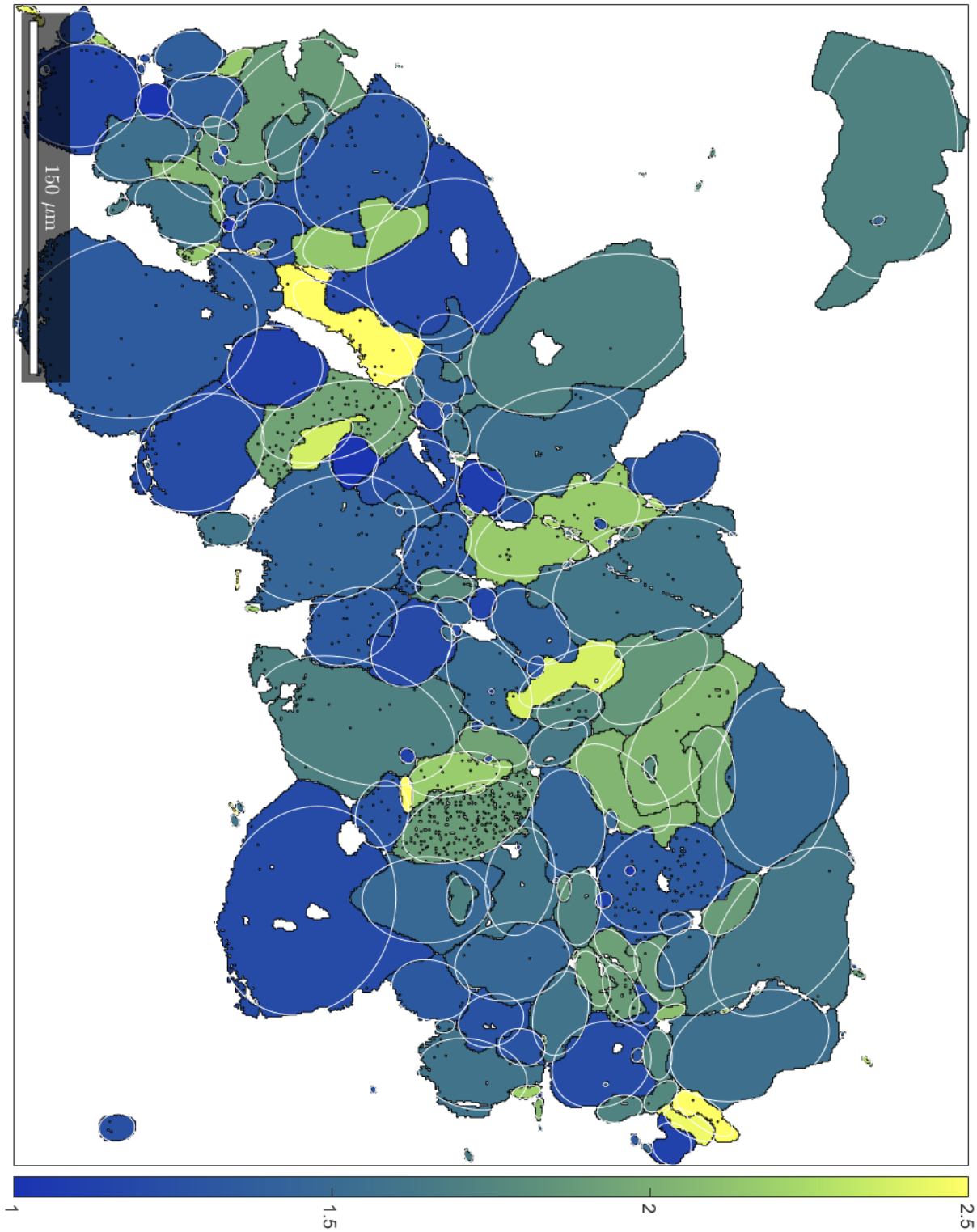

Figure B20: EC5_1A-1_M11 (724 x 591, 0.7 µm spacing)

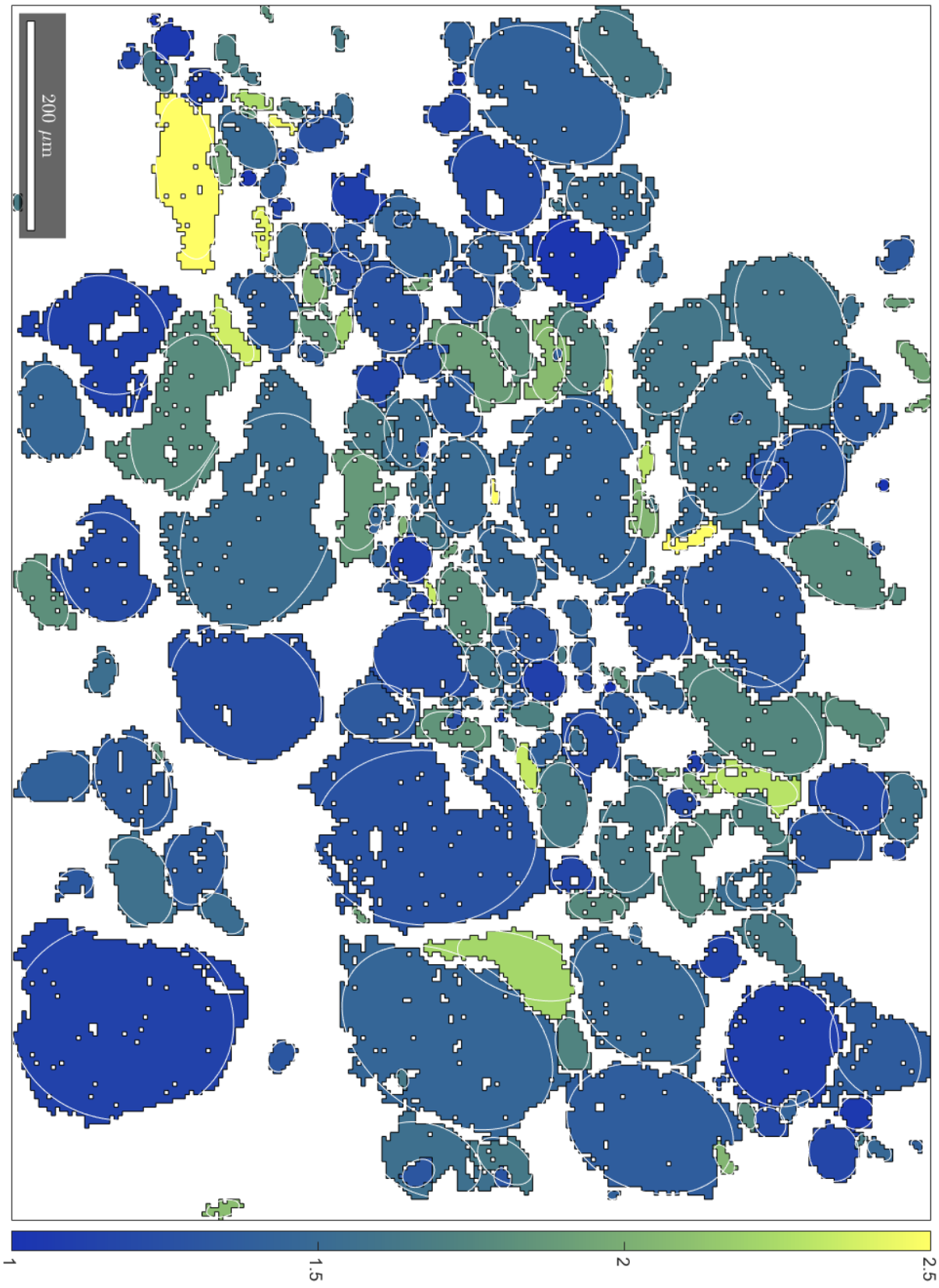

Figure B21: EC5_1A-1_M12 (294 x 221, 4 µm spacing)

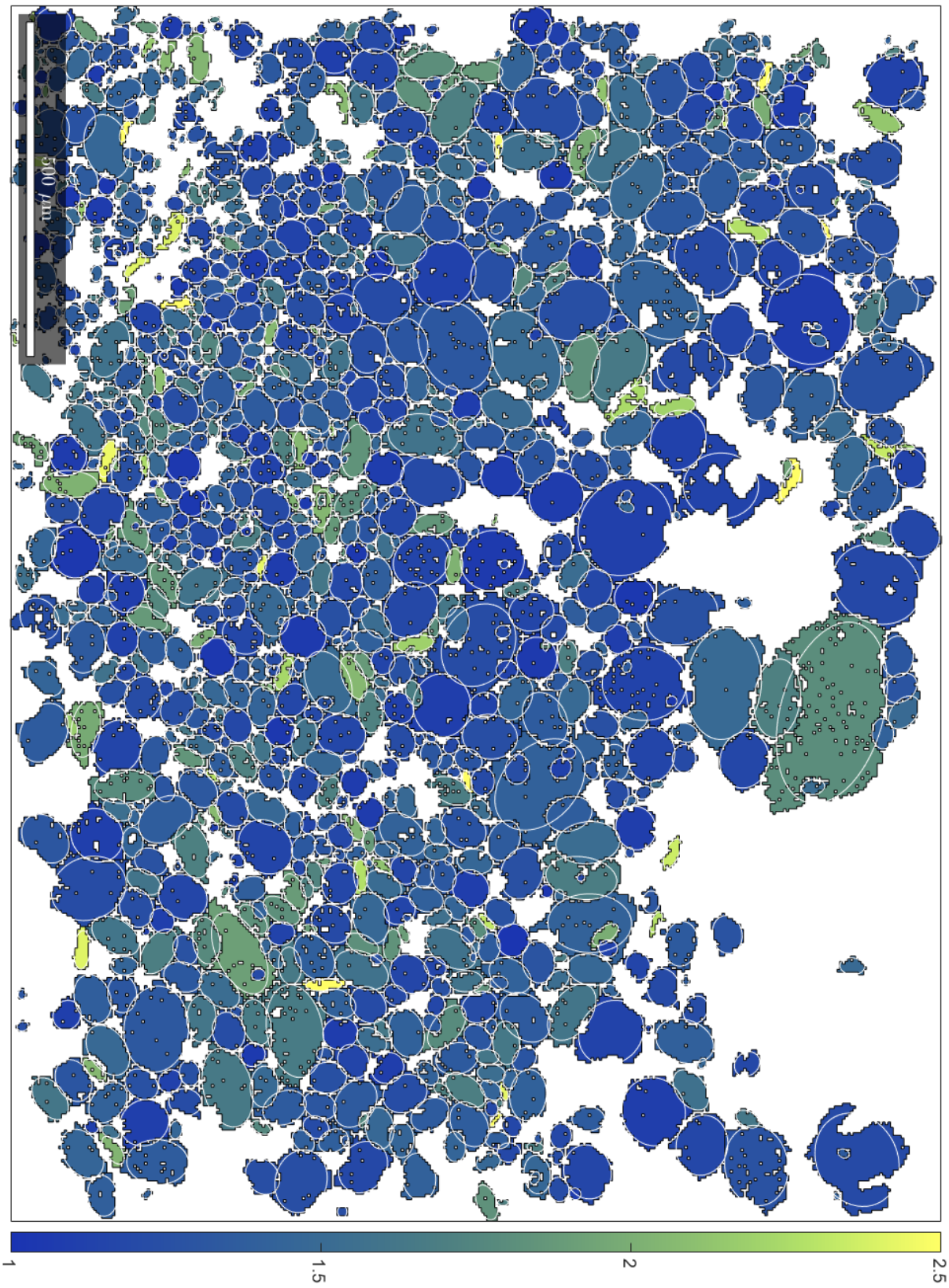

Figure B22: EC5_1A-1_M13 (456 x 350, 4 µm spacing)

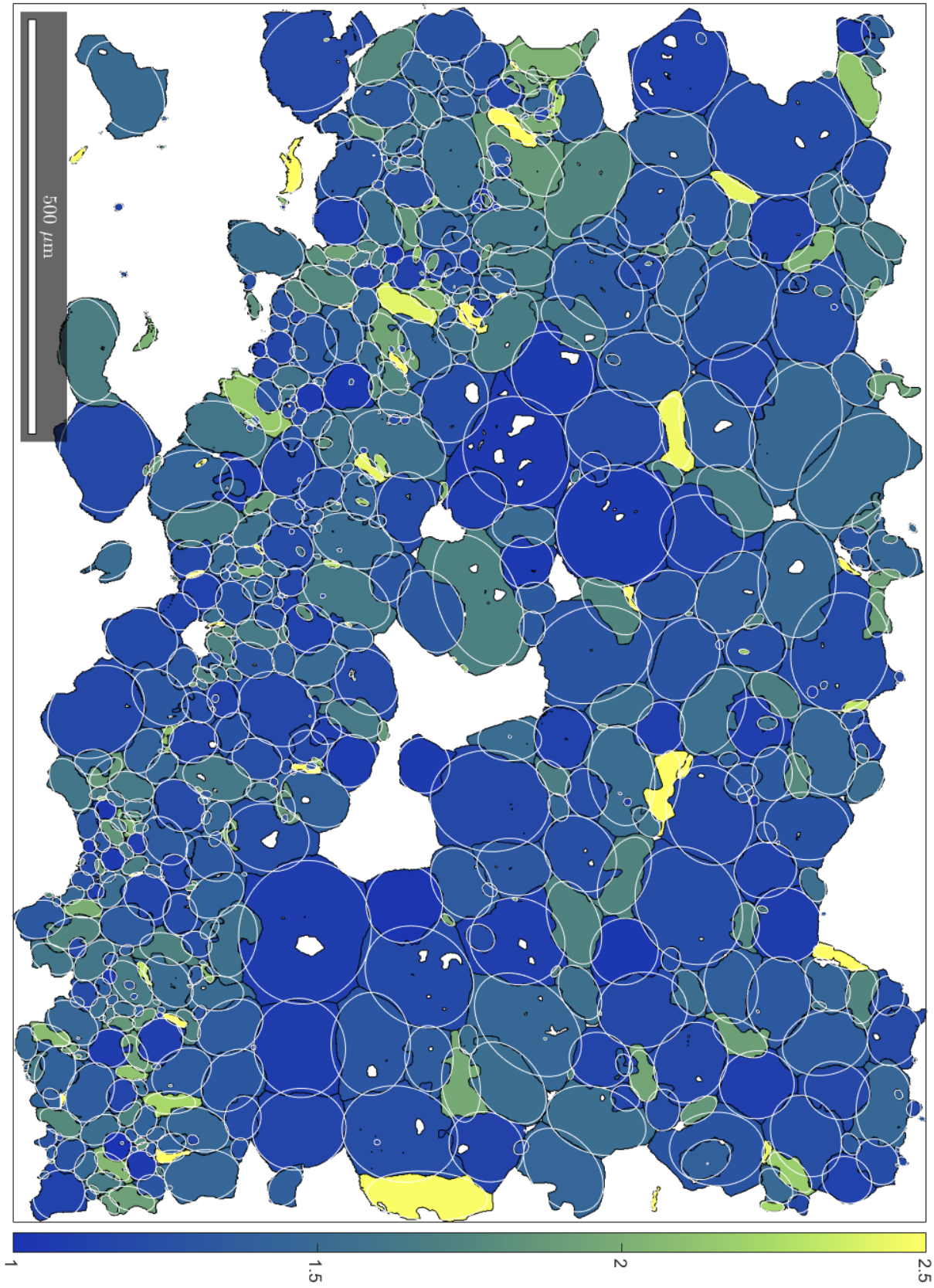

Figure B23: EC5_1A-1_2M3 (1638 x 1228, 0.9 μm spacing)

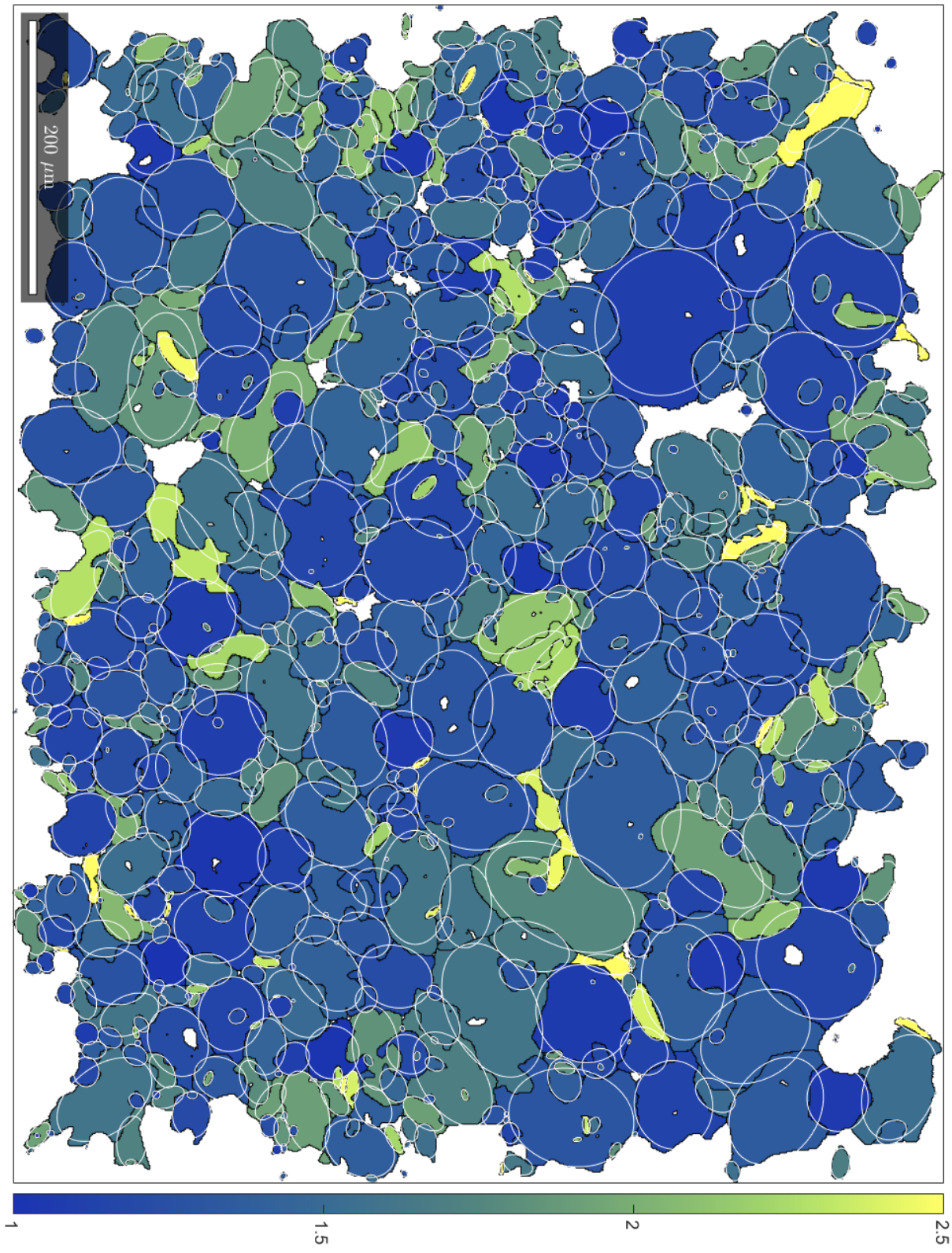

Figure B24: EC5_1A-1_2M4 (863 x 683, 1 µm spacing)

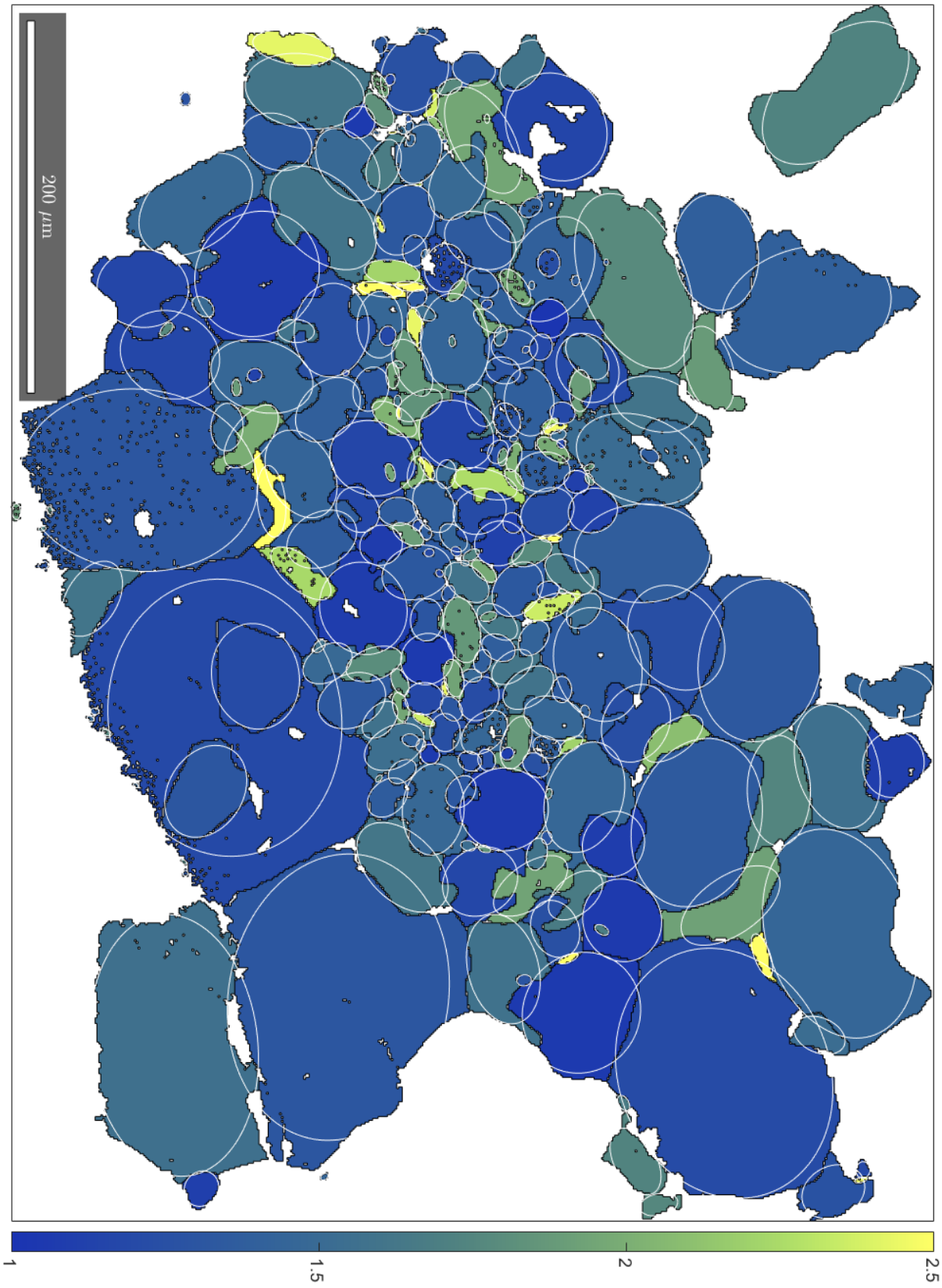

Figure B25: EC5_1A-1_2M5 (680 x 500, 1 µm spacing)

Appendix C: Supplementary data for Chapter 6

Table C1: Peak positions for the seven fitted Raman modes for all measurements on the zircon inclusions and the zircon reference crystal. Reference measurements that were rejected due to their high FWHM or a strong deviation from other reference measurements are displayed in gray. For 201, 213, 224, and 356, the fitting error is given.

msr.	date	time	dur. (s)	no.	m201	err.	m213	err.	m224	err.	m356	err.	m439	m975	m1009	FWHM
ref1vert	15-Jul	15:04:49	30		200.854	0.010	212.772	0.101	223.533	0.009			438.328	972.661	1006.022	3.884
ref2hori	15-Jul	15:10:26	30		200.778	0.009	212.896	0.044	223.595	0.009	355.467	0.006	438.411	973.379	1006.799	3.464
g996i02	15-Jul	16:40:31	30	1	200.707	0.027	213.696	0.030	223.832	0.023	357.397	0.023	439.209	975.723	1009.619	2.736
g996i04	15-Jul	16:55:06	30	2	200.920	0.278	213.851	0.092	223.943	0.221	356.723	0.472	439.297	975.866	1009.906	2.538
g996i07	15-Jul	17:11:06	30	3	200.725	0.051	213.445	0.217	223.844	0.049	357.655	0.073	439.210	976.069	1009.964	2.635
g795i01	15-Jul	18:33:55	30	4	200.612	0.117	213.014	0.351	223.431	0.105	356.645	0.155	441.079	974.717	1009.069	4.604
g795i02	15-Jul	18:38:16	30	5	200.650	0.051	213.583	0.168	223.719	0.047	357.430	0.063	439.385	975.878	1009.793	4.049
g717i03	15-Jul	18:58:59	30	6	200.424	0.048	213.543	0.025	223.490	0.048	357.358	0.065	439.025	976.293	1010.156	2.780
g717i04	15-Jul	19:04:39	30	7	200.351	0.025	213.568	0.032	223.655	0.021	357.789	0.044	439.071	976.002	1009.858	2.847
refvert1	29-Jul	11:02:42	30		201.380	0.006	214.049	0.066	224.321	0.005			439.223	973.664	1007.119	3.372
refhori1	29-Jul	11:07:27	30		201.257	0.020	213.314	0.052	224.148	0.019	355.496	0.010	438.745	973.290	1006.891	3.209
g040i02	29-Jul	17:49:40	30	8	200.631	0.018	213.627	0.018	223.677	0.017	357.410	0.013	439.143	975.831	1009.655	2.976
g040i03	29-Jul	17:54:01	30	9	200.672	0.040	213.515	0.036	223.752	0.039	357.901	0.037	439.016	976.100	1009.941	3.171
g077i01	29-Jul	18:13:34	60	10	200.729	0.091	213.861	0.329	223.977	0.089	358.833	0.085	439.809	977.572	1011.353	3.276
g096i01	29-Jul	18:22:05	30	11	200.496	0.011	213.873	0.023	223.720	0.011	358.373	0.025	439.355	976.984	1010.893	3.419
g112i01	29-Jul	18:27:49	30	12	200.916	0.082			224.033	0.080	357.177	0.179	439.497	975.971	1009.849	4.034
g212i01	29-Jul	18:33:40	30	13	200.806	0.020	213.880	0.038	223.933	0.019	357.907	0.026	439.209	976.333	1010.336	2.983
g425i01	29-Jul	18:46:20	30	14	200.692	0.011	214.722	0.253	223.966	0.013	357.730	0.028	439.554	976.269	1010.258	3.086
refvert2	29-Jul	18:55:00	30		200.867	0.007	212.900	0.073	223.710	0.006	355.020	0.003	438.242	973.039	1006.463	3.214
refhori2	29-Jul	18:57:29	30		200.936	0.025	213.041	0.037	223.853	0.023	355.318	0.010	438.599	973.089	1006.800	3.122
refvert1	30-Jul	09:45:37	30		201.174	0.004	213.413	0.036	224.085	0.003	355.625	0.002	438.809	973.600	1007.140	3.034
refhori1	30-Jul	10:15:03	15		201.350	0.037	213.001	0.054	224.171	0.032	355.181	0.018	438.602	973.073	1006.487	3.954
g302i03	30-Jul	10:32:07	30	15	201.368	0.042	214.418	0.246	224.497	0.040	357.857	0.026	439.932	976.448	1010.385	2.872
g314i01	30-Jul	10:37:43	30	16	201.251	0.122	214.375	0.736	224.323	0.109	358.242	0.070	439.534	976.552	1010.299	2.744
g565i01	30-Jul	10:43:44	30	17	200.928	0.008	214.304	0.081	224.148	0.007	357.752	0.006	439.745	976.270	1010.278	3.310
g544i01	30-Jul	10:49:36	30	18	201.178	0.007	214.764	0.043	224.563	0.006	357.760	0.004	440.031	976.690	1011.013	2.949
g548i03	30-Jul	11:07:50	30	19	201.104	0.022	213.911	0.030	224.164	0.021	358.975	0.066	439.369	976.431	1010.161	2.916
g548i05	30-Jul	11:17:40	30	20	201.114	0.032	214.150	0.026	224.409	0.029	358.538	0.020	439.605	976.279	1010.082	2.624
g591i01	30-Jul	11:38:14	30	21	200.904	0.046	213.882	0.133	224.038	0.043	357.118	0.035	440.064	976.267	1010.182	3.742
g668i01	30-Jul	11:48:37	60	22	201.233	0.070			224.451	0.039	357.489	0.091	440.648	975.812	1010.977	4.569
g668i02	30-Jul	11:58:22	30	23	201.003	0.055	214.049	0.031	224.299	0.048	357.855	0.056	440.134	976.278	1010.535	4.673
g644i01	30-Jul	12:07:21	30	24	201.494	0.019	214.496	0.139	224.534	0.019	357.916	0.015	439.862	976.517	1010.624	3.067
refvert2	30-Jul	12:44:27	15		201.079	0.007	213.561	0.070	223.998	0.006	355.853	0.005	438.790	973.715	1007.013	3.178
refhori2	30-Jul	12:48:18	15		201.205	0.017	213.096	0.024	224.007	0.015	355.662	0.006	438.626	973.546	1007.047	3.255

Appendix D: Supplementary data for Chapter 7

The supplementary data consists of seven tables of LA-ICP-MS analyses that include element concentrations, uncertainties, and detection limit. Given the large number of elements analysed and the high amount of analyses performed, these tables are too large to insert in the format of this thesis. Therefore the tables are available online at DOI: 10.5281/zenodo.4590278

Table D1: LA-ICP-MS analyses of host-rock garnet cores and rims. Core measurements are labelled with a c, e.g. gt13c, rim measurements are labelled with a r, e.g. gt13r. Measurements marked in red were labelled as contaminated during initial data processing. Values are given in ppm, except for Si28, the internal standard, which is given as wt%.

Table D2: LA-ICP-MS analyses of inner-garnetite garnet. Measurements marked in red were labelled as contaminated during initial data processing. Values are given in ppm. Si28 is the internal standard.

Table D3: LA-ICP-MS analyses of host-rock garnet rims within 1 cm distance of garnetite. Values are given in ppm. Si28 is the internal standard.

Table D4: LA-ICP-MS analyses of outer-garnetite garnet. Values are given in ppm. Si28 is the internal standard.

Table D5: LA-ICP-MS analyses of the euhedral overgrowth on the inner garnetite. Values are given in ppm. Si28 is the internal standard.

Table D6: LA-ICP-MS analyses of rutile from garnetite. Values are given in ppm, except for Ti47, the internal standard, which is given in wt%.

Table D7: LA-ICP-MS analyses of rutile from the omphacite vein in LCG1401. Values are given in ppm, except for Ti47, the internal standard, which is given in wt%.

Appendix E: Supplementary data for Chapter 8

Table E1: Acquisition conditions for the five extracted and analysed rutile needles.

	M1	M2	M3	M4	M5
Specimen	1	2	3	4	5
Instrument Model	LEAP 4000X HR				
Instrument Setting					
Laser Wavelength (nm)	355	355	355	355	355
Laser Pulse Energy (pJ)	50	70	70	70	70
Pulse Frequency (kHz)	200	200	200	200	200
Evaporation Control	Detection rate	Detection rate	Detection rate	Detection rate	Detection rate
Target Detection Rate (%)	0.8	0.8	0.8	0.8	0.8
Nominal Flight Path (mm)	382	382	382	382	382
Set Point Temperature (K)	50	50	50	50	50
Sample Temperature (K)	57.3	57.3	57.3	57.3	57.3
Chamber Pressure (Torr)					
Data Summary					
RootServer Version	44	44	44	44	44
CAMECAROOT version	18.44.416	18.44.416	18.44.416	18.44.416	18.44.416
Analysis Software	IVAS 3.8.0	IVAS 3.8.0	IVAS 3.8.0	IVAS 3.8.0	IVAS 3.8.0
Total Ions	9554093	38408013	74624407	67042738	66945638
Vol//bowl corr. Peak (Da)	32	32	32	32	32
Reconstructed					
Final specimen state	Intact	Intact	Intact	Intact	Intact
Pre-/post-analysis imaging	SEM/NA	SEM/NA	SEM/NA	SEM/NA	SEM/NA
Radius evolution	"Shank"	"Shank"	"Shank"	"Shank"	"Shank"
Field factor (k)	3.3	3.3	3.3	3.3	3.3
Image compression factor	1.65	1.65	1.65	1.65	1.65
Assumed E-field (V/nm)	26	26	26	26	26
Detector efficiency36%	36%	36%	36%	36%	
Avg, atomic volume nm3	0.0104	0.0104	0.0104	0.0104	0.0104
V initial; V final (kV)	XX; 8.8	XX; 9.5	XX; 9.6	XX; 10.0	XX; 9.3